



**HAL**  
open science

# Identification of antibody secreting cell affinity repertoires

Broketa Matteo

► **To cite this version:**

Broketa Matteo. Identification of antibody secreting cell affinity repertoires. Tissues and Organs [q-bio.TO]. Sorbonne Université, 2023. English. NNT : 2023SORUS616 . tel-04530791

**HAL Id: tel-04530791**

**<https://theses.hal.science/tel-04530791>**

Submitted on 3 Apr 2024

**HAL** is a multi-disciplinary open access archive for the deposit and dissemination of scientific research documents, whether they are published or not. The documents may come from teaching and research institutions in France or abroad, or from public or private research centers.

L'archive ouverte pluridisciplinaire **HAL**, est destinée au dépôt et à la diffusion de documents scientifiques de niveau recherche, publiés ou non, émanant des établissements d'enseignement et de recherche français ou étrangers, des laboratoires publics ou privés.



Sorbonne Université

ED394 - Physiologie, physiopathologie et thérapeutique

UMR 1222 Antibodies in Therapy and Pathology

# Identification of antibody secreting cell affinity repertoires

By Matteo Broketa

To obtain a PhD degree of Sorbonne Université in Immunology

Supervised by Dr Pierre Bruhns

Defended the 21<sup>st</sup> December 2023

Jury members:

Dr Natalia Freund	President of jury
Dr Marion Espeli	Reviewer
Pr Christoph Merten	Reviewer
Pr Behazine Combadiere	Examiner
Dr Jordan Dimitrov	Examiner
Dr Pierre Bruhns	Thesis supervisor

# Table of Contents

INTRODUCTION .....	10
What are antibodies?.....	10
Who makes antibodies? .....	13
B cell development and maturation .....	13
B cell activation and clonal expansion.....	14
Differentiation into Antibody-secreting cells.....	18
Transcriptional regulation of ASC differentiation .....	18
Fate commitment to ASC differentiation.....	19
Plasmablast to plasma cell differentiation.....	20
Homing and survival.....	22
ASCs during infection.....	23
ASCs in autoimmunity.....	26
How are ASC responses studied? .....	28
What is currently missing?.....	39
Aims .....	45
ARTICLE 1:.....	49
mRNA vaccine driven ASC response towards SARS-CoV2 RBD .....	49
ARTICLE 2.....	64
High Throughput Affinity Mapping on Anti-RBD Antibodies .....	64
ARTICLE 3.....	81
Characterization of Vaccinee Bmem-derived Ab affinities towards Omicron RBD .....	81
ARTICLE 4.....	92
Assessment of SARS-CoV-2 BA.1 breakthrough infection on Bmem repertoire remodeling .....	92
ONGOING PROJECT .....	109
DropPick: Isolation of cell-of-interest from DropMap .....	109
DropMap microfluidic assay.....	109
Linking phenotype to genotype with DropMap.....	109
Validation of photoactivable dye for DropPick .....	114
Development of fully automated uncaging protocol.....	121
Evolving DropMap Analyses.....	122
Automated illumination for droplet photoactivation.....	126
Visualizing DropPick photoactivated cells by FACS .....	130

Discussion and Perspectives for DropPick .....	131
ARTICLE 5 (MANUSCRIPT IN PREPARATION).....	142
Deep learning enabled label-free microfluidic droplet classification for single cell functional assays .....	142
ARTICLE 6.....	156
Characterizing autoreactive ASCs in multiple organs during primary ITP .....	156
GENERAL DISCUSSION .....	173
Emerging patterns from human DropMap affinity repertoires .....	173
Open Source and Standardized Microfluidics .....	179
BIBLIOGRAPHY .....	183

## List of figures

Figure 1 Overview of immunoglobulin structure .....	11
Figure 2 Phases of the T-dependent B cell response.....	15
Figure 3 Antigen affinity discrimination by germinal center B cells.....	17
Figure 4 Major transcriptional regulators of late B cell differentiation .....	19
Figure 5 Characteristics of extrafollicular (EF) and germinal center (GC) derived plasmablasts. ....	22
Figure 6 Survival signals from plasma cell niche. ....	23
Figure 7 Kinetics of antibody responses during acute SARS-CoV2 infection. ....	25
Figure 8 Conflicting models in role of affinity in ASC differentiation .....	41
Figure 9 Graphical abstract from Broketa et al (2023) .....	49
Figure 10 Overview of DropMap assay .....	110
Figure 11 DropPick Pipeline.....	113
Figure 12 Mechanism of CNB-CFSE labelling and uncaging.....	115
Figure 13 Evaluation of CMNB-CFSE photoactivatable dye.....	116
Figure 14 Effects of CMNB-CFSE on ASC proportion and IgG secretion rate .....	118
Figure 15 Diaphragm closure for single droplet illumination.....	119
Figure 16 Discrete photoconversion of Vav-H2B-Dendra2 splenocyte via DropPick. ....	121
Figure 17 Workflow of Python DropMap Analysis.....	123
Figure 18 Example images of droplets from DropMap .....	124
Figure 19 Droplet report generated by automated secondary analysis. ....	125
Figure 20 Interactive data viewer for automated DropMap analyses. ....	125
Figure 21 Example path of DropPick illumination program. ....	127
Figure 22 Overview of targeted droplet illumination procedure .....	128
Figure 23 Record-keeping of droplet illumination and photoactivation. ....	129
Figure 24 Visualizing CMNB-CFSE labeled PBMCs photoactivated by DropPick. ....	130
Figure 25 Visualizing photoconverted Vav-H2B-Dendra2 splenocytes by FACS.....	131
Figure 26 Scenarios potentially skewing relocation slope fitting. ....	138
Figure 27 Equations for Ig secretion calculation. ....	139
Figure 28 Comparison of affinity repertoires after antigen-based sorting. ....	175
Figure 29 Kinetics of ASC response during immunization with TT in mice (From Eyer et al, 2016).....	177

## List of abbreviations

ADE	Antibody-dependent enhancement
AID	Activation-induced cytidine deaminase
APC	Antigen presenting cell
APRIL	A proliferation-inducing ligand
ASC	Antibody secreting cell
BCR	B cell receptor
BLI	Bio-layer interferometry
BM	Bone marrow
Bmem	B memory cell
CDR	Complementarity-determining region
CFSE	Carboxyfluorescein succinimidyl ester
CMNB	Carboxymethoxy-2-Nitrobenzyl
CNN	Convolutional neural network
COVID	Coronavirus disease
CSR	Class switch recombination
DBMF	Droplet based microfluidics
DC	Dendritic cell
DNA	Deoxyribonucleic acid
EF	Extrafollicular
ELISA	Enzyme-linked immunosorbent assay
ELISPOT	Enzyme-linked immunosorbent spot
FACS	Fluorescence-activated cell sorting
FC	Flow cytometry
FITC	Fluorescein isothiocyanate
FLISA	Fluorescence-linked immunosorbent assay

HIV	Human immunodeficiency virus
HSC	Hematopoietic stem cell
Ig	Immunoglobulin
IL	Interleukin
ITP	Immune thrombocytopenia
KD	Dissociation constant
LLPC	Long-lived plasma cell
MACS	Magnetic activated cell sorting
MFI	Median fluorescence intensity
MHC	Major histocompatibility complex
MS	Multiple sclerosis
MZ	Marginal zone
NHEJ	Non-homologous end joining
NP	4-Hydroxy-3-nitrophenyl
PALM	Photo-activated localization microscopy
PB	Plasmablast
PBMC	Peripheral blood mononuclear cell
PBS	Phosphate buffered saline
PC	Plasma cell
PCR	Polymerase chain reaction
RBD	Receptor binding domain
RNA	Ribonucleic acid
SARS	Severe Acute Respiratory Syndrome
SD	Standard deviation
SHM	Somatic hypermutation
SLE	Systemic lupus erythematosus
SLO	Secondary lymphoid organ

SPR	Surface plasmon resonance
TCR	T cell receptor
Tfh	T follicular helper cell
Th	T helper cell
TLR	Toll-like receptor
TT	Tetanus toxoid
UCA	Unmutated common ancestor
UV	Ultraviolet
WT	Wild type

## Abstract (English)

This research aimed to explore the complexities of antibody affinities of antibody-secreting cells (ASCs) in the context of both vaccination and autoimmune responses.

The first aim was to characterize the ASC response to mRNA vaccination against SARS-CoV-2. The advent of novel mRNA vaccines to tackle the COVID-19 pandemic presented a unique opportunity to study a novel humoral B cell response post-immunization. We used a droplet microfluidic assay, DropMap, able to measure single cell antibody secretion and affinity towards antigen to characterize at high throughput the functional characteristics of ASCs in the weeks and months following mRNA vaccine administration, with a distinction made between individuals based on prior SARS-CoV-2 infection. Our characterization of the ASC response to mRNA vaccination against SARS-CoV-2 has provided valuable insights into how B cells respond to novel vaccines and affinity repertoires during human vaccination.

The second aim was to measure the affinity repertoires of a non-natively secreting B cell population, memory B cells (Bmem), following mRNA vaccination against SARS-CoV-2. This involved characterizing the affinity repertoires of Bmem-derived antibodies towards numerous SARS-CoV-2 receptor-binding domain (RBD) variants by implementing a high throughput screening system based on biolayer interferometry (BLI) measurements.

The third aim was to develop a novel technique (termed DropPick) for recovering cells of interest from DropMap. DropMap is a potent technique for direct identification of ASCs and affinity characterization. However, there is much more to be discerned from analyzing these cells of interest using additional methods, such as flow cytometry for phenotyping or B cell receptor sequencing for clonal analyses and re-expression.

My thesis work has shown that after receiving the BNT162b2 vaccine targeting the Hu-1 SARS-CoV-2 Spike protein, high-affinity plasmablasts were initially induced targeting both the Hu-1 and Omicron Spike RBD variants but exhibited a rapid decline. Surprisingly, plasmablasts with low affinity consistently constituted more than 65% of the specific plasmablast response at all observed time points. Our high throughput BLI affinity measurements on Bmem antibodies from similarly vaccinated individuals found high affinity clones against several RBD variants with signs of affinity maturation; comparing results between variants allowed for key antibody binding epitopes to be determined. Following this cohort of Bmem antibodies also found that viral evolution to the Omicron RBD variant resulted in a large evasion of Bmems mutated towards Hu-1 RBD with high affinity, with especially high evasion of potentially Hu-1 and Beta neutralizing antibodies. In parallel, I have developed a system to label cells of interest using photoactivatable markers within DropMap and the technical platform to achieve targeted cell photoactivation by targeted UV illumination. This involved the creation of automated programs for DropMap assay real-time analyses as well as macro control of microscope utilities to deliver discrete illumination to droplets. I have also shown the ability for this workflow to yield a clear population by flow cytometry with up to 70% efficiency, with the potential for sorting and future downstream analyses.

These results will aid ongoing efforts to understand the role of affinity in ASC responses and their immune contexts. Our data provide broad affinity repertoires that provide valuable functional insights into B cell responses to SARS-CoV-2 and mRNA vaccination. The development of the DropPick platform has shown the potential to further leverage these studies to collect molecular data from specific functional subsets.

## Résumé (Français)

Mon travail de thèse a consisté à explorer les répertoires d'affinités des anticorps produits par les lymphocytes B humains durant la vaccination SARS-CoV-2.

Objectif #1 : caractériser la réponse de cellules sécrétrices d'anticorps (ASC) à la vaccination par ARNm contre le SARS-CoV-2. Les nouveaux vaccins à ARNm pour lutter contre la pandémie de COVID-19 a présenté une opportunité unique d'étudier une nouvelle réponse humorale des cellules B après immunisation. Nous avons utilisé une méthode microfluidique, DropMap, capable de mesurer la sécrétion d'anticorps et l'affinité envers l'antigène pour caractériser des ASC suite à l'administration du vaccin à ARNm. Cette analyse a fourni des informations précieuses sur la façon dont les cellules B répondent aux nouveaux vaccins et a permis de décrire des répertoires d'affinité de ASC humains suite à une vaccination.

Objectif #2 : mesurer les répertoires d'affinité d'une population de cellules B non sécrétrices, les cellules B mémoire (Bmem), après vaccination par ARNm contre le SARS-CoV-2. Ceci impliquait de caractériser les répertoires d'affinité des anticorps dérivés de Bmem envers de nombreuses variants du domaine de liaison au récepteur (RBD) du SARS-CoV-2 en mettant en œuvre un système de criblage à haut débit basé sur des mesures d'interférométrie de biocouche.

Objectif #3 : développer une technique (appelée DropPick) pour récupérer des cellules d'intérêt à partir des puces microfluidiques de la méthode DropMap. DropMap est une technique puissante pour l'identification directe des ASC et la caractérisation de la spécificité et de l'affinité des anticorps qu'elles sécrètent. Beaucoup d'autres informations restent à obtenir en analysant les cellules d'intérêt à l'aide de méthodes supplémentaires, telles que la cytométrie en flux pour le phénotypage ou le séquençage des récepteurs des cellules B pour les analyses de clonalité et la réexpression sous forme d'anticorps recombinants.

Mes travaux de thèse ont montré qu'après avoir reçu le vaccin BNT162b2, des ASC de haute affinité sont initialement induits ciblant à la fois les variants de RBD Hu-1 et Omicron, mais disparaissent rapidement. Les ASC de faible affinité représentaient systématiquement plus de 65% de la réponse spécifique des ASC. Nos mesures d'affinité sur les anticorps issus de Bmem provenant d'individus vaccinés ont révélé des clones à haute affinité contre plusieurs variants de RBD et présentant une maturation d'affinité ; la comparaison des résultats entre les variants a permis de déterminer les épitopes clés de liaison aux anticorps. Grâce à cette collection d'anticorps provenant de Bmem, nous avons également découvert que l'évolution virale vers le variant Omicron entraînait une évasion de Bmems mutés qui reconnaissaient Hu-1 RBD avec une affinité élevée, et avait un fort impact négatif sur des anticorps neutralisants puissants Hu-1 et Beta.

J'ai développé un système pour marquer les cellules d'intérêt avec des marqueurs photoactivables au sein de DropMap et établi une plateforme pour réaliser une photoactivation cellulaire par illumination UV ciblée. Cela impliquait la création de programmes automatisés pour les analyses en temps réel du test DropMap ainsi que le contrôle macro des utilitaires du microscope pour fournir un éclairage discret aux gouttelettes. J'ai également montré la capacité de cette technique à sélectionner une population par cytométrie avec une efficacité jusqu'à 70% avec un potentiel de tri et de futures analyses en aval.

Ces résultats contribueront aux efforts en cours pour comprendre le rôle de l'affinité dans les réponses ASC en vaccinologie. Nos larges répertoires d'affinité fournissent des informations fonctionnelles précieuses sur les réponses des cellules B à la vaccination contre le SARS-CoV-2. La plateforme DropPick démontrera prochainement son potentiel à associer des données moléculaires de cellules uniques à des sous-ensembles fonctionnels spécifiques déterminés par DropMap.

# INTRODUCTION

# INTRODUCTION

## What are antibodies?

Antibodies, formally referred to as immunoglobulins (Ig), are highly variable proteins that play a key role in the immune system. Antibodies are assembled from 2 types of polypeptide chains, termed heavy and light chains, which are connected by disulphide bonds. Heavy-light chain pairs then form additional disulphide bonds between each other to ultimately form a Y-shaped base molecule<sup>1,2</sup>. The heavy chain determines the antibody class (IgG, IgM, IgA, etc.) through the nature of its end constant region, which determines how the antibody interacts with its environment and other heavy-light chain pairs to form complex multi-pair structures. Light chains contribute to the diversity of antibodies together with the heavy chain.

Heavy and light chains can both be divided into variable and constant regions, with the former primarily responsible for enabling binding of the antibody to a target and the latter providing structure and a means for environmental signalling<sup>3</sup>. Interestingly, the constant and variable regions of antibody chains do not act independently and influence each other through conformational changes<sup>4</sup>. Antibody variability is achieved through the selection of diverse segments from multiple sets of available genes encoding the variable regions of heavy and light chains. The variability in the antigen-binding site within the variable region is generated through a process known as V(D)J recombination, where different gene segments are combined during B cell development. This variability allows the immune system to generate a wide range of antibodies, each with a unique ability to recognize a specific antigen. Antigens can be defined as any structure capable of being bound by an antibody, with the specific site of recognition being called the epitope; an antigen may have one or more epitopes.

The Ig heavy chain gene is composed of multiple gene segments that encode for variable (V), diversity (D), and joining (J) regions. There are multiple copies of each gene segment with unique base-pair variations, allowing for approximately  $10^{11}$  combinations, although most combinations are non-productive, so the true diversity is estimated to be  $\sim 10^7$  antibodies<sup>5</sup>. V(D)J recombination is initiated by the activation-induced cytidine deaminase (AID) enzyme, which deaminates cytidine residues in the DNA to then introduce single-stranded DNA breaks<sup>6</sup>. Breaks are introduced at ends of selected V, D, and J gene segments, with the intermediate DNA removed to allow for the selected VDJ segments to be directly joined. The single-stranded breaks are then

repaired by the non-homologous end joining (NHEJ) pathway, which imprecisely joins the ends of the gene segments together for added “junctional” diversity. The recombined Ig heavy chain genes are then subject to a process of selection to ensure the proper folding and function of the antibody; this selection process involves the elimination of cells with abnormal Ig heavy chain genes. Light chain generation follows similar processes of recombination, however light chain gene segments are split across multiple loci and gene families (Kappa and Lambda). Despite the apparent diversity of light chain gene segments, public clonotypes constitute the majority of human kappa and lambda light chain repertoires<sup>7,8</sup>. Additionally, certain antigens have been shown to be significantly biased towards kappa or lambda light chain antibodies<sup>9</sup>.

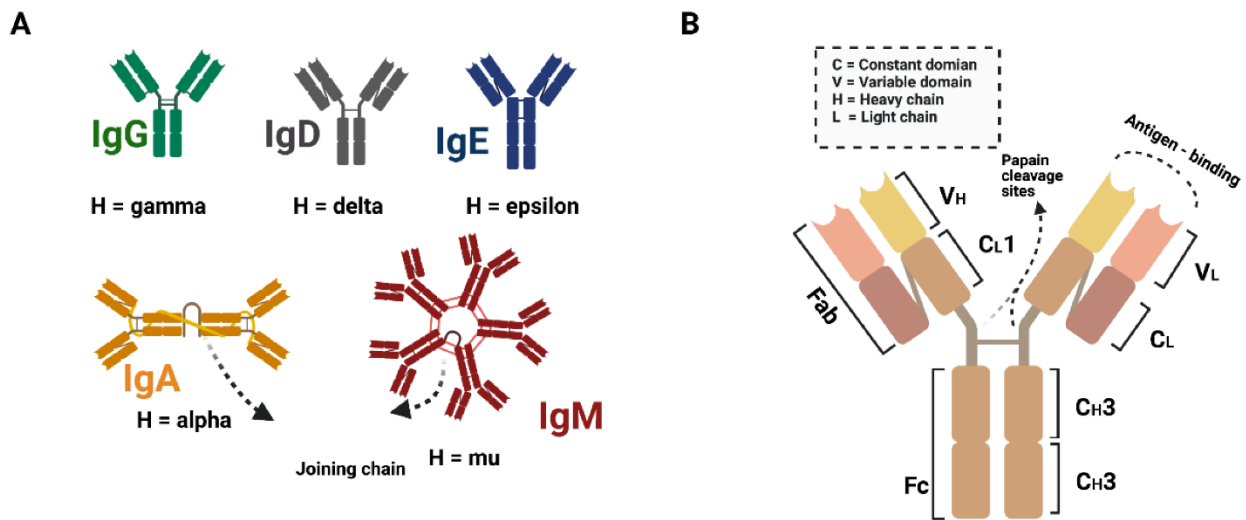


Figure 1 Overview of immunoglobulin structure. (A) Different immunoglobulin isotypes, with heavy chain designation H = heavy chain name. (B) Subunits and domains of an immunoglobulin. (Taken from Wu and Song, 2022)<sup>10</sup>.

Despite being referred to as constant, the constant region of antibody heavy chains also undergoes several transformative processes to tailor the antibodies’ function. Antibody class switching refers to the process by which B cells change the class of immunoglobulin they produce<sup>11</sup>, involving the deletion and recombination of constant gene segments, leading to the expression of a different heavy chain. Class switching occurs after B cells have been activated and expanded in response to an antigen. Class switching is regulated by signaling pathways activated by antigen binding, cytokines, and receptor engagement with T cells and other immune cells. The primary signaling pathway involved is the CD40L-CD40 pathway, where CD40L on activated T cells binds to CD40 on B cells and enables isotype switching; other cytokines and signaling pathways, such as IL-4

and TGF- $\beta$ , also play a role in regulating class switching<sup>12</sup>. The timing of class switching is critical and is influenced by several factors, including the nature of the antigen, the stage of the immune response, and the presence of other cytokines and their signaling pathways. Class switching ultimately allows for tailoring of the antibody response to the encountered antigen and is essential for generating a robust and effective immune response to a wide range of antigens.

IgM is the first Ig isotype produced by B cells in response to an antigen and is the largest Ig molecule. It is highly effective in neutralizing pathogens but is less effective in penetrating tissues compared to other isotypes. IgG is the most abundant Ig isotype in the blood and is the main antibody involved in secondary immune responses<sup>13</sup>. It has a long half-life and can penetrate tissues, making it effective in neutralizing pathogens in a variety of tissues and organs. IgA is the main Ig isotype found in mucosal secretions, such as saliva, tears, and breast milk. It provides protection against pathogens at mucosal surfaces and is involved in regulating local immune responses. IgD is found early in small amounts on the surface of B cells and plays a role in the initiation of immune responses, in conjunction with IgM. IgD also contributes to mucosal immunity when secreted by IgD plasma cells that have gone through a non-classical CSR pathway<sup>14</sup>. The evolutionary conservation of IgD and its unique features when secreted, including lambda ( $\lambda$ ) light chain bias and elongation in the antigen binding site, suggest a key role in regulation of commensals and protection from pathogenic microbes<sup>15</sup>. IgE is involved in allergic reactions and is the main antibody involved in immediate hypersensitivity reactions, binding to allergens and triggering the release of inflammatory mediators from mast cells and basophils. Importantly, the changing of isotype from IgM or IgD to IgG, IgE, and IgA likely introduces changes to signaling behavior as a B cell receptor (BCR) via elongated intracellular domains, with elevated basal activity reported particularly for IgG and IgE<sup>16</sup>.

Antigen binding by antibodies is performed by the antigen-binding site, formed by the variable regions of heavy and light chains, and contains three complementarity determining regions (CDRs), which are the most variable regions of the antibody<sup>17</sup>. These CDRs are particularly responsible for forming the specific shape and charge that allows the antibody to bind to the antigen, by interacting with specific residues on the epitope to yield hydrogen bonds and hydrophobic interactions. This interaction stabilizes the binding between the antibody and the epitope. The CDR3 is especially notable for having increased diversity, due to D gene inclusion in

heavy chains and junctional mutations from joining to both V and J segments and is often considered to largely determine specificity<sup>18</sup>. The strength of the interaction between the antibody and the epitope is known as the affinity of the binding, which is influenced by the specificity and stability of the non-covalent interactions between antibody and epitope. The presence of aromatic amino acids within the antigen binding site aids particularly in shape complementarity selection.

## **Who makes antibodies?**

### **B cell development and maturation**

B cells are components of the adaptive immune system that are uniquely capable of producing antibodies<sup>19,20</sup>. The bone marrow is the primary site of B cell development, where hematopoietic stem cells (HSCs) differentiate into B cells through a series of well-defined stages. The process of B cell maturation and selection in the bone marrow is a tightly regulated process that involves a complex network of transcription factors and signaling pathways.

B cell development in the bone marrow can be divided into several stages based on the expression of specific surface markers and the rearrangement of the immunoglobulin (Ig) genes<sup>21</sup>. These stages include the pro-B, pre-B, and immature B cell stages. B cell development begins with the commitment of HSCs to the B cell lineage in the bone marrow. The earliest B cell progenitors are known as pro-B cells, which are largely controlled by the early B cell factor 1 (EBF1) essential for the expression of other transcription factors required for B cell development such as Pax5, Ikaros, and E2A. Pro-B cells may be subdivided into early and late cells according to their stage of heavy chain formation, with D-J joining occurring in the former and V-DJ joining marking the latter.

The next stage of B cell development is the pre-B cell stage, which is characterized by the expression of the pre-B cell receptor (pre-BCR). The pre-BCR is composed of a surrogate light chain (VpreB and lambda5) and a rearranged heavy chain ( $\mu$ ), which are co-expressed on the cell surface. The pre-BCR plays a critical role in B cell development by promoting proliferation and survival of pre-B cells and initiating the process of Ig gene rearrangement<sup>22</sup>. The expression of the pre-BCR is regulated by several transcription factors, including Pax5, E2A, and the recombination-activating genes (RAG1/2), which mediate Ig gene rearrangement<sup>23</sup>.

Following successful Ig gene rearrangement, pre-B cells differentiate into immature B cells, which express IgM on the cell surface. Immature B cells are still undergoing final stages of development

and are not yet fully functional. At this stage, B cells are subject to negative selection, a process that eliminates autoreactive B cells and ensures self-tolerance. In this process, B cells that express a high-affinity B cell receptor for self-antigens undergo apoptosis or receptor editing to change their specificity.. Immature B cells that express high levels of self-reactive IgM are deleted by apoptosis through a process known as clonal deletion, whereas immature B cells that express lower levels of self-reactive IgM undergo receptor editing, a process that modifies the Ig genes to reduce self-reactivity<sup>24</sup>.

### **B cell activation and clonal expansion**

Mature naïve B cells in the periphery consist of follicular B cells and marginal zone (MZ) B cells located within secondary lymphoid organs (SLO) and B-1 B cells that may be found throughout the body but especially at mucosal boundaries<sup>25</sup>. The proximity of MZ B cells and B-1 B cells to boundaries and high flux areas allows them to directly encounter and respond to blood-borne and environmental pathogens, for which these B cell types are specialized. MZ B cells and B-1 B cells are capable of responding directly to antigens, thereby classified as T cell-independent antigens, which share considerable overlap with the pathogen-associated molecular patterns recognized by the innate immune system; coactivation of TLR is a key feature of the T-cell independent response. The result of T cell-independent antigen exposure is the rapid generation of IgM<sup>+</sup> and IgA<sup>+</sup> antibody secreting cells (ASCs), which secrete lower affinity, germline encoded antibodies and are shorter lived<sup>26</sup>. B-1 cells are also responsible for producing natural antibodies (natAbs), which are predominantly IgM and polyreactive; polyreactivity is distinct from cross-reactivity as the former concerns the ability to bind multiple unrelated epitopes that may often be of self-origin<sup>27</sup>. Importantly, natAb secretion is not primarily antigen or infection driven and rather is constitutively secreted by B-1 cells at low levels. NatAbs from B-1 cells form an immediate, broad form of defense that has been shown to significantly affect early pathogen replication and survival outcomes<sup>28,29</sup>.

The alternative means of initiating a B cell response and ASC differentiation is through T cell-dependent antigens characterized through two stages, an immediate extrafollicular (EF) response and a later developing germinal center (GC) mediated response (Figure 2). Binding of the BCR to either soluble antigen or antigen displayed by antigen presenting cells (APCs), as well as the

influence of stimulatory cytokines secreted by other responding immune cells, activates B cells and drives them to migrate towards T-cell rich zones of SLOs. Stimulation of activated B cells by

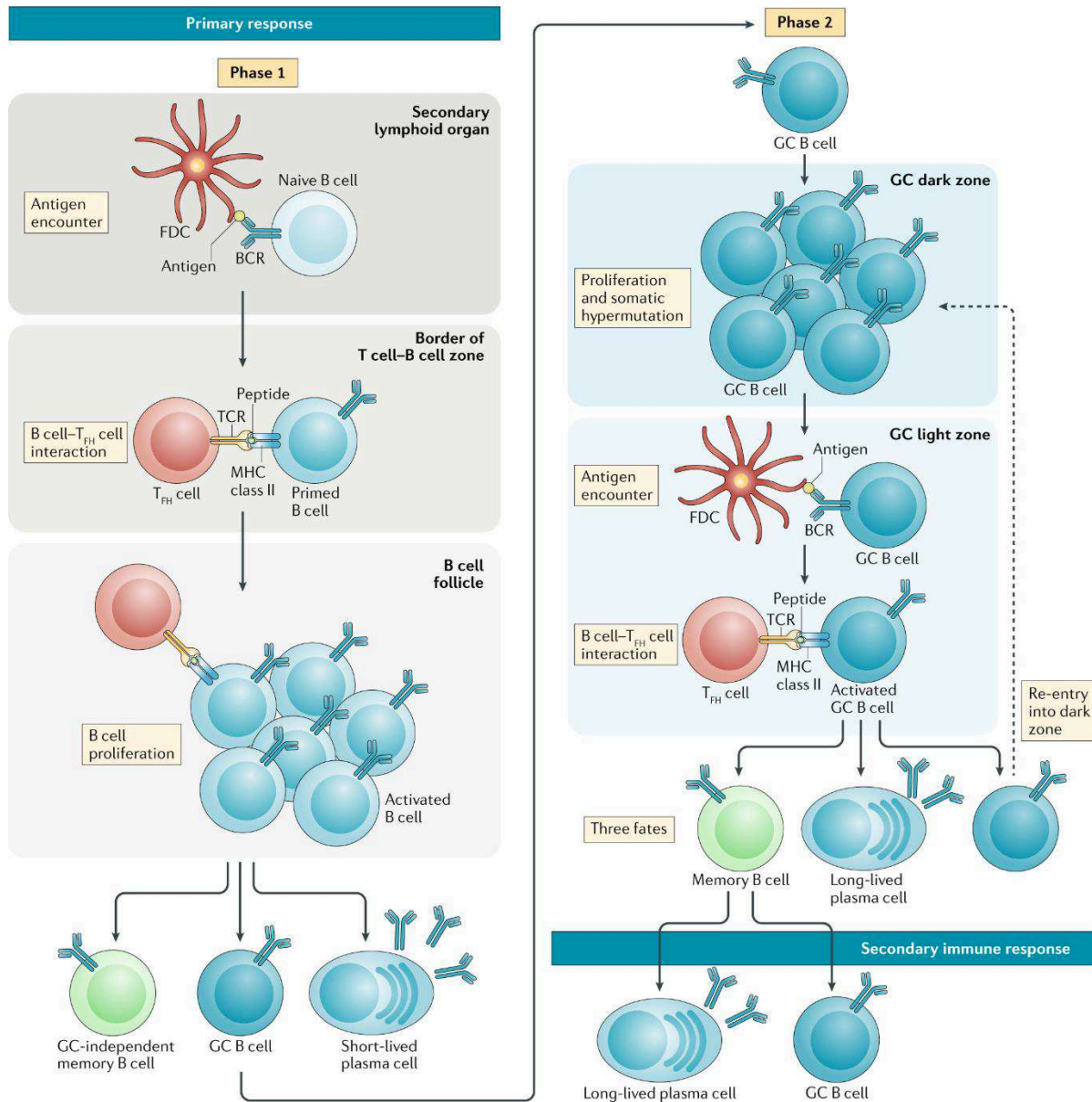


Figure 2 Phases of the T-dependent B cell response. T-dependent B cell activation begins with the recognition of antigens by membrane-bound B cell receptors (BCR) on the B cell surface. These antigens can also be internalized, processed, and presented as peptide-MHC-II complexes. A T helper (TH) cell then recognizes this complex via its T cell receptor (TCR), and this interaction is facilitated by costimulatory molecules like CD28. Following this interaction, the TH cell expresses CD40 ligand (CD40L), which interacts with CD40 on the B cell, providing a crucial second signal for B cell activation. After receiving these signals, the B cell is activated and rapidly proliferates, producing many cells carrying the same antigen receptor. These cells then differentiate into effector cells that defend the body and memory cells that provide long-term immunity. Some cells continue to proliferate and undergo somatic hypermutation, forming a germinal center (GC). The newly mutated GC B cells move from the proliferative dark zone towards the

light zone containing antigen and T cells. In the light zone, GC B cells compete for stimulatory input from antigen and T follicular helper cells, which selects higher affinity B cell clones. Surviving clones differentiate into memory B cells or plasma cells or can re-enter the GC process. (Taken from Akkaya et al, 2020)<sup>30</sup>.

cognate T helper cells through CD40 and CD40L interaction, IL-4, and IL21, promotes activated B cell proliferation and further differentiation. Activation at this stage also promotes class switch recombination, in which the Ig isotype is changed from IgM or IgD to either IgG, IgE, or IgA depending on the nature of the antigen and elicited cytokine environment<sup>31</sup>. The EF and GC responses then deviate with a portion of activated cells migrating away to form extrafollicular foci centered around CD11c<sup>high</sup> dendritic cells (DCs), which are heterogeneous in their recruitment of CD4+ T cells<sup>32,33</sup>. EF activated B cells are notable for their elevated propensity for ASC differentiation and produce the majority of antibodies during the early days of antigen encounters<sup>34</sup>.

The activated B cells that remain in contact with T cells proliferate extensively and are joined by T follicular helper cells (Tfh) and follicular dendritic cells to form a complex cellular structure, the germinal center. The primary purpose of the GC is to drive clonal evolution to obtain higher affinity antibodies through somatic hypermutation (SHM). Notably, GCs are not structures expressly intended for the mass production of B cells, as once the GC reaches maturity there is minimal further expansion despite a consistent rate of proliferation<sup>35</sup>; instead, GCs represent regions of net cell death as clones are aggressively modified and selected on the basis of affinity. Affinity maturation within the GC begins with clonal expansion in the GC dark zone marked by SHM, which introduces mutations within the variable region encoding genes of the BCR; these mutations are intended to yield subtle alterations in the antigen binding site of the antibody to improve affinity. GC B cells then migrate to the light zone, where they encounter APCs, including follicular DCs and macrophages, and Tfh cells that provide stimulatory signals to GC B cells bearing antigen<sup>30</sup>. Two models for affinity selection have been formulated, based on the competition for either antigen binding or Tfh cell help. Ultimately these models compare the relative decisiveness between BCR-linked activation and Tfh costimulatory help for GC B cell survival, with both inputs evidently necessary for efficient and robust GC selection but Tfh input acting as the limiting factor<sup>36</sup>.

A key aspect of affinity maturation that is often overlooked is the biomechanical basis for affinity sensing; how B cell clones of differing affinity may be differentiated by Tfh cells to selectively promote proliferation of the fittest clones (Figure 3)<sup>30</sup>.

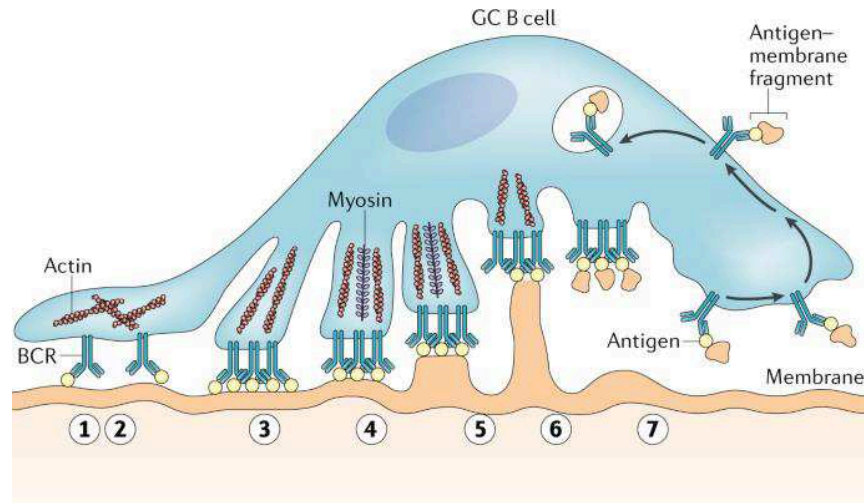


Figure 3 Antigen affinity discrimination by germinal center B cells. (1-2) When antigen is bound by germinal center (GC) B cells, B cell receptors (BCR) are concentrated onto actin rich extensions of the cell. (3-5) Myosin then engages with actin to deform the immune synapse. (6-7) Once sufficient force has been exerted, the antigen and associated membrane are captured by the GC B cell and internalized. Taken from Akkaya et al (2019)<sup>30</sup>.

GC B cells migrating towards Tfh cells encounter antigen on the surfaces of APCs and bind the antigens if specific; a lack of binding quickly discards the GC clones that underwent deleterious changes during SHM. Upon sensing antigen-BCR binding, the cytoskeleton of the GC B cell retracts the binding region of its membrane until the antigen is ripped away from the APC, at which point the GC B cell is now able to use these “stolen” antigens to obtain stimulation from cognate Tfh cells. Higher affinity binding interactions are more stable and successfully capture more APC bound antigens before reaching Tfh cells<sup>37,38</sup>. However, a potential criticism of this model is that the mechanical differences between medium, high, and very high affinity interactions are not entirely clear and may not be sufficient to separate these groups *in vivo*. Differences in the expression of supporting receptors (VLA4) available to stabilize immune complex formation has been proposed to regulate the ease of antigen binding and tearing<sup>39</sup>. However, it is unclear how this regulation may evolve during the GC reaction and the full diversity of this regulatory axis *in vivo*. Despite this model for membrane-associated antigens, the mechanism of affinity discrimination for largely soluble antigens remains poorly understood.

The outcomes of GC B cells migration through the light zone include the exit of the cell from the GC to differentiate into a memory B cell (Bmem) or a plasmablast (PB), the rejoining of the GC selection cycle via the dark zone (approximately 30% of GC B cells)<sup>40</sup>, or apoptosis due to insufficient survival signal input. Notably, in a murine immunization model it has been reported that GC reactions appear biased towards generation of Bmems during the first week of the immune response before transitioning to PB production<sup>41</sup>; this temporal switch has been linked to division mediated changes in B cell transcriptional programs causing a favoring of ASC differentiation. However, this model has been recently challenged by a murine influenza infection model that showed sustained, concurrent output of PBs and Bmems by GCs for at least 28 days after infection<sup>42</sup>.

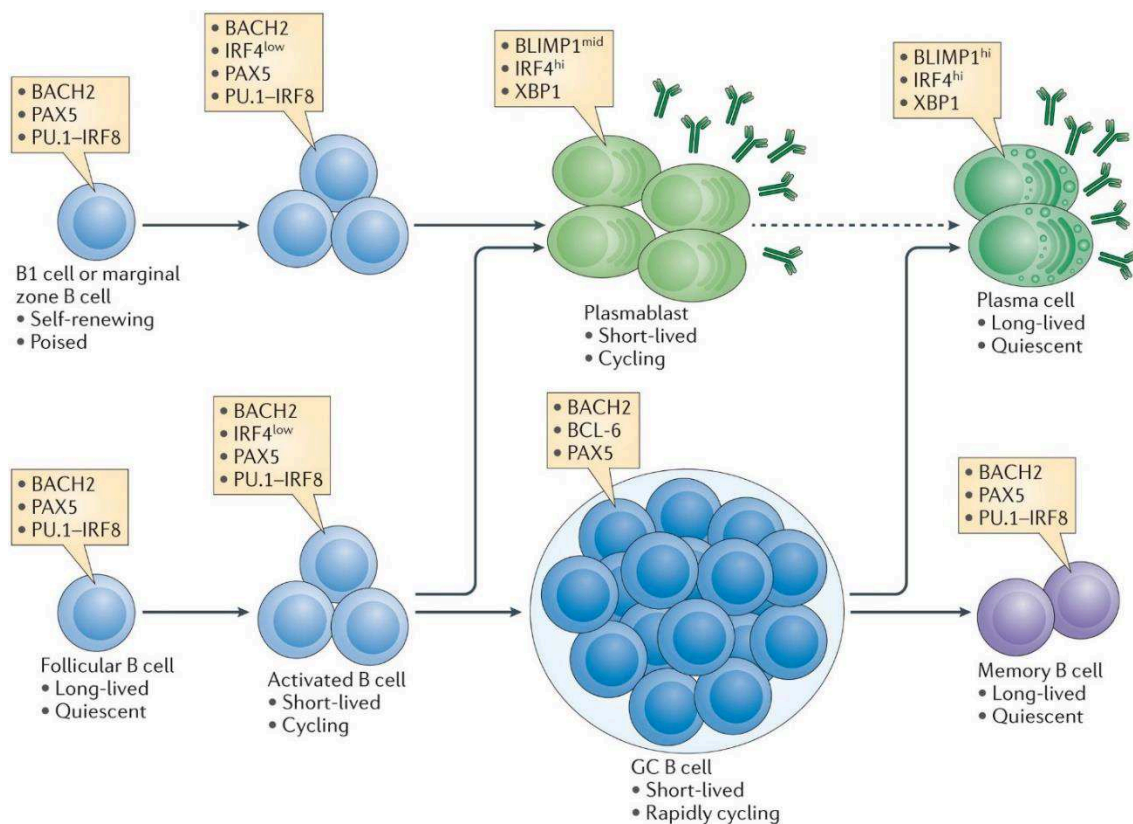
### **Differentiation into Antibody-secreting cells**

Antibody secreting cells (ASCs) are terminally differentiated B cells with a transcriptional profile distinct from other B cell subsets, with the primary purpose of secreting large quantities of their antibodies. ASCs are phenotypically divided between plasmablasts (PB) and plasma cells (PC), with the former consisting of recently activated and selected B cells with a short intrinsic life span and the latter representing plasmablasts that successfully home to survival niches and generate long lasting humoral immune memory<sup>43</sup>. Plasmablasts and plasma cells also differ in their metabolic pathways to sustain antibody production and whether they can proliferate or are post-mitotic, respectively.

### **Transcriptional regulation of ASC differentiation**

B cells arriving at the point of ASC differentiation must undergo a substantial transition from the B cell transcriptional program to the ASC program, which both intrinsically suppress the emergence of the other. B cells are distinguished by the expression of PAX5, BCL-6, BACH2, and OBF1, as well as other factors, which are responsible for coordinating genes related to Ig expression and sequence maturation (CSR, SHM)<sup>44</sup> and repression of ASC program factors<sup>45</sup>. The ASC transcriptional program is predominantly driven by the BLIMP1, IRF4, and XBP1 transcription factors (Figure 4). BLIMP1 is considered the most accurate transcription marker for identifying ASCs<sup>46</sup>, with higher levels of expression often distinguishing plasma cells from plasmablasts. BLIMP1 is responsible for repressing many major B cell program transcription factors, although the full physiology of BLIMP1 is not well understood. BLIMP1 does not appear

to be responsible for initiating the ASC differentiation pathway but rather reinforcing and solidifying the ASC fate, particularly through repression of B cell genes<sup>47</sup>. Notably, *BLIMP1* expression has been reported to be differently regulated between TLR- or BCR-mediated activation, which suggests altered differentiation capacities towards T cell independent or dependent antigens, respectively<sup>48</sup>. IRF4 regulates both the B cell and ASC transcriptional programs in a dose-dependent manner, as low concentrations promote PAX5 expression and influence *Ig* loci and higher concentrations result in *BLIMP1* activation and downregulation of BCL6 expression. IRF4 is similarly useful for identifying ASCs<sup>49</sup>. Finally, XBP1 is responsible for scaling the cell's capacity for protein synthesis and secretion<sup>50</sup>, though loss of XBP1 can be compensated for and the factor is not integral to differentiation<sup>51</sup>.



Nature Reviews | Immunology

Figure 4 Major transcriptional regulators of late B cell differentiation. (Taken from Nutt et al, 2015)<sup>47</sup>.

### Fate commitment to ASC differentiation

Several models have been proposed to reconcile how the various outcomes of B cell differentiation towards the ASC phenotype are coordinated<sup>47</sup>. The mechanism by which a B cell commits to the

ASC transcriptional program appears to rely heavily on cell division to regulate differentiation. Both the frequencies of CSR events and ASC differentiation have been demonstrated to correlate with the number of cell divisions<sup>52,53</sup>. Extrinsic stimulatory drivers of B cells are considered to exert the predominant deterministic influence on ASC differentiation. Several lines of evidence suggest this to be the case, including observations that antigen availability, contact with Tfh cells, and antibody affinity positively correlate with ASC differentiation<sup>54-56</sup>. Further, strong antigen mediated stimulation (BCR/Tfh cell mediated) of GC B cells has been directly linked to disinhibition of IRF4 activity, enabling *BLIMP1* expression and ASC differentiation<sup>57</sup>. Alternative models have also been proposed that place greater importance towards intrinsic regulation of ASC commitment, including asymmetric divisions<sup>58</sup>, programmed series of transcriptional shifts across divisions<sup>54,59</sup>, or internal competition between transcriptional programs. This final stochastic model posits that the outcomes of B cell differentiation (division, death, CSR, and ASC commitment) have different yet relatively stable probabilities of occurring after any one division, which with sufficient cell divisions yields satisfactory quantities of ASCs with varying isotypes while still supplying cells to the evolving B cell response<sup>60,61</sup>. There are numerous means by which these various models may be reconciled, however precisely specifying how each mechanism contributes to various contexts remains an unanswered topic.

It is also important to consider the differences in ASC differentiation between the various mature naïve B cell subsets. MZ B cells and B1 B cells have been demonstrated to express higher levels of Blimp1 compared to follicular B cells<sup>62</sup>. Similarly, memory B cells are another alternative source for ASC differentiation during the B cell response that upon re-exposure to antigen are capable of rapidly generating ASCs, partly due to lower expression levels of Bach2<sup>63</sup>.

### **Plasmablast to plasma cell differentiation**

The B cell response generates large quantities of antigen specific PBs to quickly increase titers of circulating antibodies, which are usually no longer necessary following successful clearance of the antigen<sup>34</sup>. PBs are therefore intrinsically destined to apoptose within several days, so that within approximately 2 weeks the circulating frequency of plasmablasts is returned to pre-antigen exposure levels, although some have been reported to survive for longer (3-4 weeks). The antibodies formed by the B cell response are still highly valuable after clearance of the antigen

nonetheless to offer immediate protection upon re-exposure, and so retention of moderate to low levels of antibody production forms a key component of adaptive immune memory.

In contrast to the relative specificity and clarity in characterizing the B cell subsets during the T cell-dependent response, the phenotypical distinctions between EF- and GC-derived plasmablasts are less clear; this is especially true regarding how each source fairs in managing the short-lived plasmablast to long-lived plasma cell (LLPC) transition. Comparisons between EF and GC plasmablasts have been largely limited to metabolic analyses (Figure 5)<sup>64,65</sup>. EF-plasmablasts utilize more diverse energy sources, including glucose, lipid, and amino acids, whereas GC-plasmablasts primarily utilize lipid-mediated oxidative phosphorylation. Several groups have made progress in distinguishing between EF and GC plasmablasts by FACS<sup>66-68</sup>, which should enable further insight into the transcriptional differences between EF- and GC-plasmablasts. GC-derived plasmablasts are largely considered to represent the precursors of LLPCs. Plasma cells are often found to have higher affinities compared to most circulating plasmablasts, which suggests most of these cells have undergone extensive affinity maturation and SHM within GCs. Additionally, the predominantly oxidative phosphorylation-based metabolism of GC-derived plasmablasts is shared with LLPCs, which may underly an improved capacity for survival or altered physiology. However, this binary model is challenged by observations that EF-derived plasmablasts can undergo CSR, SHM, and affinity maturation during both acute<sup>69,70</sup> and chronic<sup>71</sup> responses. Despite this, the LLPC repertoire appears to be derived mostly by GC-derived plasmablasts, as EF-dominant B cell responses with impaired GCs yield few LLPCs<sup>72</sup>. Whether the improved survival of GC-derived plasmablasts to become LLPCs is based on a given affinity threshold obtained through GC-mediated affinity maturation or via GC-driven stimulatory conditions (CD40L, IL-21, etc.) also remains unclear. Importantly, GC-derived plasmablasts do not appear to egress secondary lymphoid organs (SLO) with an already developed plasma cell phenotype<sup>73,74</sup>.

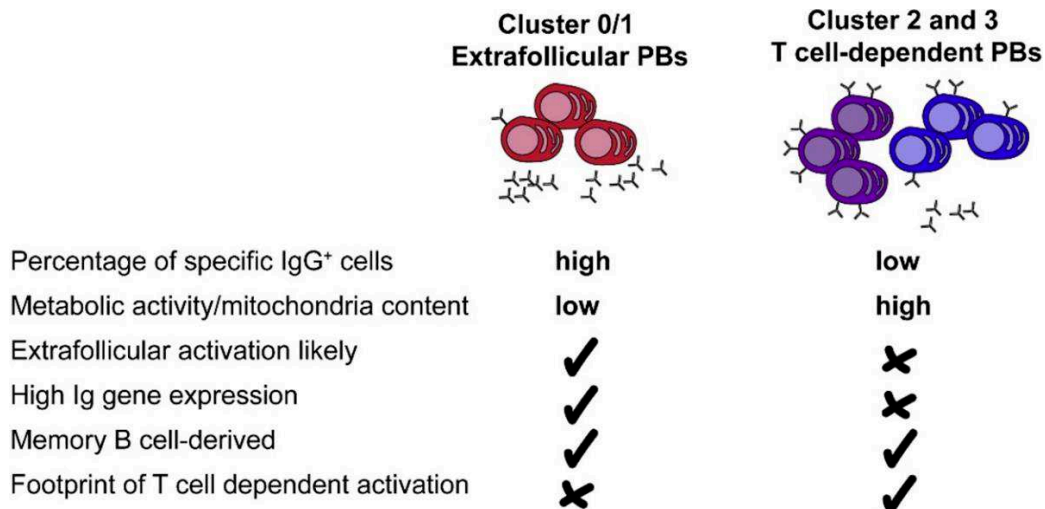


Figure 5 Characteristics of extrafollicular (EF) and germinal center (GC) derived plasmablasts. Plasmablasts of EF or GC origins are distinguishable by their metabolic activities, with EF PBs showing upregulation of genes relating to Ig secretion and GC PBs possessing more mitochondria with higher activity. GC PBs also have upregulated genes downstream of CD40L signaling, indicative of T cell-dependent activation. Taken from Rouers et al (2021)<sup>75</sup>.

### Homing and survival

The long-term survival of plasmablasts depends on their successful homing to specialized microenvironments to avoid clearance by apoptosis, largely located within the bone marrow (BM) (Figure 6). Plasmablast homing to survival niches of the bone marrow is predominantly mediated by the CXCR4-CXCL12 chemokine axis<sup>76</sup>, with several other factors participating such as VLA4 and CD44<sup>47</sup>. BM mesenchymal cells are responsible for expressing CXCL12, which promotes ASC transmigration into the BM parenchyma, and offer cell adhesion molecules such as VCAM1 necessary for retention<sup>77</sup>. PCs appear to heterogeneously utilize BM stromal cell types according to their associated chemokines and adhesins depending on the PC's Ab-isotype, which may represent a means of modulating BM PC retention between various isotypes, with IgG<sup>+</sup> PCs being favored overall<sup>78</sup>. Other cell types such as basophils, megakaryocytes, and monocytes have been shown to contribute in sustaining PC survival in the bone marrow. Eosinophils have also been proposed to be key elements,<sup>79</sup> however subsequent studies found eosinophils to be redundant in multiple immune contexts<sup>80,81</sup>. Another essential survival factor for PCs relies on the B cell maturation antigen (BCMA) receptor activated by the APRIL cytokine, which mediates survival by upregulating Mcl-1; Mcl-1 is short lived and therefore PCs require constitutive APRIL-BCMA signaling. The role of eosinophils in bone marrow PC maintenance is highlighted by findings that a lack of eosinophils through genetic deficiency severely impairs PC accumulation in the bone marrow in both mice and humans and induced depletion of eosinophils in WT mice results in the

rapid loss of PCs from the bone marrow<sup>82</sup>. The mechanisms governing selection of newly arrived plasmablasts for retention and long-term survival during competition for inclusion in survival niches are not entirely understood. LLPCs were long considered to be non-motile and resident in relatively static niches. However, the majority of LLPCs have been demonstrated to regularly migrate between niches, clusters of PCs, and even between bones<sup>83</sup>. The full implications of this motility and the physiological justifications for this behavior, perhaps searching for novel, stronger survival niches, offering space for new PCs, or the population of PC niches elsewhere in the body, are still under investigation.

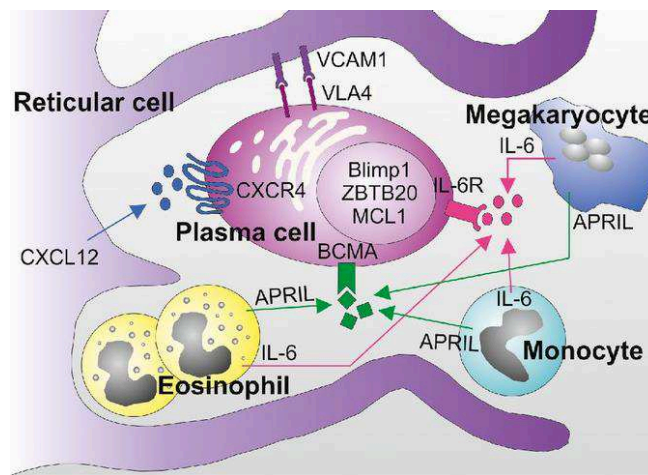


Figure 6 Survival signals from plasma cell niche. Bone marrow serves as a crucial environment for the long-term survival of plasma cells. Plasma cells remain within the bone marrow closely associated with specialized reticular cells expressing CXCL12. Plasma cells express the corresponding CXCR4 receptor, which may play a role in guiding them to the bone marrow. An interaction between VLA4 and VCAM1 further aids in keeping plasma cells in the bone marrow. To ensure their survival within this niche, plasma cells receive essential signals for survival from APRIL and IL-6, produced by various immune cells like eosinophils, megakaryocytes, and monocytes. Taken from Nera et al (2015)<sup>84</sup>.

### ASCs during infection

The machinery for PB and PC generation are capable of rapidly responding to antigens through the various mechanisms described. However, the dynamics and nature of the ASC response can be markedly different depending on the antigen encountered. Quantifying the precise kinetics of the ASC response to infection is made difficult through practical limitations in patient sampling and often the inability to define the time of exposure, for which vaccination studies are often favored. However, vaccine-induced ASC responses frequently do not entirely recreate infection-induced repertoires and kinetics owing to structural differences in the antigen of interest, the time course of antigen availability, and mechanisms of antigenic escape or immune evasion<sup>85</sup>.

The response to acute viral infections has been thoroughly studied owing to their robust and reproducible kinetics of antigen and antibody generation, with numerous historical precedents for pandemic events spurring interest. Despite the broad genetic and pathophysiological spectrum among known viruses, several global features are conserved during the elicited ASC responses. Human coronaviruses have provided considerable insights to build our current understandings of ASC kinetics, both through the many recent studies on SARS-CoV2 and earlier studies involving endemic human coronaviruses (HCoVs), whose mild symptoms allowed for human challenge observations<sup>86</sup>. The consistent features across infection studies include a lack of antibody responses during the first week after inoculation, which is immediately followed by the emergence of specific antibodies during the second week that increases and reach peak levels approximately 1-3 weeks later (Figure 7). IgM is initially produced, predominantly contributed by extrafollicular ASCs, and is joined 3-7 days later by IgG; conversely, IgM peaks and wanes in the serum before IgG. The plasmablasts responsible for these increases in circulating antibodies follow similar kinetics of appearance with an advance lead of 24-48 hours (5-7 days after exposure), which are reliably observable during both vaccination and infection<sup>87,88</sup>; however, reports of plasmablast emergence following infection are frequently obfuscated by unclear determinations of when exposure specifically occurred. The ASC response is characterized by a high degree of specificity, normally ranging between 30-50%<sup>89,90</sup>, which contrasts with Bmems that rarely have more than 1% antigen-specificity<sup>91</sup>. Importantly, the kinetics of ASCs are distinguished between naïve and recall responses, with the latter significantly advantaged by the presence of memory B cells acting as express conduits for ASC differentiation. The ASC response during recall is accelerated by approximately 2-3 days on subsequent antigen exposures, primarily for IgG plasmablasts<sup>92</sup>. As previously mentioned, the increased speed for ASC differentiation by Bmems is largely attributed to decreased Bach2 expression<sup>63</sup>.

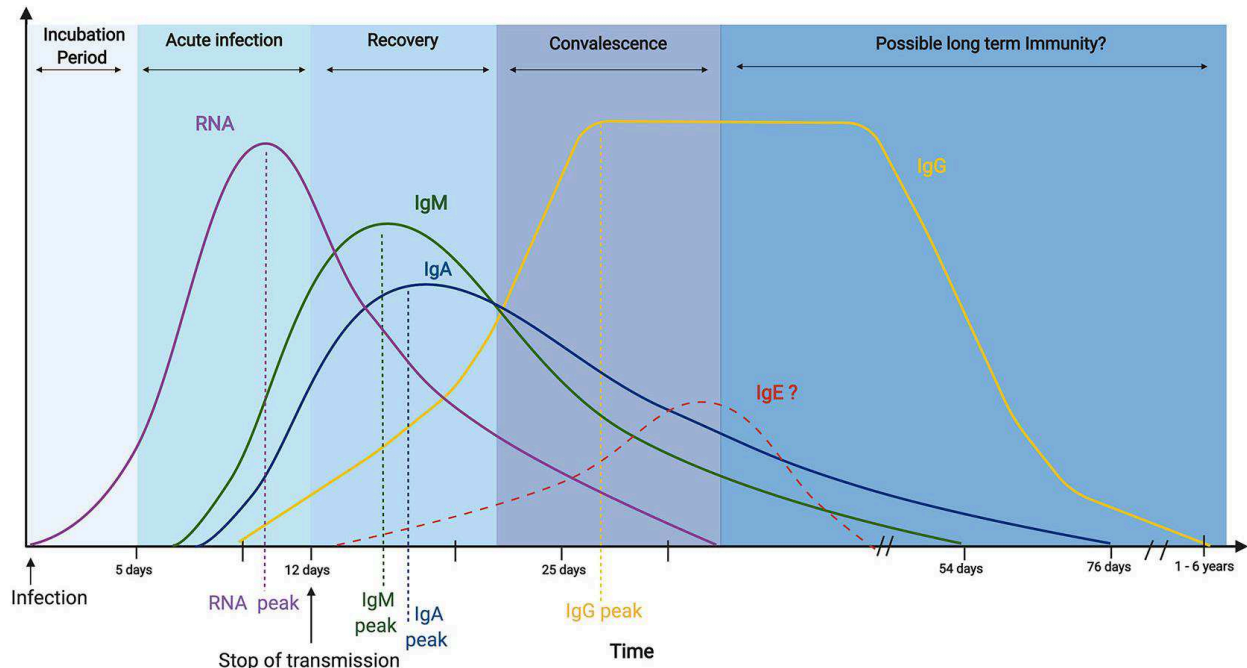


Figure 7 Kinetics of antibody responses during acute SARS-CoV2 infection. IgM and IgA are detectable 1 week after infection, reaching their peak 2 weeks after infection. IgG appears approximately 2 weeks after infection and reaches peak values within 1 month and remains detectable in serologies for 1 or more years. Taken from Galipeau et al (2020)<sup>93</sup>.

Bmem isotype is an especially important factor in the trajectory of ASC differentiation.  $IgM^+$  B cells were observed upon recall to yield both GC B cells with IgM and IgG isotypes and few  $IgM^+$  plasmablasts, whereas  $IgG^+$  B cells predominantly generated  $IgG^+$  plasmablasts without rejoining the GC reaction<sup>94</sup>. Another study comparing  $IgM^+$  vs  $IgG^+$  Bmem responses upon adoptive transfer found similar results and posited an inhibitory relationship between these Bmem types<sup>95</sup>. The rapid induction of  $IgG^+$  ASCs by  $IgG^+$  Bmem was credited with limiting the availability of antigen for GC reactions and  $IgM^+$  Bmem. These differences in response and persistence of Bmem according to isotype have important implications for vaccination strategies and the nature of the ASC responses to recall.

Another important factor during the ASC response to infection is the balance between EF and GC ASC differentiation, with the former often being associated with detrimental outcomes. In the context of COVID-19, strong extrafollicular generation of ASCs was associated with worsened symptoms and clinical outcomes despite the early availability of anti-SARS-CoV2 antibodies<sup>66</sup>; this effect was shown to not be caused by increased viral loads. Excessive extrafollicular ASC responses during severe COVID-19 was also concurrently linked to the emergence of autoreactive ASCs that may exacerbate pathophysiology, of which over half possessed binding towards SARS-

CoV2<sup>96</sup>. Attenuation of the immune response by EF-derived ASCs may potentially be explained by increased PD-L1 expression, with immune-modulatory effects on T cells primarily<sup>67</sup>.

Several circumstances have been described where ASC responses to infections are detrimental, owing to excess inflammation or proliferation of ASCs or situations where antibodies themselves are at fault. Perhaps the most known is antibody-dependent enhancement (ADE), in which antibody-bound viral particles are endocytosed via FC receptors and viral entry to the cell is thereby facilitated or where antibody-mediated inflammation exacerbates disease<sup>97</sup>. ADE is particularly pronounced during non-primary flaviviral infections, such as Dengue and Zika, which especially complicates vaccination strategies<sup>98</sup>. Excess antibody production also harms type 2 immune responses, as helminth infections have been shown to induce large amounts of IgE secretion by B-1 cells. These B-1 derived IgE are overwhelmingly non-specific and thereby block effective mast cell degranulation elicited by IgE from GC (B2) derived ASCs<sup>99</sup>.

### **ASCs in autoimmunity**

B cell tolerance is the process by which the immune system recognizes and eliminates or attenuates autoreactive B cells to prevent the production of autoantibodies that may ultimately lead to autoimmune diseases. In some cases, B cells can escape tolerance mechanisms and produce autoantibodies that attack the body's own tissues, significantly driving several autoimmune diseases.

One way in which B cells can escape regulation is through defects in central tolerance mechanisms, which occur during B cell development in the bone marrow<sup>100</sup>. During early B cell development, self-reactive B cells are eliminated through negative selection, a process that involves clonal deletion or receptor editing. Clonal deletion involves the programmed cell death of self-reactive B cells, while receptor editing allows self-reactive B cells to undergo further rearrangement of their immunoglobulin genes to generate a non-self-reactive B cell.

However, despite the evidence for negative selection in B cell development, autoreactive B cells are present among mature B cells and participate in B cell responses and affinity maturation<sup>101,102</sup>. The rationale for incomplete removal of autoreactive clones is likely to avoid gaps in the B cell repertoire into which pathogens may develop their antigens to be highly self-mimicking. Up to 7% of naïve and pre-GC B cells in healthy human spleens were shown to be autoreactive towards carbohydrate I/i antigens<sup>103</sup>, attributable to a *IGHV4-34* heavy chain, and approximately 20% of

mature naïve B cell antibodies in another study showed reactivity towards lysate mixtures of self-nuclear and cytoplasmic proteins<sup>102</sup>. The full extent of autoreactivity in mature B cells remains unestablished due to limitations in autoantigen panels and screening methods. Despite the apparent prevalence of autoreactive B cells, autoantibodies are not prevalent in the serum of most healthy individuals. Autoreactive mature B cells are characterized by a state of anergy due to constant signaling via their BCRs without cognate T cell help, which is more pronounced in IgM than IgD B cells<sup>104</sup>. These B cells have nonetheless been shown as capable of becoming beneficial and may lose self-reactivity through the process of clonal redemption<sup>105,106</sup>. This concept was well demonstrated by the reversion of 3 vaccine induced antibodies using *IGHV4-34* with strong specificity to foreign antigen into their nearest germline VDJ sequences<sup>107</sup>. These germline-reverted *IGHV4-34* antibodies were indeed specific to autoantigen, to which binding was eliminated through a common mutation and afterwards maturation towards the foreign antigen can proceed; approximately 2.5% of CD27- Bmem have been found to use *IGHV4-34*, highlighting the apparent contribution of these formerly autoreactive clones<sup>108</sup>.

In addition to defects in central tolerance mechanisms, B cells can also escape regulation through defects in peripheral tolerance mechanisms. Peripheral tolerance mechanisms act to prevent the activation of self-reactive B cells that have escaped central tolerance. Peripheral tolerance is globally divisible between extrinsic and intrinsic regulatory axes, with the former consisting of input from cytokines and regulatory cells in the environment and the latter involving modulatory signaling by the BCR or other receptors on the autoreactive cell itself<sup>109</sup>. One major intrinsic mechanism is anergy, which renders self-reactive B cells unresponsive to antigen stimulation. Anergy can be induced by antigen encounter in the absence of T cell help or by signals from inhibitory receptors, such as FcγRIIB<sup>110</sup>. However, defects in peripheral tolerance mechanisms can also lead to the activation of self-reactive B cells. For example, deficiency in regulatory T cells, which play a crucial role in maintaining immune tolerance, can result in the activation of self-reactive B cells<sup>111</sup>. Another mechanism by which B cells can escape regulation is through epitope spreading, which occurs when an autoimmune response is triggered by a non-self-antigen that is structurally similar to a self-antigen. This can lead to the activation of previously down-regulated, self-reactive B cells, leading to the production of autoantibodies<sup>112</sup>.

ASCs have been identified as major inflammatory drivers in several autoimmune diseases, including systemic lupus (SLE), immune thrombocytopenia (ITP), and multiple sclerosis (MS)<sup>113</sup>. ITP presents a notable example of ASCs in autoimmunity with both well-established demonstrations of concepts central to autoimmune disorders yet still significant potential for further insight. ITP is a highly heterogeneous disease, presenting a wide range of clinical manifestations where some individuals may remain asymptomatic yet possess autoantibodies, while others may experience life-threatening bleeding episodes. ITP is particularly difficult to diagnose directly via autoantibody serology as is commonly done for other autoimmune disorders. This is likely due to an excess availability of platelet antigens compared to the number of autoreactive antibodies, which leaves insufficient quantities of unbound antibody in serum for detection. There is an ongoing need for better characterization of the autoantibody repertoires present in ITP. The clonal repertoire of autoreactive B cells in ITP appears to be restricted to a small handful of clonotypes. One study reported near exclusive usage of the *IGHV3-30* clonotype in 2 ITP patients<sup>114</sup>, while another report on high-throughput sequencing of B cells from 11 ITP patients found increased prevalence of *IGHV4-28* clones in all individuals<sup>115</sup>; both studies also found extensive somatic hypermutation within these predominant clonal families indicating the involvement of GC reactions during ITP pathology. The restriction of the autoreactive repertoire to a few clonal families also supports the notion of an “escape” event where a unique clone breaks free from peripheral tolerance mechanisms. Despite these findings, there is insufficient data regarding the diversity and potency of autoantibodies in ITP, especially how these factors relate to the clinical presentation of ITP patients. The localization of autoreactive ASCs driving autoimmunity is another major consideration when devising potential therapies to eliminate these offending cells., which remains poorly understood. ITP presents a unique set of challenges within the realm of autoimmune diseases. Its clinical heterogeneity, limited treatment options, and potential insights into immune dysregulation make it a compelling subject for further research.

### **How are ASC responses studied?**

During this thesis, we published a concise review of current and emerging single cell technologies for characterizing ASCs, with a primary focus on functional assays<sup>116</sup>. ASCs are particularly notable for their combination of a “secreted” phenotype paired with the sequence diversity that is characteristic of lymphocytes. Other immune cell types are also characterized by secretory phenotypes, but their secreted molecules are generally the same irrespective of their origin cell,

which simplifies assay design considerably. Antibodies secreted by B cells are unique in that they are highly variable and possess several additional layers of intrinsic function; antibodies are functionally distinguishable in terms of their specificity, affinity, binding site, and neutralization or agonistic capacity. Hence, merely detecting antibody secretion often proves insufficient for addressing the complex biological questions associated with ASC responses, as the properties of the antibodies themselves are arguably as critical as the act of secretion.

Conversely, techniques designed to probe the genotypic diversity of B cells offer a versatile array of solutions for investigating ASC clonal relationships and trajectories. Understanding the genetic makeup and evolution of B cells as they transition into ASCs not only provides insights into their functional characteristics but also sheds light on the underlying processes driving immune responses. This approach allows researchers to unravel the intricate dynamics of ASC differentiation and clonal expansion, offering a deeper understanding of the immune system's ability to adapt and respond to diverse challenges. Together, the integration of functional assays and genotypic profiling presents a comprehensive toolkit for unraveling the complexities of ASC responses and advancing our knowledge of immune defense mechanisms.



# Single-Cell Technologies for the Study of Antibody-Secreting Cells

Matteo Broketa<sup>1,2\*</sup> and Pierre Bruhns<sup>1\*</sup>

<sup>1</sup> Institut Pasteur, Université de Paris, INSERM UMR 1222, Unit of Antibodies in Therapy and Pathology, Paris, France,

<sup>2</sup> Sorbonne Université, Collège doctoral, Paris, France

## OPEN ACCESS

### Edited by:

Ludvig M. Sollid,  
University of Oslo, Norway

### Reviewed by:

Ida Lindeman,  
Oslo University Hospital, Norway  
George Georgiou,  
University of Texas at Austin,  
United States

### \*Correspondence:

Matteo Broketa  
matteo.broketa@pasteur.fr  
Pierre Bruhns  
bruhns@pasteur.fr

### Specialty section:

This article was submitted to  
Systems Immunology,  
a section of the journal  
Frontiers in Immunology

**Received:** 24 November 2021

**Accepted:** 29 December 2021

**Published:** 31 January 2022

### Citation:

Broketa M and Bruhns P (2022)  
Single-Cell Technologies for the Study  
of Antibody-Secreting Cells.  
Front. Immunol. 12:821729.  
doi: 10.3389/fimmu.2021.821729

Antibody-secreting cells (ASC), plasmablasts and plasma cells, are terminally differentiated B cells responsible for large-scale production and secretion of antibodies. ASC are derived from activated B cells, which may differentiate extrafollicularly or form germinal center (GC) reactions within secondary lymphoid organs. ASC therefore consist of short-lived, poorly matured plasmablasts that generally secrete lower-affinity antibodies, or long-lived, highly matured plasma cells that generally secrete higher-affinity antibodies. The ASC population is responsible for producing an immediate humoral B cell response, the polyclonal antibody repertoire, as well as in parallel building effective humoral memory and immunity, or potentially driving pathology in the case of autoimmunity. ASC are phenotypically and transcriptionally distinct from other B cells and further distinguishable by morphology, varied lifespans, and anatomical localization. Single cell analyses are required to interrogate the functional and transcriptional diversity of ASC and their secreted antibody repertoire and understand the contribution of individual ASC responses to the polyclonal humoral response. Here we summarize the current and emerging functional and molecular techniques for high-throughput characterization of ASC with single cell resolution, including flow and mass cytometry, spot-based and microfluidic-based assays, focusing on functional approaches of the secreted antibodies: specificity, affinity, and secretion rate.

**Keywords:** plasma cell (PC), high-throughput technique, antibody secreting cell, droplet microfluidics, antibodies, B cells, functional bioassay

## INTRODUCTION

Antibody-secreting cells (ASC) are B cells that have differentiated following activation to secrete various soluble isotypes of their immunoglobulin receptor with the purpose of binding their target antigen throughout the body (1). ASC are predominantly generated within the germinal center reactions of secondary lymphoid organs (2), although extra-follicular responses may also generate ASC (3, 4). Following antigen exposure, parallel downregulation of major regulatory genes of activated B cells and upregulation of a unique ASC transcriptional program drives differentiation of B cells into early-ASC or plasmablasts. Several mechanisms have been proposed to govern ASC fate determination, but a unifying model has not yet been determined (1, 5). Plasmablasts are an unstable ASC intermediate that require input from a survival niche to persist long term. The bone marrow has been extensively studied as an ASC niche for its role in harboring ASC following

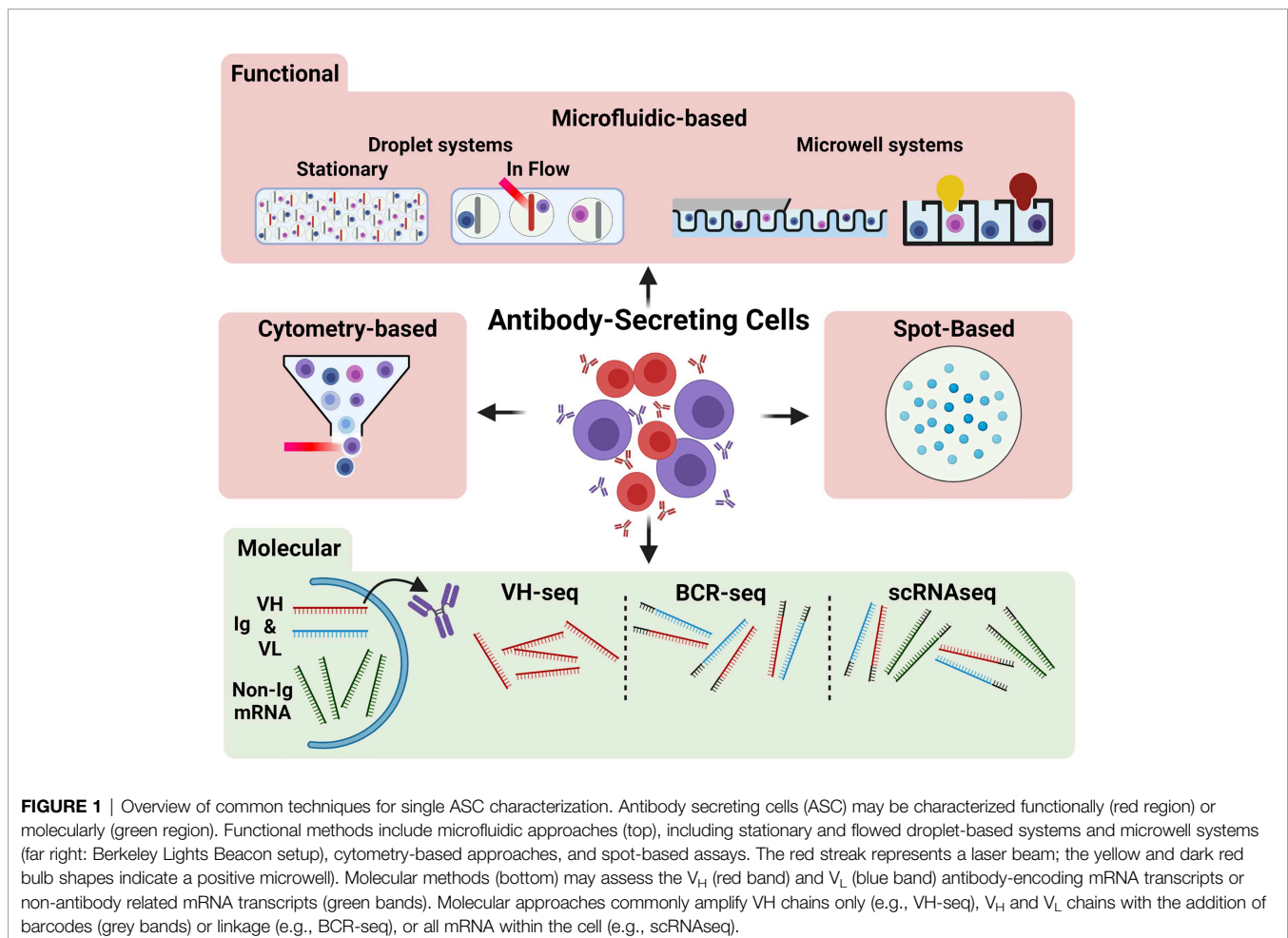
infection and immunization, however the majority of ASC are located in the gut-associated lymphoid tissue and produce IgA (6); the thymus has also recently emerged as an ASC niche (7, 8). The factors involved in early-ASC homing to survival niches are not completely understood. Plasmablasts may also be drawn towards sites of inflammation, where they act locally and acutely without persistence (9). Plasma cells are a long-lived ASC subset, characterized by reinforced expression of genes within the ASC differentiation network, responsible for secreting large quantities of antibodies from within their survival niches.

ASC are often considered the “apex” of B cell differentiation as they actualize antibody-mediated humoral immunity and are terminally differentiated. ASC contribute to both the acute humoral response to infection by rapidly generating early antibodies at sites of infection as well as later secreting higher affinity antibodies produced by germinal center reactions to aid in pathogen clearance and protective immunity. While the ASC response is advantageous during infection and when co-opted for immunization, emergence of ASC secreting antibodies towards self-antigens is a deleterious factor in many autoimmune disorders (10). Despite their importance, much is still unknown regarding ASC differentiation, selection, and

heterogeneity, particularly in autoimmune disorders. High throughput (HT) analyses of single cells are becoming more accessible, affordable, and common in literature concerning adaptive immune responses. This review will outline current and emerging HT techniques to characterize single ASC (Figure 1), with discussion of recent applications of these techniques to study the role of ASC in various pathologies as well as to expand understanding of fundamental ASC biology.

## FUNCTIONAL ANALYSES

The primary effector functions of ASC are mediated by their secreted antibodies, and thereby are characterized by a secreted phenotype. Polyclonal antibody responses of ASC are routinely assessed by sampling the serum or ASC-containing organs for binding antibodies and their global potency (11). Such methods provide an overview of the cumulative ASC response but are unable to interrogate ASC diversity. Techniques with single cell resolution are required to uncover the contributions of individual clones to the polyclonal ASC pool, the prevalence of specific groups of ASC, and the relationships between the factors



and markers that differentiate ASC. It should be noted that many other soluble effectors besides antibodies are also known to be secreted from ASC (12, 13), including various interleukins and transforming growth factor-beta one (TGF- $\beta$ 1), and HT functional assays may also be readily adapted to study the role of these soluble factors.

The topic of techniques for measuring single-cell protein secretion in immunology and their origins have been previously described (14, 15). Three general strategies are available for characterizing the secreted effectors of immune cells, each with applicability to ASC: spot-based assays, cytometry-based assays, and microfluidic-assays. These approaches globally share the strategy of isolating ASC, either by distance or compartmentalization, to ensure that “positive” loci or compartments reflect secretions or markers of single cells. Here we will focus on what these techniques offer to describe ASC behavior and highlight notable demonstrations of their use.

### Spot-Based Assays

Spot-based assays spatially distribute ASC by dilution and rely on localized membrane capture of secreted antibody or cytokine from ASC, followed by visualization with enzyme- or fluorophore-linked secondary antibodies (16, 17), termed enzyme-linked immunospot (ELISpot) and Fluorospot, respectively. The number of “spots” formed is indicative of the prevalence of ASC and/or antigen-specific ASC from a given sample. The strength of spot-based assays are their ease of use, robustness, and versatility between models (18, 19). Spot-based assays also directly observe secretion and therefore robustly identify ASC, in contrast to indirect-functional or molecular techniques where the ASC definition is inferred. However, ELISpot and Fluorospot are limited to the detection of only 1-2 or 1-4 soluble analytes, respectively, cannot precisely quantify secretion rates, and the ASC identified cannot be recovered for further analysis. ELISpot has seen extensive use in characterizing the ASC response during pathogenic infections (19, 20), in autoimmune disorders (21–23), and following immunization (24). Bonezi et al (25) recently used ELISpot to demonstrate the contribution of altered tryptophan metabolism to the hyperabundance of ASC frequently seen during flavivirid infections, Dengue virus being the most common example.

### Cytometry-Based Assays

Flow cytometry and its derivative, fluorescence-activated cell sorting (FACS), have become a staple in investigations of B cells and ASC, allowing for relatively straightforward and rapid evaluation of multiple samples or experimental conditions (26, 27). Multicolor flow cytometry allows for immense diversity and depth of information gathered through the customization of antibody panels to target surface and intracellular markers. In contrast to ELISpot, flow cytometry can precisely identify the proportions of different ASC, B cell, and lymphocyte populations in each sample. Flow cytometry and ELISpot are frequently used in concert to measure global changes in the proportion of ASC and other B cells and the robustness and antigen-specificity of the ASC response, respectively (28, 29).

Human ASC are often defined in flow cytometry as larger cells with CD27 and CD38<sup>high</sup> expression among CD3<sup>-</sup> CD20<sup>-</sup> cells, and may be subdivided by expression of CD138, CD19, CD45, CD81, HLA-DR, and immunoglobulin isotypes (30–33). Plasma cells secreting human IgA or IgM, but not IgG, express surface immunoglobulin and may be identified by direct surface staining (34, 35). Local capture of IgG antibodies secreted by ASC onto their surface has been proposed to identify human IgG-secreting ASC by flow cytometry, using CD45 as a membrane anchor onto which IgG antibodies are captured by their constant region (Fc) (36), but has not yet been widely used. Surface markers and soluble effectors, namely antibodies and cytokines, not expressed at the cell membrane may be assessed using cell permeabilization and fixation to allow labelling reagents access within the cell; such intracellular staining normally precludes downstream assessment of cells by other functional or molecular methods. However, Price et al (37) demonstrated the feasibility to molecularly characterize ASC following intracellular staining for both antibody isotype as well as antibody specificity using tetramer constructs of antigens bound to fluorophore-conjugated streptavidin. Alternatively, early IgG-expressing ASC (IgG-ASC) often continue to bear their antibodies at the cell membrane, and surface staining for antibody isotype and antigen-specificity with tetramers offers a simpler method for isolating such IgG-ASC, though represents a restricted view of the whole IgG-ASC population (38, 39). Flow cytometry is also a valuable tool for scouting potential novel markers of ASC subsets (40). The use of intracellular tracing dyes further allows for assessment of ASC proliferation, as Scharer et al (41) have applied to ASC emergence from activated B cells.

Flow cytometry has identified ASC and ASC subsets in the context of autoimmune disorders and their contributions to acute and chronic disease states (42–45), and the ASC response to natural infection, as recently shown by Woodruff et al (46) in the context of COVID-19. The authors showed by flow cytometry a predominance of extrafollicularly-activated ASC in circulation, based on varied expression of CD11c, CXCR5, and CD21, and demonstrate its effect on infection morbidity. Noticeably, distinction between ASC derived from germinal centers or extrafollicularly is not possible with most other functional assays and is often overlooked. Application of FACS to *in vitro* models of ASC differentiation (47) and survival (48, 49) also highlights the ability of flow cytometry to distinguish ASC subpopulations. FACS isolation of populations of interest may be followed by a spot-based assay to query the subsequent prevalence of ASC within those populations (50–52).

It should be noted that current cytometric-gating strategies for ASC populations have not been demonstrated to completely define all ASC without exclusion of rarer phenotypes. Strategies often vary considerably, utilize a unique marker that may not be ASC-identifying in all contexts, or rely on intracellular staining of transcription factors (31, 53). ASC are distinct in their transcriptional regulation compared to other B cells, and the transcription factors IRF4, BLIMP-1, and XBP1 are ideal for complete identification of ASC (1, 53). Indeed, BLIMP1-YFP

mice have been invaluable to studying ASC differentiation, behavior, and transcriptional regulation (54, 55). IRF4-based labelling has similarly been used to identify differentiating human plasma cells following influenza vaccination (56).

Mass cytometry is based on a similar principle as flow cytometry, using heavy metal ions instead of fluorophores to distinguish the antibodies in the cytometry panel. Glass et al (57) utilized multiple mass cytometry panels to characterize over 350 B cell surface markers, combined with analyses of isotype usage, BCR sequence, metabolic profile, biosynthesis activity, and signaling response, which together constitute an expansive single-cell atlas of human B cells. An additional mass cytometry panel targeting enzymes associated with different metabolic pathways (58) found plasma cells to be highly metabolically active, and further subdivisible based on transcriptional activity; such metabolic distinctions have largely been restricted to molecular studies or classical metabolomics (49, 59). Although mass cytometry can simultaneously detect ~40 parameters per panel, the vaporization of analyzed cells prevents further study of the precise subsets identified, which remains the advantage of FACS.

## Microfluidics

Microfluidic single cell assays essentially miniaturize existing techniques to assess ASC secretions, to increase the scale and throughput of analyses and enable single cell resolution *via* compartmentalization into either wells or droplets (14, 15). Miniaturization also allows for greatly reduced reagent usage and less cells are needed per experiment. The functional measurements within microfluidic ASC assays largely share the concept of capturing secreted antibody or cytokine onto a physical surface followed by visualization with fluorescent detection reagents. The advantages of microfluidic-based functional analyses of ASC include their direct identification of ASC *via* antibody secretion, a high throughput, and the ability to absolutely quantify ASC secretions over time.

Micro- and nano-well microfluidic approaches use microfabrication techniques to create thousands of wells into which individual ASC can be introduced (60–62). The nature of the wells and coating and reagent strategy used can be readily customized to assay different antibodies, antigens, or secretions. The small volumes of these wells allow for absolute quantification of secreted molecules, in contrast to ELISpot where only relative measurements can be made (14). Well-based microfluidic assays also have lower detection thresholds than ELISpot, making them more sensitive and more capable of wholly representing ASC (63). Importantly, as ASC are identified and sustained within the static well array, cells can be recovered following the assay for additional functional or molecular assessment. The Berkeley Lights “nanopen” platform introduces considerable advancement to well-based ASC assays using optofluidics, offering integrated workflows for antibody screening of ASC followed by targeted recovery of specific cells for molecular analysis (64). This rapid pipeline for functional antibody assessment was recently used to characterize antibody repertoires following SARS-COV2 infection (65). Despite their advantages over ELISpot, well-based microfluidic assays have seen limited application beyond

technical demonstrations and antibody discovery (66–68), mainly due to their cost and limited throughput.

Droplet microfluidics achieves single cell compartmentalization using two immiscible fluids, an aqueous phase containing the cell and assay reagents and an oil phase that separates the aqueous phase into droplets with single cells (14). Large numbers of droplets can be quickly produced for each new sample and the assay composition can be easily changed. Secretion by encapsulated ASC is assessed by beads or other cells within the droplet that act as capture surfaces for secreted cytokine or antibody, to which fluorescent reagents in the droplet can localize for measurement. Flow-based or flowed droplet assays can characterize ASC with high throughput by passing droplets at high frequency through a laser for rapid detection of fluorescence relocation within droplets (69–71). Droplet measurement may also be paired with dielectrophoretic sorting, which pushes or pulls droplets into separate channels by manipulating electric fields, allowing for further assessment of directly identified ASC or antigen-specific ASC (69, 72). We reported in Gerard et al (69) the CelliGo assay using a double fluorescent sandwich ELISA in microfluidic droplets for the identification, sorting, and  $V_H$ - $V_L$  sequencing of antigen-specific IgG antibodies produced by ASC from immunized mice. In this study, we demonstrated screening of a bacterial antigen (tetanus toxoid), an autoantigen linked to Rheumatoid Arthritis (Glucose-6-phosphate Isomerase), and an insoluble, membrane-expressed antigen (tetraspanin-8; TSPAN8); antigen-specific ASC against all 3 model antigens were able to be sorted by this flowed droplet microfluidic technique.

An alternative approach to study ASC in droplets is to collect droplets in a horizontal plane and measure changes in droplet fluorescence over multiple timepoints, termed a stationary droplet-assay (14) or DropMap (73, 74). DropMap measures fluorescence relocation to a central line of antibody-capturing beads aligned using a magnetic field within each droplet. Both secreted antibody relocation and soluble antigen relocation to the beadline are measured. The ability to measure relocation over time within DropMap allows for the determination of both antibody affinity and secretion rate, in addition to determining the proportion of antigen-specific and total ASC within a sample as with other microfluidic techniques. DropMap has been applied to investigate the physiology of ASC in viral infection (75), autoimmunity (74), and fundamental ASC biology (73, 76). In our view, DropMap offers a major advancement in current capabilities to functionally characterize ASC, particularly for defining the specificity and affinity repertoire of ASC. An example alternative strategy to DropMap for affinity repertoire mapping is to sort large numbers of B cells or ASC for their BCR sequences, followed by gene synthesis or direct cloning, re-expression, and kinetic analysis of these antibodies by a technique such as bio-layer interferometry (BLI) (77–79) (Figure 2); this approach is significantly more complex, costly, and time consuming than DropMap. Recently however, we reported antigen-specific single cell memory B cell *in vitro* differentiation into ASC that allowed for fast and large scale (~400) affinity measurements by BLI from culture supernatants without costly antibody re-expression (80). Initial sorting for

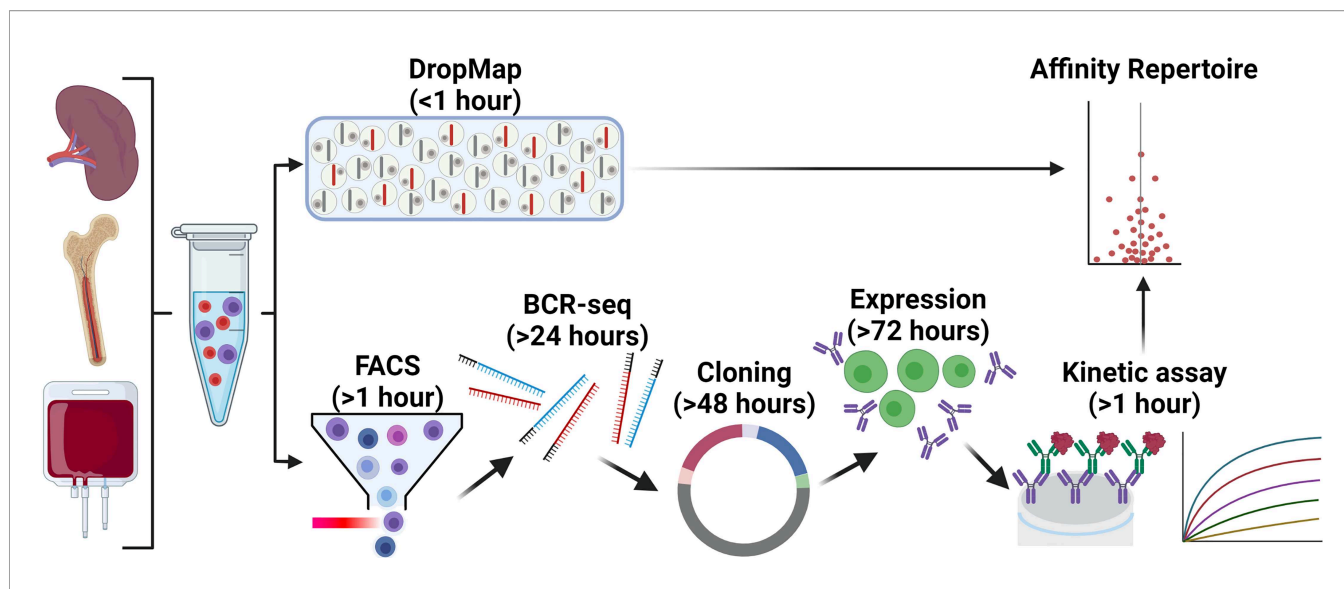


**FIGURE 2** | Comparison of DropMap vs a classical pipeline to define affinity repertoires. The affinity repertoire of ASC towards a given antigen is an important metric for the quality of the ASC response. ASC are commonly isolated from the spleen, bone marrow, or blood of donor/patients or experimental animals. The DropMap assay (top) offers a platform that within 1 hour can return the affinity repertoire in a single assay, as well as the IgG secretion rate and frequency of ASC according to direct *ex vivo* measurement (refer to main text for details); this approach is limited by requiring ASC to secrete antibodies at the time of data acquisition, data can only be acquired once, and afterwards cells of interest are lost. An alternative strategy (bottom) to yield a similar affinity repertoire first requires cell isolation by FACS, followed by  $V_H$  and  $V_L$  targeted RT-PCR (& BCR-seq if required) and cloning into an expression vector, transfection of the vector into an expression system and cell culture, purification and finally assessment of the recombinant expressed antibody by BLI or SPR; this pipeline requires 1½ -2 weeks to complete, is significantly more complex and costly, and can only assess  $V_H$ - $V_L$  pairs that could be successfully amplified, cloned and expressed as recombinant antibodies.

ASC may also bias the antibody repertoire through restrictive FACS gating strategies unless a direct functional assay is used prior to directly select for ASC, whereas DropMap offers an unbiased screen of PBMCs or an enriched B cell pool for ASC. Another novel approach involving BCR sequencing paired with liquid chromatography–tandem mass spectrometry proteomics (81, 82) allows for unbiased molecular assessment of antibodies from the serum, but requires infrastructure and specialist supervision, and is currently largely restricted to the most represented antibodies in the serum.

The major limitation to widespread adoption of functional, droplet-based assays of ASC is their bespoke nature. Although droplet microfluidics is a growing field, with most reagents commercially available, labs must produce their own consumables for droplet production and the apparatus for assay observation, which require specialized equipment and expertise.

## MOLECULAR ANALYSES

The molecular basis for the behavior of ASC is equally important to understanding ASC physiology. The molecular aspects of ASC most investigated are (i) the heavy and light chain variable regions ( $V_H$  and  $V_L$ ) sequences, formed by gene rearrangements and sequence diversification mechanisms (83), encoding the antigen binding domains of antibodies and (ii) the transcriptional profile of ASCs; these aspects may be probed using bulk  $V_H$ -seq or RNAseq, BCR-seq, and increasingly now single-cell RNAseq (scRNAseq) following either single-cell ASC

FACS into 96 or 384 well plates, or microfluidic droplet-based barcoded scRNAseq (e.g., 10xGenomics Chromium). Importantly, BCR sequences can be computationally inferred from scRNA-seq data using open-source libraries (e.g. BraCeR (84), VDJPuzzle (85)), linking antibody sequence (i.e., genotype, clonal information) to transcriptome phenotype. Recent advances on ASC characterization using RNAseq, ATAC-seq and ChIP-seq have been reviewed elsewhere (86), as well as molecular mechanisms leading to plasma cell differentiation from the germinal center reaction (87). Glaros et al (38) highlight the capacity for scRNAseq to identify B cell subsets and observe shifts in differentiation, identifying antigen availability as a key regulator of the plasmablast response.

A common strategy for molecular ASC clonal identification is bulk sequencing of  $V_H$  regions (37), which allows for large numbers of cells to be assayed without the cost and limitations imposed by a need for single cell approaches. However, the  $V_L$  sequence information is lost, and it is not possible to re-express the original antibody recombinantly. Alternatively, Price et al (37) recently used bulk RNAseq to identify unique transcriptional profiles for IgG, IgM, and IgA ASC subsets, with the ability to assess both clonality and gene expression. Such approaches offer insight into the clonal diversity of ASC responses but have less resolution than paired  $V_H$ - $V_L$  chain sequencing and have no possibility for functional assessment of clones within the antibody repertoire. When the full  $V_H$ - $V_L$  sequence is required, single-cell approaches are required, and currently available techniques for HT BCRseq have been reviewed by Curtis and Lee (88), who highlight advances in  $V_H$

and  $V_L$  chain pairing by barcoding (69) or linkage as well as increased cell-throughput through the use of microfluidics. Moreover, techniques such as LIBRA-seq (89) or CelliGo (69) allow for assessment of antigen specificity or antigen specificity coupled to antibody secretion, respectively, integrated within their BCRseq pipelines. Wang et al (90) used microfluidics to compartmentalize human plasmablasts as single cells and generate paired  $V_H$ - $V_L$  repertoires for direct Fab display on yeast and functional assessment. Notably, Jiang et al (91) utilized a combination of bulk  $V_H$ -seq, BCRseq, and full scRNAseq to identify autoreactive ASC persisting after treatment with rituximab. Such an approach leverages the complexity and throughput of each technique with the depth of information required to address the authors' underlying question, saving considerable time, and lowering costs overall. Using the 10x genomics technology, integrating emulsion-based single cell separation with barcoded RNAseq (Chromium), plasmablast-derived mAbs from individuals who received SARS-CoV-2 spike mRNA vaccine were characterized for antigen specificity, epitope mapping and neutralization potential (92).

A final molecular approach worth mentioning is the use of mass spectrometry to assess the relative abundance of specific antibodies in serum or a tissue sample, known as Ab-seq (93). Pairing Ab-seq with any of the RNA-seq approaches above allows for inferences to be made regarding the contribution of specific ASC clones to the polyclonal ASC response, providing invaluable insight into the immunological relevance of ASC clonal diversity. Lee et al (94) utilized Ab-seq to identify potently neutralizing antibodies and ASC clones persisting across multiple exposures to influenza. Ab-seq has also been applied in similar studies for antibodies against norovirus (95) and HIV-1 (96).

## DISCUSSION

### Multiplexing Is the Future for High Throughput Single ASC Analyses

The availability of high throughput methods for the study of ASC at the single cell level has progressed immensely for both functional and molecular characterization. Considerable progress has been made in understanding ASC development and differentiation, but with limited information regarding the relationships between population surface marker expression, transcriptional and metabolic activity, and the functional "quality" of the ASC (affinity, specificity, secretion rate).

The presence of immunoglobulins within all plasmablasts or plasma cells does not exclude the possibility for significant stratification of secretion rates from high to nearly

undetectable. As we showed in Eyer et al. (73), antibody secretion by a seemingly homogenous population of ASC may vary by several orders of magnitude. The causes of such secretory diversity remain poorly understood. Current techniques for direct measurement of single cell immunoglobulin secretion (spot- and microfluidic-based assays) are currently unable to distinguish precise B cell populations alone. ASC identified and isolated from direct functional assays have not been assessed afterwards with higher parameter techniques such as flow and mass cytometry or scRNAseq, to interrogate the source of this secretory diversity.

Ultimately, investigations of ASC physiology should strive to employ a combination of the techniques discussed. In the context of antibodies, with only a repertoire of  $V_H$ - $V_L$  sequences the contribution and quality of a given antibody to the humoral immune response is difficult to appreciate. Likewise, knowing the affinity or neutralization repertoire of antibodies from ASC without knowing their clonality and molecular basis limits insight into ASC population dynamics and distribution.

Evolution of the existing and emerging methods for HT ASC phenotypic characterization to readily integrate with the various single cell molecular techniques should be an immediate goal to overcome current limitations. HT single cell molecular (scRNA-seq) techniques are becoming more accessible and affordable, with great efforts to increase the fidelity and ease of analysis. HT single cell assays will be central to unravelling how ASC phenotypic markers relate to their developmental stage, antibody affinity, and antibody or cytokine secretion rate, and to what degree these elements are interrelated.

## AUTHOR CONTRIBUTIONS

All authors listed have made a substantial, direct and intellectual contribution to the work, and approved it for publication.

## FUNDING

PB acknowledges funding from the French National Research Agency grant ANR-14-CE16-0011 project *DROPmAbs* and ANR-18-CE15-0001 project *Autoimmuni-B*, by the Institut Carnot Pasteur Microbes et Santé (ANR 11 CARN 0017-01), the Institut Pasteur and the Institut National de la Santé et de la Recherche Médicale (INSERM). MB is a recipient of a CIFRE fellowship from the French Association Nationale de la Recherche et de la Technologie (ANRT). None of the sources of funding have an interest in the subject matter or materials discussed in the submitted manuscript.

## REFERENCES

1. Nutt SL, Hodgkin PD, Tarlinton DM, Corcoran LM. The Generation of Antibody-Secreting Plasma Cells. *Nat Rev Immunol* (2015) 15(3):160–71. doi: 10.1038/nri3795

2. Shlomchik MJ, Weisel F. Germinal Center Selection and the Development of Memory B and Plasma Cells. *Immunol Rev* (2012) 247(1):52–63. doi: 10.1111/j.1600-065X.2012.01124.x
3. Di Niro R, Lee SJ, Vander Heiden JA, Elsner R, Trivedi N, Bannock J. SalmOnella Infection Drives Promiscuous B Cell Activation Followed By

- Extrafollicular Affinity Maturation. *Immunity* (2015) 43(1):120–131. doi: 10.1016/j.immuni.2015.06.013
4. Allman D, Wilmore JR, Gaudette BT. The Continuing Story of T-Cell Independent Antibodies. *Immunol Rev* (2019) 288(1):128–35. doi: 10.1111/imr.12754
  5. Shaffer AL, Lin KI, Kuo TC, Yu X, Hurt E, Rosenwald A, et al. Blimp-1 Orchestrates Plasma Cell Differentiation by Extinguishing the Mature B Cell Gene Expression Program. *Immunity* (2002) 17(1):51–62. doi: 10.1016/S1074-7613(02)00335-7
  6. Lightman SM, Utley A, Lee KP. Survival of Long-Lived Plasma Cells (LLPC): Piecing Together the Puzzle. *Front Immunol* (2019) 10:965. doi: 10.3389/fimmu.2019.00965
  7. Cordero H, King RG, Dogra P, Dufeu C, See S, Chong A, et al. Intrathymic Differentiation of Natural Antibody-Producing Plasma Cells in Human Neonates. *Nat Commun* (2021) 12(1):5761. doi: 10.1038/s41467-021-26069-2
  8. Nuñez S, Moore C, Gao B, Rogers K, Hidalgo Y, Del Nido P, et al. The Human Thymus Perivascular Space is a Functional Niche for Viral-Specific Plasma Cells. *Sci Immunol* (2016) 1(6). doi: 10.1126/sciimmunol.aah4447
  9. Hauser AE, Debes GF, Arce S, Cassese G, Hamann A, Radbruch A, et al. Chemotactic Responsiveness Toward Ligands for CXCR3 and CXCR4 Is Regulated on Plasma Blasts During the Time Course of a Memory Immune Response. *J Immunol* (2002) 169(3):1277–82. doi: 10.4049/jimmunol.169.3.1277
  10. Chang HD, Tokoyoda K, Hoyer B, Alexander T, Khodadadi L, Mei H, et al. Pathogenic Memory Plasma Cells in Autoimmunity. *Curr Opin Immunol* (2019) 61:86–91. doi: 10.1016/j.coi.2019.09.005
  11. Galipeau Y, Greig M, Liu G, Driedger M, Langlois MA. Humoral Responses and Serological Assays in SARS-CoV-2 Infections. *Front Immunol* (2020) 11:610688. doi: 10.3389/fimmu.2020.610688
  12. Pioli PD. Plasma Cells, the Next Generation: Beyond Antibody Secretion. *Front Immunol* (2019) 10:2768. doi: 10.3389/fimmu.2019.02768
  13. Upasani V, Id IR, Id TC, Rodenhuis-Zybert I, Cantaert T. Antibody-Independent Functions of B Cells During Viral Infections. *PLoS Pathog* (2021) 17(7):e1009708. doi: 10.1371/journal.ppat.1009708
  14. Bucheli OTM, Sigvaldadóttir I, Eyer K. Measuring Single-Cell Protein Secretion in Immunology: Technologies, Advances, and Applications. *Eur J Immunol* (2021) 51(6):1334–47. doi: 10.1002/eji.202048976
  15. Jammes FC, Maerk SJ. How Single-Cell Immunology is Benefiting From Microfluidic Technologies. *Microsystems Nanoeng* (2020) 6(1):45. doi: 10.1038/s41378-020-0140-8
  16. Tzeng SJ. The Isolation, Differentiation, and Quantification of Human Antibody-Secreting B Cells From Blood: Elispot as a Functional Readout of Humoral Immunity. *J Vis Exp* (2016) 2016(118):e54582. doi: 10.3791/54582
  17. Janetzki S, Rueger M, Dillenbeck T. Stepping Up ELISpot: Multi-Level Analysis in FluoroSpot Assays. *Cells* (2014) 3(4):1102–15. doi: 10.3390/cells3041102
  18. Meyer Sauter PM, Seiler M, Trück J, Unger WWJ, Paioni P, Rely C, et al. Diagnosis of Mycoplasma Pneumoniae Pneumonia With Measurement of Specific Antibody-Secreting Cells. *Am J Respir Crit Care Med* (2019) 200(8):1066–9. doi: 10.1164/rccm.201904-0860LE
  19. Carter MJ, Mitchell RM, Sauter PM, Kelly DF, Trück J. The Antibody-Secreting Cell Response to Infection: Kinetics and Clinical Applications. *Front Immunol* (2017) 8:630. doi: 10.3389/fimmu.2017.00630
  20. Lima-Junior J, Morgado F, Conceição-Silva F. How Can Elispot Add Information to Improve Knowledge on Tropical Diseases? *Cells* (2017) 6(4):31. doi: 10.3390/cells6040031
  21. Faresjö M. Enzyme Linked Immuno-Spot; a Useful Tool in the Search for Elusive Immune Markers in Common Pediatric Immunological Diseases. *Cells* (2012) 1(2):141–52. doi: 10.3390/cells1020141
  22. Mahévas M, Michel M, Weill JC, Reynaud CA. Long-Lived Plasma Cells in Autoimmunity: Lessons From B-Cell Depleting Therapy. *Front Immunol* (2013) 4:494(DEC). doi: 10.3389/fimmu.2013.00494
  23. Kuwana M, Okazaki Y, Kaburaki J, Kawakami Y, Ikeda Y. Spleen Is a Primary Site for Activation of Platelet-Reactive T and B Cells in Patients With Immune Thrombocytopenic Purpura. *J Immunol* (2002) 168(7):3675–82. doi: 10.4049/jimmunol.168.7.3675
  24. Saletti G, Çuburu N, Yang JS, Dey A, Czerkinsky C. Enzyme-Linked Immunospot Assays for Direct Ex Vivo Measurement of Vaccine-Induced Human Humoral Immune Responses in Blood. *Nat Protoc* (2013) 8(6):1073–87. doi: 10.1038/nprot.2013.058
  25. Bonezi V, Cataneo AHD, Branquinho MSF, Silva M, Gonzalez-Dias P, Pereira S, et al. Flavivirus-Mediated B Cell Differentiation Into Antibody-Secreting Cells in Humans Is Associated With the Activation of the Tryptophan Metabolism. *Front Immunol* (2020) 11:20. doi: 10.3389/fimmu.2020.00020
  26. Cossarizza A, Chang HD, Radbruch A, Acs A, Adam D, Adam-Klages S, et al. Guidelines for the Use of Flow Cytometry and Cell Sorting in Immunological Studies (Second Edition). *Eur J Immunol* (2019) 49(10):1457–973. doi: 10.1002/eji.201970107
  27. Boonyaratanakornkit J, Taylor JJ. Techniques to Study Antigen-Specific B Cell Responses. *Front Immunol* (2019) 10:1694. doi: 10.3389/fimmu.2019.01694
  28. Ellebedy AH, Jackson KJL, Kissick HT, Nakaya H, Davis C, Roskin K, et al. Defining Antigen-Specific Plasmablast and Memory B Cell Subsets in Blood Following Viral Infection and Vaccination of Humans. *Nat Immunol* (2016) 17(10):1226. doi: 10.1038/NI.3533
  29. Quách TD, Rodríguez-Zhurbenko N, Hopkins TJ, Guo X, Hernández A, Li W, et al. Distinctions Among Circulating Antibody-Secreting Cell Populations, Including B-1 Cells, in Human Adult Peripheral Blood. *J Immunol* (2016) 196(3):1060–9. doi: 10.4049/jimmunol.1501843
  30. Carrell J, Groves CJ. OMIP-043: Identification of Human Antibody Secreting Cell Subsets. *Cytom Part A*. (2018) 93(2):190–3. doi: 10.1002/cyto.a.23305
  31. Sanz I, Wei C, Jenks SA, Cashman K, Tipton C, Woodruff M, et al. Challenges and Opportunities for Consistent Classification of Human B Cell and Plasma Cell Populations. *Front Immunol* (2019) 10:2458(OCT). doi: 10.3389/fimmu.2019.02458
  32. Landsverk OJB, Snir O, Casado RB, Richter L, Mold J, Réu P, et al. Antibody-Secreting Plasma Cells Persist for Decades in Human Intestine. *J Exp Med* (2017) 214(2):309–17. doi: 10.1084/JEM.20161590
  33. Paiva B, Puig N, Cedena MT, de Jong B, Ruiz Y, Rapado I, et al. Differentiation Stage of Myeloma Plasma Cells: Biological and Clinical Significance. *Leukemia* (2017) 31(2):382–92. doi: 10.1038/leu.2016.211
  34. Blanc P, Moro-Sibilot L, Barthly L, Jagot F, This S, de Bernard S, et al. Mature IgM-Expressing Plasma Cells Sense Antigen and Develop Competence for Cytokine Production Upon Antigenic Challenge. *Nat Commun* (2016) 7:13600. doi: 10.1038/ncomms13600
  35. Pinto D, Montani E, Bolli M, Garavaglia G, Sallusto F, Lanzavecchia A, et al. A Functional BCR in Human IgA and IgM Plasma Cells. *Blood* (2013) 121(20):4110–4. doi: 10.1182/BLOOD-2012-09-459289
  36. Pinder CL, Kratochvil S, Cizmeci D, Muir L, Guo Y, Shattock R, et al. Isolation and Characterization of Antigen-Specific Plasmablasts Using a Novel Flow Cytometry-Based Ig Capture Assay. *J Immunol* (2017) 199(12):4180–8. doi: 10.4049/jimmunol.1701253
  37. Price MJ, Hicks SL, Bradley JE, Randall TD, Boss JM, Scharer CD. IgM, IgG, and IgA Influenza-Specific Plasma Cells Express Divergent Transcriptomes. *J Immunol* (2019) 203(8):2121–9. doi: 10.4049/JIMMUNOL.1900285
  38. Glaros V, Rauschmeier R, Artemov AV, Reinhardt A, Ols S, Emmanouilidi A, et al. Limited Access to Antigen Drives Generation of Early B Cell Memory While Restraining the Plasmablast Response. *Immunity* (2021) 54(9):2005–2023.e10. doi: 10.1016/j.immuni.2021.08.017
  39. Franz B, May KF, Dranoff G, Wucherpfennig K. Ex Vivo Characterization and Isolation of Rare Memory B Cells With Antigen Tetramers. *Blood* (2011) 118(2):348. doi: 10.1182/BLOOD-2011-03-341917
  40. Llinàs L, Lázaro A, de Salort J, Matesanz-Isabel J, Sintés J, Engel P. Expression Profiles of Novel Cell Surface Molecules on B-Cell Subsets and Plasma Cells as Analyzed by Flow Cytometry. *Immunol Lett* (2011) 134(2):113–21. doi: 10.1016/j.imlet.2010.10.009
  41. Scharer CD, Patterson DG, Mi T, Price MJ, Hicks SL, Boss JM. Antibody-Secreting Cell Destiny Emerges During the Initial Stages of B-Cell Activation. *Nat Commun* (2020) 11:3989. doi: 10.1038/s41467-020-17798-x
  42. Mahévas M, Patin P, Huetz F, Descatoire M, Cagnard N, Bole-Feysot C, et al. B Cell Depletion in Immune Thrombocytopenia Reveals Splenic Long-Lived Plasma Cells. *J Clin Invest* (2013) 123(1):432–42. doi: 10.1172/JCI65689
  43. Xu M, Jiang Y, Wang J, Liu J, Liu C, Liu D, et al. Distinct Variations of Antibody Secreting Cells and Memory B Cells During the Course of Kawasaki Disease. *BMC Immunol* (2019) 20(1):16. doi: 10.1186/s12865-019-0299-7
  44. Tipton CM, Fucile CF, Darce J, Chida A, Ichikawa T, Gregoretti I, et al. Diversity, Cellular Origin and Autoreactivity of Antibody-Secreting Cell Population Expansions in Acute Systemic Lupus Erythematosus. *Nat Immunol* (2015) 16(7):755–65. doi: 10.1038/ni.3175

45. Jin W, Luo Z, Yang H. Review Article Peripheral B Cell Subsets in Autoimmune Diseases: Clinical Implications and Effects of B Cell-Targeted Therapies. *J Immunol Res* (2020) 2020:9518137. doi: 10.1155/2020/9518137. Published online.
46. Woodruff MC, Ramonell RP, Nguyen DC, Cashman K, Saini A, Haddad N, et al. Extrafollicular B Cell Responses Correlate With Neutralizing Antibodies and Morbidity in COVID-19. *Nat Immunol* 2020 2112 (2020) 21(12):1506–16. doi: 10.1038/s41590-020-00814-z
47. Ramadani F, Bowen H, Upton N, Hobson P, Chan Y, Chen J, et al. Ontogeny of Human IgE-Expressing B Cells and Plasma Cells. *Allergy Eur J Allergy Clin Immunol* (2017) 72(1):66–76. doi: 10.1111/all.12911
48. Nguyen DC, Lewis HC, Joyner C, Warren V, Xiao H, Kissick H, et al. Extracellular Vesicles From Bone Marrow-Derived Mesenchymal Stromal Cells Support Ex Vivo Survival of Human Antibody Secreting Cells. *J Extracell Vesicles* (2018) 7(1):1463778. doi: 10.1080/20013078.2018.1463778
49. Nguyen DC, Joyner CJ, Sanz I, Lee FEH. Factors Affecting Early Antibody Secreting Cell Maturation Into Long-Lived Plasma Cells. *Front Immunol* (2019) 10:2138. doi: 10.3389/fimmu.2019.02138
50. Auladell M, Nguyen TH, Garcillán B, Mackay F, Kedzierska K, Fox A. Distinguishing Naive- From Memory-Derived Human B Cells During Acute Responses. *Clin Transl Immunol* (2019) 8(11):e01090. doi: 10.1002/cti.21090
51. Doucett VP, Gerhard W, Owler K, Curry D, Brown L, Baumgarth N. Enumeration and Characterization of Virus-Specific B Cells by Microfluidic Flow Cytometry. *J Immunol Methods* (2005) 303(1-2):40–52. doi: 10.1016/j.jim.2005.05.014
52. Di Niro R, Mesin L, Raki M, Zheng N, Lund-Johansen F, Lundin K, et al. Rapid Generation of Rotavirus-Specific Human Monoclonal Antibodies From Small-Intestinal Mucosa. *J Immunol* (2010) 185(9):5377–83. doi: 10.4049/jimmunol.1001587
53. Tellier J, Nutt SL. Standing Out From the Crowd: How to Identify Plasma Cells. *Eur J Immunol* (2017) 47(8):1276–9. doi: 10.1002/eji.201747168
54. Fooksman DR, Schwickert TA, Victora GD, Dustin ML, Nussenzweig MC, Skokos D. Development and Migration of Plasma Cells in the Mouse Lymph Node. *Immunity* (2010) 33(1):118–27. doi: 10.1016/j.immuni.2010.06.015
55. Kallies A, Hasbold J, Tarlinton DM, Dietrich W, Corcoran L, Hodgkin P, et al. Plasma Cell Ontogeny Defined by Quantitative Changes in Blimp-1 Expression. *J Exp Med* (2004) 200(8):967–77. doi: 10.1084/jem.20040973
56. Arumugakani G, Stephenson SJ, Newton DJ, Rawstron A, Emery P, Doody G, et al. Early Emergence of CD19-Negative Human Antibody-Secreting Cells at the Plasmablast to Plasma Cell Transition. *J Immunol* (2017) 198(12):4618–28. doi: 10.4049/jimmunol.1501761
57. Glass DR, Tsai AG, Oliveria JP, Hartmann F, Kimmey S, Calderon A, et al. An Integrated Multi-Omic Single-Cell Atlas of Human B Cell Identity. *Immunity* (2020) 53(1):217–32.e5. doi: 10.1016/j.immuni.2020.06.013
58. Hartmann FJ, Mrdjen D, McCaffrey E, Glass D, Greenwald N, Bharadwaj A, et al. Single-Cell Metabolic Profiling of Human Cytotoxic T Cells. *Nat Biotechnol* 2020 392 (2020) 39(2):186–97. doi: 10.1038/s41587-020-0651-8
59. Guo M, Price MJ, Patterson DG, Barwick B, Haines R, Kania A, et al. EZH2 Represses the B Cell Transcriptional Program and Regulates Antibody-Secreting Cell Metabolism and Antibody Production. *J Immunol* (2018) 200(3):1039–52. doi: 10.4049/jimmunol.1701470
60. Han Q, Bradshaw EM, Nilsson B, Haflercd DA, Love JC. Multidimensional Analysis of the Frequencies and Rates of Cytokine Secretion From Single Cells by Quantitative Microengraving. *Lab Chip* (2010) 10(11):1391–400. doi: 10.1039/B926849A
61. Zhu H, Stybayeva G, Silangcruz J, Yan J, Ramanculov E, Dandekar S, et al. Detecting Cytokine Release From Single T-Cells. *Anal Chem* (2009) 81(19):8150–6. doi: 10.1021/AC901390J
62. Torres AJ, Hill AS, Love JC. Nanowell-Based Immunoassays for Measuring Single-Cell Secretion: Characterization of Transport and Surface Binding. *Anal Chem* (2014) 86(23):11562–9. doi: 10.1021/AC4030297
63. Rybczynska M, Baudry J, Klaus E. The Impact of Frost-Damage on the Quality and Quantity of the Secreted Antigen-Specific IgG Repertoire. *Vaccine* (2020) 38(33):5337–42. doi: 10.1016/j.vaccine.2020.05.066
64. Winters A, McFadden K, Bergen J, Landas J, Berry K, Gonzalez A, et al. Rapid Single B Cell Antibody Discovery Using Nanopens and Structured Light. *MAbs* (2019) 11(6):1025. doi: 10.1080/19420862.2019.1624126
65. Zost SJ, Gilchuk P, Chen RE, Case J, Reidy J, Trivette A, et al. Rapid Isolation and Profiling of a Diverse Panel of Human Monoclonal Antibodies Targeting the SARS-CoV-2 Spike Protein. *Nat Med* (2020) 26(9):1422. doi: 10.1038/s41591-020-0998-X
66. Ogunniyi AO, Story CM, Papa E, Guillen E, Love JC. Screening Individual Hybridomas by Microengraving to Discover Monoclonal Antibodies. *Nat Protoc* (2009) 4(5):767–82. doi: 10.1038/NPROT.2009.40
67. Ogunniyi AO, Thomas BA, Politano TJ, Varadarajan N, Landais E, Poignard P, et al. Profiling Human Antibody Responses by Integrated Single-Cell Analysis. *Vaccine* (2014) 32(24):2866–73. doi: 10.1016/j.vaccine.2014.02.020
68. Story CM, Papa E, Hu CC, Ronan JL, Herlihy K, Ploegh HL, et al. Profiling Antibody Responses by Multiparametric Analysis of Primary B Cells. *Proc Natl Acad Sci U S A* (2008) 105(46):17902–7. doi: 10.1073/PNAS.0805470105
69. Gérard A, Woolfe A, Mottet G, Reichen M, Castrillon C, Menrath V, et al. High-Throughput Single-Cell Activity-Based Screening and Sequencing of Antibodies Using Droplet Microfluidics. *Nat Biotechnol* (2020) 38(6):715–21. doi: 10.1038/s41587-020-0466-7
70. Matutis L, Gilbert J, Ung WL, Weitz DA, Griffiths AD, Heyman JA. Single-Cell Analysis and Sorting Using Droplet-Based Microfluidics. *Nat Protoc* (2013) 8(5):870–91. doi: 10.1038/NPROT.2013.046
71. Ding R, Hung KC, Mitra A, Ung L, Lightwood D, Tu R, et al. Rapid Isolation of Antigen-Specific B-Cells Using Droplet Microfluidics. *RSC Adv* (2020) 10(45):27006–13. doi: 10.1039/d0ra04328a
72. Shembekar N, Hu H, Eustace D, Merten CA. Single-Cell Droplet Microfluidic Screening for Antibodies Specifically Binding to Target Cells. *Cell Rep* (2018) 22(8):2206–15. doi: 10.1016/j.celrep.2018.01.071
73. Eyer K, Doineau RCL, Castrillon CE, Briseño-Roa L, Menrath V, Mottet G, et al. Single-Cell Deep Phenotyping of IgG-Secreting Cells for High-Resolution Immune Monitoring. *Nat Biotechnol* (2017) 35(10):977–82. doi: 10.1038/nbt.3964
74. Canales-Herrerias P, Crickx E, Broketa M, Sokal A, Chenon G, Azzaoui I, et al. Single-Cell Analyses of Immune Thrombocytopenic Patients Reveal Multiorgan Dissemination of High-Affinity Autoreactive Plasma Cells. *bioRxiv* (2021) 2021.06.29.450355. doi: 10.1101/2021.06.29.450355
75. Kräutler NJ, Yermanos A, Pedrioli A, Welten S, Lorgé D, Greczmiel U, et al. Quantitative and Qualitative Analysis of Humoral Immunity Reveals Continued and Personalized Evolution in Chronic Viral Infection. *Cell Rep* (2020) 30(4):997–1012.e6. doi: 10.1016/j.celrep.2019.12.088
76. Eyer K, Castrillon C, Chenon G, Bibette J, Bruhns P, Griffiths A, et al. The Quantitative Assessment of the Secreted IgG Repertoire After Recall to Evaluate the Quality of Immunizations. *J Immunol* (2020) 205(4):1176–84. doi: 10.4049/jimmunol.2000112
77. Alanine DGW, Quinkert D, Kumarasingha R, Gilson PR, Higgins MK, Draper Correspondence SJ. Human Antibodies That Slow Erythrocyte Invasion Potentiate Malaria-Neutralizing Antibodies. *Cell* (2019) 178:216–228.e21. doi: 10.1016/j.cell.2019.05.025
78. Viant C, Weymar GHJ, Escolano A, Cipolla M, Gazumyan A, Correspondence MCN. Antibody Affinity Shapes the Choice Between Memory and Germinal Center B Cell Fates. *Cell* (2020) 183:1298–1311.e11. doi: 10.1016/j.cell.2020.09.063
79. Bornholdt ZA, Turner HL, Murin CD, Li W, Sok D, Souders CA, et al. Isolation of Potent Neutralizing Antibodies From a Survivor of the 2014 Ebola Virus Outbreak. *Science* (2016) 351(6277):1078–83. doi: 10.1126/SCIENCE.AAD5788
80. Sokal A, Barba-Spaeth G, Fernández I, Broketa M, Azzaoui I, de la Selle A, et al. mRNA Vaccination of Naive and COVID-19-Recovered Individuals Elicits Potent Memory B Cells That Recognize SARS-CoV-2 Variants. *Immunity* (2021) 54(12):2893–907.e5. doi: 10.1016/j.immuni.2021.09.011
81. Williams LD, Ofek G, Schätzle S, McDaniel J, Lu X, Nicely N, et al. Potent and Broad HIV-Neutralizing Antibodies in Memory B Cells and Plasma. *Sci Immunol* (2017) 2(7):27. doi: 10.1126/SCIIMMUNOL.AAL2200
82. Lee J, Boutz DR, Chromikova V, Joyce M, Vollmers C, Leung K, et al. Molecular-Level Analysis of the Serum Antibody Repertoire in Young Adults Before and After Seasonal Influenza Vaccination. *Nat Med* 2016 2212. (2016) 22(12):1456–64. doi: 10.1038/nm.4224
83. Rees AR. Understanding the Human Antibody Repertoire. *mAbs* (2020) 12(1):e1729683. doi: 10.1080/19420862.2020.1729683

84. Lindeman I, Emerton G, Mamanova L, Snir O, Polanski K, Qiao S, et al. BraCeR: B-Cell-Receptor Reconstruction and Clonality Inference From Single-Cell RNA-Seq. *Nat Methods* 2018 15(8):563–5. doi: 10.1038/s41592-018-0082-3
85. Rizzetto S, Koppstein DNP, Samir J, Singh M, Reed J, Cai C, et al. B-Cell Receptor Reconstruction From Single-Cell RNA-Seq With VDJpuzzle. *Bioinformatics* (2018) 34(16):2846–7. doi: 10.1093/BIOINFORMATICS/BTY203
86. Delaloy C, Schuh W, Jäck H-M, Bonaud A, Espéli M. Single Cell Resolution of Plasma Cell Fate Programming in Health and Disease. *Eur J Immunol* (2021). doi: 10.1002/EJL.202149216
87. Ise W, Kurosaki, Tomohiro, Kurosaki T. Plasma Cell Differentiation During the Germinal Center Reaction. *Immunol Rev* (2019) 288:64–74. doi: 10.1111/imr.12751
88. Curtis NC, Lee J. Beyond Bulk Single-Chain Sequencing: Getting at the Whole Receptor. *Curr Opin Syst Biol* (2020) 24:93–9. doi: 10.1016/j.coisb.2020.10.008
89. Setliff I, Shiakolas AR, Pilewski KA, Murji A, Mapengo R, Janowska K, et al. High-Throughput Mapping of B Cell Receptor Sequences to Antigen Specificity. *Cell* (2019) 179(7):1636–1646.e15. doi: 10.1016/j.cell.2019.11.003
90. Wang B, Dekosky BJ, Timm MR, Lee J, Normandin E, Misasi J, et al. Functional Interrogation and Mining of Natively Paired Human VH:VL Antibody Repertoires. *Nature Biotechnol* (2018) 36:152–5. doi: 10.1038/nbt.4052
91. Jiang R, Fichtner ML, Hoehn KB, Pham M, Stathopoulos P, Nowak R, et al. Single-Cell Repertoire Tracing Identifies Rituximab-Resistant B Cells During Myasthenia Gravis Relapses. *JCI Insight* (2020) 5(14):e136471. doi: 10.1172/JCI.INSIGHT.136471
92. Amanat F, Thapa M, Lei T, Ahmed S, Adelsberg D, Carreño J, et al. SARS-CoV-2 mRNA Vaccination Induces Functionally Diverse Antibodies to NTD, RBD, and S2. *Cell* (2021) 184(15):3936–48.e10. doi: 10.1016/j.cell.2021.06.005
93. Snapkov I, Chernigovskaya M, Sinitcyn P, Lê Quý K, Nyman TA, Greiff V. Progress and Challenges in Mass Spectrometry-Based Analysis of Antibody Repertoires. *Trends Biotechnol* (2021). doi: 10.1016/j.tibtech.2021.08.006
94. Lee J, Paparoditis P, Horton AP, Frühwirth A, McDaniel J, Jung J, et al. Persistent Antibody Clonotypes Dominate the Serum Response to Influenza Over Multiple Years and Repeated Vaccinations. *Cell Host Microbe* (2019) 25(3):367–76.e5. doi: 10.1016/j.chom.2019.01.010
95. Lindesmith LC, McDaniel JR, Changela A, Verardi R, Kerr S, Costantini V, et al. Sera Antibody Repertoire Analyses Reveal Mechanisms of Broad and Pandemic Strain Neutralizing Responses After Human Norovirus Vaccination. *Immunity* (2019) 50(6):1530–41.e8. doi: 10.1016/j.immuni.2019.05.007
96. Sajadi MM, Dashti A, Rikhtegaran Tehrani Z, Tolbert W, Seaman M, Ouyang X, et al. Identification of Near-Pan-Neutralizing Antibodies Against HIV-1 by Deconvolution of Plasma Humoral Responses. *Cell* (2018) 173(7):1783–95.e14. doi: 10.1016/j.cell.2018.03.061

**Conflict of Interest:** The authors declare that the research was conducted in the absence of any commercial or financial relationships that could be construed as a potential conflict of interest. PB is a paid consultant to Regeneron Pharmaceuticals. MB declares that he has no relevant conflicts of interest.

**Publisher's Note:** All claims expressed in this article are solely those of the authors and do not necessarily represent those of their affiliated organizations, or those of the publisher, the editors and the reviewers. Any product that may be evaluated in this article, or claim that may be made by its manufacturer, is not guaranteed or endorsed by the publisher.

Copyright © 2022 Broketa and Bruhns. This is an open-access article distributed under the terms of the Creative Commons Attribution License (CC BY). The use, distribution or reproduction in other forums is permitted, provided the original author(s) and the copyright owner(s) are credited and that the original publication in this journal is cited, in accordance with accepted academic practice. No use, distribution or reproduction is permitted which does not comply with these terms.

## **What is currently missing?**

The organization and drivers of ASC responses are numerous and complex, with several key regulatory and physiological aspects remaining unclear. The advent of accessible high-throughput methods for transcriptome and VDJ gene characterization has been a breakthrough in B cell research. We now appreciate the broad spectrum of heterogeneous B cell subsets that highlight the unique biology of B cells depending on localization and disease context<sup>117</sup>, with insights into the functional diversity of ASCs<sup>118</sup>. Moreover, the integration of spatial transcriptomics into this framework could provide spatial context, shedding light on the intricate interplay between B cells and their microenvironment. The application of machine learning to large-scale B cell datasets is another avenue of growth. These technologies aid in deciphering complex patterns, identifying novel biomarkers, and predicting B cell behavior in response to various stimuli. Harnessing computational models can accelerate the discovery of key regulatory pathways, offering new targets for therapeutic intervention in autoimmune diseases, immunodeficiencies, and cancer immunotherapies.

These advancements in genotypic profiling have not been matched by advances in B cell antibody phenotyping, which has made it challenging to develop cohesive models that bridge the gap between genetic information and functional insights. The complexity of B cell responses extends beyond genetics to encompass intricate interactions between B cells and their environment. Traditional methods such as ELISA and flow cytometry provide valuable but limited information, often focusing on a subset of known antigens and epitopes. The advent of high-throughput sequencing has allowed for more comprehensive profiling of antibody repertoires, but ultimately the functional relevance of these antibodies remains challenging to decipher. One of the key challenges in bridging the gap between genetics and B cell function lies in understanding the relationship between antibody sequence and its functional properties. The need for better antibody characterization, including specificity and affinity, during repertoire analyses is particularly important for improving computational methods for structural and binding predictive modelling<sup>119</sup>, which could eventually reduce the necessity for more intensive phenotyping methods.

The role of antibody affinity in B cell differentiation has been the topic of intensive investigation and debate. The requirement for antigen binding is clear and there are numerous studies demonstrating that a higher affinity antibody leads to increased ASC differentiation

outcomes<sup>120,121</sup>. The basis for antibody affinity providing increased B cell fitness during maturation lies within the increased mechanical resilience provided by higher binding affinities as well as the increased rate and stability of immune complex formation during the immune-synapse mediated activation<sup>30</sup>. Considering the comprehensive, mechanistic studies demonstrating the advantages afforded to B cells with higher affinity antibodies, affinity maturation has been understandably considered to be an absolute rule within the GC. Further differentiated, matured B cells are considered to have higher affinities. Moreover, antibody affinity is widely treated as a strict threshold or limit during the stages of differentiation, i.e., affinity must be below the threshold for deletion in the bone marrow, then above the threshold for binding free or presented antigen and being activated, and finally once affinity is within an unknown threshold (either unmutated or through maturation) the B cell may differentiate into specific subsets.

A major publication in the discussion of affinity in B cell responses was recently published by Viant et al in 2020 (Figure 8A)<sup>122</sup>. The authors adopted an unbiased fate mapping approach in mice immunized with HIV antigen, providing a fresh perspective when compared to previous studies that relied on transgenic B cells or sorting based on antigen-labelling. It was shown that a significant portion of GC B cells express high-affinity antibodies derived from unmutated common ancestors (UCAs) with similarly elevated affinity, whereas the majority of concurrently emerging Bmem had weak affinities for the antigen. Importantly, the disparity between GC B cells and Bmem was not related to differences in SHM, as both strongly and poorly mutated clones showed this division. This affinity deterministic model for B cell fate commitment was reinforced by another recent study of the B cell response to flaviviruses (Figure 8B)<sup>123</sup>. The authors report that the majority of Bmem were derived from naïve precursors with poor affinity towards flaviviral antigen, with minimal clonal overlap to the ASC compartment.

However, despite the evidence for an affinity determinism model, there is a growing body of work demonstrating broader ranges of affinities in ASCs and Bmem and questioning established principles in the relation of affinity to B cell development. A recent study performed comprehensive single cell RNAseq and BCRseq in a murine model of influenza infection<sup>42</sup>, across multiple SLOs and the lungs (Figure 8C). The authors demonstrate that plasmablasts and Bmem from the same clonotypes emerge concurrently and importantly that their antibodies were of similar affinities. Antibody affinity was also attributed in this study to be determined primarily by

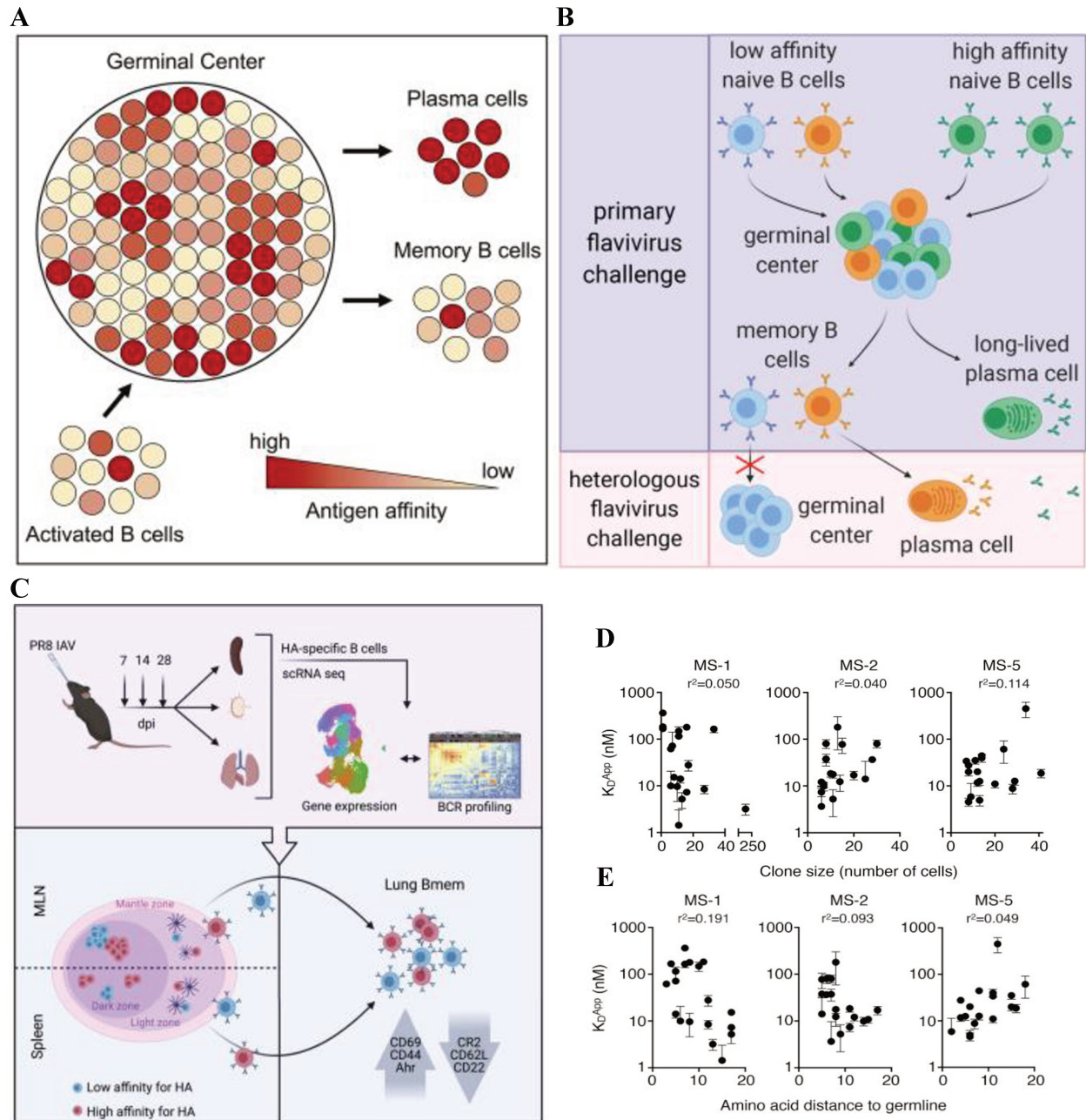


Figure 8 Conflicting models in role of affinity in ASC differentiation. Various studies have found ASCs to be either (A-B) predominantly populated by higher affinity clones or (C-E) contain a broad spectrum of affinities. (A-C) Graphical abstracts from (A) Viant et al. (2020)<sup>122</sup>, (B) Wong et al. (2020)<sup>123</sup>, and (C) Mathew et al (2021)<sup>42</sup>. (D-E) Shows Figure 2A-B from Neumeier et al (2022)<sup>124</sup>, demonstrating the lack of correlation between antibody affinity towards the model antigen ovalbumin and clone size or degree of mutation among mouse-derived bone marrow plasma cells. Error bars indicate SD (n = 2–3 measurements of Kd).

clonotype and not the extent of SHM or B cell type (Bmem vs ASC). Another recent study profiling plasma cell genotype and phenotype provides evidence for affinity being unrelated to expansion in plasma cell repertoires<sup>124</sup>, with similar reported affinity repertoires as our DropMap studies. The

authors reported no correlation between affinity and clonal representation or likewise between affinity and the degree of SHM, with examples of high affinity clones with weak clonal expansion (Figure 8D-E); analyses of the most highly expanded clonal lineages also reinforced the concept of an affinity ceiling, with minimal changes in affinity despite the accumulation of mutations. Ultimately, antigen specificity was the primary determinant of clonal expansion and representation in the bone marrow and not affinity. Together these studies provide examples of Bmem, plasmablasts, and plasma cells displaying broad repertoires of affinities towards their antigens, with clonal expansion and B cell subset differentiation not appearing to be determined by affinity.

The divergent findings regarding affinity in B cell differentiation may be related to differences in pathogens and antigens used in models. The use of smaller antigens, including haptens (NP) or monovalent proteins (ovalbumin or lysozyme), was common during the formulation of many B cell response principles. However, studies are now increasingly assessing responses to whole pathogens or large, multimeric antigens, which increases the potential for BCR cross-linking, bivalent antibody binding and avidity, and the recruitment of B cells towards diverse sets of epitopes. The effect of antigen valency has been demonstrated to have profound effects on the scale and nature of the ASC response, using HIV antigen constructs containing between 1 and 60 domains<sup>125</sup>. Immunization with a lower valency construct was found to limit the B cell response to high affinity clones, whereas high valency immunogen yielded broader affinity repertoires; a similar difference was found regarding the magnitude of ASC differentiation. Moreover, differences in monovalent antigen “footprints” have been proposed to also influence the threshold for B cell activation<sup>126</sup>.

Collectively, these various studies have provided compelling evidence that calls into question several established B cell principles, including the division between Bmem and ASCs regarding possession of low or high affinity antibodies and the role of antibody affinity in GC reactions. Subsequent questions raised include whether low-to-medium affinity ASCs are generated intentionally as a consequence of maintaining repertoire diversity, if these potentially weaker antibodies are also important elements of humoral immune memory for cross-reactivity, or if these observations represent “mistakes” in ASC differentiation gatekeeping; answering this question would be valuable in assessing whether vaccinations should aim for depth and higher affinity ASCs or if improved protection may lie in cultivating an increased breadth of ASC coverage<sup>123,127</sup>.

To develop cohesive models that encompass both genetic information and functional insights, there is a need for integrated approaches that combine genotypic and phenotypic data. Currently, the route pursued by most investigators is to leverage the high throughput of single cell genotyping methods to broadly survey antibody repertoires, followed by limited re-expression of a small fraction of the repertoire (10-100 clones). It is not unreasonable to consider antibody phenotype as an equally important marker when forming B cell subsets; integrating specificity and affinity values with transcriptional expression data during bioinformatic clustering analyses may elucidate further heterogeneity. The gap in studies concerning antibody affinities is not the result of a lack of interest or awareness but rather reflects the technical limitations imposed by such a challenge. However, the need for more affinity-driven investigations of ASC responses is clear to address the role of affinity in ASC differentiation and to obtain more robust characterizations of the functional diversity during ASC responses.

# AIMS

## Aims

The global aim of this thesis has been to investigate the antibody affinities of antibody-secreting cells (ASC) in vaccination and autoimmune responses, with the goal of better understanding the role of antibody affinity in these immune contexts.

*Note: Initially my PhD project consisted of developing a technique to recover ASC of interest from a droplet microfluidic chamber to link phenotype to genotype and describe the clonal distribution of ASC in human thrombocytopenia. Due to the COVID-19 outbreak and the possibility to collaborate with the lab of Dr Matthieu Mahévas (INEM, Paris) on the B cell response during COVID-19 infection and SARS-CoV-2 mRNA vaccination programs, we decided to prioritize the analyses of ASC and memory B cells from infected and vaccinated individuals.*

### **Aim 1: Characterize the ASC response to mRNA vaccination against SARS-CoV-2**

The development of novel mRNA vaccinations to combat the COVID-19 pandemic created a unique need and opportunity to characterize a novel humoral B cell response following immunization. We aimed to use the DropMap technique to characterize at a large scale and high throughput the functional characteristics of ASCs in the weeks and months after mRNA vaccine administration, with distinction between individuals according to prior SARS-CoV-2 infection.

→ 1 publication : Broketa M, *et al. J Clin Invest Insight* 2023.

### **Aim 2: Measure the affinity repertoires of Bmem following mRNA vaccination against SARS-CoV2**

We also aimed to characterize the affinity repertoires of Bmem-derived antibodies towards numerous SARS-CoV-2 RBD variants by implementing a high throughput screening system based on biolayer interferometry measurements.

→ 3 publications : Sokal A, *et al. Immunity* 2021. Broketa, M: co-first author

Sokal A, *et al. Immunity* 2022. Broketa, M: co-first author

Sokal A, *et al. Immunity* 2023. Broketa, M: co-second author

### **Aim 3: Develop a novel technique to recover cells of interest from DropMap**

DropMap is a powerful technique for direct identification of ASCs and affinity characterization. There is however much more to be learned from analyzing these cells of interest by additional

methods, such as FACS for surface marker phenotyping or BCRseq for clonal analyses and re-expression. The ability to recover cells of interest from the DropMap assay would allow for unprecedented depth of ASC characterization, and immensely reduce the time and expense of obtaining this data in comparison to other methods. We therefore aimed to develop a workflow to specifically label and isolate cells from within DropMap.

→ 1 manuscript in preparation: Broketa, M: last and corresponding author.

#### **Aim 4: Characterize the autoreactive ASCs of ITP patients**

We aimed to continue ongoing characterization of anti-platelet, GPIIbIIIa-specific ASCs from individuals with ITP as well as healthy donors. We also performed measurements to compare the influence of cryopreservation on DropMap measurements, specifically the affinity and IgG secretion rate of ASCs.

→ 1 publication : Canales-Herrerias, et al. J Clin Invest 2022. Broketa, M: co-author

# RESULTS

# ARTICLE 1

## ARTICLE 1:

### mRNA vaccine driven ASC response towards SARS-CoV2 RBD

The mRNA vaccination against SARS-CoV-2 is known to elicit protective B cell responses specifically targeting the spike glycoprotein of the virus. While memory B cell responses directed at the spike protein endure for extended periods, the humoral antibody response targeting the same spike protein gradually diminishes over time. Consequently, booster vaccinations become essential to sustain the protective immunity conferred by the initial vaccination. There was also a lack of insight into the kinetics of the antibody-related physiology of ASCs following mRNA vaccination, which we sought to address. To delve into this phenomenon, our study conducted a qualitative examination of plasmablast responses, assessing the affinity of antibodies secreted by individual cells for the receptor binding domain (RBD) of the SARS-CoV-2 spike protein. We conducted this analysis on two distinct groups: individuals who were previously unvaccinated and individuals who had recovered from COVID-19. Our approach employed droplet microfluidics and imaging techniques, allowing us to scrutinize over 4,000 single IgG-secreting cells. This approach holds promise for optimizing vaccination protocols, enabling us to gain valuable insights into the dynamics of antibody affinity during the immune response to SARS-CoV-2 and the development of immunity following vaccination. See below Broketa et al (2023)<sup>128</sup>

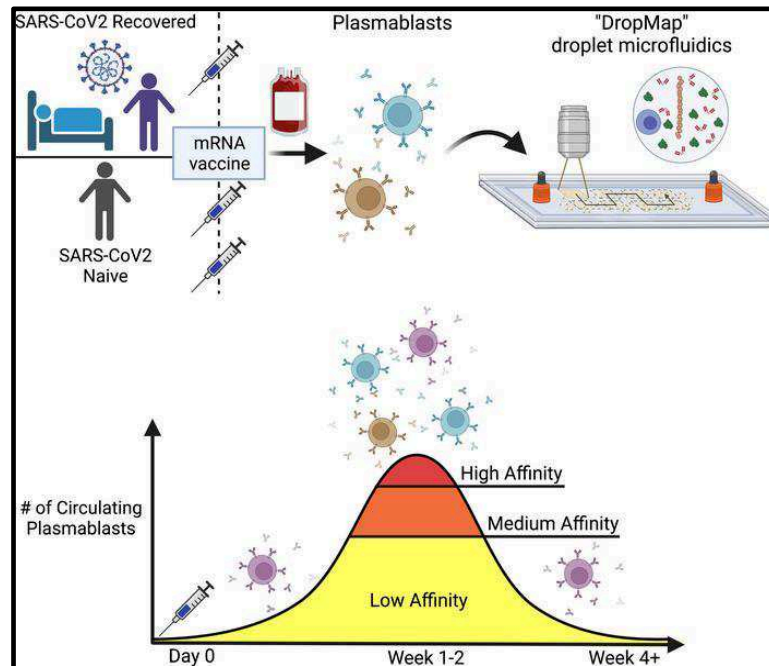


Figure 9 Graphical abstract from Broketa et al (2023)

# Qualitative monitoring of SARS-CoV-2 mRNA vaccination in humans using droplet microfluidics

Matteo Broketa,<sup>1,2,3</sup> Aurélien Sokal,<sup>4</sup> Michael Mor,<sup>5</sup> Pablo Canales-Herrerias,<sup>1</sup> Angga Perima,<sup>1</sup> Annalisa Meola,<sup>6</sup> Ignacio Fernández,<sup>6</sup> Bruno Iannascoli,<sup>1</sup> Guilhem Chenon,<sup>7</sup> Alexis Vandenberghe,<sup>4,8,9</sup> Laetitia Languille,<sup>8</sup> Marc Michel,<sup>8</sup> Bertrand Godeau,<sup>8</sup> Sébastien Gallien,<sup>10</sup> Giovanna Melica,<sup>10</sup> Marija Backovic,<sup>6</sup> Felix A. Rey,<sup>6</sup> Jean Baudry,<sup>7</sup> Natalia T. Freund,<sup>5</sup> Matthieu Mahévas,<sup>4,8,9,11</sup> and Pierre Bruhns<sup>1,11</sup>

<sup>1</sup>Institut Pasteur, Université Paris Cité, Inserm UMR1222, Antibodies in Therapy and Pathology, 75015 Paris, France.

<sup>2</sup>Diaccurate SA, Paris, France. <sup>3</sup>Sorbonne Université, Collège Doctoral, F-75005 Paris, France. <sup>4</sup>Institut Necker Enfants Malades (INEM), INSERM U1151/CNRS UMS 8253, Université de Paris, Paris, France. <sup>5</sup>Department of Clinical Microbiology and Immunology, Sackler Faculty of Medicine, Tel Aviv University, Tel Aviv, Israel. <sup>6</sup>Institut Pasteur, Université Paris Cité, CNRS UMR3569, Structural Virology, 75015 Paris, France. <sup>7</sup>Laboratoire Colloïdes et Matériaux Divisés (LCMD), ESPCI Paris, PSL Research University, CNRS UMR8231 Chimie Biologie Innovation, Paris, France. <sup>8</sup>Service de Médecine Interne, Centre Hospitalier Universitaire Henri-Mondor, Assistance Publique-Hôpitaux de Paris (AP-HP), Université Paris-Est Créteil (UPEC), Créteil, France. <sup>9</sup>INSERM U955, Équipe 2. Institut Mondor de Recherche Biomédicale (IMRB), Université Paris-Est Créteil (UPEC), Créteil, France. <sup>10</sup>Service de Maladies Infectieuses, Centre Hospitalier Universitaire Henri-Mondor, Assistance Publique-Hôpitaux de Paris (AP-HP), Université Paris-Est Créteil (UPEC), Créteil, France. <sup>11</sup>Paris Est Créteil University UPEC, Assistance Publique-Hôpitaux de Paris (AP-HP), Henri Mondor Hospital, Fédération Hospitalo-Universitaire TRUE InnoVaTive theRapy for immUne disordErs, Créteil, France.

**Authorship note:** M Broketa and AS contributed equally to this work. M Mahévas and PB are co-senior authors.

**Conflict of interest:** Outside of the submitted work, PB received consulting fees from Regeneron Pharmaceuticals; M. Mahévas received research funds from GSK and consulting fees from LFB and Amgen. FAR is a member of the board of MELETIOS Therapeutics and of the Scientific Advisory Board of eureKARE.

**Copyright:** © 2023, Broketa et al. This is an open access article published under the terms of the Creative Commons Attribution 4.0 International License.

**Submitted:** October 24, 2022

**Accepted:** May 25, 2023

**Published:** July 10, 2023

**Reference information:** *JCI Insight*. 2023;8(13):e166602.  
<https://doi.org/10.1172/jci.insight.166602>.

**SARS-CoV-2 mRNA vaccination generates protective B cell responses targeting the SARS-CoV-2 spike glycoprotein. Whereas anti-spike memory B cell responses are long lasting, the anti-spike humoral antibody response progressively wanes, making booster vaccinations necessary for maintaining protective immunity. Here, we qualitatively investigated the plasmablast responses by measuring from single cells within hours of sampling the affinity of their secreted antibody for the SARS-CoV-2 spike receptor binding domain (RBD) in cohorts of BNT162b2-vaccinated naive and COVID-19-recovered individuals. Using a droplet microfluidic and imaging approach, we analyzed more than 4,000 single IgG-secreting cells, revealing high interindividual variability in affinity for RBD, with variations over 4 logs. High-affinity plasmablasts were induced by BNT162b2 vaccination against Hu-1 and Omicron RBD but disappeared quickly thereafter, whereas low-affinity plasmablasts represented more than 65% of the plasmablast response at all time points. Our droplet-based method thus proves efficient at fast and qualitative immune monitoring and should be helpful for optimization of vaccination protocols.**

## Introduction

Since the SARS-CoV-2 pandemic began in early 2020, close to 760 million cases of infection and over 6.8 million deaths have been reported by the WHO. The emergency use authorization by drug administration agencies worldwide allowed anti-SARS-CoV-2 vaccination to start by the end of 2020, with over 5.5 billion people receiving at least 1 dose and more than 5.1 billion fully vaccinated (at least 2 doses) as of April, 2023. This astounding global vaccination effort has been kick-started by mRNA-based vaccines encoding a stabilized version of the trimeric spike protein of SARS-CoV-2, developed by either Moderna or Pfizer-BioNTech. Both vaccines had indeed demonstrated rapid and strong immune responses and efficacy in phase III studies, eliciting effective B cell-dependent humoral immunity, with high titers of neutralizing antibodies, which are key to prevention of severe COVID-19 and mortality (1–7). Yet, the neutralizing antibody titers in sera from vaccinees decreased rapidly for the first 3 months, with a relatively slow decrease thereafter (8, 9).

An additional challenge is the rapid emergence of SARS-CoV-2 variants, particularly with mutations in the receptor-binding domain (RBD) of the spike protein, raising concerns that the immunity raised against the initial SARS-CoV-2 strain Wuhan-Hu-1 (termed Hu-1 herein), either following natural infection or following vaccination, would not be protective against SARS-CoV-2 variants of concern (VOCs) (10, 11). Whereas most VOCs (B.1.1.7 [Alpha], B.1.351 [Beta], P.1 [Gamma], B.1.617.2 [Delta]) harbor relatively few (8–12) amino acid mutations in their spike protein as compared with the original Hu-1 strain, the Omicron BA.1, BA.2, BA.3, and BA.4/BA.5 variants harbor 24–34 mutations, making immune escape by these latter variants highly probable (12). Most clinically approved monoclonal antibodies (mAbs) indeed fail to protect from these newest variants (13, 14). This continuous emergence of novel viral variants isolated from patients drives a continuous vaccination effort to induce long-term immune responses with the hope to cover all present and future viral variants.

The main efforts to characterize the patient's immune response to natural infection and/or vaccination focused on serological profiling of the circulating neutralizing antibody responses, and on spike- or RBD-specific memory B cells (MBCs), from which a selection of antibodies was expressed and assayed *in vitro* for neutralization potency and binding affinity (15, 16). While convergent results following natural infection and/or vaccination report a fast decrease in serum neutralization over the first 3 months, the MBC response over time remains relatively stable against the original Hu-1 strain as well as most VOCs, with antibodies expressed from these repertoires exhibiting a wide range of 0.2–2,000 nM binding affinity against Hu-1 spike/RBD (3, 7, 15, 17). Moreover, the cross-reactivity of anti-Hu-1 antibody and MBC responses with Omicron was reported to be approximately 30% after 2 vaccine doses (18, 19) and up to 50% after 3 doses (16).

Rare studies have included the analysis of spike-specific antibody-secreting cells (ASCs), *i.e.*, plasmablasts and plasma cells. Two investigations published by the Ellebedy lab analyzed bone marrow cells and fine-needle aspirates of lymph nodes (9, 20). These studies described expression of antibodies from bone marrow, lymph node plasma cells, and circulating plasmablasts, with up to 1,500 mAbs recombinantly expressed for a single study (20). This impressive work nevertheless required single-cell sorting, antibody variable region (VH-VL) gene sequencing, repertoire analyses, cloning/synthesis, recombinant expression, and finally, affinity measurements. Therefore, while being extremely informative, such an approach entails a large workload, cost, and time investments, and thus the total number of antibodies that can be eventually analyzed is limited.

The ability to measure large numbers of spike-specific antibody binding affinity directly can shed light on the immune response following infection or vaccination in a rapid fashion that will help evaluate vaccination protocols and public health measures. We describe here an adaptation for such human studies of a droplet-based microfluidic technology (DropMap) with same-day results obtained at highly reduced workload and costs (21). DropMap combines the immobilization within an observation chamber of approximately 100,000 picoliter-size droplets containing nonsorted single cells with an ultrasensitive fluorescent bioassay. DropMap was reported for mouse studies to qualitatively follow immune responses to protein immunization (22), bacteria (23), viruses (24), and abnormal IgG secretion (25), and for clinical studies to measure single-cell cytokine secretion from sepsis patients (26), cytotoxicity from single human NK cells (27), and affinity and secretion rate of IgGs secreted by autoreactive IgG-secreting cells from blood, spleen, and bone marrow of patients with immune thrombocytopenia (28). Using this massively parallel kinetic analyses of single ASCs, we evaluated the initial circulating ASC responses in cohorts of individuals vaccinated with BNT162b2 (Pfizer-BioNTech). Two cohorts were included, one of individuals with no prior SARS-CoV-2 infection (COVID-19-naïve), and one of individuals who had recovered from a SARS-CoV-2 infection 1 year before (COVID-19-recovered). We followed these cohorts over time, after 1 or 2 doses of SARS-CoV-2 mRNA vaccine and analyzed their ASC response against Hu-1 RBD, and for selected individuals also for BA.1 RBD.

## Results

*Single-cell bioassay allows phenotypic characterization of RBD-specific ASCs.* For this study, we adapted a single-cell bioassay in microfluidic droplets termed DropMap that we have described previously (22, 26, 28). DropMap allows for a direct sorting-free assessment of the antibody-based cellular immune response, while characterizing the secretion rate, specificity, and affinity for SARS-CoV-2 Hu-1 RBD of human IgG secreted by circulating plasmablasts and plasma cells, which here we collectively term IgG-secreting cells (IgG-SCs), allowing for analysis of 10,000–20,000 cells/hour.

Human peripheral blood mononuclear cells (PBMCs) of volunteers were coencapsulated in droplets along with paramagnetic nanoparticles and fluorescent bioassay reagents that were immobilized within an observation chamber and imaged over 1 hour by time-lapse fluorescence imaging (Figure 1A

and Supplemental Figure 1A; supplemental material available online with this article; <https://doi.org/10.1172/jci.insight.166602DS1>). Including paramagnetic beads in the droplets allows the use of a magnetic field to align them and make a clearly distinguishable pattern (termed the “beadline”) by microscopy. The beads were coated with an IgG capture reagent, and the droplets contained a fluorescently labeled IgG detection reagent and fluorescently labeled monomeric RBD, leading to a fluorescent beadline when IgG is secreted within the droplet. The beadline thus serves as a physical surface for a double-fluorescent sandwich immunoassay, revealing IgG secretion from the cell and specificity of that IgG for the antigen (i.e., Hu-1 RBD; Figure 1, B and C). Image analyses consisted of 5 stages: (i) identifying each droplet and its spatial coordinates within the DropMap chamber; (ii) identifying the beadline within each droplet; (iii) selecting droplets containing a single cell; (iv) extracting for each time point the fluorescence signals of the beadline, and of the entire droplet without the beadline; and (v) calculating the fluorescence accumulation on the beadline over time. Each droplet is assessed individually, both computationally and visually, to ensure proper assay formation and data fidelity. The time-resolved fluorescence signals allow for the estimation of IgG secretion rates and affinity for RBD of the secreted IgG by using calibration curves generated with a monoclonal anti-RBD IgG with known affinity ( $K_D$ ) encapsulated at various concentrations (Supplemental Figure 1B). The resulting anti-Hu-1 RBD reference curve, generated using 7 different anti-RBD IgG mAbs of various affinities (29), allows for measurements with certainty over 2 logs of affinities, i.e.,  $2 \times 10^{-10} \leq K_D \leq 5 \times 10^{-8}$  M (Figure 1D). Therefore herein, IgG interacting with RBD at a calculated  $K_D$  below  $5 \times 10^{-8}$  M is considered binding, i.e., anti-RBD IgG antibodies, and the cell secreting such IgGs is termed RBD-specific IgG-SCs.

Selected individuals were part of 2 longitudinal cohorts: a first cohort of recovered COVID-19 patients (4 severe [S-CoV] and 14 mild [M-CoV]), which is part of the MEMO-COV-2 cohort (7) followed for 1 year after initial infection prior to vaccination; and a second cohort of 11 COVID-19-naïve healthcare workers, with no clinical history of COVID-19 and no serological evidence of previous SARS-CoV-2 infection (verified by the absence of anti-SARS-CoV-2 nucleocapsid antibodies), vaccinated as part of the French vaccination program. All individuals received the BNT162b2 vaccine and were sampled for circulating IgG-SC analyses after prime and/or boost (17). At the time of this clinical study, COVID-19-naïve individuals could receive a primary vaccination and a booster vaccination, whereas COVID-19-recovered individuals were considered already primed by the infection, and therefore were given only 1 vaccine dose. As an example, blood was obtained from 1 COVID-19-naïve donor (donor Na-5; 33 y/o, male) who was sampled 6 days after booster vaccination, from 1 mild COVID-19-recovered patient (patient M-CoV39; 34 y/o, male) and 1 severe COVID-19-recovered patient (patient S-CoV16; 61 y/o, male) who were sampled 7 days after vaccination (Figure 1E), with detectable Hu-1 RBD-specific IgG-SCs for all 3 individuals. These cells displayed a large range of secretion rates of IgG (~15–300 molecules per second [IgG/s]), with median values of approximately 30, 60, and 60 IgG/s in these 3 individuals, respectively.

*Anti-Hu-1 RBD IgG-SC populations following vaccination in naïve or COVID-19-recovered individuals.* Our 2 cohorts included a total of 29 individuals, with a median age of 47 years (ranging from 27 to 65 years). Clinical characteristics are presented in Supplemental Table 1 and anti-Hu-1 RBD titers in Supplemental Figure 2, A and B. To investigate the affinity and secretion rate of anti-RBD IgG-SCs, fresh blood samples were acquired in duplicate and analyzed on the same day, enabling the analysis of 10,000–20,000 single cells in total for each sample. We found that the frequency of IgG-SCs was from 0.01% to 2.5% of the mononuclear cell pool in the blood across all time points in the cohort. RBD-specific IgG-SCs could be identified in all samples, with high reproducibility in total and RBD-specific IgG-SC detection per replicate (exemplified in Supplemental Figure 2C). The 2 COVID-19-naïve sampled before vaccination exhibited rare but detectable low-affinity ( $50 \text{ nM} \leq K_D \leq 10 \text{ nM}$ , median of 34 nM) anti-RBD IgG-producing IgG-SCs (Figure 2A), even if their serum anti-RBD IgG titers were negative (Supplemental Figure 2A). IgG-SCs represented approximately 1% of total PBMCs, with approximately 6% RBD-binding among total IgG-SCs in both naïve individuals. We also identified rare low-affinity anti-RBD ASCs in frozen prepandemic PBMC samples of 3 blood bank donors (Supplemental Figure 2D), suggesting that seasonal Betacoronavirus led to the generation of these cross-reactive low-affinity IgG-SCs to SARS-CoV-2 Hu-1 RBD. The 2 COVID-19-recovered individuals sampled before vaccination also exhibited only low-affinity (median of 47 nM) anti-RBD IgG-producing IgG-SCs, with IgG-SCs representing approximately 1% of total PBMCs and with 2% RBD-binding among total IgG-SCs (Figure 2A). Based on these data, we conclude that previous COVID-19

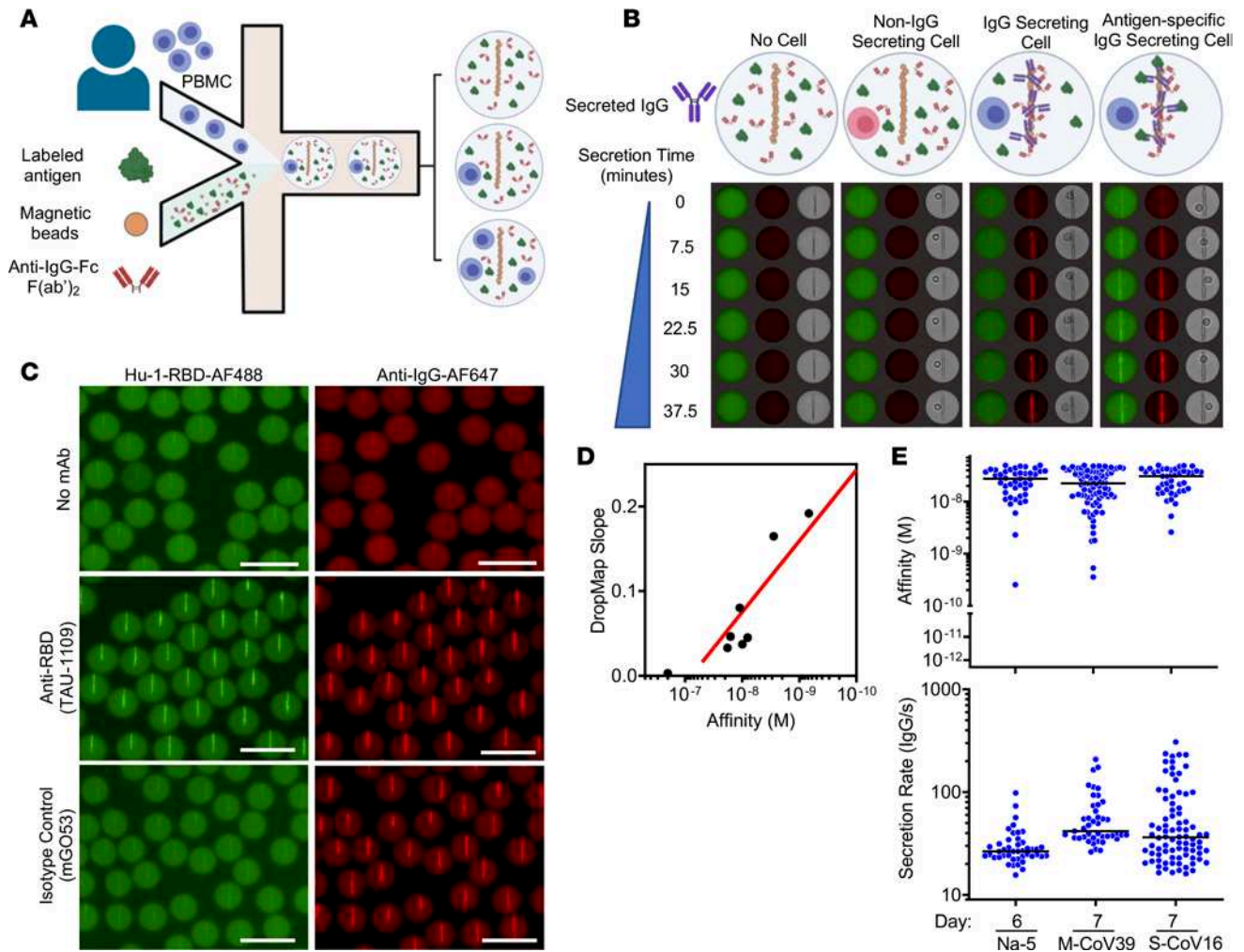


**Figure 1. DropMap technique for the detection of anti-Hu-1 IgG-secreting cells.** (A) Schematic showing the inputs and outputs of microfluidic encapsulation. PBMCs (top) are flowed in parallel with bioassay components (RBD–Alexa Fluor 488, magnetic beads coated with anti- $\kappa$  light chain nanobody (VHH), and anti-IgG F(ab)<sub>2</sub>–Alexa Fluor 647) on the droplet nozzle. Oil flow closes the collected aqueous phases (cell component and bioassay component) into a water-in-oil droplet. The column of droplets depicts the potential outcomes of cell encapsulation. (B) Schematic showing the composition of the DropMap assay and potential changes to the assay as it progresses. In the absence of a cell (outer left) or with a non-IgG-SC (inner left), there is no change in RBD (green) or anti-IgG F(ab)<sub>2</sub> (red) fluorescence distributions over time. An IgG-SC (inner right) in the droplet causes anti-IgG F(ab)<sub>2</sub> (red) fluorescence to relocate to the beadline over time. An RBD-specific IgG-SC (outer right) causes both RBD (green) and anti-IgG F(ab)<sub>2</sub> (red) fluorescence to relocate to the beadline. (C) Example of droplets containing no mAb (top), 5 nM TAU-1109 anti-RBD mAb (center), or 5 nM isotype control IgG (clone mG053, bottom), showing fluorescence relocation of Hu-1 RBD–Alexa Fluor 488 (green, left) and anti-IgG F(ab)<sub>2</sub>–Alexa Fluor 647 (red, right). Scale bars: 50  $\mu$ m. (D) Hu-1 RBD affinity reference curve calibrated with anti-RBD mAbs with known  $K_D$  and DropMap slope determined from methods exemplified in (Supplemental Figure 1B). Each dot represents the values for 1 mAb or isotype control. (E) Representative examples of anti-RBD antibody affinity (top) and IgG secretion (bottom) by circulating, single IgG-SCs ( $n = 171$ ) from indicated individuals; each dot represents 1 IgG-SC; black bars indicate median values.

infection does not result in high-affinity IgG-SCs circulating in the blood after 6 months, and rather leaves no detectable RBD-specific IgG-SC signature that can be distinguished from previously uninfected individuals.

BNT162b2 vaccination induced an increase in anti-RBD IgG titers (Supplemental Figure 2, A and B) and in IgG-SC numbers in COVID-19-naïve individuals readily detectable 3–4 weeks after the first dose, representing on average 24% of all IgG-SCs, with low ( $50 \text{ nM} \leq K_D \leq 10 \text{ nM}$ ), medium ( $10 \text{ nM} < K_D \leq 1 \text{ nM}$ ), and high-affinity ( $K_D < 1 \text{ nM}$ ) anti-RBD IgG-SCs (pooled data in Figure 2A; for individual data refer to Supplemental Figures 3 and 4). Rare IgG-SCs displayed very high estimated affinity ( $K_D$  below  $10^{-10} \text{ M}$ ) that were mathematically extrapolated from values outside the boundaries of the reference curve presented in Figure 1D, and led to a median affinity of 18 nM for anti-RBD IgG-SCs in that group. One to 2 weeks after receiving the second dose (booster, performed 27–29 days after the first dose), COVID-19-naïve individuals had anti-RBD IgG-SCs (24% among total IgG-SCs) that displayed a similar range of affinities compared to 3–4 weeks after the first dose, but with a predominance of low-affinity IgG-SCs, leading to a

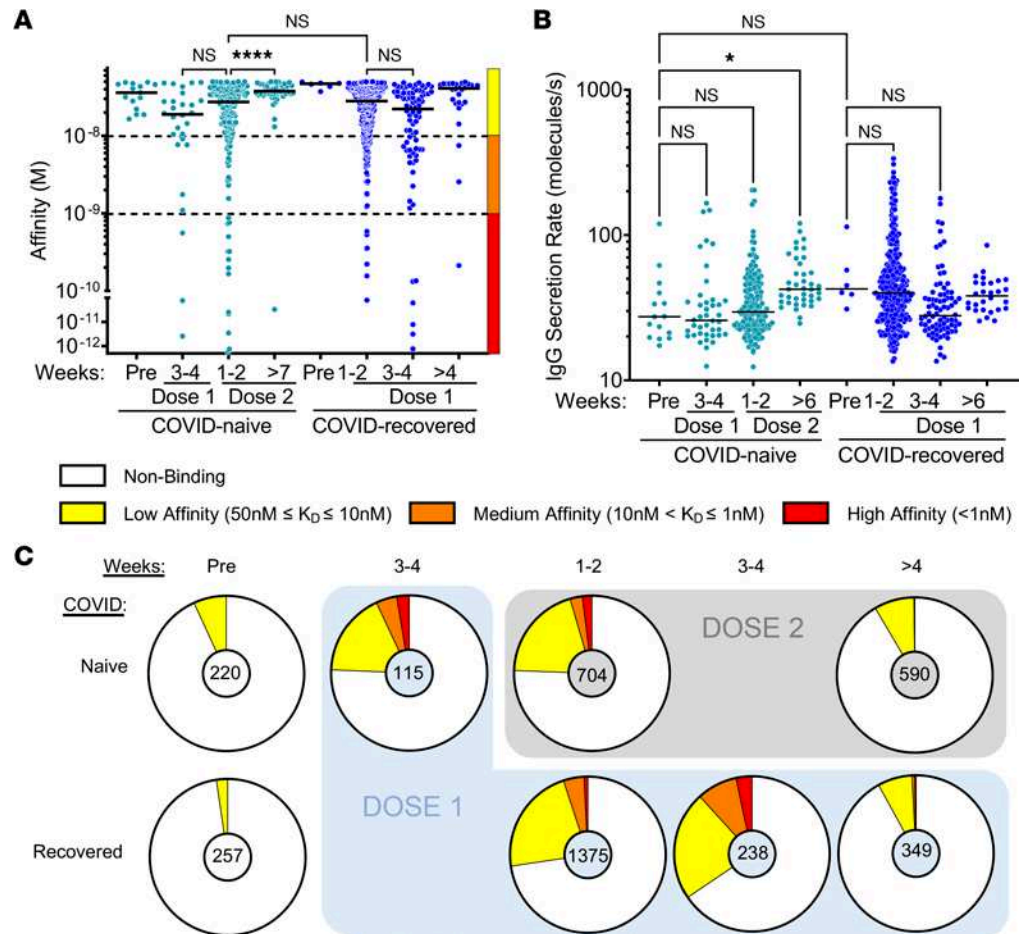


**Figure 2. Anti-Hu-1 RBD IgG-SC responses following vaccination.** (A and B) (A) Affinities for SARS-CoV-2 Hu-1 RBD and (B) secretion rates of a single IgG-SC ( $n = 762$ ) from pooled vaccinee data, with naive and recovered individuals shown in light blue and dark blue, respectively. Each dot represents a value from a single cell. Medians are shown. NS, nonsignificant. \* $P < 0.05$ ; \*\*\*\* $P < 0.0001$  using Kruskal-Wallis test with Dunn's test for multiple comparisons. Affinities are grouped as low (yellow), medium (orange), and high (red) affinity, shown by the bar on the right and separated by the dotted lines. (C) Frequencies of RBD-specific IgG-SCs classified into low (yellow), medium (orange), high affinity (red), or no detectable binding (white), among total IgG-SCs (total numbers indicated in center).

median affinity of 28 nM (Figure 2A). Overall, more than 7 weeks after the second dose (53–71 days), anti-RBD IgG-SCs (~10% among IgG-SCs) were mainly low-affinity IgG-SCs, leading to a median affinity of 38 nM. This median affinity was comparable to nonvaccinated COVID-19-naïve individuals, showing that RBD-specific ASCs generated after the boost rapidly disappeared from the circulation.

In the group of COVID-19-recovered individuals, BNT162b2 vaccination induced a large increase in anti-RBD IgG-SC numbers also within 1–2 weeks after the first vaccine dose, representing on average 27% of all IgG-SCs, with a large predominance of low-affinity over medium-affinity anti-RBD IgG-SCs, and only rare high-affinity anti-RBD IgG-SCs, resulting in a median affinity of 28 nM. No significant difference could be observed between vaccinated mild- and severe-COVID-19-recovered patients (Supplemental Figure 5A). Three to 4 weeks after the first dose, the distribution of affinities did not change significantly, with a median affinity of 22 nM (Figure 2A), and maintenance of a high proportion (34%) of anti-RBD IgG-SCs among IgG-SCs. More than 4 weeks after the first dose (31–63 days), low-affinity IgG-SCs represented almost all anti-RBD IgG-SCs (~10% among IgG-SCs) with rare exceptions, leading to a median affinity of 35 nM, which was similar to prevaccination values of these COVID-19-recovered individuals.

As exemplified in Figure 1E, in parallel with measuring affinity of the secreted IgG for SARS-CoV-2 RBD, DropMap allows measurement of the secretion rate of IgG within each droplet. Circulating anti-RBD IgG-SCs from all individuals in this cohort displayed a wide range of IgG secretion (12–320 IgG/s), with a global median value of approximately 36 IgG/s (Figure 2B). A significant

increase (1.5-fold) in IgG secretion rate was detected more than 6 weeks after the second dose in COVID-19-naïve individuals compared with prevaccination. Noticeably, this increase reached the levels found in COVID-19-recovered individuals (Figure 2B). No correlation was found, however, between affinity for RBD and IgG secretion rate using either the pooled data from all individuals or pooled data from subgroups of individuals (Supplemental Figure 5, B–K).

In terms of range of affinities and their distribution, the anti-RBD IgG-SC response appeared very similar between COVID-19-naïve and COVID-19-recovered within 1 to 2 weeks after receiving the second and the first vaccine dose, respectively, with both cohorts displaying similar proportions between low-, medium-, and high-affinity IgG-SCs. Both groups demonstrated over the following weeks a rapid disappearance of high- and medium-affinity IgG-SCs in circulation, while keeping a similar fraction of low-affinity RBD-specific IgG-SCs among circulating IgG-SCs (Figure 2C).

Thus, in both cohorts, the recall response mobilizing RBD-specific B cells generated a few weeks after mRNA vaccination in COVID-19-naïve or in COVID-19-recovered individuals (1 year after infection) elicits a burst of low-affinity anti-RBD IgG-SCs that rapidly wanes in the circulating blood.

*Anti-Omicron BA.1 RBD IgG-SC populations following vaccination in naïve or recovered individuals.* The Omicron BA.1 variant of SARS-CoV-2 appeared in France in early December, 2021, and we considered whether we could detect anti-BA.1 RBD cross-binding IgG-SCs in the samples collected before its emergence. Using fluorescently labeled BA.1 RBD, we generated a droplet bioassay (Figure 3A) and reference curve using BA.1 RBD cross-binding mAbs (Figure 3, B and C). Frozen samples of 1 vaccinated COVID-19-naïve individual (Na-15; 41 y/o female; 6 days after second dose), 1 vaccinated mild-COVID-19-recovered individual (M-CoV-45; 41 y/o female; 8 days after first dose), and 1 vaccinated severe-COVID-19-recovered (S-CoV16; 61 y/o male; 55 days after first dose) individual were assayed in duplicate and in parallel the same day for measurement of affinity of their IgG-SCs for Hu-1 and BA.1 RBD. The distribution and affinity ranges of anti-Hu-1 RBD IgG-SCs in these thawed samples (Figure 3D) were similar to those detected in the fresh samples (panels Na-15, M-CoV-45, and S-CoV-16 in Supplemental Figures 3 and 4). Interestingly, anti-BA.1 RBD IgG-SCs could be detected in all 3 samples collected before the appearance of this SARS-CoV-2 variant, with 20%–50% fewer BA.1 RBD IgG-SCs compared with Hu-1 RBD IgG-SCs (Figure 3, D and E). Medium- and high-affinity anti-BA.1 RBD IgG-SCs were detected, with similar median affinities in each individual for BA.1 and Hu-1 RBD, and also between these 3 individuals. As in our analyses of anti-Hu-1 RBD IgG-SCs, low-affinity anti-BA.1 RBD IgG-SCs largely predominated in circulation over high-affinity IgG-SCs (Figure 3E). We conclude that approximately 50%–80% of the Hu-1 RBD IgG-SCs elicited by booster vaccination were cross-reactive with the Omicron BA.1 VOC.

## Discussion

This study demonstrates the power of the droplet-based microfluidic approach (DropMap) (22, 28) for the rapid follow-up of the human immune response to a pathogen, with results obtained within hours of sampling. Herein we provide a broad “affinity repertoire” characterization of circulating IgG-SCs over several time points following SARS-CoV-2 mRNA vaccination for the original Hu-1 SARS-CoV-2 RBD. It describes similar expansion and contraction of the circulating RBD-specific plasmablast pool following mRNA-based vaccination for prime/boosted COVID-19-naïve and boosted COVID-19-recovered individuals, reaching high proportions (up to a third) of the total circulating plasmablast pool, in agreement with flow cytometry analyses (9, 30, 31) and proportions of RBD-specific antibodies among circulating antibodies (15).

We make the unanticipated observation that the majority of RBD-specific IgG-SCs were of lower affinity both in COVID-19-naïve and -recovered individuals. The Ellebody lab also reported that a large majority of plasmablasts producing antibodies with lower affinities — median of 80 nM — were also found in individuals who had received 2 doses of the BNT162b2 vaccine 6 months earlier (20). Unexpectedly, we identified in the prevaccination samples of 2 COVID-19-naïve donors with no evidence of previous SARS-CoV-2 exposure, as well as in 3 prepandemic blood bank samples, rare IgG-SCs with low affinity for Hu-1 RBD. As Betacoronaviruses (OC43, HKU1) shared some, albeit limited, degree of homology with the Hu-1 RBD (32), this suggests, as previously described in the MBC compartment (7), a cross-reactivity against conserved epitopes. Alternatively, the detection of IgG-SCs with low affinity for Hu-1 RBD may also reflect intrinsic polyreactivity in the plasma cell compartment (33, 34).

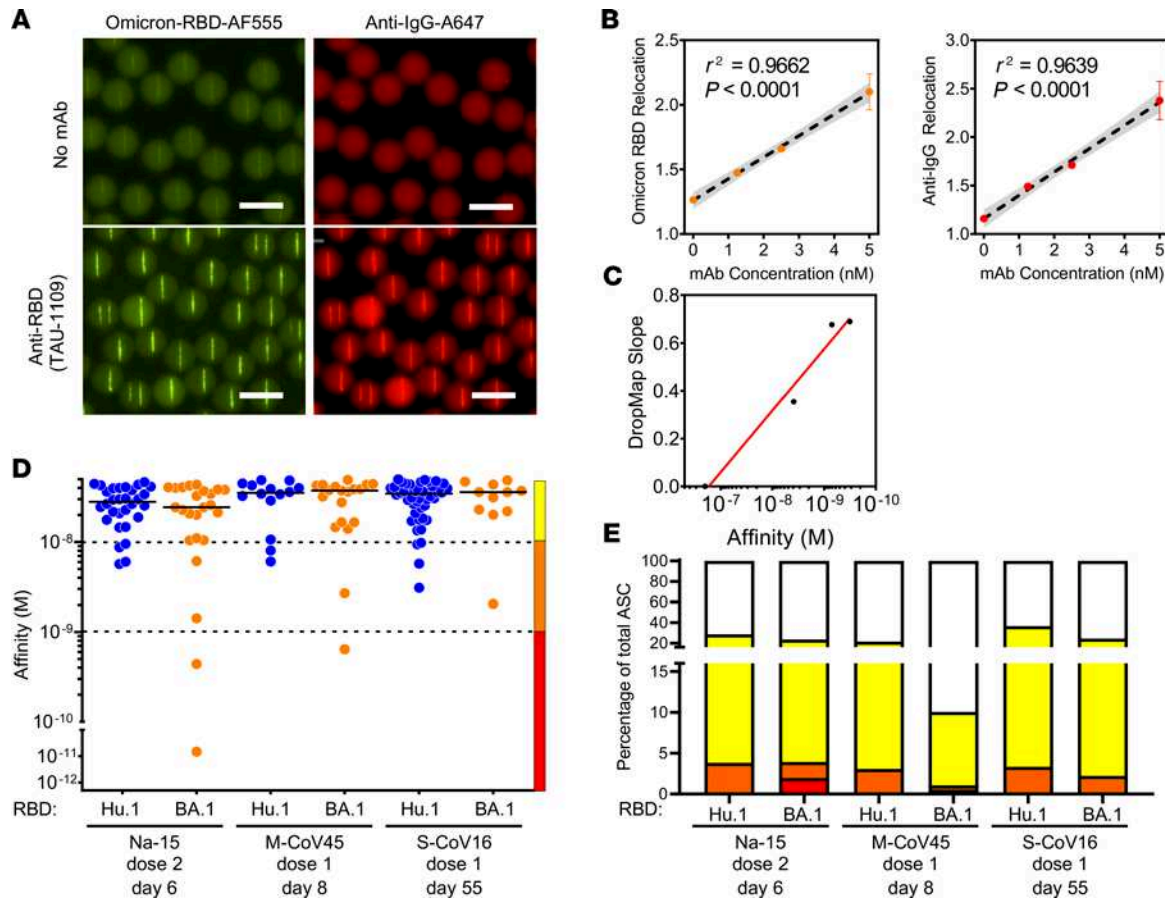


**Figure 3. DropMap for the detection of anti-BA.1 IgG-secreting cells.** (A) Example of droplets containing no mAb (top) or 5 nM TAU-1109 mAb (bottom), showing fluorescence relocation of Omicron BA.1 RBD–Alexa Fluor 555 (yellow, left) and anti-IgG F(ab)<sub>2</sub>–Alexa Fluor 647 (red, right). Scale bars: 50  $\mu$ m. (B) In-droplet mAb (TAU-1109) measurement of fluorescence relocation at 0, 1.25, 2.5, and 5 nM in droplet concentration performed in triplicate. Each dot represents the mean of a triplicate measure. Linear regression is represented, with 95% confidence intervals in gray,  $n = 3$ . (C) Omicron affinity reference curve calibrated with anti-RBD mAbs with known  $K_D$  for BA.1 RBD and DropMap slope determined from method exemplified in B. (D) Affinities for SARS-CoV-2 RBD of a single IgG-SC ( $n = 181$ ) from naive and recovered individuals using either Hu-1 (blue) or BA.1 (orange) RBD. Each dot represents a value from a single cell. Medians are shown. (E) Frequencies of Hu-1-specific (top) or BA.1-specific (bottom) IgG-SCs classified into low (yellow), medium (orange), high affinity (red), or no detectable binding (white), among total IgG-SCs, with total numbers indicated in center.

In vaccinated COVID-19-naïve individuals, the predominance of lower-affinity RBD-specific clones in circulation strongly suggest that they derive from extrafollicular maturation of activated B cells into plasmablasts harboring few mutations in IgVH, as described in patients with severe SARS-CoV-2 infection (35). By contrast, MBCs drive a recall response after antigenic rechallenge by differentiating into new ASCs that display the diverse array of high-affinity antibodies contained in the MBC repertoire, making the dominance of low-affinity clones quite unexpected. We have previously reported that some RBD-specific ASCs from COVID-19-recovered patients expressed enough B cell receptor (BCR) on the surface to be sorted 7 days after the boost (7). These clones displayed highly mutated V<sub>H</sub> sequences corresponding to the recruitment of MBCs. The results obtained using DropMap suggest that while these high-affinity clones are mobilized, other clones with low affinity were also engaged in the response. Indeed, minor fractions of high-affinity ( $K_D < 1$  nM) anti-RBD IgG-SCs in both COVID-19-naïve and -recovered individuals were detected with affinities reaching picomolar values.

The regular and frequent emergence of SARS-CoV-2 variants with mutations in the ACE2 RBD has complicated monitoring of the vaccination response against COVID-19. In this context, here we provide the first reported affinities to our knowledge of IgG-SCs against the Omicron BA.1 variant RBD. The median affinities between Hu-1 and BA.1 RBD-specific IgG-SCs were similar for the 3 samples we analyzed, but with a consistently lower frequency of BA.1-specific compared with Hu-1-specific IgG-SCs. These findings are largely consistent with existing analyses of the MBC compartment (16, 18, 19) and from neutralizing plasma titers (10). Numerous studies have found the prevalence of Hu-1 RBD-specific MBCs among the total MBC population to range between 0.01% and 10% (4, 5, 16, 29, 36–38), markedly lower than the

prevalence of Hu-1 RBD-specific IgG-SCs among the total IgG-SC population (9, 31). Our results thus further support the notion that the reduced neutralization capacity of vaccinee plasma toward BA.1 SARS-CoV-2 is largely due to a drop in the number of antibodies recognizing the BA.1 RBD, as opposed to a global shift in affinity, within the context of RBD-specific clones.

The DropMap technique also allows for precise quantification of single-cell antibody secretion. The amount of Ig secreted by single IgG-SCs remains poorly characterized, with most studies assessing only global Ig concentrations or titers. Previous attempts to quantify IgG secretion by human IgG-SCs were performed only on in vitro-derived B cells and have reported a broad range of estimated secretion rates, including approximately 450,000 IgG/s (~1 ng/cell/day) (39) down to approximately 10 IgG/s (~20 fg/cell/day) (40). We have recently reported that ex vivo IgG-SCs from healthy individuals had IgG secretion rates between approximately 5 and 500 IgG/s in the blood, bone marrow, and spleen (28), which are consistent with the secretion rates we describe here for vaccine-induced IgG-SCs. Our data show that COVID-19-recovered individuals display a higher basal IgG secretion level in anti-Hu-1 RBD IgG-SCs compared with COVID-19-naïve individuals. This heightened level of secretion was reached in COVID-19-naïve individuals several weeks after the second dose of BNT162b2. More investigation would be valuable to further establish physiological secretion rates of IgG-SCs and what conditions either attenuate or potentiate Ig secretion over time, and to guide alternative vaccine design.

This study is the second application of DropMap to monitor human IgG-SCs, with several consistent findings regarding IgG-SC physiology between 2 different antigens (a human glycoprotein [28] versus a viral surface protein) and models driving IgG-SC generation (autoimmunity versus immunization). DropMap has also been used in other aspects of immune monitoring, including cytokine secretion by T cells from healthy or sepsis patients (26) and cytokine secretion and cytotoxicity from single human NK cells (27, 41). Despite the advantages afforded by droplet microfluidic techniques, it should be noted that such analyses require precise fabrication of imaging apparatuses and microfluidics consumables, which are currently not commercially available. Nonetheless, the affinity repertoire is a valuable component of the B cell responses to evaluate. Combining DropMap with other single-cell technologies, such as BCR sequencing and single-cell transcriptomics to correlate phenotype with genotype, and liquid chromatography–tandem mass spectrometry proteomics will ultimately allow for a more complete understanding of the key aspects in antibody-mediated immunity (reviewed in ref. 21).

This study provides direct ex vivo, sorting-free analyses to assess the prevalence and quality of antigen-specific cells among circulating IgG-SCs following human vaccination. Application of similar DropMap screenings following vaccination could be valuable to determine whether the proportions of specific IgG-SCs we observed is consistent between vaccine designs (adenovirus-, protein-, or mRNA-based), different types of pathogens (bacteria vs. viruses), and different antigens and doses. Together, these endeavors highlight the functional diversity of antibodies generated following immunization and offer demonstration of efficient, high-throughput methods for characterizing B cell responses.

## Methods

### Cloning, expression, and purification of SARS-CoV-2 RBD

The codon-optimized sequence encoding the SARS-CoV-2 RBD was downloaded from the NCBI database, synthesized by Syntezza, and cloned into the pcDNA3.1 mammalian expression vector. The construct contained an N-terminal signal peptide (MKAPAVLAPGILVLLFTLVQRSNG) and 2 C-terminal tags: a hexahistidine tag (His-tag) for downstream protein purification and a site-specific biotinylation tag (GLNDIFEAQKIEWHE, AviTag). The RBD-containing vector was used to transiently transfect Expi293F cells (Thermo Fisher Scientific) using the ExpiFectamine 293 Transfection Kit (Thermo Fisher Scientific) or FectoPRO (Polyplus). Seven days after transfection, the cell supernatant was collected, filtered (0.22  $\mu$ m), and incubated with Ni<sup>2+</sup>-NTA agarose beads (Cytiva Life Sciences) for 2 hours at room temperature. The protein was eluted with 200 mM imidazole, buffer-exchanged to PBS, and aliquoted and stored at –80°C.

### Antibody expression and purification

The human mAbs used in this study (TAU-1109, TAU-2220, TAU-1115, TAU-2230, TAU-1145, TAU-2303, TAU-2189, TAU-2310, and mGO53) were isolated, cloned, and expressed as previously described (29, 42). Briefly, cloned antibody vectors for IgG1 heavy chain (H) and  $\kappa$  or  $\lambda$  light chains were

cotransfected at a ratio of 1:3 (H/ $\kappa$  or H/ $\lambda$ ) into Expi293F cells using the ExpiFectamine 293 Transfection Kit. Seven days after transfection, the cell supernatant was collected, filtered (0.22  $\mu\text{m}$ ), and incubated with protein A-coated agarose beads (GE Life Sciences) for 2 hours at room temperature. The antibodies were eluted using 50 mM sodium phosphate (pH 3.0) and the pH was immediately adjusted using 1 M Tris-HCl (pH 8.0). Following buffer exchange to PBS, the reactivity of each mAb was confirmed by ELISA before it was aliquoted and stored at  $-80^{\circ}\text{C}$ .

### Protein labeling

NHS-ester dyes used included AF488 (FP-M17231, FluoProbes) and AF555 (FP-U90663, FluoProbes). The Hu-1 RBD was conjugated with AF488 and the BA.1 RBD with AF555 according to the manufacturer's recommendations.

### Sample preparation

PBMCs were isolated from venous blood samples via standard density gradient centrifugation (Ficoll) and used fresh or after cryopreservation at  $-150^{\circ}\text{C}$  in fetal bovine serum with 20% DMSO. PBMCs were enriched in ASCs by negative selection using anti-CD3 microbeads (Miltenyi Biotec) following the manufacturer's protocol.

### Aqueous phase I: preparation of cells for droplet compartmentalization

Cell suspensions were centrifuged (300g, 5 minutes) and resuspended twice using MACS buffer (PBS pH 7.2, 0.2% bovine serum albumin, and 2 mM EDTA). After each resuspension, cells were filtered through a 40- $\mu\text{m}$  cell strainer to eliminate aggregates. Cells were then spun (300g, 5 minutes) and resuspended in DropMap buffer (RPMI without phenol red supplemented with 0.1% Pluronic F68, 25 mM HEPES pH 7.4, 5% KnockOut serum replacement [Thermo Fisher Scientific], and 0.5% human serum albumin [Sigma-Aldrich]). Cell density was adjusted to achieve a mean number of cells per droplet of approximately 0.3. For calibration curves, monoclonal IgG antibodies were diluted in DropMap buffer.

### Aqueous phase II: preparation of beads and bioassay reagents

Paramagnetic nanoparticles (Strep Plus 300 nm, Ademtech) were washed with Dulbecco's PBS with calcium and magnesium (DPBS $^{++}$ , Thermo Fisher Scientific). Nanoparticles were resuspended in DPBS $^{++}$  containing 1  $\mu\text{M}$  CaptureSelect biotin-labeled anti-human  $\kappa$  light chain (Ig $\kappa$ ; 7103272100, Thermo Fisher Scientific) for Hu-1 RBD assays or CaptureSelect anti-human constant heavy chain 1 (IgG-CH1; 7103202100, Thermo Fisher Scientific) for assays shown in Figure 3, and incubated 20 minutes at room temperature. After another wash with DPBS $^{++}$ , nanoparticles were resuspended in 5% pluronic F127 solution (Thermo Fisher Scientific) and incubated 20 minutes at room temperature. The nanoparticles were washed again and resuspended in DropMap buffer containing fluorescent reporter proteins for a final concentration of 1.25 mg/mL beads. Reporter proteins included Alexa Fluor 647-labeled F(ab') $_2$  fragment of a rabbit anti-human IgG Fc-specific antibody (309-606-008, Jackson ImmunoResearch) used at 75 nM final in-droplet concentration; fluorophore-conjugated RBD(s) were used at 30 nM final in-droplet concentration.

### Droplet production and collection

Droplets were generated using hydrodynamic flow focusing on a microfluidic chip, as described previously (22). The wafer master of the SU-8 photoresist layer (MicroChem) approximately 40  $\mu\text{m}$  in thickness was manufactured using soft lithography (43) and microfluidic chips were fabricated using soft lithography in polydimethylsiloxane (PDMS; Sylgard) (22). The continuous phase comprised 2% (wt/wt) 008 Fluorosurfactant (RAN Biotechnologies) in Novec HFE7500 fluorinated oil (3M). Aqueous phases I and II were co-flowed and partitioned into droplets. The flow rate of aqueous phases I and II was 70  $\mu\text{L}/\text{h}$ , with an oil flow rate of 600  $\mu\text{L}/\text{h}$  to achieve monodispersed droplets of approximately 40 pL volume. Newly generated droplets were directly injected into the DropMap 2D chamber system (22) and mounted on a widefield fluorescence microscope (Ti2-Eclipse, Nikon). The emulsion was exposed to a magnetic field, forcing the nanoparticles inside each droplet to form an elongated aggregate termed the "headline."

### Data acquisition

Images were acquired using a Nikon inverted microscope with a motorized stage (Ti2-Eclipse). Excitation light was provided by a light-emitting diode (LED) source (AURA III light source, Lumencor Inc.). Fluorescence for the specific channels was recorded using appropriate band-pass filters and camera settings (Orca Flash 4.0, Hamamatsu) at room temperature and ambient oxygen concentration. Images were acquired using a 10× objective (NA 0.45). An array of 9 × 9 images was acquired for each replicate, every 7.5 minutes, in all channels over 37.5 min (6 measurements total). A 9 × 9 image array describes a matrix of 81 individual 10× objective image acquisitions that are stitched together to form a single image with a height and width of 9 × (single image height/width). Each chamber (chip) contains droplets corresponding to a single sample, with the experiment repeated in duplicate. Duplicates were systematically acquired for every sample, with each replicate being the filling of the DropMap 2D chamber with a novel droplet population acquired over time on a 9 × 9 image array.

### Image analysis and calculations

Images were analyzed using a custom-made MATLAB script (MathWorks) to identify each droplet and its beadline. In each fluorescence channel and for each droplet, the pixel intensities of the beadline and the mean pixel intensities except the beadline (background fluorescence) were extracted. Droplet fluorescence relocation at each time point was calculated by dividing the intensity of the beadline by that of the background. Data were exported to Excel (Microsoft) and sorted for droplets showing an increase in relocation of the anti-IgG reporter fluorescence (Alexa Fluor 647) over time and above a threshold of Alexa Fluor 647 relocation greater than 1.3. Sorted droplets were visually assessed for the presence of a single cell within the droplet, no droplet movement between image acquisitions, the absence of fluorescent particles other than the beadline (e.g., fluorescent protein aggregates, cell debris), and undesired aggregation of fluorescent reporters on the cell surface inside the droplet. IgG secretion rate and dissociation constant ( $K_D$ ) were estimated as described previously (22).

*Estimation of  $K_D$  for RBD within each droplet.* A reference curve was obtained by defining relocation values for anti-IgG (Alexa Fluor 647) and RBD with a panel of 7 anti-RBD mAbs with a 1 log  $K_D$  range, determined using bio-layer interferometry (ForteBio). Droplet populations were generated with different concentrations of each mAb or buffer and the DropMap bioassay. A curve was defined by plotting the relocation from the anti-IgG (Alexa Fluor 647) against relocation of RBD, and the slope of the resulting line was calculated and termed “DropMap slope.” The reference curve was defined by the linear relationship between  $K_D$  for RBD as defined by bio-layer interferometry and the DropMap slope of each mAb.

### Affinity determination of mAbs

Bio-layer interferometry measurements were performed using anti-human IgG sensors in an OctetHTX system (ForteBio). Biosensors were equilibrated in assay buffer (PBS with 0.05% Tween 20 [Xantec, B PBST 10-500] diluted to 1× in sterile water + 0.1% BSA) for at least 10 minutes prior to measurement. Anti-RBD mAbs (10 µg/mL) diluted in assay buffer were immobilized on sensors (90 seconds), followed by a baseline in assay buffer (30 seconds), association with Hu-1 or Omicron BA.1 RBD in solution across 6 serial 2-fold dilutions (300 seconds), and dissociation (600 seconds) steps. Traces were preprocessed by reference sample subtraction, alignment to the baseline average, and Savitzky-Golay filtering.  $K_D$  was determined using a 1:1 binding model with global fitting in HT Analysis 11.1 software (ForteBio).

### Data availability

Assay microscopy images and droplet detections with beadline/droplet intensity measurements are available upon request.

### Statistics

GraphPad Prism version 9.4.1 was used for all analyses. Data were not normalized or normalized prior to being analyzed. All data points present single-cell values unless otherwise stated. Each sample (1 patient at a designated time point) was measured in 2 independent experiments and data points were pooled between duplicate experiments. Samples were not pooled unless explicitly stated. Affinity and secretion data were determined to be neither normally distributed nor log-normally distributed according to the D’Agostino and Pearson, Anderson-Darling, and Kolmogorov-Smirnov tests. The Kruskal-Wallis test was used for

comparing samples or groups of samples, with Dunn's multiple-comparison test for hypothesis testing. Statistical significance was set to a *P* value of 0.05 or less.

### Study approval

This study was conducted in compliance with the Declaration of Helsinki principles and was approved by the Agence de la Biomédecine and the Institutional Review Board Comité de Protection des Personnes (CPP) Ile-de-France VI (number 40-20 HPS).

All patients provided written informed consent before the collection of samples. In total, 34 COVID-19-recovered patients from the original MEMO-COV-2 cohort were followed up to 12 months after infection and/or vaccination. Among them, 17 patients had severe COVID-19 (patients requiring oxygen, S-CoV) and 17 had a mild COVID-19 disease (mainly healthcare workers, M-CoV). An additional cohort of 9 patients who experienced mild COVID-19 during the first wave and were vaccinated at least 6 months after the infection were recruited. SARS-CoV-2 infection was defined as confirmed reverse transcriptase polymerase chain reaction (RT-PCR) on nasal swab or clinical presentation associated with typical aspect on CT scan and/or serological evidence. Twenty-five healthcare workers who had no history of COVID-19 and negative IgG anti-nucleocapsid (and/or anti-spike) were enrolled in the naive group (IRB 2018-A01610-55).

All vaccinated participants received the BNT162b2 mRNA vaccine. COVID-19-recovered patients received only 1 dose, in line with French guidelines. The first injection was realized in a mean of 309 days ( $\pm 44.6$  days SD) after the infection. Naive patients received 2 doses at a mean of 27.7 days ( $\pm 1.8$  days SD).

Prior to vaccination, samples were collected from COVID-19-recovered patients 12 months after symptoms onset (mean  $\pm$  SD 329.1  $\pm$  15: 8.8 days after disease onset for S-CoV, and 342.0  $\pm$  8.6 days after disease onset for M-CoV). Samples at 12 months after disease onset were defined as "pre-boost." For patients not sampled before vaccination ( $n = 9/34$ ), the sample at 6 months was considered "pre-boost." For naive patients, the "prime" time point was defined as the sampling between the 2 doses and was drawn at a mean of 20.2  $\pm$  5.9 days after the first vaccine injection.

Samples were additionally collected shortly after the boost (mean  $\pm$  SD: 10  $\pm$  5.3 days for S-CoV, 23  $\pm$  6.1 days for M-CoV, and 9  $\pm$  4.0 days for naive), and 2 months after the boost (mean  $\pm$  SD: 64.7  $\pm$  15.3 days for S-CoV, 63.2  $\pm$  11.9 days for M-CoV, and 63.3  $\pm$  9.0 days for naive). Clinical and biological characteristics of these patients are summarized in Supplemental Table 1. Patients were recruited at the Henri Mondor University Hospital (AP-HP) between March and April 2021. The MEMO-COV-2 study (ClinicalTrials.gov NCT04402892) was approved by the ethical committee Ile-de-France VI (number 40-20 HPS), and was performed in accordance with French law. Written informed consent was obtained from all participants.

### Author contributions

M Broketa, NTF, M Mahévas, and PB conceptualized the study and developed the methodology. M Broketa and AS curated the data. M Broketa, NTF, M Mahévas, and PB formally analyzed and validated the data. M Broketa, AS, M Backovic, AM, IF, M Mor, PCH, AP, BI, and GC carried out the investigation. JB, NTF, M Mahévas, and PB acquired funding. AV, LL, M Michel, BG, SG, GM, and FAR provided resources. M Broketa, AP, GC, and JB contributed to code writing and software development. M Broketa generated the figures. FAR, JB, NTF, M Mahévas, and PB supervised the study. M Mahévas and PB provided project administration. M Broketa, NTF, M Mahévas, and PB wrote the original draft of the manuscript. All authors reviewed and edited the manuscript.

### Acknowledgments

We thank the physicians, Constance Guillaud, Raphael Lepeule, Frédéric Schlemmer, Elena Fois, Henri Guillet, Nicolas De Prost, and Pascal Lim (all Henri Mondor Hospital, Créteil, France), whose patients were included in this study. We thank A. Boucharlat and the Chemogenomic and Biological screening core facility headed by F. Agou for support during the course of this work. M Broketa is the recipient of a CIFRE PhD fellowship. PCH was supported by a fellowship from the French Fondation pour la Recherche Médicale (FRM). AS was supported by a Poste d'Accueil from INSERM, and IF by a fellowship from the French Agence Nationale de Recherches sur le Sida et les Hépatites Virales (ANRS). PB acknowledges funding from the Agence Nationale de la Recherche (ANR) (ANR-18-CE15-0001

project Autoimmuni-B and ANR-14-CE16-0011 project DROPmAbs), from the Institut Carnot Pasteur Microbes et Santé, from the CAPNET (Comité ad-hoc de pilotage national des essais thérapeutiques et autres recherches, French government) MEMO-VOC, from the Institut Pasteur and from the Institut National de la Santé et de la Recherche Médicale (INSERM). M Mahévas acknowledges funding from the ANR (MEMO-COV-2 -FRM). Assistance Publique – Hôpitaux de Paris (AP-HP, Département de la Recherche Clinique et du Développement) was the promotor and the sponsor of MEMO-COV-2. JB acknowledges funding from the French government through BPIFrance under the frame Programme d'Investissements d'Avenir (CELLIGO Project), the Institut Pierre-Gilles de Gennes through the laboratoire d'excellence, Investissements d'avenir programs ANR-10-IDEX-0001-02 PSL, ANR-10-EQPX-34 and ANR-10-LABX-3. NTF acknowledges funding from the Israeli Science Foundation grants 1422/18 and 3711/20 and Marguerite Stolz Research Fellowship. Work in the Unit of Structural Virology was funded by Institut Pasteur, Urgence COVID-19 Fundraising Campaign of Institut Pasteur.

Address correspondence to: Pierre Bruhns, Unit of Antibodies in Therapy and Pathology, Institut Pasteur, 75015 Paris, France. Phone: 33.145688629; Email: pierre.bruhns@pasteur.fr.

1. Yuan M, et al. Structural basis of a shared antibody response to SARS-CoV-2. *Science*. 2020;369(6507):1119–1123.
2. Cho A, et al. Anti-SARS-CoV-2 receptor-binding domain antibody evolution after mRNA vaccination. *Nature*. 2021;600(7889):517–522.
3. Gaebler C, et al. Evolution of antibody immunity to SARS-CoV-2. *Nature*. 2021;591(7851):639–644.
4. Goel RR, et al. Distinct antibody and memory B cell responses in SARS-CoV-2 naïve and recovered individuals following mRNA vaccination. *Sci Immunol*. 2021;6(58):eabi6950.
5. Wec AZ, et al. Broad neutralization of SARS-related viruses by human monoclonal antibodies. *Science*. 2020;369(6504):731–736.
6. Amanat F, et al. SARS-CoV-2 mRNA vaccination induces functionally diverse antibodies to NTD, RBD, and S2. *Cell*. 2021;184(15):3936–3948.
7. Sokal A, et al. Maturation and persistence of the anti-SARS-CoV-2 memory B cell response. *Cell*. 2021;184(5):1201–1213.
8. Levin EG, et al. Waning immune humoral response to BNT162b2 Covid-19 vaccine over 6 months. *N Engl J Med*. 2021;385(24):e84.
9. Turner JS, et al. SARS-CoV-2 mRNA vaccines induce persistent human germinal centre responses. *Nature*. 2021;596(7870):109–113.
10. Gupta SL, et al. Loss of Pfizer (BNT162b2) vaccine-induced antibody responses against the SARS-CoV-2 Omicron variant in adolescents and adults. *J Virol*. 2022;96(17):e0058222.
11. DeGrace MM, et al. Defining the risk of SARS-CoV-2 variants on immune protection. *Nature*. 2022;605(7911):640–652.
12. Laidlaw BJ, Ellebedy AH. The germinal centre B cell response to SARS-CoV-2. *Nat Rev Immunol*. 2022;22(1):7–18.
13. Tao K, et al. Susceptibility of SARS-CoV-2 Omicron variants to therapeutic monoclonal antibodies: systematic review and meta-analysis. *Microbiol Spectr*. 2022;10(4):e0092622.
14. Takashita E, et al. Efficacy of antibodies and antiviral drugs against Omicron BA.2.12.1, BA.4, and BA.5 subvariants. *N Engl J Med*. 2022;387(5):468–470.
15. Wang Z, et al. Naturally enhanced neutralizing breadth against SARS-CoV-2 one year after infection. *Nature*. 2021;595(7867):426–431.
16. Muecksch F, et al. Increased memory B cell potency and breadth after a SARS-CoV-2 mRNA boost. *Nature*. 2022;607(7917):128–134.
17. Sokal A, et al. mRNA vaccination of naïve and COVID-19-recovered individuals elicits potent memory B cells that recognize SARS-CoV-2 variants. *Immunity*. 2021;54(12):2893–2907.
18. Kotaki R, et al. SARS-CoV-2 Omicron-neutralizing memory B cells are elicited by two doses of BNT162b2 mRNA vaccine. *Sci Immunol*. 2022;7(70):eabn8590.
19. Sokal A, et al. Analysis of mRNA vaccination-elicited RBD-specific memory B cells reveals strong but incomplete immune escape of the SARS-CoV-2 Omicron variant. *Immunity*. 2022;55(6):1096–1104.
20. Kim W, et al. Germinal centre-driven maturation of B cell response to mRNA vaccination. *Nature*. 2022;604(7904):141–145.
21. Broketa M, Bruhns P. Single-cell technologies for the study of antibody-secreting cells. *Front Immunol*. 2021;12:821729.
22. Eyer K, et al. Single-cell deep phenotyping of IgG-secreting cells for high-resolution immune monitoring. *Nat Biotechnol*. 2017;35(10):977–982.
23. Heo M, et al. Deep phenotypic characterization of immunization-induced antibacterial IgG repertoires in mice using a single-antibody bioassay. *Commun Biol*. 2020;3(1):614.
24. Krautler NJ, et al. Quantitative and qualitative analysis of humoral immunity reveals continued and personalized evolution in chronic viral infection. *Cell Rep*. 2020;30(4):997–1012.
25. Bonaud A, et al. Sec22b is a critical and nonredundant regulator of plasma cell maintenance. *Proc Natl Acad Sci U S A*. 2023;120(2):e2213056120.
26. Bounab Y, et al. Dynamic single-cell phenotyping of immune cells using the microfluidic platform DropMap. *Nat Protoc*. 2020;15(9):2920–2955.
27. Subedi N, et al. An automated real-time microfluidic platform to probe single NK cell heterogeneity and cytotoxicity on-chip. *Sci Rep*. 2021;11(1):17084.

28. Canales-Herrerias P, et al. High-affinity autoreactive plasma cells disseminate through multiple organs in patients with immune thrombocytopenic purpura. *J Clin Invest.* 2022;132(12):e153580.
29. Mor M, et al. Multi-clonal SARS-CoV-2 neutralization by antibodies isolated from severe COVID-19 convalescent donors. *PLoS Pathog.* 2021;17(2):e1009165.
30. Amanat F, et al. The plasmablast response to SARS-CoV-2 mRNA vaccination is dominated by non-neutralizing antibodies that target both the NTD and the RBD [preprint]. <https://doi.org/10.1101/2021.03.07.21253098>. Posted on medRxiv March 9, 2021.
31. Pape KA, et al. High-affinity memory B cells induced by SARS-CoV-2 infection produce more plasmablasts and atypical memory B cells than those primed by mRNA vaccines. *Cell Rep.* 2021;37(2):109823.
32. Hicks J, et al. Serologic cross-reactivity of SARS-CoV-2 with endemic and seasonal Betacoronaviruses. *J Clin Immunol.* 2021;41(5):906–913.
33. Yurasov S, et al. Defective B cell tolerance checkpoints in systemic lupus erythematosus. *J Exp Med.* 2005;201(5):703–711.
34. Scheid JF, et al. Differential regulation of self-reactivity discriminates between IgG<sup>+</sup> human circulating memory B cells and bone marrow plasma cells. *Proc Natl Acad Sci U S A.* 2011;108(44):18044–18048.
35. Woodruff MC, et al. Extrafollicular B cell responses correlate with neutralizing antibodies and morbidity in COVID-19. *Nat Immunol.* 2020;21(12):1506–1516.
36. Robbiani DF, et al. Convergent antibody responses to SARS-CoV-2 in convalescent individuals. *Nature.* 2020;584(7821):437–442.
37. Rogers TF, et al. Isolation of potent SARS-CoV-2 neutralizing antibodies and protection from disease in a small animal model. *Science.* 2020;369(6506):956–963.
38. Dan JM, et al. Immunological memory to SARS-CoV-2 assessed for up to 8 months after infection. *Science.* 2021;371(6529):eabf4063.
39. Brinkmann V, Heusser CH. T cell-dependent differentiation of human B cells into IgM, IgG, IgA, or IgE plasma cells: high rate of antibody production by IgE plasma cells, but limited clonal expansion of IgE precursors. *Cell Immunol.* 1993;152(2):323–332.
40. Huggins J, et al. CpG DNA activation and plasma-cell differentiation of CD27<sup>-</sup> naive human B cells. *Blood.* 2007;109(4):1611–1619.
41. Subedi N, et al. Single-cell profiling reveals functional heterogeneity and serial killing in human peripheral and ex vivo-generated CD34<sup>+</sup> progenitor-derived natural killer cells. *Adv Biol (Weinh).* 2023;7(4):e2200207.
42. Wardemann H, et al. Predominant autoantibody production by early human B cell precursors. *Science.* 2003;301(5638):1374–1377.
43. Mazutis L, et al. Single-cell analysis and sorting using droplet-based microfluidics. *Nat Protoc.* 2013;8(5):870–891.

# **ARTICLE 2**

## ARTICLE 2

### High Throughput Affinity Mapping on Anti-RBD Antibodies

I collaborated in January 2021 with the group of Immune System Development at Institut Necker Enfants Malades (INEM) directed by Dr Matthieu Mahévas to characterize the B cell response to vaccination against SARS-COV2 with Pfizer/BioNTech COMIRNATY. In this section I have included the published manuscript (Sokal et al. 2021)<sup>129</sup> of this work, for which I am a co-first author.

An integral component of the immune response to immunization is the generation of memory B cells (Bmems), responsible for ensuring rapid, robust immune responses to later infection and surveilling tissues and the circulation for their targets. The affinity of antibodies expressed by Bmems is inextricably linked to their ability to bind to their target antigen and eventually respond to natural infection. My individual contribution to this manuscript was to characterize by biolayer interferometry (BLI - Octet HTX) the affinity of approximately 600 individual memory B cells cultured to differentiate into IgG-secreting cells against WT SPIKE-RBD and 5 additional variants. This required the adaptation of a high throughput screening method (Lad, L. et al.) published for hybridoma characterization to be suitable for human antibody characterization, using anti-RBD mAbs as internal controls before analyzing the soluble IgG from memory B cell cultures.

Article

# mRNA vaccination of naive and COVID-19-recovered individuals elicits potent memory B cells that recognize SARS-CoV-2 variants

Aurélien Sokal,<sup>1,2,15</sup> Giovanna Barba-Spaeth,<sup>3,15</sup> Ignacio Fernández,<sup>3,15</sup> Matteo Broketa,<sup>4,14,15</sup> Imane Azzaoui,<sup>2,5,16</sup> Andréa de La Selle,<sup>1,2,16</sup> Alexis Vandenberghe,<sup>2,5,16</sup> Slim Fourati,<sup>6,7,16</sup> Anais Roeser,<sup>1,2</sup> Annalisa Meola,<sup>3</sup> Magali Bouvier-Alias,<sup>6,7</sup> Etienne Crickx,<sup>1,2</sup> Laetitia Languille,<sup>2</sup> Marc Michel,<sup>2</sup> Bertrand Godeau,<sup>2</sup> Sébastien Gallien,<sup>8</sup> Giovanna Melica,<sup>8</sup> Yann Nguyen,<sup>9</sup> Virginie Zarrouk,<sup>9</sup> Florence Canoui-Poitrine,<sup>10</sup> France Pirenne,<sup>5,11</sup> Jérôme Mégret,<sup>12</sup> Jean-Michel Pawlotsky,<sup>6,7</sup> Simon Fillatreau,<sup>1</sup> Pierre Bruhns,<sup>4,17</sup> Felix A. Rey,<sup>3,17</sup> Jean-Claude Weill,<sup>1,17,\*</sup> Claude-Agnès Reynaud,<sup>1,17,\*</sup> Pascal Chappert,<sup>1,13,17,\*</sup> and Matthieu Mahévas<sup>1,2,5,17,18,\*</sup>

<sup>1</sup>Institut Necker Enfants Malades (INEM), INSERM U1151/CNRS UMS 8253, Université de Paris, Paris, France

<sup>2</sup>Service de Médecine Interne, Centre Hospitalier Universitaire Henri-Mondor, Assistance Publique-Hôpitaux de Paris (AP-HP), Université Paris-Est Créteil (UPEC), Créteil, France

<sup>3</sup>Institut Pasteur, Université de Paris, Unité de Virologie Structurale, CNRS UMR 3569, Paris 75015, France

<sup>4</sup>Institut Pasteur, Université de Paris, INSERM UMR 1222, Unit of Antibodies in Therapy and Pathology, Paris 75015, France

<sup>5</sup>INSERM U955, Équipe 2, Institut Mondor de Recherche Biomédicale (IMRB), Université Paris-Est Créteil (UPEC), Créteil, France

<sup>6</sup>Département de Virologie, Bactériologie, Hygiène et Mycologie-Parasitologie, Centre Hospitalier Universitaire Henri-Mondor, Assistance Publique-Hôpitaux de Paris (AP-HP), Créteil, France

<sup>7</sup>INSERM U955, Équipe 18, Institut Mondor de Recherche Biomédicale (IMRB), Université Paris-Est Créteil (UPEC), Créteil, France

<sup>8</sup>Service de Maladies Infectieuses, Centre Hospitalier Universitaire Henri-Mondor, Assistance Publique-Hôpitaux de Paris (AP-HP), Université Paris-Est Créteil (UPEC), Créteil, France

<sup>9</sup>Service de Médecine Interne, Hôpital Beaujon, Assistance Publique-Hôpitaux de Paris, Université de Paris, Clichy, France

<sup>10</sup>Département de Santé Publique, Unité de Recherche Clinique (URC), CEpiA (Clinical Epidemiology and Ageing), EA 7376, Institut Mondor de Recherche Biomédicale (IMRB), Centre Hospitalier Universitaire Henri-Mondor, Assistance Publique-Hôpitaux de Paris (AP-HP), Université Paris-Est Créteil (UPEC), Créteil, France

<sup>11</sup>Etablissement Français du Sang (EFS) Ile de France, Créteil, France

<sup>12</sup>Plateforme de Cytométrie en Flux, Structure Fédérative de Recherche Necker, INSERM US24-CNRS UMS3633, Paris, France

<sup>13</sup>Inovation, Paris, France

<sup>14</sup>Sorbonne Université, Collège doctoral, Paris 75005, France

<sup>15</sup>These authors contributed equally

<sup>16</sup>These authors contributed equally

<sup>17</sup>Senior author

<sup>18</sup>Lead contact

\*Correspondence: [jean-claude.weill@inserm.fr](mailto:jean-claude.weill@inserm.fr) (J.-C.W.), [claudes-agnes.reynaud@inserm.fr](mailto:claudes-agnes.reynaud@inserm.fr) (C.-A.R.), [pascal.chappert@inserm.fr](mailto:pascal.chappert@inserm.fr) (P.C.), [matthieu.mahevas@aphp.fr](mailto:matthieu.mahevas@aphp.fr) (M.M.)

<https://doi.org/10.1016/j.immuni.2021.09.011>

## SUMMARY

In addition to serum immunoglobulins, memory B cell (MBC) generation against severe acute respiratory syndrome coronavirus 2 (SARS-CoV-2) is another layer of immune protection, but the quality of MBC responses in naive and coronavirus disease 2019 (COVID-19)-recovered individuals after vaccination remains ill defined. We studied longitudinal cohorts of naive and disease-recovered individuals for up to 2 months after SARS-CoV-2 mRNA vaccination. We assessed the quality of the memory response by analysis of antibody repertoires, affinity, and neutralization against variants of concern (VOCs) using unbiased cultures of 2,452 MBCs. Upon boosting, the MBC pool of recovered individuals expanded selectively, matured further, and harbored potent neutralizers against VOCs. Although naive individuals had weaker neutralizing serum responses, half of their RBD-specific MBCs displayed high affinity toward multiple VOCs, including delta (B.1.617.2), and one-third retained neutralizing potency against beta (B.1.351). Our data suggest that an additional challenge in naive vaccinees could recall such affinity-matured MBCs and allow them to respond efficiently to VOCs.

## INTRODUCTION

The coronavirus disease 2019 (COVID-19) pandemic, caused by severe acute respiratory syndrome coronavirus 2 (SARS-CoV-2), has resulted in more than 220 million infections and at least 4.5 million deaths as of September 6, 2021. Vaccination is the main hope to control the pandemic. COVID-19 vaccines containing nucleoside-modified mRNA encoding the original Wuhan-Hu-1 SARS-CoV-2 spike glycoprotein (S), developed by Pfizer/BioNTech (BNT162b2) and Moderna (mRNA-1273), are now being deployed worldwide. They have been shown to be safe and highly effective to prevent infection and control disease severity (Baden et al., 2021; Dagan et al., 2021; Polack et al., 2020).

The emergence of SARS-CoV-2 variants bearing mutations in key B cell epitopes, however, has raised concerns that virus evolution will erode natural immunity or the protection offered by vaccination. One early mutation in the S protein (D614G), which shifts the equilibrium between the open and closed protein conformation without modifying antibody neutralization, has become globally dominant (Plante et al., 2021; Weissman et al., 2021; Yurkovetskiy et al., 2020), and novel variants of concern (VOCs) or variants of interest (VOIs) have spread around the world, with additional combinations of mutations and deletions located mainly in the ACE-2 receptor-binding domain (RBD) and the N-terminal domain of the S protein. Mutations in the RBD are of particular importance because a large fraction of neutralizing antibodies elicited after infection and vaccination target this domain. The selective advantage provided by these mutations has resulted in their increasing prevalence: N501Y in the B.1.1.7 (alpha) variant; K417N, E484K, N501Y in the B.1.351 (beta) variant; K417T, E484K, N501Y in the P.1 (gamma) variant; and L452R, E484Q, or L452R, T478K in the B.1.617.1 (kappa) and B.1.617.2 (delta) variants, respectively (Cherian et al., 2021; Davies et al., 2021; Greaney et al., 2021a; Tegally et al., 2021).

The higher infectiousness of the B.1.1.7 variant does not impair the neutralizing antibody response (Davies et al., 2021; Garcia-Beltran et al., 2021; Planas et al., 2021a; Supasa et al., 2021). In contrast, the E484K and K417T/N mutations in the B.1.351 and P.1 strains markedly reduced the neutralization potency in COVID-19-recovered or naive vaccinated individuals (Cele et al., 2021; Edara et al., 2021; Greaney et al., 2021a; Hoffmann et al., 2021; Planas et al., 2021a; Wang et al., 2021a; Xie et al., 2021). Even though infection with VOCs or VOIs remains possible after successful vaccination (Hacisuleyman et al., 2021), the effectiveness of the BNT162b2 vaccine against B.1.351 in preventing severe disease has been demonstrated recently during a vaccination campaign in Qatar (Abu-Raddad et al., 2021).

In parallel to the rapid antibody-secreting cell (ASC) and serum immunoglobulin G (IgG) response, progressive generation of memory B cells (MBCs) against the SARS-CoV-2 virus is another layer of immune protection (Dugan et al., 2021; Gaebler et al., 2021; Rodda et al., 2021; Sakharkar et al., 2021; Sokal et al., 2021). MBCs not only persist after infection but evolve continuously and mature by progressive acquisition of somatic mutations in their variable-region genes to improve affinity through an ongoing germinal center response, potentially driven by anti-

genic persistence (Gaebler et al., 2021; Rodda et al., 2021; Sokal et al., 2021). MBCs further drive the recall response after antigenic rechallenge by differentiating into new ASCs displaying the diverse array of high-affinity antibodies contained in the MBC repertoire. However, a strong convergence of the anti-RBD response across COVID-19-recovered and naive vaccinated individuals shaped by recurrent germline gene families has been described. This could favor viral mutational escape because one single mutation in the RBD can confer a selective advantage by reducing the binding and neutralizing activity of antibodies (Garcia-Beltran et al., 2021; Greaney et al., 2021a).

Upon vaccination, COVID-19-recovered individuals showed a striking expansion of RBD-specific MBCs (Goel et al., 2021a; Wang et al., 2021b) and elicited a strong serum antibody response, including cross-neutralizing antibodies against VOCs (Ebinger et al., 2021; Konstantinidis et al., 2021; Krammer et al., 2021; Manisty et al., 2021; Saadat et al., 2021; Samanovic et al., 2021; Stamatatos et al., 2021; Wang et al., 2021b). Much less is known about the long-term stability, dynamics, and functionality of the MBC repertoire after repeated antigenic stimulation. How the MBC pool will contract or expand its diversity after a new challenge is of major importance in the context of vaccination schemes with repeated homologous or heterologous booster doses and coexistence of multiple VOCs.

Here we longitudinally characterized the dynamics, clonal evolution, affinity, and neutralization capacity of anti-SARS-CoV-2 MBCs after mRNA vaccination in naive and SARS-CoV-2-recovered individuals from an analysis of over 2,000 naturally expressed antibodies from single-cell cultured, RBD-specific MBCs. We demonstrate that mRNA vaccination selects high-affinity neutralizing clones without compromising the overall MBC pool.

## RESULTS

### mRNA vaccination boosts serum IgG levels in SARS-CoV-2-recovered and naive individuals

The B cell immune response elicited by vaccination was analyzed in two cohorts, one of individuals infected previously with SARS-CoV-2 (SARS-CoV-2 recovered) and one of virus-naive individuals (SARS-CoV-2 naive). We previously characterized the longitudinal evolution and maturation, up to 6 months after infection, of SARS-CoV-2-responding B cells in a cohort of mild ambulatory (M-CoV) and severe forms of COVID-19 requiring oxygen (S-CoV) (Sokal et al., 2021). Thirty-four individuals from this original cohort were included in this study, along with 9 additional individuals with COVID-19, for a total of 17 S-CoV and 26 M-CoV individuals (Figure 1A; Table S1). All individuals in this first cohort received one dose of the Pfizer-BioNTech mRNA (BNT162b2) vaccine between 6 and 12 months after infection (median, 309 days after COVID-19 symptom onset; range, 183–362 days; Table S1C). This unique vaccine dose for SARS-CoV-2-recovered individuals is referred to as “boost.” As a parallel cohort, we recruited 25 healthcare workers with no clinical history of COVID-19 and no serological evidence of previous SARS-CoV-2 infection. SARS-CoV-2-naive individuals in this second cohort received 2 doses of the BNT162b2 vaccine as part of the French vaccination campaign. The second vaccine dose, also referred to as “boost,” was received, in

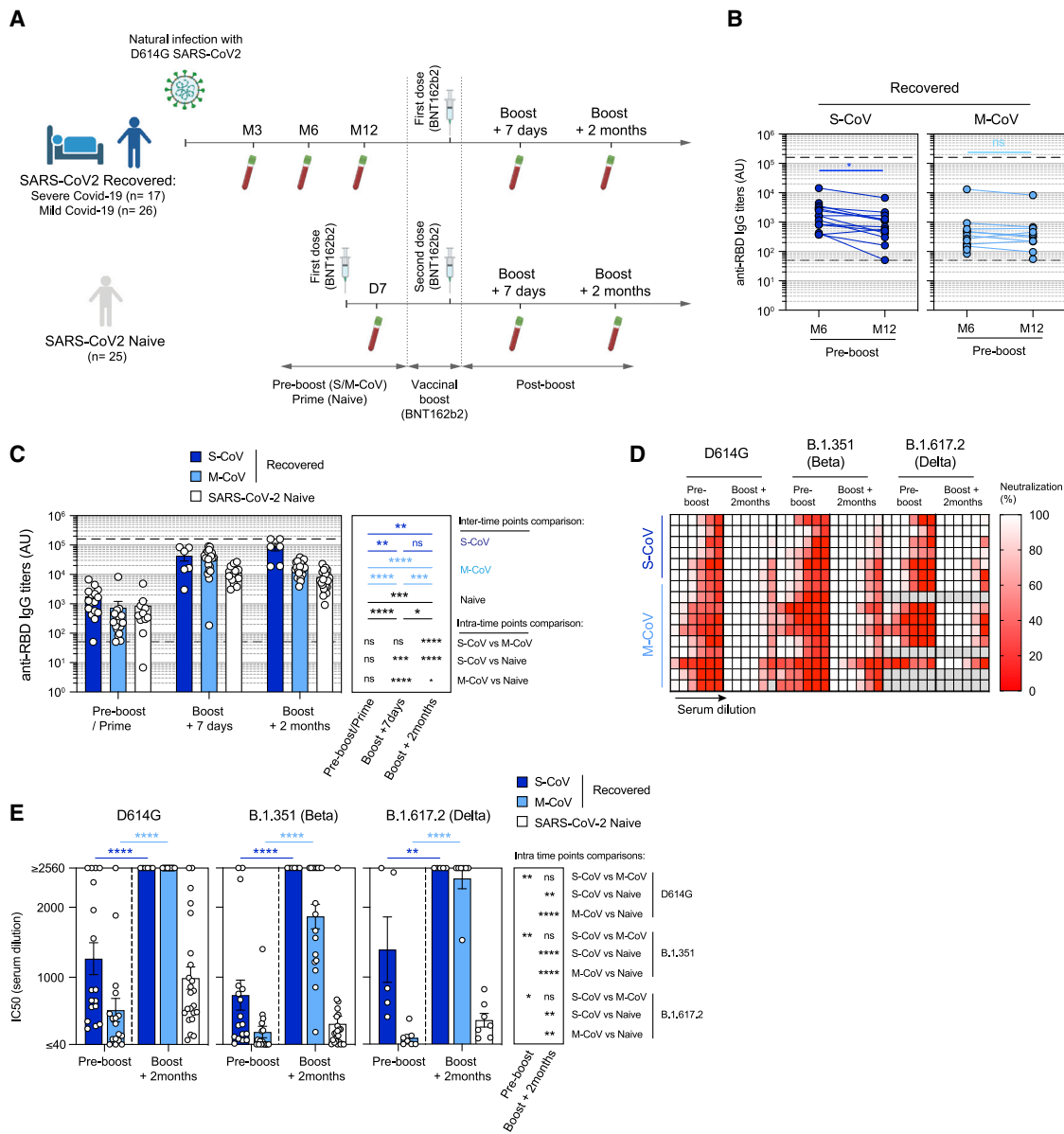


**Figure 1. The mRNA vaccine boosts humoral response against SARS-CoV-2 and VOCs in naive and SARS-CoV-2-recovered individuals**

(A) Cohort design.

(B) Anti-SARS-CoV-2 RBD serum IgG titers measured by ELISA in S-CoV (n = 16, left panel, dark blue) and M-CoV (n = 15, right panel, light blue) 6 and 12 months after symptom onset.

(C) Evolution of anti-SARS-CoV-2 RBD serum IgG titers after BNT162b2 vaccination. IgG titers (arbitrary units [a.u.]) are shown at pre-boost (month 6 or month 12) for SARS-CoV-2-recovered (S-CoV, dark blue; M-CoV, light blue) or after the prime for naive individuals (white) as well as 7 days and 2 months after the vaccine boost. Bars indicate mean ± SEM.

(B and C) The lower dashed line indicates the positivity threshold, and the upper dashed line indicates the upper limit of detection as provided by the manufacturer.

(D) Heatmap representing the observed *in vitro* neutralization of D614G SARS-CoV-2 (left), B.1.351 (center), and B.1.617.2 VOCs (right) by sera from SARS-CoV-2-recovered individuals at the pre-boost and boost + 2 months time points (serial dilutions: 1/10, 1/40, 1/160, 1/640, 1/2,560, and 1/10,240). Each line represents one individual.

(E) Half-maximal inhibitory concentration (IC<sub>50</sub>) for all sera tested from SARS-CoV-2-recovered and naive individuals at pre-boost and boost + 2 months time points against D614G SARS-CoV-2, B.1.351, and B.1.617.2 VOCs. Bars indicate mean ± SEM.

We performed two-way ANOVA with multiple comparisons of all groups (B), repeated-measures mixed-effects model analysis with two sets of multiple comparisons (between donor groups inside each time point and between time points for each donor group) (C), and repeated-measures mixed-effects model analysis with multiple comparisons between time points for each recovered donor group and Kruskal-Wallis with multiple comparisons between donor groups inside each time point (E) (Benjamini, Krieger, and Yekutieli false discovery rate [FDR] correction was used for all multiple comparisons). \*\*\*\*p < 0.0001, \*\*\*p < 0.001, \*\*p < 0.01, \*p < 0.05. See also Figure S1 and Tables S1 and S2.

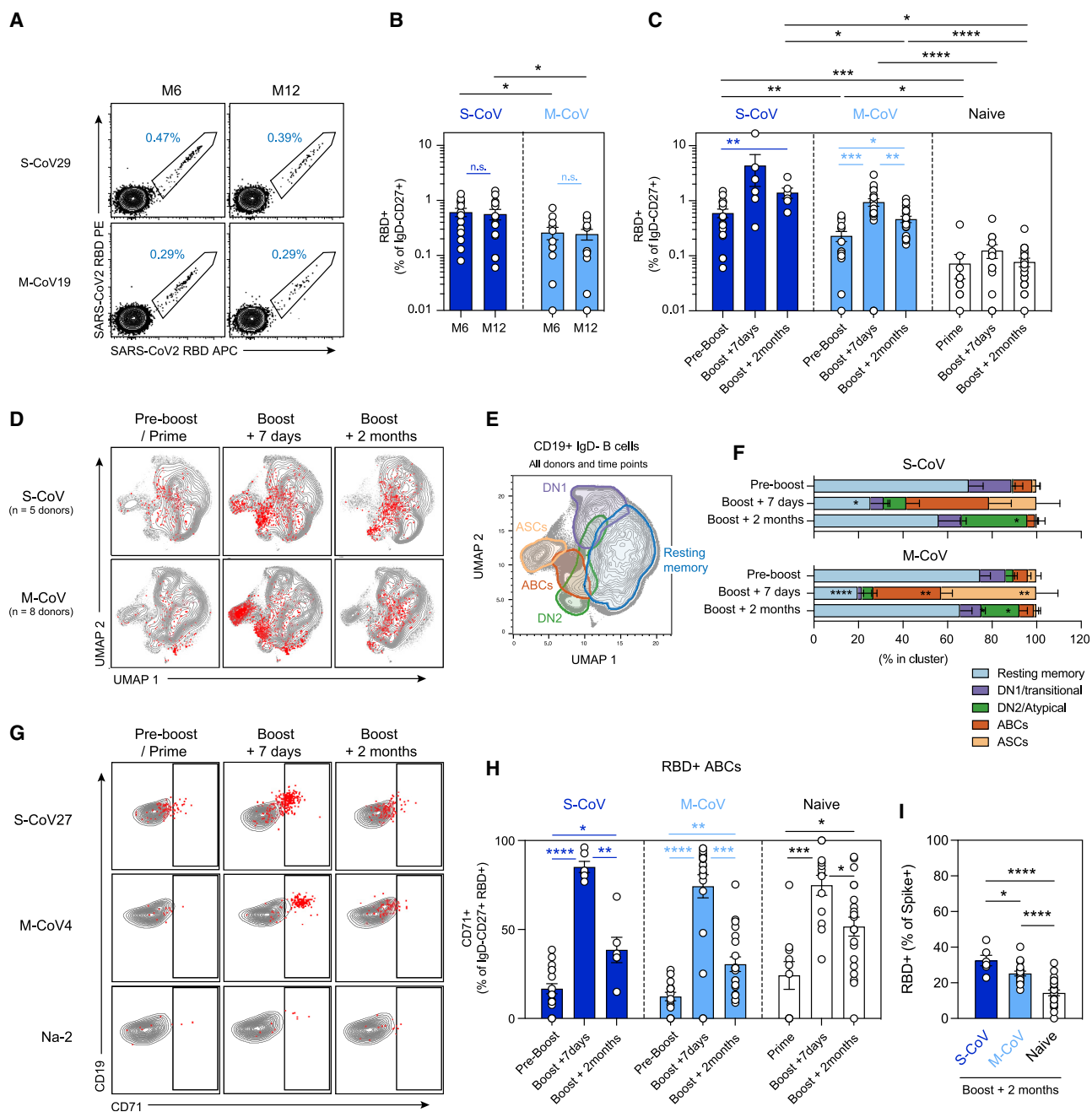


**Figure 2. mRNA vaccination activates multiple SARS-CoV-2 RBD-specific B cell subsets in SARS-CoV-2-recovered and naive individuals**  
 (A) Representative dot plot of SARS-CoV-2 RBD staining of CD19<sup>+</sup>IgD<sup>-</sup>CD27<sup>+</sup>CD38<sup>int/low</sup> MBCs at 6 and 12 months in one S-CoV and one M-CoV representative individual.  
 (B and C) Frequencies of SARS-CoV-2 RBD-specific cells in live CD19<sup>+</sup>IgD<sup>-</sup>CD27<sup>+</sup>CD38<sup>int/low</sup> MBCs 6 and 12 months after symptom onset in SARS-CoV-2-recovered individuals (S-CoV: dark blue, n = 14/14; M-CoV: light blue, n = 11/12) (B) and at pre-boost, boost + 7 days, and boost + 2 months time points in S-CoV (dark blue, n = 17/6/6), M-CoV (light-blue, n = 14/21/20), and naive (white, n = 10/13/23) individuals. Bars indicate mean ± SEM.  
 (D) UMAP projections of concatenated CD19<sup>+</sup>IgD<sup>-</sup> B cells multiparametric fluorescence-activated cell sorting (FACS) analysis from 5 S-CoV and 8 M-CoV individuals, analyzed longitudinally. His-tagged labeled SARS-CoV-2 RBD-specific cells are overlaid as red dots.  
 (E and F) Unsupervised clustering (FlowSOM) performed on the concatenated FACS dataset. Main defined clusters (>2% of total CD19<sup>+</sup>IgD<sup>-</sup> B cells) are shown as overlaid contour plots on the global UMAP representation (E). Cluster distribution of SARS-CoV-2 RBD-specific cells in identified clusters, at the indicated time point, is further displayed as bar plots (F). Bars indicate mean ± SEM.  
 (G) Representative dot plots for CD71 and CD19 expression in IgD<sup>-</sup>CD19<sup>+</sup>CD38<sup>int/low</sup> B cells at the indicated time points from representative S-CoV, M-CoV, and naive individuals. SARS-CoV-2 RBD-specific MBCs are overlaid as red dots.

(legend continued on next page)

median, 28 days after the first dose of the vaccine, referred to as “prime.” Post-boost blood samples were collected from all vaccinated participants, in median, 8 days (range, 5–22 days) and 2 months after the injection (Figure 1A; Table S1C). Eight SARS-CoV-2-naive donors were sampled additionally after initial priming.

We first measured the pre- and post-boost evolution of IgG serum titers against the wild-type (WT) RBD in both cohorts. Anti-RBD IgG titers remained stable between 6 and 12 months after infection in SARS-CoV-2-recovered individuals, with only a mild decrease seen in S-CoV individuals (Figure 1B). In line with previous reports, a single dose of mRNA vaccine elicited a strong recall response in all individuals, with anti-RBD IgG titers increasing, on average, by 24-fold in S-CoV and 53-fold in M-CoV individuals compared with pre-boost titers (Figures 1C and S1A; Table S2A). In SARS-CoV-2-naive individuals, the mRNA vaccine boost also induced a robust anti-RBD IgG response (average of 25-fold-increase), although titers remained inferior to SARS-CoV-2-recovered individuals at all time points (mean 10,870 versus 75,511 a.u./mL in S-CoV and 55,024 in M-CoV,  $p = 0.005$  and  $p < 0.0001$ , respectively). Despite contraction of the response in all groups, anti-RBD IgG titers were at least 10-fold higher than pre-boost/prime titers 2 months after boost (Figures 1C and S1A).

Twelve months after infection, all sera from SARS-CoV-2-recovered individuals demonstrated neutralization potential in a focus reduction assay against an authentic SARS-CoV-2 virus carrying the dominant D614G amino acid change in the S1 domain of its S protein (Figures 1D, 1E, S1B, and S1C). This potential was more pronounced in S-CoV than in M-CoV individuals but, as expected, was reduced similarly in both groups against the B.1.351 VOC strain, harboring three mutations in its RBD (N501Y, which increases the affinity for the ACE2 receptor, and E484K and K417N, which are implicated in escape from neutralizing antibodies; Harvey et al., 2021), along with several mutations in other S domains. As reported previously (Goel et al., 2021a; Reynolds et al., 2021; Stamatatos et al., 2021; Wang et al., 2021b), a boost mRNA vaccine strongly enhanced the overall neutralizing potency of SARS-CoV-2-recovered individuals against the D614G and B.1.351 viruses, with all S-CoV and M-CoV sera achieving a half-maximal inhibitory concentration ( $IC_{50}$ ) lower than 1/2,560 for the D614G strain. All sera from S-CoV individuals also reached strong neutralizing potency against the B.1.351 and B.1.617.2 (delta) virus ( $IC_{50} < 1/2,560$ ), although we cannot exclude differences above the tested dilution range for both VOCs (Figures 1D, 1E, and S1B; Table S2B). For M-CoV individuals, the gain in neutralization potency against B.1.351 and B.1.617.2 VOCs was also clear but more modest for the B.1.351 virus. Sera from all naive individuals also showed detectable neutralizing activity against the D614G strain at the final time point in our study (mean  $IC_{50}$ , 1/988; range, <2,560 to 1/103), but never reached the  $IC_{50}$  seen in

SARS-CoV-2-recovered individuals. This potency was reduced further against the B.1.351 VOC strain (mean  $IC_{50}$ , 1/332), with 8 of 23 individuals (35%) displaying an  $IC_{50}$  above 1/100 against this variant. In contrast, all naive individuals tested displayed low but detectable neutralization capacity against the B.1.617.2 variant.

These data show that a boost of mRNA vaccine based on the Wuhan-Hu-1 S protein induces a strong recall response in all SARS-CoV-2-recovered individuals, with strong neutralizing IgG serum titers against D614G SARS-CoV-2 as well as B.1.351 and B.1.617.2 VOCs in most individuals. The lower neutralization potency achieved in naive individuals suggests a key role of the matured MBC pool present in SARS-CoV-2-recovered patients in modeling the quality of the vaccine response, including cross-neutralization of VOCs.

### mRNA vaccination mobilizes MBCs in SARS-CoV-2-recovered individuals

Similar to the serum IgG titers, the percentage of RBD-specific and S-specific  $CD27^+IgD^-$  B cells remained stable between 6 and 12 months in SARS-CoV-2-recovered individuals irrespective of initial disease severity, confirming generation of germinal center-derived, long-lived MBCs after natural infection (Figures 2A, 2B, S2A, and S2B). RBD-specific MBCs, which represent a large fraction of the neutralizing MBC pool against SARS-CoV-2, expanded substantially after one dose of the mRNA vaccine before a modest contraction at 2 months (Figures 2C and S2C; Table S2). In contrast, only low numbers of RBD-specific B cells were detectable in naive individuals after prime, with a non-significant effect of boost vaccination (Figure 2C), although RBD-specific ASCs were observed in all donors in the early steps of the post-boost response (Figure S2D). The frequency of RBD-specific MBCs persisting 2 months after the boost in naive individuals remained significantly lower than the frequency of MBCs observed in SARS-CoV-2-recovered individuals before vaccination (Figure 2C), with similar profiles observed for S-specific MBCs (Figure S2E). The overall frequency of S-specific MBCs in naive individuals 2 months after the boost (3 months after the prime) even appeared to be reduced compared with the 3-month post-infection time point in SARS-CoV-2-recovered individuals (Figure S2F).

Unsupervised analysis of  $CD19^+IgD^-$  switched B cell populations, using a multiparametric flow panel we used previously to describe the initial response against SARS-CoV-2 in these individuals (Sokal et al., 2021), showed that RBD-specific cells mostly resided in the  $CD21^+CD27^+IgD^-CD38^{int/-}CD71^{int/-}$  resting MBC compartment before vaccination (Figures 2D–2F; Tables S2C and S2D). These cells switched rapidly to a  $CD27^+CD38^{int/+}CD71^+$  activated B cell phenotype (ABC cluster) in the first 7 days after the boost, together with emergence of a population of  $RBD^+CD38^{high}CD27^{high}$  ASCs. The persistent expression of the BCR on the surface of these cells

(H) Frequencies of SARS-CoV-2 RBD-specific cells displaying an ABC ( $CD19^+CD27^+IgD^-CD71^+$ ) phenotype at the indicated time points.

(I) Proportion of S-specific MBCs recognizing the RBD in each individual at the 2-month time point. Bars indicate mean  $\pm$  SEM.

We performed two-way ANOVA with multiple comparisons of all groups (B), repeated-measures mixed-effects model analysis with two sets of multiple comparisons (between donor groups inside each time point [black lines] and between time points for each donor group [colored lines]) (C and H), and ordinary one-way ANOVA (I) (Benjamini, Krieger, and Yekutieli FDR correction was used for all multiple comparisons). Only significant comparisons are highlighted in (C), (H), and (I). \*\*\* $p < 0.0001$ , \*\* $p < 0.001$ , \* $p < 0.01$ ,  $p < 0.05$ . See also Figure S2 and Table S2.

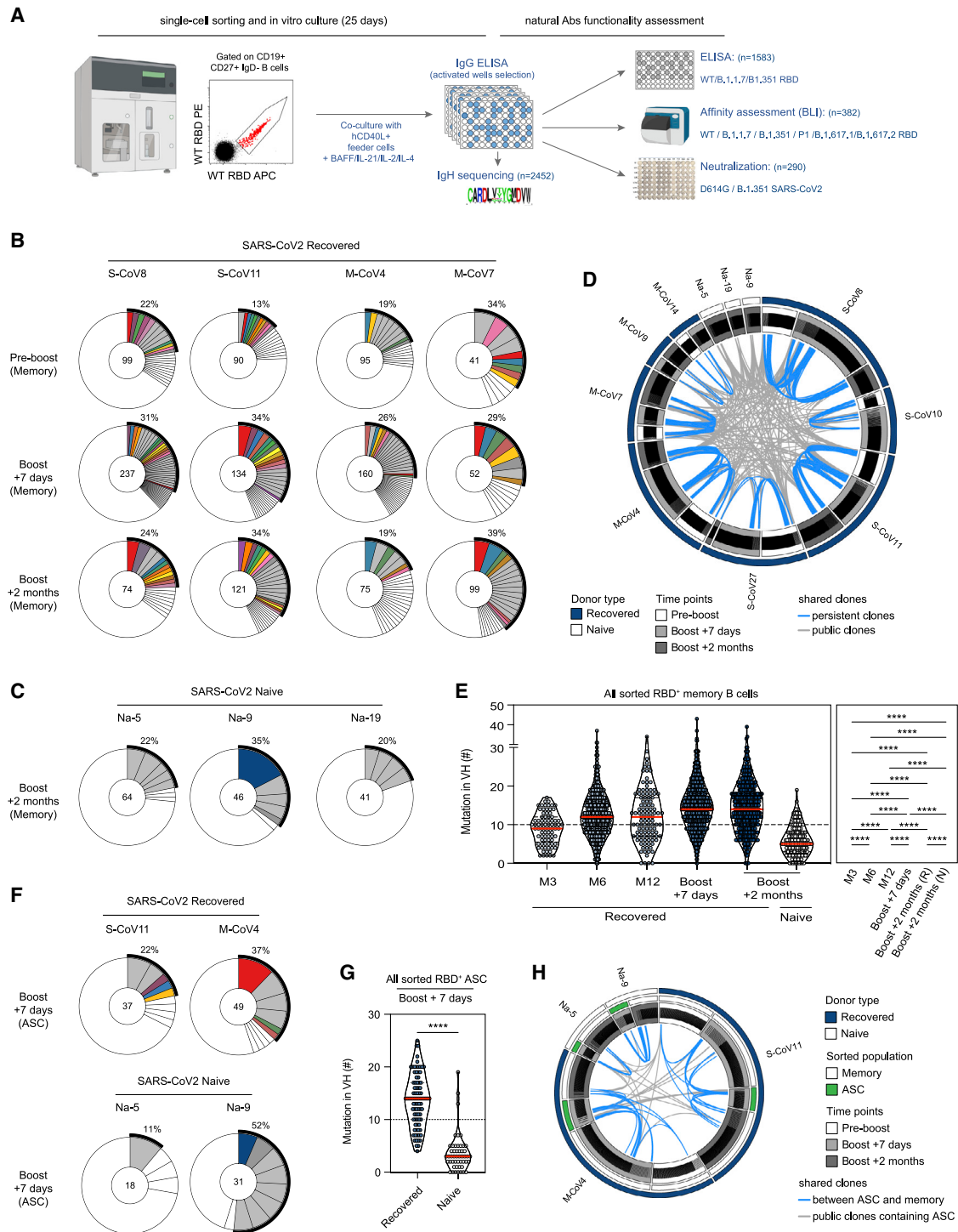


**Figure 3. mRNA vaccination elicits a diverse RBD-specific MBC repertoire in SARS-CoV-2-recovered and naive individuals**

(A) Experimental scheme for functional assessment of naturally expressed monoclonal antibodies from RBD-specific MBCs.

(B and C) Pie charts representing the clonal distribution of RBD-specific MBCs sorted from 2 S-CoV and 2 M-CoV individuals at the pre-boost, boost + 7 days, and boost + 2 months time points (B) and 2 naive individuals at boost + 2 months (C). Clonal representation is depicted according to Wang et al. (2021b): colored slices indicate an expanded MBC clone (2 or more sequences at a given time point) found at several time points in the same individual (persistent clone) or in clonal relationship with ASCs at boost + 7 days, gray slices indicate an expanded MBC clone found at a single time point, and white slices indicate unique sequences found at several time points. The main white sector in each pie chart represents unique sequences observed at a single time point. The outer black semi-circular line indicates the proportion of sequences belonging to expanded clones at a given time point. The total number of sequences is indicated at the pie center.

(legend continued on next page)

harboring a classical ASC phenotype suggests that they were mainly newly generated plasmablasts. These activated subsets contracted progressively and matured as resting MBCs at the latest time point in our study. Atypical MBCs (DN2; IgD<sup>-</sup>CD27<sup>+/-</sup>CD11c<sup>+</sup>) and ASC precursors (DN1; IgD<sup>-</sup>CD27<sup>-</sup>) RBD-specific clusters were also observed, with a small DN2 fraction persisting up to 2 months after boost, notably in S-CoV individuals (Figure 2F).

The low numbers of RBD-specific B cells in naive individuals precluded a robust unsupervised analysis, and we therefore characterized the phenotype of RBD-specific MBCs from the whole cohort using manual gating, based on the CD19 and CD71 expression profiles, to delineate ABCs (CD19<sup>high</sup>CD71<sup>+</sup>) (Ellebedy et al., 2016) and resting MBCs (CD19<sup>+</sup>CD71<sup>low</sup>) among RBD-specific cells over time. A large fraction of RBD-specific MBCs acquired a CD19<sup>high</sup>CD71<sup>+</sup> ABC phenotype in the days following the boost in naive individuals, similarly to M-CoV and S-CoV patients (Figures 2G and 2H; Table S2E), demonstrating that vaccine induced a robust expansion of an RBD-specific ABC population in all groups of donors.

The proportion of RBD-specific ABCs decreased over time, favoring an increase of RBD-specific resting MBCs consistent with the contraction of the vaccine response. This contraction appeared to be more pronounced in SARS-CoV-2-recovered individuals, suggesting persistence of GC output in naive individuals (Figure 2H). Similar kinetics were observed for S-specific B cells (Figure S2G), although it should be noted that RBD-specific B cells still represented a smaller proportion of S-specific cells in naive than in SARS-CoV-2 recovered individuals at the 2-month time point (Figures 2I and S2H).

### mRNA vaccination maintains the overall diversity of the MBC repertoire

To address how mRNA vaccine boost affects the MBC repertoire, we performed single-cell sorting and culture of RBD-specific MBCs before and 7 days and 2 months after the boost in SARS-CoV-2-recovered individuals and 2 months after the boost in naive individuals (Figure 3A). We obtained a total of 2,452 V<sub>H</sub> sequences from 4 S-CoV, 4-M-CoV, and 3 naive individuals (Tables S1D and S3A–S3H). Clonally expanded RBD-specific MBCs were found before vaccination in all SARS-CoV-2-recovered individuals, representing 13%–34% of total V<sub>H</sub> sequences for each donor (Figures 3B and S3A). Vac-

cine-activated MBCs showed no evidence of further clonal dominance and conserved their overall diversity despite the major increase in their numbers. The fraction of the repertoire belonging to these clones varies from 19%–39% and remains comparable during contraction, with clones persisting over the pre/post-vaccination period observed in all SARS-CoV-2-recovered individuals. This overall clonal stability was reflected by similar Shannon entropy values at all studied time points (Figure S3B). Similar clonal expansion was observed in naive individuals (Figure 3C), who also harbored a high frequency of convergent RBD-specific clones with SARS-CoV-2-recovered individuals based on immunoglobulin heavy chain (IgH) variable, diversity, and joining (VDJ) sequences (Figure 3D).

We previously reported a progressive accumulation of somatic mutations in RBD-specific clones up to 6 months after infection in this cohort of SARS-CoV-2-recovered individuals (Sokal et al., 2021). The number of mutations in RBD-specific V<sub>H</sub> sequences remained stable between 6 and 12 months. In contrast, V<sub>H</sub> mutation numbers were increased shortly after the boost and maintained in the MBC pool 2 months thereafter (Figure 3E). This evolution in mutation profile could be confirmed at the individual level for 2 individuals with complete follow-up from 3 or 6 months after symptom onset to 2 months after boost (Figures S3C and S3D; Table S3A). This rapid increase in overall mutational load suggests that a fraction of matured, pre-existing MBCs was mobilized selectively upon vaccine response and persisted over time.

RBD-specific MBCs from naive individuals obtained 2 months after the boost harbored low mutation numbers in their V<sub>H</sub> genes, consistent with recruitment of naive B cells in the early phase of the vaccine response. It should also be noted that MBCs from naive individuals harbor an even lower mutational load than MBCs from SARS-CoV-2-recovered individuals at a similar 3-month time point after natural infection (Figure 3E). This suggests that natural infection might drive a faster maturation process of the MBC response.

RBD-specific ASCs from SARS-CoV-2-recovered individuals sorted 7 days after the boost showed clonal relationships with MBCs and highly mutated V<sub>H</sub> sequences (Figures 3F–3H and S2A; Tables S3F and S3H). In contrast, RBD-specific ASCs from naive individuals displayed near-germline V<sub>H</sub> sequences corresponding to recruitment of naive B cells in the extrafollicular response (Figure 3G). Overall, these results show that activation

(D) Circos plot showing clonal relationships between all sequenced RBD-specific MBCs grouped by donors and time points. Blue lines connect persistent clones, and gray lines connect clones shared by at least two donors (public clones).

(E) Violin plots showing the number of mutations in the V<sub>H</sub> segment of RBD-specific MBCs at successive time points in SARS-CoV-2-recovered (month 3, 81 sequences; month 6, 600; month 12, 109; boost + 7 days, 930; boost + 2 months, 430) and naive donors (boost + 2 months, 151). The red line indicates the median.

(F) Pie chart representing the clonal distribution of RBD-specific ASCs sorted for 2 SARS-CoV-2-recovered and 2 naive individuals at boost + 7 days. Colored slices indicate a clone in clonal relationship with an expanded MBC clone from the same donor, gray slices indicate an expanded ASC clone not found in MBCs from the same donor, and white slices indicate unique ASC sequences in a clonal relationship with a non-expanded MBC clone. The outer black semi-circular line indicates the proportion of sequences belonging to expanded ASC clones. The total number of sequences is indicated at the pie center.

(G) Violin plots showing the number of mutations in the V<sub>H</sub> segment of RBD-specific ASCs sorted from 2 SARS-CoV-2-recovered (n = 86 sequences) and 2 naive donors (n = 49 sequences) at boost + 7 days. The red line indicates the median.

(H) Circos plot showing clonal relationships between RBD-specific MBCs (white mid-semicircular slice) and RBD-specific ASCs (green mid-semicircular slice) sorted at boost + 7 days from 2 SARS-CoV-2-recovered (one S-CoV, one M-CoV, dark blue outer circular slice) and 2 naive (white outer circular slice) individuals. Blue lines indicate shared clones between ASCs and MBCs, and gray lines indicate public clones containing ASCs.

Ordinary one-way ANOVA with multiple comparisons (Benjamini, Krieger, and Yekutieli FDR correction) (G) and a two-tailed Mann-Whitney test (E) were performed (\*\*\*\*p < 0.0001). See also Figure S3 and Table S2.

of the previously matured pool of MBCs by the mRNA vaccine does not bias the clonal diversity of their repertoire in previously infected individuals while selectively amplifying MBCs with a higher mutation load.

### MBCs mobilized by mRNA vaccine contain high-affinity clones against VOCs

To determine the potency of the MBC compartment mobilized or elicited by mRNA vaccine against the main natural RBD variants, we first performed ELISA on 1,583 supernatants from single-cell culture of sorted RBD-specific MBCs from 4 S-CoV, 4 M-CoV, and 3 naive individuals (Figure 4A). To normalize for IgG concentration in culture supernatants, we plotted ELISA optical density (OD) values for WT (Wuhan) versus B.1.1.7 or B.1.351 RBD variants. Almost all supernatants similarly recognized the WT and B.1.1.7 RBD, but 20% of them showed a 10-fold decrease in B.1.351 RBD recognition, with similar frequencies of affected supernatants in SARS-CoV-2-recovered and naive individuals (Figures 4A and 4B; Table S2F).

We next assayed the affinity of MBCs against the B.1.1.7, B.1.351, P1, B.1.617.1, and B.1.617.2 RBD variants using biolayer interferometry (BLI), in which naturally expressed monoclonal IgG from single-cell culture supernatants were loaded on anti-human IgG biosensors (Figure S4A). Monoclonal antibodies expressed by MBCs from recovered individuals were highly enriched for high affinity binders against the WT RBD compared with naive patients (73.9%  $\pm$  5.8% versus 46.5%  $\pm$  4.3%,  $p < 0.01$ ; Figures 4C and 4D; Table S2G), and comparable frequencies were observed against the B.1.1.7 variant. However, overall affinity profiles were no longer different between recovered and naive donors when the B.1.351, P1, B.1.617.1, or B.1.617.2 variants were tested, with approximately 20%–25% of clones with no or low affinity ( $K_D > 10^{-8}$  M) in both groups (Figures 4C, 4D, S4B, and S4C). Somatic hypermutation of  $V_H$  genes and antigen-driven affinity maturation against the WT RBD accounts for the higher frequency of high-affinity binders ( $K_D < 10^{-9}$  M) in SARS-CoV-2-recovered compared with naive individuals (Figures 4E and 4F). As expected, the number of  $V_H$  mutations showed reduced correlation with affinity against the B.1.351 RBD (Figures 4E and 4F), in line with selection of these clones against the WT and not the mutated RBD during the GC maturation process.

Two-by-two comparisons of binding affinities between the WT and the different RBD variants allowed us to validate the sensitivity of our approach with nearly all B.1.351-affected monoclonal antibodies (2-fold increase in variant  $K_D$  compared with WT  $K_D$ ) also affected in their binding of the P.1 RBD variant sharing a similar set of mutations (N501Y, E484K, and K417T/N) but not of the B.1.1.7 RBD variant, which only harbors the N501Y mutation (Figures 5A and 5B). Additional comparisons with B.1.617.1 and B.1.617.2 RBD variants, which harbor the L452R mutation in addition to E484Q for B.1.617.1 and T478K for B.1.617.2 but not the K417N/T mutation, further revealed cases of antibodies affected in their binding to one or more RBD variants (Figures S5A–S5D). Overall, the natural distribution of mutations in the various VOC RBDs (Figures 5C and 5D) allowed us to predict the identity of key binding amino acid residues (i.e., N501, K417, E484, L452, and T478) within the RBD for 164 of 382 tested MBC-derived monoclonal antibodies (Figures

5C–5E). Antibodies affected in their recognition of the B.1.351.1, P.1, and B.1.167.1 RBD were identified as binding to E484, with some antibodies using E484 and L452 for binding, as illustrated by the three-dimensional structure of the RBD (Figures 5C–5E and S5A–S5D). In agreement with a recent structural study (Yuan et al., 2021), clones recognizing the K417 residue were highly enriched for the IGHV3–53 and 3–66 genes, whereas clones recognizing the E484K/Q residue were mostly enriched for the IGHV1–2 and 1–69 genes (Figure S5E; Table S2H). These results also allowed us to ascribe RBD binding residues of B cells within individual MBC repertoires of naive and recovered individuals, confirming the major targeting of the E484 and/or L452 residues within the vaccine-activated pool (Figure 5E), but also highlighting significant inter-donor variability in the overall recognition profile of the SARS-CoV-2 RBD by the MBC repertoire.

### Affinity maturation and clonal diversity support B.1.351 neutralization by MBCs

Finally, to evaluate the cross-neutralization potential of RBD-specific clones mobilized after vaccination, 279 randomly selected single MBC culture supernatants from S-CoV, M-CoV, and naive vaccinated individuals were tested in our focus reduction neutralization assay against authentic D614G and B.1.351 SARS-CoV-2 viruses. The majority of RBD-specific MBC clones efficiently neutralized D614G, but a higher frequency of non-neutralizing clones was observed in naive compared with recovered individuals (Figures 6A and S6A; Table S2I). Among potent D614G neutralizers, 40%–60% of monoclonal antibodies efficiently neutralized B.1.351, without a quantitative difference between M-CoV and naive individuals (Figure 6B) or clear association with the  $V_H$  mutational load or binding affinity to the WT RBD (Figures 6C and S6A). Nonetheless, potent neutralizing MBC-derived monoclonal antibodies could be detected in all analyzed donors, including SARS-CoV-2-naive vaccinees (ranging from 5%–60% of the overall repertoire in the different donors; Figure S6B).

Loss of affinity against the B.1.351 RBD mainly affected potent D614G neutralizers (Figure 6D), highlighting the strong evolutionary pressure at the virus level to selectively evade this part of the immune response. Plotting  $K_D$  values for the WT versus B.1.351 RBD among potent D614G neutralizers further revealed four different profiles correlated with B.1.351 neutralization (Figure 6E); clones could be classified according to whether they retained a similar affinity for binding the B.1.351 RBD compared with the WT one (white and gray sectors, respectively; the gray sector corresponds to lower affinities). Among these two categories, clones could be further divided according to whether they retained neutralization potency against the B.1.351 virus (white and red dots, respectively). Accordingly, MBC-derived monoclonal antibodies displaying similar affinities against the WT and B.1.351 RBD (white sector in Figure 6E) were enriched in strong neutralizers against the B.1.351 variant (white dots), but a subset of these antibodies did display reduced neutralization potency (red dots in the white sector, Figure 6F). These monoclonal antibodies, however, showed a selectively reduced affinity against the whole B.1.351 S ectodomain (Figure 6G), suggesting alteration in their binding in the context of the trimeric protein. Among monoclonal antibodies affected in their binding to the B.1.351 RBD (gray sector in Figure 6E), maintenance of

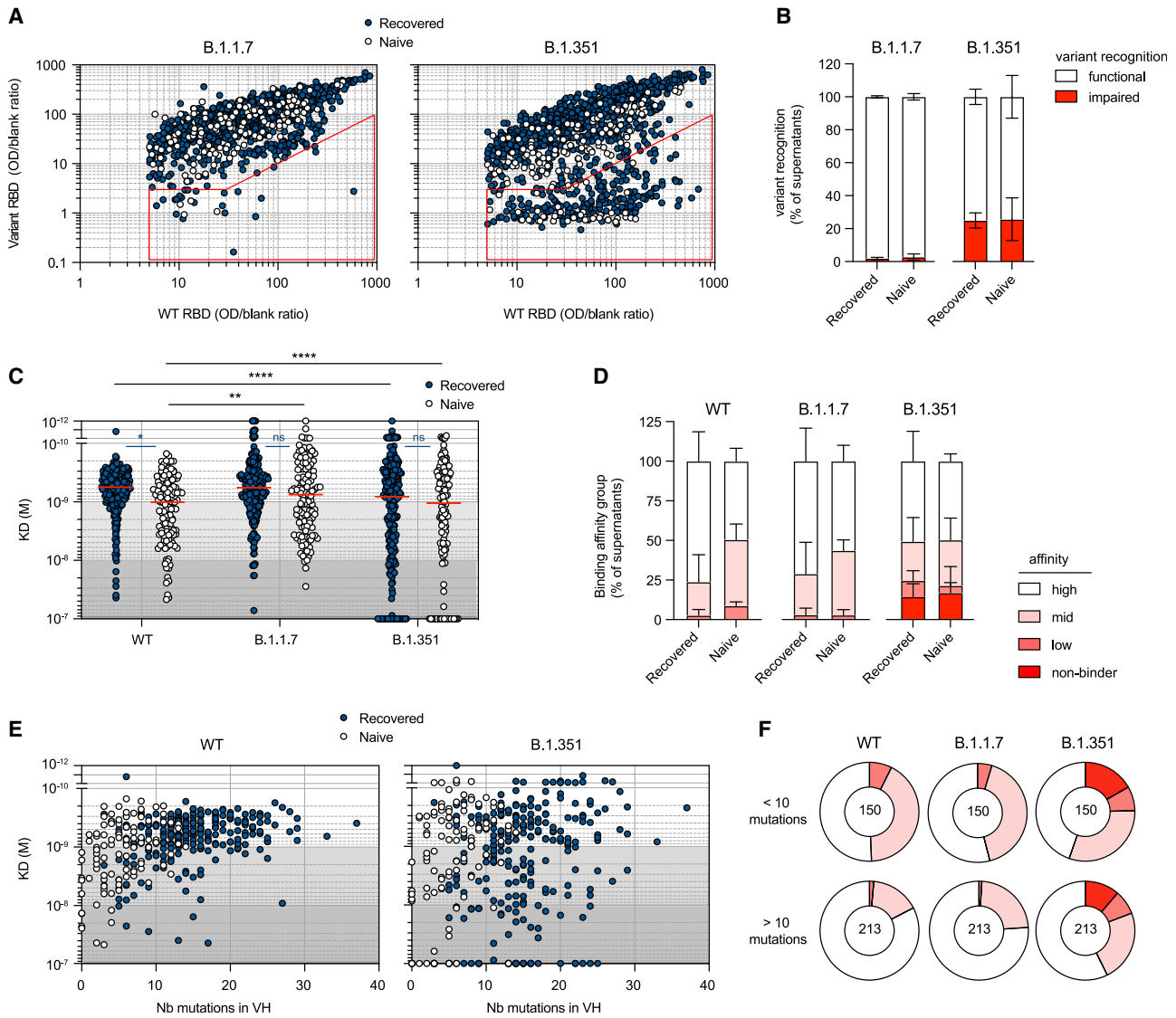


**Figure 4. The MBC pool of vaccinated individuals contains high-affinity clones against WT SARS-CoV-2 and B.1.1.7 and B.1.351 VOCs**

(A) WT RBD versus B.1.1.7 RBD (left) or B.1.351 RBD ELISA values (right) for all single-cell culture supernatants of RBD-specific MBCs isolated from SARS-CoV-2-recovered (dark blue,  $n = 952$ ) and naive (white,  $n = 373$ ) donors. Only supernatants with WT ELISA OD/blank ratio  $\geq 5$  are displayed. The red sector identifies naturally expressed antibodies defined as impaired in the recognition of a given variant (variant ELISA OD/blank ratio  $< 3$  or  $\geq 10$ -fold decrease in variant recognition).

(B) Frequencies of single RBD-specific MBC culture supernatants with functional or impaired recognition of B.1.1.7 or B.1.351 RBD variants as assessed by ELISA.

(C) Dissociation constants ( $K_D$ , expressed as moles/L) measured by BLI for 382 naturally expressed monoclonal antibodies against WT, B.1.1.7, and B.1.351 RBD. Tested monoclonal antibodies were selected randomly from single-cell culture supernatants of RBD-specific MBCs isolated from SARS-CoV-2-recovered ( $n = 251$ ) and naive donors ( $n = 131$ ) and displaying WT RBD ELISA OD/blank ratio  $\geq 3$ . Background colors define high-affinity ( $K_D < 10^{-9}$  M), mid-affinity ( $10^{-9} \leq K_D < 10^{-8}$  M), and low-affinity ( $10^{-8} \leq K_D < 10^{-7}$ ) monoclonal antibodies. All monoclonal antibodies with no measurable affinity ( $K_D \geq 10^{-7}$ ) were considered non-binders.

(D) Histogram showing the intra-donor binding affinity distribution of monoclonal antibodies tested against WT, B.1.1.7, and B.1.351 RBD variants, as defined in (C), for SARS-CoV-2-recovered or naive donors. Bars indicate mean  $\pm$  SEM.

(E) Measured  $K_D$  (M) against WT (left) or B.1.351 RBD (right) versus number of  $V_H$  mutations for all tested monoclonal antibodies with available  $V_H$  sequence from SARS-CoV-2-recovered (dark blue,  $n = 249$ ) and naive (white,  $n = 114$ ) donors (Spearman correlations for all sequences:  $V_H$  mutation/WT  $K_D$ ,  $r = 0.3791$ ,  $p < 0.0001$ ;  $V_H$  mutation/B.1.351  $K_D$ ,  $r = 0.152$ ,  $p = 0.0033$ ).

(F) Pie chart showing the binding affinity distribution of all tested monoclonal antibodies with low ( $< 10$  mutations, top panel) or high  $V_H$  mutation numbers ( $> 10$ , bottom panel) against WT, B.1.1.7, and B.1.351 RBD variants as defined in (C). Numbers at center of the pie chart indicate the total number of tested monoclonal antibodies in each group.

A two-way ANOVA with two sets of multiple comparisons (between tested variants inside each group (black lines) and between groups for each tested variants (colored lines)) was performed (C; Benjamini, Krieger and Yekutieli FDR correction). \*\*\*\* $p < 0.0001$ , \*\* $p < 0.01$ , \* $p < 0.05$ . See also Figure S4 and Table S2.

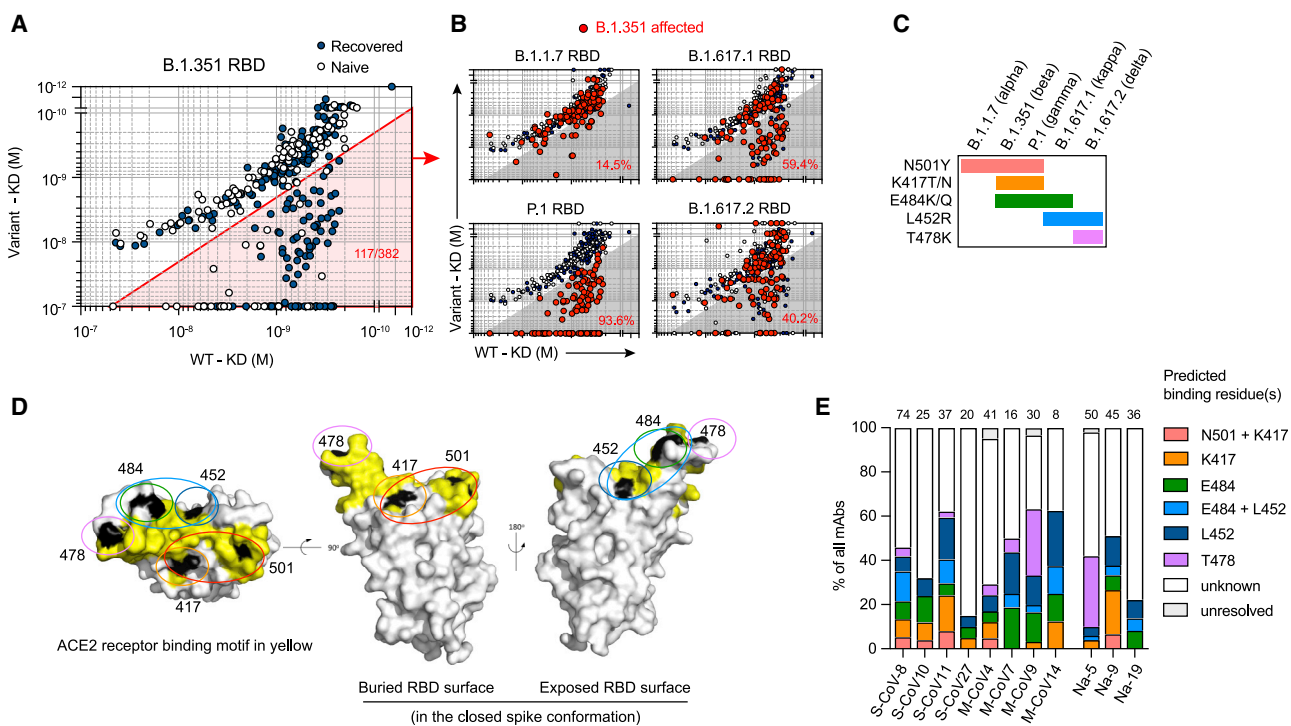


**Figure 5. The variant RBD recognition profile reveals key residues recognized by MBCs mobilized by the mRNA vaccine boost**

(A) Dot plot representing the  $K_D$  values for B.1.351 RBD versus WT RBD for all tested monoclonal antibodies from SARS-CoV-2-recovered (dark blue dots) and naive donors (white dots). The red shaded zone indicates B.1.351-affected monoclonal antibodies, defined as those with at least 2-fold increased  $K_D$  for B.1.351 compared with the WT RBD.

(B) Dot plots representing the  $K_D$  values for B.1.1.7, P.1, B.1.617.1, and B.1.617.2 RBD versus WT RBD. B.1.351-affected monoclonal antibodies are highlighted as larger red dots (corresponding to clones present in the red sector in A). Percentages indicate the proportion of B.1.351-affected monoclonal antibodies also affected by the indicated RBD variant.

(C) Distribution of known mutations in the RBD domain between B.1.1.7, B.1.351, P.1, B.1.617.1, and B.1.617.2 SARS-CoV-2 variants.

(D) RBD (extracted from the PDB: 6XR8 S protein trimer structure) shown in three orthogonal views, with the ACE2 receptor binding motif highlighted in yellow and the residues found mutated in at least one of the tested variants (L452, K417, T478, E484, and N501) highlighted in black. Single or a group of predicted binding residues are further highlighted by colored ovals according to the color scheme used in (E).

(E) Frequencies of predicted essential binding residues, as defined by RBD variants recognition profile in BLI, for all monoclonal antibodies isolated from each of the 11 tested donors. Numbers of tested monoclonal antibodies for each donor are indicated on top of each histogram.

See also [Figure S5](#) and [Table S2](#).

neutralization activity against the VOC was strongly dictated by their original affinity against the WT RBD. Although clones with weak initial affinity against the WT RBD were mostly impaired (red dots in the gray sector), 40% of clones with high initial affinity remained potent neutralizers against the VOC (white dots in the gray sector, [Figures 6E](#) and [6F](#)). This included monoclonals directed against the E484 and K417 residues of the SARS-CoV-2 RBD ([Figure S6C](#)). This highlights the key role of affinity maturation in shaping the humoral response and anticipating viral escape.

These results demonstrate that the MBC pool selected by the WT RBD after mRNA vaccination contains, among its diverse and affinity matured repertoire, a substantial fraction of potent neutralizers against VOCs.

## DISCUSSION

MBCs display a diverse repertoire allowing an adaptive response upon re-exposure to the pathogen, especially in the case of variants ([Purtha et al., 2011](#); [Weisel et al., 2016](#)). However, repeated

antigenic stimulation with vaccinations or viral challenge may be deleterious, reducing the diversity of the overall response in which drifted epitopes are less well targeted ([Andrews et al., 2015](#); [Mesin et al., 2020](#)). Thus, understanding how mRNA vaccination affects the MBC pool shaped by a previous exposure to SARS-CoV-2 and to determine its capacity to neutralize variants is critical. More generally, to decipher how MBCs from naive vaccinees differ and evolve in comparison with SARS-CoV-2-recovered individuals is also of major importance in the pandemic context.

We report here a longitudinal study of SARS-CoV-2-recovered individuals followed over 1 year after their initial infection and vaccinated with the BNT162b2 mRNA vaccine. The vaccine response of SARS-CoV-2-naive individuals was analyzed in parallel. The strength of our approach is the large-scale, unbiased study of the MBC response against SARS-CoV-2 at the single-cell scale using *in vitro* activation of randomly sampled MBCs/ABCs. This allowed a deep functional analysis that included affinity assessment against the WT RBD and against 5 variants, including B.1.617.2, and determination of neutralization potency of these secreted IgG against two SARS-CoV-2 viruses without

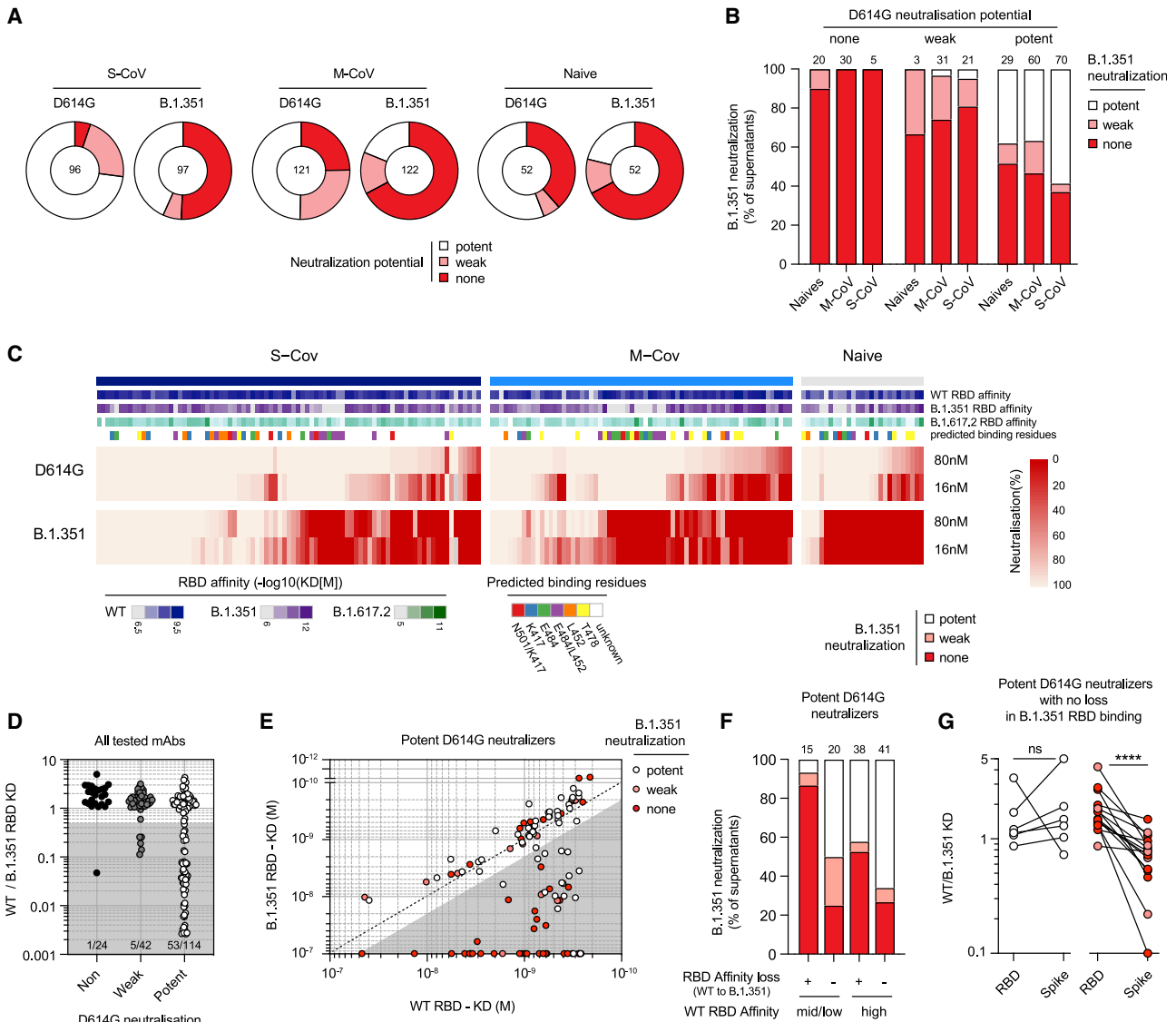


**Figure 6. A substantial proportion of MBCs in vaccinated individuals neutralizes D614G SARS-CoV-2 and B.1.351 VOCs**

(A) Pie charts showing the proportion of single-cell culture supernatants of RBD-specific MBCs isolated from SARS-CoV-2-recovered (S-CoV,  $n = 104$ ; M-CoV,  $n = 123$ ) and naive donors ( $n = 52$ ) displaying potent, weak, or no neutralization potential (none) against the D614G SARS-CoV-2 and B.1.351 SARS-CoV-2 variants. Potent neutralizers are defined as more than 80% neutralization at 16 nM and weak neutralizer as neutralization less than 80% at 16 nM but more than 80% at 80 nM. Others were defined as non-neutralizing.

(B) Histogram showing the proportion of B.1.351 SARS-CoV-2 potent, weak, and non-neutralizing single-RBD-specific MBC culture supernatants, grouped based on their neutralization potency against D614G SARS-CoV-2.

(C) Heatmap showing *in vitro* neutralization of the D614G SARS-CoV-2 and B.1.351 variants at 80 nM and 16 nM for all culture supernatants whose monoclonal antibodies were also tested in BLI against all variants (S-CoV,  $n = 85$ ; M-CoV,  $n = 67$ ; naive,  $n = 27$ ).  $K_D$  (M) values against the WT, B.1.351, and B.1.617.2 RBD for each monoclonal antibody are represented on top, along with predicted binding residues.

(D) Ratio of WT over B.1.351 RBD  $K_D$  values for all monoclonal antibodies displayed in (C), grouped based on their neutralization potency against D614G SARS-CoV-2.

(E)  $K_D$  (M) values against B.1.351 versus WT RBD for all D614G SARS-CoV-2 potent neutralizer monoclonal antibodies. Dot color indicates the neutralization potency against the B.1.351 SARS-CoV-2 variant. Gray shade highlights binding-impaired clones against the B.1.351 RBD variant as defined in Figure 5A.

(F) B.1.351 SARS-CoV-2 neutralization potency distribution of all tested potent D614G SARS-CoV-2 neutralizers, grouped based on their affinity for the WT RBD and affinity loss against B.1.351.

(G) WT versus B.1.351 variant RBD or S  $K_D$  ratio for selected monoclonal antibodies showing no clear B.1.351 RBD binding impairment and no loss (left) or clear loss (right) of neutralization potency against the B.1.351 SARS-CoV-2 variant. A paired Wilcoxon test was performed (\*\*\*\* $p < 0.0001$ ).

See also Figure S6 and Table S2.

cloning and re-expression intermediates. We focused on the RBD because anti-RBD antibodies contribute to the majority of neutralizing antibodies, and its mutations allow immune escape of VOCs (Ju et al., 2020; Robbiani et al., 2020) together with additional targets in the N-terminal domain of the S (McCallum et al., 2021; Tong et al., 2021).

Our study highlights the stability of the overall RBD-specific MBC population up to 12 months after infection with a stable mutation profile, extending observations on memory persistence in COVID-19 (Wang et al., 2021b). The dynamics of RBD-specific cells after mRNA vaccination in SARS-CoV-2-recovered individuals reflect the plasticity of the MBC pool, which promptly and widely activates, proliferates, and generates ASCs and then contracts as resting MBCs (Goel et al., 2021a; Reynolds et al., 2021; Wang et al., 2021b). This mobilized population contains highly mutated affinity-matured clones that settle, expand, and persist for up to 2 months after the boost with a higher frequency and mutational load than before the vaccinal boost. Despite this, longitudinal VDJ sequencing revealed a limited effect on the diversity of this previously matured repertoire. Thus, expansion of the MBC pool does not seem to impair archives of the B cell specificities that have been selected during the amplification. In contrast, and mirroring early stages of the extrafollicular response after infection (Woodruff et al., 2020), RBD-specific B cells expressing near-germline recurrent  $V_H$  genes with potent affinity are recruited after mRNA vaccination in naive individuals. MBCs from naive individuals also acquired somatic mutations with time but, 2 months after the boost, harbored fewer mutations than SARS-CoV-2-recovered individuals 3 months after COVID-19. Thus, although the MBC pool matures progressively in naive vaccinees, its maturation and amplification were less pronounced, resulting in less RBD-specific MBCs compared with SARS-CoV-2-recovered individuals 12 months after infection (7.8 and 3 times less than S-CoV and M-CoV, respectively) and 2 months after the boost (18.2 and 6 times less than S-CoV and M-CoV, respectively).

As reported previously, most sera of SARS-CoV-2-recovered individuals efficiently neutralized the B.1.351 variant after the mRNA vaccine, which contrasted with the significant lower neutralization potency of the sera of naive vaccinated individuals (Goel et al., 2021a; Reynolds et al., 2021; Stamatos et al., 2021; Wang et al., 2021b). This likely reflects the quality and maturation of the B cell pool mobilized by the vaccine; i.e., an extrafollicular response in naive vaccinees and a mature MBC response in recovered individuals.

A fraction of recurrent and convergent  $V_H$  genes of MBCs failed to recognize the B.1.351 variant RBD in both cohorts, but a large proportion of clones retained high affinity against this variant. This is consistent with a recent report showing that B cell clones expressing potent antibodies are retained selectively in the repertoire over time (Wang et al., 2021b). This phenomenon occurs independent of the mutational load, with high-affinity clones against variants present “randomly” in the MBC repertoire of SARS-CoV-2-recovered or naive individuals. So, despite the fact that the amplitude and quality of the MBC response after the mRNA vaccine appears to be lower in naive than in previously infected individuals, high-affinity clones with neutralizing potency against VOCs settle in their repertoire, suggesting that their MBC pool could compensate for the time-dependent decay of the initial antibody response.

Correlation of neutralization and affinity shows a complex profile for antibodies expressed by MBCs. Immune escape can affect high-affinity clones against the WT RBD, but, at the same time, a proportion of clones with high affinity for the WT RBD maintain neutralizing potency against B.1.351, contrasting with clones with low or weak affinity that constantly failed to neutralize variants. It indicates that high affinity provides some flexibility for antibodies to cope with mutations affecting their binding target and to conserve their neutralization potency. Consistent with a structural analysis (Yuan et al., 2021), determination of targeted epitopes using binding of different RBDs of VOCs shows that E484 preferentially affected the binding affinity of the IGHV1-2/1-69 genes and K417N and N501Y that of IGHV3-53/3-66 and IGHV1-2. It underlines that, if particular antibody lineages are affected by RBD mutations, then others may retain neutralizing properties (Barnes et al., 2020; Greaney et al., 2021a, 2021b; Muecksch et al., 2021; Scheid et al., 2021; Wang et al., 2021b).

These data describe an immune response maturing with time in SARS-CoV-2 convalescent individuals and resulting in a massive, high-affinity response after vaccination, which, even imprinted by the Wuhan-type RBD, displays improved recognition of the RBD variants as well. In this immune evolution scheme, the response of naive vaccinees nevertheless lags behind the maturation process that took place during infection. As proposed recently, vaccinated individuals will further improve the affinity and diversity of their MBC response with time and, therefore, probably also improve their quantitative and qualitative antibody response through persistence of vaccine-induced germinal centers (Cho et al., 2021; Goel et al., 2021b; Turner et al., 2021). Nonetheless, our observations in SARS-CoV-2-recovered individuals suggest that repeated challenges, even using the original S protein, will help to reduce any persisting differences and allow vaccinated people to respond more efficiently to current SARS-CoV-2 variants by recall of affinity-matured MBCs.

## LIMITATIONS OF THE STUDY

The relatively small size and the limited follow-up of the cohorts do not allow us to identify characteristics of the individuals that would predict the response to the mRNA vaccine and its persistence. Furthermore, individuals with a severe form of COVID-19 were not matched for age and comorbidities with those who presented a mild form or with naive individuals; thus, differences between these groups must be interpreted with caution. Finally, we focused our study on the RBD domain of the SARS-CoV-2 S protein as it represents the major known target for neutralizing antibodies. However, neutralizing antibodies against other domains of the trimeric S have been described, notably against the N-terminal domain (NTD). Larger cohorts of individuals with a wider spectrum of age and comorbidities, extended follow-up (up to 6 months or more), and dedicated studies of non-RBD-specific neutralizing MBCs would be important in the future to provide a comprehensive picture of B cell memory responses directed against VOCs after mRNA vaccination.

## STAR★METHODS

Detailed methods are provided in the online version of this paper and include the following:

- **KEY RESOURCES TABLE**
- **RESOURCE AVAILABILITY**
  - Lead contact
  - Materials availability
  - Data and code availability
- **EXPERIMENTAL MODEL AND SUBJECT DETAILS**
  - Study participants
  - Virus strains
- **METHOD DETAILS**
  - Anti-RBD (S) SARS-CoV-2 antibodies assay
  - Recombinant protein purification
  - Flow cytometry and cell sorting
  - Single-cell culture
  - ELISA
  - Single-cell IgH sequencing
  - Computational analyses of VDJ sequences
  - 3D representation of known mutations to the RBD surface
  - Affinity measurement using biolayer interferometry (Octet)
  - Virus neutralization assay
- **QUANTIFICATION AND STATISTICAL ANALYSIS**
- **ADDITIONAL RESOURCES**

#### SUPPLEMENTAL INFORMATION

Supplemental information can be found online at <https://doi.org/10.1016/j.immuni.2021.09.011>.

#### ACKNOWLEDGMENTS

We thank Garnett Kelsoe for providing the human cell culture system and invaluable advice. We thank A. Bouchartat and the Chemogenomic and Biological screening core facility headed by F. Agou as well as P. England and the Molecular Biophysics core facility at the Institut Pasteur, Paris, France for support during the course of this work. We also thank Sébastien Storck, Lucie Da Silva, and Sandra Weller for advices and support and the physicians, Constance Guillaud, Raphael Lepeule, Frédéric Schlemmer, Elena Foïs, Henri Guillet, Nicolas De Prost, and Pascal Lim, whose patients were included in this study. The graphical abstract and **Figures 1A** and **S4A** were created using BioRender. This work was initiated by a grant from the Agence Nationale de la Recherche and the Fondation pour la Recherche Médicale (ANR; MEMO-COV-2 -FRM) and funded by the Fondation Princesse Grace and by an ERC Advanced Investigator Grant (B-response). Assistance Publique – Hôpitaux de Paris (AP-HP; Département de la Recherche Clinique et du Développement) was the promotor and the sponsor of MEMO-COV-2. Work in the Unit of Structural Virology was funded by the Institut Pasteur Urgence COVID-19 Fundraising Campaign. A.S. was supported by a Poste d'Accueil from the Institut National de la Santé et de la Recherche Médicale (INSERM), I.F. by a fellowship from the Agence Nationale de Recherches sur le Sida et les Hépatites Virales (ANRS), M.B. by a CIFRE fellowship from the Association Nationale de la Recherche et de la Technologie (ANRT), and A.d.L.S. by a SNFMI fellowship. P.B. acknowledges funding from ANR (ANR-14-CE16-0011-DROPmAbs), the Institut Carnot Pasteur Microbes et Santé (ANR 11 CARN 0017-01), the Institut Pasteur, and INSERM.

#### AUTHOR CONTRIBUTIONS

Conceptualization, P.C., A.S., J.-C.W., C.-A.R., and M. Mahévas; data curation, P.C., A.S., M.B., G.B.-S., and I.A.; formal analysis, A.S., P.C., M.B., G.B.-S., I.A., M.B.-A., A.d.L.S., A.V., S. Fourati., and I.F.; funding acquisition, S. Fillatreau., J.-C.W., C.-A.R., and M. Mahévas; investigation, A.S., P.C., A.d.L.S., I.A., and A.V.; methodology, A.S., J.-C.W., C.-A.R., P.C., and M. Mahévas; project administration, P.C., F.C.-P., J.-C.W., C.-A.R., and M. Mahé-

vas; resources, J.-M.P., F.N.-P., S. Fourati., E.C., L.L., M. Michel, B.G., S.G., G.M., Y.N., V.Z., P.B., F.A.R., C.-A.R., and M. Mahévas; software, P.C.; supervision, P.C., J.-C.W., C.-A.R., P.B., F.R., and M. Mahévas; validation, A.S., I.A., A.V., A.d.L.S., M.B., C.-A.R., P.C., and M. Mahévas; visualization, P.C., A.S., I.A., A.d.L.S., and M. Mahévas; writing – original draft, P.C., A.S., J.-C.W., C.-A.R., and M. Mahévas; writing – review & editing, all authors.

#### DECLARATION OF INTERESTS

Outside of the submitted work, M. Mahévas. received research funds from GSK and personal fees from LFB and Amgen. J.-C.W. received consulting fees from Institut Mérieux. P.B. received consulting fees from Regeneron Pharmaceuticals. J.-M.P. received personal fees from Abbvie, Gilead, Merck, and Siemens Healthcare. F.R. is a member of the board of MELETIOS Therapeutics and of the Scientific Advisory Board of eureKARE.

Received: June 17, 2021

Revised: August 5, 2021

Accepted: September 14, 2021

Published: September 21, 2021

#### REFERENCES

- Abu-Raddad, L.J., Chemaitelly, H., and Butt, A.A.; National Study Group for COVID-19 Vaccination (2021). Effectiveness of the BNT162b2 Covid-19 Vaccine against the B.1.1.7 and B.1.351 Variants. *N. Engl. J. Med.* **385**, 187–189.
- Andrews, S.F., Huang, Y., Kaur, K., Popova, L.I., Ho, I.Y., Pauli, N.T., Henry Dunand, C.J., Taylor, W.M., Lim, S., Huang, M., et al. (2015). Immune history profoundly affects broadly protective B cell responses to influenza. *Sci. Transl. Med.* **7**, 316ra192.
- Baden, L.R., El Sahly, H.M., Essink, B., Kotloff, K., Frey, S., Novak, R., Diemert, D., Spector, S.A., Rouphael, N., Creech, C.B., et al.; COVE Study Group (2021). Efficacy and Safety of the mRNA-1273 SARS-CoV-2 Vaccine. *N. Engl. J. Med.* **384**, 403–416.
- Barnes, C.O., West, A.P., Jr., Huey-Tubman, K.E., Hoffmann, M.A.G., Sharaf, N.G., Hoffman, P.R., Koranda, N., Gristick, H.B., Gaebler, C., Muecksch, F., et al. (2020). Structures of Human Antibodies Bound to SARS-CoV-2 Spike Reveal Common Epitopes and Recurrent Features of Antibodies. *Cell* **182**, 828–842.e16.
- Cai, Y., Zhang, J., Xiao, T., Peng, H., Sterling, S.M., Walsh, R.M., Jr., Rawson, S., Rits-Volloch, S., and Chen, B. (2020). Distinct conformational states of SARS-CoV-2 spike protein. *Science* **369**, 1586–1592.
- Cele, S., Gazy, I., Jackson, L., Hwa, S.-H., Tegally, H., Lustig, G., Giandhari, J., Pillay, S., Wilkinson, E., Naidoo, Y., et al.; Network for Genomic Surveillance in South Africa; COMMIT-KZN Team (2021). Escape of SARS-CoV-2 501Y.V2 from neutralization by convalescent plasma. *Nature* **593**, 142–146.
- Cherian, S., Potdar, V., Jadhav, S., Yadav, P., Gupta, N., Das, M., Das, S., Agarwal, A., Singh, S., Abraham, P., et al. (2021). Convergent evolution of SARS-CoV-2 spike mutations, L452R, E484Q and P681R, in the second wave of COVID-19 in Maharashtra, India. *bioRxiv*. <https://doi.org/10.1101/2021.04.22.440932>.
- Cho, A., Muecksch, F., Schaefer-Babajew, D., Wang, Z., Finkin, S., Gaebler, C., Ramos, V., Cipolla, M., Agudelo, M., Bednarski, E., et al. (2021). Antibody Evolution after SARS-CoV-2 mRNA Vaccination. *bioRxiv*. <https://doi.org/10.1101/2021.07.29.454333>.
- Crickx, E., Chappert, P., Sokal, A., Weller, S., Azzaoui, I., Vandenberghe, A., Bonnard, G., Rossi, G., Fadeev, T., Storck, S., et al. (2021). Rituximab-resistant splenic memory B cells and newly engaged naive B cells fuel relapses in patients with immune thrombocytopenia. *Sci. Transl. Med.* **13**, eabc3961.
- Dagan, N., Barda, N., Kepten, E., Miron, O., Perchik, S., Katz, M.A., Hernán, M.A., Lipsitch, M., Reis, B., and Balicer, R.D. (2021). BNT162b2 mRNA Covid-19 Vaccine in a Nationwide Mass Vaccination Setting. *N. Engl. J. Med.* **384**, 1412–1423.
- Davies, N.G., Abbott, S., Barnard, R.C., Jarvis, C.I., Kucharski, A.J., Munday, J.D., Pearson, C.A.B., Russell, T.W., Tully, D.C., Washburne, A.D., et al.;

- CMMID COVID-19 Working Group; COVID-19 Genomics UK (COG-UK) Consortium (2021). Estimated transmissibility and impact of SARS-CoV-2 lineage B.1.1.7 in England. *Science* 372, eabg3055.
- Dugan, H.L., Stamper, C.T., Li, L., Changrob, S., Asby, N.W., Halfmann, P.J., Zheng, N.-Y., Huang, M., Shaw, D.G., Cobb, M.S., et al. (2021). Profiling B cell immunodominance after SARS-CoV-2 infection reveals antibody evolution to non-neutralizing viral targets. *Immunity* 54, 1290–1303.e7.
- Ebinger, J.E., Fert-Bober, J., Printsev, I., Wu, M., Sun, N., Prostko, J.C., Frias, E.C., Stewart, J.L., Van Eyk, J.E., Braun, J.G., et al. (2021). Antibody responses to the BNT162b2 mRNA vaccine in individuals previously infected with SARS-CoV-2. *Nat. Med.* 27, 981–984.
- Edara, V.V., Norwood, C., Floyd, K., Lai, L., Davis-Gardner, M.E., Hudson, W.H., Mantis, G., Nyhoff, L.E., Adelman, M.W., Fineman, R., et al. (2021). Infection- and vaccine-induced antibody binding and neutralization of the B.1.351 SARS-CoV-2 variant. *Cell Host Microbe* 29, 516–521.e3.
- Ellebedy, A.H., Jackson, K.J.L., Kissick, H.T., Nakaya, H.I., Davis, C.W., Roskin, K.M., McElroy, A.K., Oshansky, C.M., Elbein, R., Thomas, S., et al. (2016). Defining antigen-specific plasmablast and memory B cell subsets in human blood after viral infection or vaccination. *Nat Immunol.* 17, 1226–1234.
- Gaebler, C., Wang, Z., Lorenzi, J.C.C., Muecksch, F., Finkin, S., Tokuyama, M., Cho, A., Jankovic, M., Schaefer-Babajew, D., Oliveira, T.Y., et al. (2021). Evolution of antibody immunity to SARS-CoV-2. *Nature* 597, 639–644.
- Garcia-Beltran, W.F., Lam, E.C., St Denis, K., Nitido, A.D., Garcia, Z.H., Hauser, B.M., Feldman, J., Pavlovic, M.N., Gregory, D.J., Poznansky, M.C., et al. (2021). Multiple SARS-CoV-2 variants escape neutralization by vaccine-induced humoral immunity. *Cell* 184, 2372–2383.e9.
- Goel, R.R., Apostolidis, S.A., Painter, M.M., Mathew, D., Pattekar, A., Kuthuru, O., Gouma, S., Hicks, P., Meng, W., Rosenfeld, A.M., et al. (2021a). Distinct antibody and memory B cell responses in SARS-CoV-2 naïve and recovered individuals following mRNA vaccination. *Sci. Immunol.* 6, eabi6950.
- Goel, R.R., Painter, M.M., Apostolidis, S.A., Mathew, D., Meng, W., Rosenfeld, A.M., Lundgreen, K.A., Reynaldi, A., Khoury, D.S., Pattekar, A., et al. (2021b). mRNA Vaccination Induces Durable Immune Memory to SARS-CoV-2 with Continued Evolution to Variants of Concern. *bioRxiv*. <https://doi.org/10.1101/2021.08.23.457229>.
- Greaney, A.J., Loes, A.N., Crawford, K.H.D., Starr, T.N., Malone, K.D., Chu, H.Y., and Bloom, J.D. (2021a). Comprehensive mapping of mutations in the SARS-CoV-2 receptor-binding domain that affect recognition by polyclonal human plasma antibodies. *Cell Host Microbe* 29, 463–476.e6.
- Greaney, A.J., Starr, T.N., Barnes, C.O., Weisblum, Y., Schmidt, F., Caskey, M., Gaebler, C., Cho, A., Agudelo, M., Finkin, S., et al. (2021b). Mapping mutations to the SARS-CoV-2 RBD that escape binding by different classes of antibodies. *Nat. Commun.* 12, 4196.
- Gupta, N.T., Vander Heiden, J.A., Uduman, M., Gadala-Maria, D., Yaari, G., and Kleinstein, S.H. (2015). Change-O: a toolkit for analyzing large-scale B cell immunoglobulin repertoire sequencing data. *Bioinformatics* 31, 3356–3358.
- Hacisuleyman, E., Hale, C., Saito, Y., Blachere, N.E., Bergh, M., Conlon, E.G., Schaefer-Babajew, D.J., DaSilva, J., Muecksch, F., Gaebler, C., et al. (2021). Vaccine Breakthrough Infections with SARS-CoV-2 Variants. *N. Engl. J. Med.* 384, 2212–2218.
- Harvey, W.T., Carabelli, A.M., Jackson, B., Gupta, R.K., Thomson, E.C., Harrison, E.M., Ludden, C., Reeve, R., Rambaut, A., Peacock, S.J., and Robertson, D.L.; COVID-19 Genomics UK (COG-UK) Consortium (2021). SARS-CoV-2 variants, spike mutations and immune escape. *Nat. Rev. Microbiol.* 19, 409–424.
- Hoffmann, M., Arora, P., Groß, R., Seidel, A., Hörnich, B.F., Hahn, A.S., Krüger, N., Graichen, L., Hofmann-Winkler, H., Kempf, A., et al. (2021). SARS-CoV-2 variants B.1.351 and P.1 escape from neutralizing antibodies. *Cell* 184, 2384–2393.e12.
- Hsieh, C.-L., Goldsmith, J.A., Schaub, J.M., DiVenere, A.M., Kuo, H.-C., Javanmardi, K., Le, K.C., Wrapp, D., Lee, A.G., Liu, Y., et al. (2020). Structure-based design of prefusion-stabilized SARS-CoV-2 spikes. *Science* 369, 1501–1505.
- Ju, B., Zhang, Q., Ge, J., Wang, R., Sun, J., Ge, X., Yu, J., Shan, S., Zhou, B., Song, S., et al. (2020). Human neutralizing antibodies elicited by SARS-CoV-2 infection. *Nature* 584, 115–119.
- Konstantinidis, T.G., Zisaki, S., Mitroulis, I., Konstantinidou, E., Kontekaki, E.G., Romanidou, G., Karvelas, A., Nanousi, I., Lazidis, L., Cassimos, D., et al. (2021). Levels of Produced Antibodies after Vaccination with mRNA Vaccine; Effect of Previous Infection with SARS-CoV-2. *J. Clin. Med.* 10, 2842.
- Krammer, F., Srivastava, K., Alshammary, H., Amoako, A.A., Awawda, M.H., Beach, K.F., Bermúdez-González, M.C., Bielak, D.A., Carreño, J.M., Chernet, R.L., et al. (2021). Antibody Responses in Seropositive Persons after a Single Dose of SARS-CoV-2 mRNA Vaccine. *N. Engl. J. Med.* 384, 1372–1374.
- Lad, L., Clancy, S., Kovalenko, M., Liu, C., Hui, T., Smith, V., and Pragrats, N. (2015). High-throughput kinetic screening of hybridomas to identify high-affinity antibodies using bio-layer interferometry. *J. Biomol. Screen.* 20, 498–507.
- Luo, X.M., Maarschalk, E., O’Connell, R.M., Wang, P., Yang, L., and Baltimore, D. (2009). Engineering human hematopoietic stem/progenitor cells to produce a broadly neutralizing anti-HIV antibody after in vitro maturation to human B lymphocytes. *Blood* 113, 1422–1431.
- Manisty, C., Otter, A.D., Treibel, T.A., McKnight, Á., Altmann, D.M., Brooks, T., Noursadeghi, M., Boyton, R.J., Semper, A., and Moon, J.C. (2021). Antibody response to first BNT162b2 dose in previously SARS-CoV-2-infected individuals. *Lancet* 397, 1057–1058.
- McCallum, M., De Marco, A., Lempp, F.A., Tortorici, M.A., Pinto, D., Walls, A.C., Beltramello, M., Chen, A., Liu, Z., Zatta, F., et al. (2021). N-terminal domain antigenic mapping reveals a site of vulnerability for SARS-CoV-2. *Cell* 184, 2332–2347.e16.
- Mesin, L., Schiepers, A., Ersching, J., Barbulescu, A., Cavazzoni, C.B., Angelini, A., Okada, T., Kurosaki, T., and Victoria, G.D. (2020). Restricted Clonality and Limited Germinal Center Reentry Characterize Memory B Cell Reactivation by Boosting. *Cell* 180, 92–106.e11.
- Muecksch, F., Weisblum, Y., Barnes, C.O., Schmidt, F., Schaefer-Babajew, D., Lorenzi, J.C.C., Flyak, A.I., DeLaitch, A.T., Huey-Tubman, K.E., Hou, S., et al. (2021). Affinity maturation of SARS-CoV-2 neutralizing antibodies confers potency, breadth, and resilience to viral escape mutations. *Immunity* 54, 1853–1868.e7.
- Planas, D., Bruel, T., Grzelak, L., Guivel-Benhassine, F., Staropoli, I., Porrot, F., Planchais, C., Buchrieser, J., Rajah, M.M., Bishop, E., et al. (2021a). Sensitivity of infectious SARS-CoV-2 B.1.1.7 and B.1.351 variants to neutralizing antibodies. *Nat. Med.* 27, 917–924.
- Planas, D., Veyer, D., Baidaliuk, A., Staropoli, I., Guivel-Benhassine, F., Rajah, M.M., Planchais, C., Porrot, F., Robillard, N., Puech, J., et al. (2021b). Reduced sensitivity of SARS-CoV-2 variant Delta to antibody neutralization. *Nature* 596, 276–280.
- Plante, J.A., Liu, Y., Liu, J., Xia, H., Johnson, B.A., Lokugamage, K.G., Zhang, X., Muruato, A.E., Zou, J., Fontes-Garfias, C.R., et al. (2021). Spike mutation D614G alters SARS-CoV-2 fitness. *Nature* 592, 116–121.
- Polack, F.P., Thomas, S.J., Kitchin, N., Absalon, J., Gurtman, A., Lockhart, S., Perez, J.L., Pérez Marc, G., Moreira, E.D., Zerbini, C., et al.; C4591001 Clinical Trial Group (2020). Safety and Efficacy of the BNT162b2 mRNA Covid-19 Vaccine. *N. Engl. J. Med.* 383, 2603–2615.
- Purtha, W.E., Tedder, T.F., Johnson, S., Bhattacharya, D., and Diamond, M.S. (2011). Memory B cells, but not long-lived plasma cells, possess antigen specificities for viral escape mutants. *J. Exp. Med.* 208, 2599–2606.
- Reynolds, C.J., Pade, C., Gibbons, J.M., Butler, D.K., Otter, A.D., Menacho, K., Fontana, M., Smit, A., Sackville-West, J.E., Cutino-Moguel, T., et al.; UK COVIDsortium Immune Correlates Network; UK COVIDsortium Investigators (2021). Prior SARS-CoV-2 infection rescues B and T cell responses to variants after first vaccine dose. *Science*, eabh1282.
- Robbiani, D.F., Gaebler, C., Muecksch, F., Lorenzi, J.C.C., Wang, Z., Cho, A., Agudelo, M., Barnes, C.O., Gazumyan, A., Finkin, S., et al. (2020). Convergent antibody responses to SARS-CoV-2 in convalescent individuals. *Nature* 584, 437–442.

- Rodda, L.B., Netland, J., Shehata, L., Pruner, K.B., Morawski, P.A., Thouvenel, C.D., Takehara, K.K., Eggenberger, J., Hemann, E.A., Waterman, H.R., et al. (2021). Functional SARS-CoV-2-Specific Immune Memory Persists after Mild COVID-19. *Cell* 184, 169–183.e17.
- Saadat, S., Rikhtegar Tehrani, Z., Logue, J., Newman, M., Frieman, M.B., Harris, A.D., and Sajadi, M.M. (2021). Binding and Neutralization Antibody Titers After a Single Vaccine Dose in Health Care Workers Previously Infected With SARS-CoV-2. *JAMA* 325, 1467–1469.
- Sakharkar, M., Rappazzo, C.G., Wieland-Alter, W.F., Hsieh, C.-L., Wrapp, D., Esterman, E.S., Kaku, C.I., Wec, A.Z., Geoghegan, J.C., McLellan, J.S., et al. (2021). Prolonged evolution of the human B cell response to SARS-CoV-2 infection. *Sci. Immunol.* 6, eabg6916.
- Samanovic, M.I., Cornelius, A.R., Wilson, J.P., Karmacharya, T., Gray-Gaillard, S.L., Allen, J.R., Hyman, S.W., Moritz, G., Ali, M., Korolov, S.B., et al. (2021). Poor antigen-specific responses to the second BNT162b2 mRNA vaccine dose in SARS-CoV-2-experienced individuals. *medRxiv*. <https://doi.org/10.1101/2021.02.07.21251311>.
- Scheid, J.F., Barnes, C.O., Eraslan, B., Hudak, A., Keeffe, J.R., Cosimi, L.A., Brown, E.M., Muecksch, F., Weisblum, Y., Zhang, S., et al. (2021). B cell genomics behind cross-neutralization of SARS-CoV-2 variants and SARS-CoV. *Cell* 184, 3205–3221.e24.
- Sokal, A., Chappert, P., Barba-Spaeth, G., Roeser, A., Fourati, S., Azaoui, I., Vandenberghe, A., Fernandez, I., Meola, A., Bouvier-Alias, M., et al. (2021). Maturation and persistence of the anti-SARS-CoV-2 memory B cell response. *Cell* 184, 1201–1213.e14.
- Stamatatos, L., Czartoski, J., Wan, Y.-H., Homad, L.J., Rubin, V., Glantz, H., Neradilek, M., Seydoux, E., Jennewein, M.F., MacCamy, A.J., et al. (2021). mRNA vaccination boosts cross-variant neutralizing antibodies elicited by SARS-CoV-2 infection. *Science*, eabg9175.
- Starr, T.N., Greaney, A.J., Dingens, A.S., and Bloom, J.D. (2021). Complete map of SARS-CoV-2 RBD mutations that escape the monoclonal antibody LY-CoV555 and its cocktail with LY-CoV016. *Cell Rep Med* 2, 100255.
- Supasa, P., Zhou, D., Dejnirattaisai, W., Liu, C., Mentzer, A.J., Ginn, H.M., Zhao, Y., Duyvesteyn, H.M.E., Nutalai, R., Tuekprakhon, A., et al. (2021). Reduced neutralization of SARS-CoV-2 B.1.1.7 variant by convalescent and vaccine sera. *Cell* 184, 2201–2211.e7.
- Tegally, H., Wilkinson, E., Giovanetti, M., Iranzadeh, A., Fonseca, V., Giandhari, J., Doolabh, D., Pillay, S., San, E.J., Msomi, N., et al. (2021). Detection of a SARS-CoV-2 variant of concern in South Africa. *Nature* 592, 438–443.
- Tiller, T., Meffre, E., Yurasov, S., Tsuiji, M., Nussenzweig, M.C., and Wardemann, H. (2008). Efficient generation of monoclonal antibodies from single human B cells by single cell RT-PCR and expression vector cloning. *J. Immunol. Methods* 329, 112–124.
- Tong, P., Gautam, A., Windsor, I.W., Travers, M., Chen, Y., Garcia, N., Whiteman, N.B., McKay, L.G.A., Storm, N., Malsick, L.E., et al. (2021). Memory B cell repertoire for recognition of evolving SARS-CoV-2 spike. *Cell* 184, 4969–4980.
- Turner, J.S., O'Halloran, J.A., Kalaidina, E., Kim, W., Schmitz, A.J., Zhou, J.Q., Lei, T., Thapa, M., Chen, R.E., Case, J.B., et al. (2021). SARS-CoV-2 mRNA vaccines induce persistent human germinal centre responses. *Nature* 596, 109–113.
- Wang, P., Nair, M.S., Liu, L., Iketani, S., Luo, Y., Guo, Y., Wang, M., Yu, J., Zhang, B., Kwong, P.D., et al. (2021a). Antibody resistance of SARS-CoV-2 variants B.1.351 and B.1.1.7. *Nature* 593, 130–135.
- Wang, Z., Muecksch, F., Schaefer-Babajew, D., Finkin, S., Viant, C., Gaebler, C., Hoffmann, H.-H., Barnes, C.O., Cipolla, M., Ramos, V., et al. (2021b). Naturally enhanced neutralizing breadth against SARS-CoV-2 one year after infection. *Nature* 595, 426–431.
- Weisel, F.J., Zuccarino-Catania, G.V., Chikina, M., and Shlomchik, M.J. (2016). A Temporal Switch in the Germinal Center Determines Differential Output of Memory B and Plasma Cells. *Immunity* 44, 116–130.
- Weissman, D., Alameh, M.-G., de Silva, T., Collini, P., Hornsby, H., Brown, R., LaBranche, C.C., Edwards, R.J., Sutherland, L., Santra, S., et al. (2021). D614G Spike Mutation Increases SARS CoV-2 Susceptibility to Neutralization. *Cell Host Microbe* 29, 23–31.e4.
- Woodruff, M.C., Ramonell, R.P., Nguyen, D.C., Cashman, K.S., Saini, A.S., Haddad, N.S., Ley, A.M., Kyu, S., Howell, J.C., Ozturk, T., et al. (2020). Extrafollicular B cell responses correlate with neutralizing antibodies and morbidity in COVID-19. *Nat. Immunol.* 21, 1506–1516.
- Xie, X., Liu, Y., Liu, J., Zhang, X., Zou, J., Fontes-Garfias, C.R., Xia, H., Swanson, K.A., Cutler, M., Cooper, D., et al. (2021). Neutralization of SARS-CoV-2 spike 69/70 deletion, E484K and N501Y variants by BNT162b2 vaccine-elicited sera. *Nat. Med.* 27, 620–621.
- Yuan, M., Huang, D., Lee, C.D., Wu, N.C., Jackson, A.M., Zhu, X., Liu, H., Peng, L., van Gils, M.J., Sanders, R.W., et al. (2021). Structural and functional ramifications of antigenic drift in recent SARS-CoV-2 variants. *Science* 373, 818–823.
- Yurkovetskiy, L., Wang, X., Pascal, K.E., Tomkins-Tinch, C., Nyalile, T.P., Wang, Y., Baum, A., Diehl, W.E., Dauphin, A., Carbone, C., et al. (2020). Structural and Functional Analysis of the D614G SARS-CoV-2 Spike Protein Variant. *Cell* 183, 739–751.e8.

# ARTICLE 3

## **ARTICLE 3**

### **Characterization of Vaccinee Bmem-derived Ab affinities towards Omicron RBD**

Following my collaboration for the work published in Sokal et al. (2021)<sup>129</sup>, I also continued this collaboration with the group of Immune System Development at Institut Necker Enfants Malades (INEM) directed by Dr Matthieu Mahévas in December 2021 to assess the affinities and binding behaviors of the previously characterized antibodies towards the Omicron variant RBD. In the following section I have included the published manuscript (Sokal et al. 2022)<sup>130</sup> of this work, for which I am a co-first author.

We had previously shown that the proportions of RBD-specific antibodies, high affinity antibodies, and neutralizing antibodies are reduced as the SARS-CoV-2 RBD accumulates mutations. The emergence of the Omicron variant caused great concern due to its large mutational leap compared to previous variants. We therefore sought to use our existing “bank” of vaccinee-derived anti-RBD antibodies to characterize the extent of the immune escape caused by Omicron mutations as well as potential global changes in binding affinities. My contribution to this manuscript was to characterize by BLI (Octet HTX) the affinity of our approximately 600 antibody panel towards Omicron RBD.

## Article

# Analysis of mRNA vaccination-elicited RBD-specific memory B cells reveals strong but incomplete immune escape of the SARS-CoV-2 Omicron variant

Aurélien Sokal,<sup>1,14</sup> Matteo Broketa,<sup>2,14</sup> Giovanna Barba-Spaeth,<sup>3,14</sup> Annalisa Meola,<sup>3,14</sup> Ignacio Fernández,<sup>3,15</sup> Slim Fourati,<sup>4,5,15</sup> Imane Azzaoui,<sup>6,7,15</sup> Andrea de La Selle,<sup>1,6,15</sup> Alexis Vandenberghe,<sup>6,7,15</sup> Anais Roeser,<sup>1,6</sup> Magali Bouvier-Alias,<sup>4,5</sup> Etienne Crickx,<sup>1,6</sup> Laetitia Languille,<sup>6</sup> Marc Michel,<sup>6</sup> Bertrand Godeau,<sup>6</sup> Sébastien Gallien,<sup>8</sup> Giovanna Melica,<sup>8</sup> Yann Nguyen,<sup>9</sup> Virginie Zarrouk,<sup>9</sup> Florence Canoui-Poitrine,<sup>10</sup> France Noizat-Pirenne,<sup>7,11</sup> Jérôme Megret,<sup>12</sup> Jean-Michel Pawlotsky,<sup>4,5</sup> Simon Fillatreau,<sup>1</sup> Etienne Simon-Lorière,<sup>13</sup> Jean-Claude Weill,<sup>1,16</sup> Claude-Agnès Reynaud,<sup>1,16</sup> Félix A. Rey,<sup>3,16</sup> Pierre Bruhns,<sup>2,16</sup> Pascal Chappert,<sup>1,7,16,\*</sup> and Matthieu Mahévas<sup>1,6,7,16,17,\*</sup>

<sup>1</sup>Institut Necker Enfants Malades (INEM), INSERM U1151/CNRS UMR 8253, Université Paris Cité, Paris, France

<sup>2</sup>Institut Pasteur, Université Paris Cité, INSERM UMR1222, Unit of Antibodies in Therapy and Pathology, Paris, France

<sup>3</sup>Institut Pasteur, Université Paris Cité, CNRS UMR 3569, Unité de Virologie Structurale, Paris, France

<sup>4</sup>Département de Virologie, Bactériologie, Hygiène et Mycologie-Parasitologie, Centre Hospitalier Universitaire Henri-Mondor, Assistance Publique-Hôpitaux de Paris (AP-HP), Créteil, France

<sup>5</sup>INSERM U955, équipe 18, Institut Mondor de Recherche Biomédicale (IMRB), Université Paris-Est Créteil (UPEC), Créteil, France

<sup>6</sup>Service de Médecine Interne, Centre Hospitalier Universitaire Henri-Mondor, Publique-Hôpitaux de Paris (AP-HP), Université Paris-Est Créteil, Créteil, France

<sup>7</sup>INSERM U955, équipe 2, Institut Mondor de Recherche Biomédicale (IMRB), Université Paris-Est Créteil, Créteil, France

<sup>8</sup>Service de Maladies Infectieuses, Centre Hospitalier Universitaire Henri-Mondor, Assistance Publique-Hôpitaux de Paris (AP-HP), Université Paris-Est Créteil (UPEC), Créteil, France

<sup>9</sup>Service de Médecine interne, Hôpital Beaujon, Assistance Publique-Hôpitaux de Paris, Université de Paris, Clichy, France

<sup>10</sup>Département de Santé Publique, Unité de Recherche Clinique (URC), CEpiA (Clinical Epidemiology and Ageing), EA 7376, Institut Mondor de Recherche Biomédicale (IMRB), Centre Hospitalier Universitaire Henri-Mondor, Assistance Publique-Hôpitaux de Paris (AP-HP), Université Paris-Est Créteil (UPEC), Créteil, France

<sup>11</sup>Etablissement Français du Sang (EFS) Ile de France, Créteil, France

<sup>12</sup>Plateforme de Cytométrie en Flux, Structure Fédérative de Recherche Necker, INSERM US24-CNRS UMS3633, Paris, France

<sup>13</sup>Institut Pasteur, Evolutionary genomics of RNA viruses, Université Paris Cité, Paris, France

<sup>14</sup>These authors contributed equally

<sup>15</sup>These authors contributed equally

<sup>16</sup>Senior author

<sup>17</sup>Lead contact

\*Correspondence: [pascal.chappert@inserm.fr](mailto:pascal.chappert@inserm.fr) (P.C.), [matthieu.mahevas@aphp.fr](mailto:matthieu.mahevas@aphp.fr) (M.M.)

<https://doi.org/10.1016/j.immuni.2022.04.002>

## SUMMARY

The SARS-CoV-2 Omicron variant can escape neutralization by vaccine-elicited and convalescent antibodies. Memory B cells (MBCs) represent another layer of protection against SARS-CoV-2, as they persist after infection and vaccination and improve their affinity. Whether MBCs elicited by mRNA vaccines can recognize the Omicron variant remains unclear. We assessed the affinity and neutralization potency against the Omicron variant of several hundred naturally expressed MBC-derived monoclonal IgG antibodies from vaccinated COVID-19-recovered and -naive individuals. Compared with other variants of concern, Omicron evaded recognition by a larger proportion of MBC-derived antibodies, with only 30% retaining high affinity against the Omicron RBD, and the reduction in neutralization potency was even more pronounced. Nonetheless, neutralizing MBC clones could be found in all the analyzed individuals. Therefore, despite the strong immune escape potential of the Omicron variant, these results suggest that the MBC repertoire generated by mRNA vaccines still provides some protection against the Omicron variant in vaccinated individuals.

## INTRODUCTION

The Omicron variant of SARS-CoV-2 has overcome the previously dominant Delta lineage in most countries, suggesting a

strong selective advantage. The spike protein of SARS-CoV-2 Omicron harbors 32 mutations as compared with the ancestral strain (Hu-1) originally identified in Wuhan, with particular hotspots of mutations in the angiotensinogen-converting enzyme



2 (ACE2) receptor-binding domain (RBD) (15-amino-acid substitutions) and in the N-terminal domain (NTD) (3 deletions, 1 insertion, and 4 substitutions). Of particular concern, the Omicron variant displays not only key mutations previously associated with immune escape (K417N, E484A, and T478K in the RBD) or enhanced infectivity (N501Y, P681H) but also numerous mutations rarely detected in previous variants. SARS-CoV-2 Omicron may have thus emerged after extensive selection based on beneficial combinatorial effects, as was predicted *in silico* for the Q498R mutation, for example (Zahradnik et al., 2021). The overall mutational profile of the Omicron variant thus suggests both increased immune escape and increased infectivity.

Despite sizable immune evasion by some of the previous variants of concern (VOCs), SARS-CoV-2 mRNA vaccines have so far maintained strong protection in recently vaccinated individuals due to an initially broad and strong serum immunoglobulin G (IgG) response. This response is nonetheless waning with time. We and others have been able to show that SARS-CoV-2-specific memory B cells (MBCs) represent a potent layer of additional immune protection (Dugan et al., 2021; Gaebler et al., 2021; Rodda et al., 2021; Sokal et al., 2021a, 2021b). MBCs not only persist after infection but evolve and mature over several months by the progressive acquisition of somatic mutations in their variable region genes to improve affinity through an ongoing germinal center response (Gaebler et al., 2021; Rodda et al., 2021; Sokal et al., 2021a, 2021b). MBCs display a diverse repertoire, allowing for an adaptive response upon re-exposure to the pathogen, especially in the case of variants (Purtha et al., 2011; Weisel and Shlomchik, 2017). Upon re-stimulation, either in the context of natural infection or vaccinal boost, MBCs can rapidly differentiate into the plasma cell lineage, secreting the diverse array of high-affinity antibodies contained in their repertoire (Purtha et al., 2011; Weisel and Shlomchik, 2017). A deep analysis of the repertoire of vaccinated individuals has so far suggested that a sizable proportion of such MBCs is able to neutralize all VOCs up to the Beta variant (Sokal et al., 2021b; Wang et al., 2021). Recent reports demonstrate that SARS-CoV-2 Omicron escapes vaccine-elicited antibodies or antibodies from SARS-CoV-2 recovered sera to a large extent (Cameroni et al., 2022; Carreño et al., 2022; Dejnirattisai et al., 2022; Garcia-Beltran et al., 2022; Hoffmann et al., 2022; Muik et al., 2022; Planas et al., 2022). Yet, the intrinsic capacity of the MBC pool to recognize the Omicron variant remains largely unexplored.

## RESULTS

### Omicron RBD evades recognition from a large proportion of MBC-derived monoclonal antibodies from mRNA-vaccinated individuals

We recently performed an in-depth characterization of over 400 single-cell sorted and cultured RBD-specific MBCs isolated from 8 vaccinated SARS-CoV-2 recovered and 3 vaccinated naive individuals (Sokal et al., 2021b). Our analyses included affinity measurements against VOCs and variants of interest (VOIs) (B.1.1.7, Alpha; B.1.351, Beta; P.1, Gamma; B.1.617.2, Delta; and B.1.617.1 Kappa) and neutralization potency against the D614G and Beta SARS-CoV-2 variants. Selected individuals were part of two longitudinal cohorts. 8 SARS-CoV-2-recovered

COVID-19 patients (4 severe [S-CoV] and 4 mild [M-CoV] patients) were selected from the MEMO-COV-2 cohort (Sokal et al., 2021a), which is constituted of patients infected during the first wave in France and longitudinally followed up since, including after their vaccine boost. Additionally, 3 vaccinated SARS-CoV-2-naive subjects were selected from a cohort of healthcare workers, with no clinical history of COVID-19 and no serological evidence of previous SARS-CoV-2 infection. All subjects were vaccinated with the BNT162b2 vaccine as part of the French vaccination program. All the individuals were then sampled for circulating MBCs 7 days and 2 months after their vaccine boost (Sokal et al., 2021b). In all the individuals, we detected a sizable fraction of MBCs encoding antibodies with high affinity and neutralizing potential against all the tested VOCs, with the Beta variant showing the largest extent of immune escape at the time. This suggested that MBCs elicited by prior infection or vaccination would be able to provide an efficient secondary layer of protection in case of the waning of the serological protective antibodies or escape of a novel SARS-CoV-2 variant from this antibody pool.

To test whether such a conclusion still holds true in the context of the newly emerging B.1.1.529 (Omicron) variant, we generated a recombinant Omicron RBD harboring the 15 described mutations, including N501Y, K417T/N, E484K/Q/A, and T478K found in other VOCs and additional mutations G339D, S371L, S373P, S375F, N440K, G446S, S477N, Q493R, G496S, Q498R, and Y505H (Figures 1A and 1B). All the previously described naturally expressed monoclonal IgGs from single-cell culture supernatants of MBCs were assayed anew using biolayer interferometry (BLI) to assess their affinity against the Omicron RBD, and 313 monoclonal supernatants passed quality controls. As previously reported, monoclonal antibodies encoded by MBCs isolated from vaccinated COVID-19-recovered patients and vaccinated naive patients contained a vast majority of high-affinity binders against the ancestral Hu-1 RBD, among which ~50% retained high affinity ( $KD < 10^{-9}$  M) against the Beta and Delta RBD (160/312 and 170/306, respectively). This proportion further decreased against the Omicron RBD to 33% (102/313; Figures 1C and 1D). Importantly, ~40% of the clones showed no detectable or low affinity ( $KD > 10^{-8}$  M) to the Omicron RBD, in both vaccinated recovered and vaccinated naive individuals, which is in line with the prediction that Omicron accumulated numerous mutations associated with antibody evasion. Similar conclusions could be drawn when focusing only on the highly mutated antibodies found in the recovered individuals (Figures 2A and 2B). By contrast, a few clones ( $n = 14$ ) displayed ultra-high affinity toward Omicron ( $KD < 10^{-10}$  M). Overall, this suggests that the result of the affinity maturation process, which takes place in the germinal centers of both infected and vaccinated individuals and selects over time for a narrow range of high-affinity clones ( $KD < 10^{-9}$  M) against the ancestral Hu-1 RBD (Figures 2A–2C), is greatly altered in the context of such a highly mutated variant like Omicron.

### Omicron-specific RBD mutations expand their overall escape of memory B cell-derived antibodies

A direct comparison of binding affinities toward the ancestral Hu-1 RBD and the Omicron RBD variant for all antibodies extensively characterized against other variants showed that

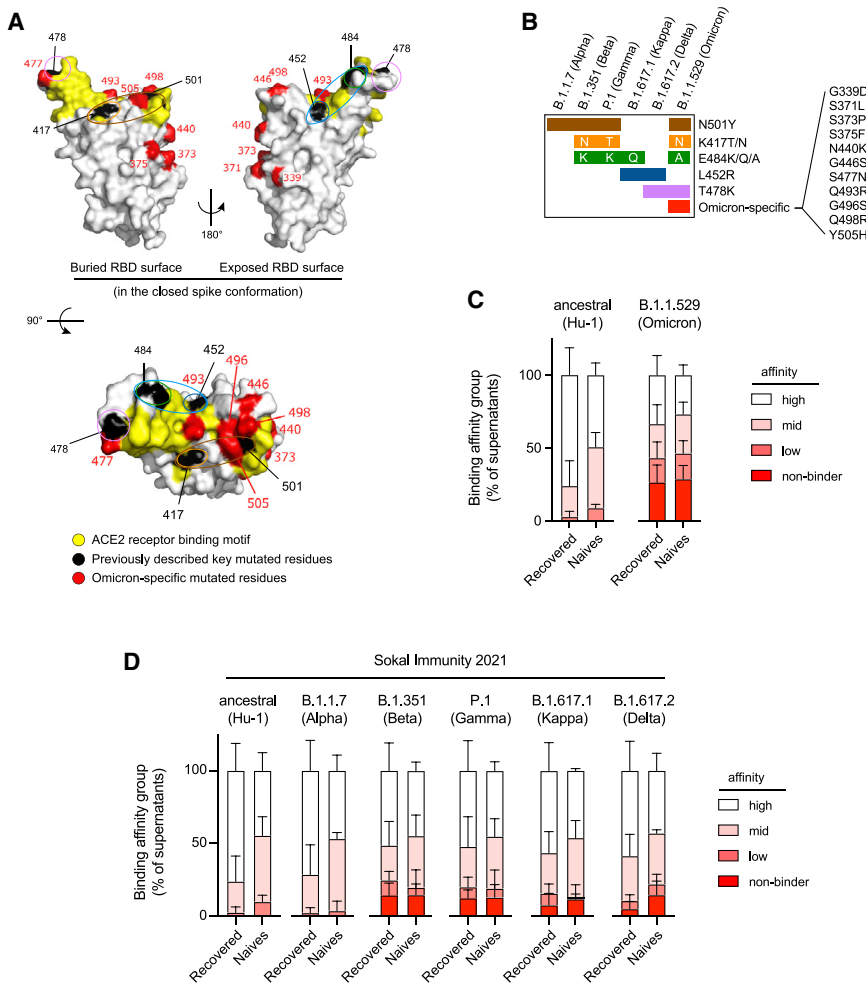


**Figure 1. The memory B cell pool of vaccinated individuals contains a reduced frequency of high-affinity clones against the Omicron RBD**

(A) RBD (extracted from the PDB:6XR8 spike protein trimer structure) shown in three orthogonal views with the ACE2-receptor-binding motif highlighted in yellow and the residues found mutated in at least one of the Alpha, Beta, Gamma, Kappa, or Delta variants (L452, K417, T478, E484, and N501) highlighted in black. Residues specifically mutated in Omicron (G339, S371, S373, N440K, G446, S477, Q493, G496, Q498, and Y505H) are highlighted in red. Single or groups of mutations predicted as key binding residues for particular antibodies are further highlighted by colored ovals according to the color scheme used in (B) and Figure 2B.

(B) The distribution of known mutations in the RBD domain between B.1.1.7 (Alpha), B.1.351 (Beta), P.1 (Gamma), B.1.617.1 (Kappa), B.1.617.2 (Delta), and B.1.1.529 (Omicron) SARS-CoV-2 variants.

(C) Histograms showing the binding affinity distribution of monoclonal antibodies from single-cell culture supernatants of RBD-specific MBCs isolated from vaccinated SARS-CoV-2 recovered (n = 225) and vaccinated naive donors (n = 88) against the ancestral (Hu-1) RBD and the B.1.1.529 (Omicron) RBD variant, defined as follows: high ( $KD < 10^{-9}$  M), mid ( $10^{-9} \leq KD < 10^{-8}$  M), and low ( $10^{-8} \leq KD < 10^{-7}$ ).

(D) Histograms showing the binding affinity distribution of monoclonal antibodies from the same single-cell culture supernatants against the ancestral (Hu-1) RBD and the B.1.351 (Beta), P.1 (Gamma), B.1.617.1 (Kappa), B.1.617.2 (Delta), and B.1.1.529 (Omicron) RBD variants, defined as follows: high ( $KD < 10^{-9}$  M), mid ( $10^{-9} \leq KD < 10^{-8}$  M), and low ( $10^{-8} \leq KD < 10^{-7}$ ).

The clones with  $KD \geq 10^{-7}$  reflecting an undetectable binding using the BLI were defined as “non-binders.” All the data from (D) come from previously published affinity measurements (Sokal et al., 2021b), whereas all the data in (C), including the Hu-1 RBD measurement, represent new measurements on these supernatants. (C and D) Bars indicate mean  $\pm$  SEM. See also Table S1.

~50% (153/310) of the monoclonal antibodies had reduced binding to the Omicron RBD compared with Hu-1 RBD (Omicron/Hu-1 RBD equilibrium dissociation constant [KD] ratio > 2; Figure 3A). Additional two-by-two comparisons of the binding affinities toward the Hu-1 and the previous RBD variants for these Omicron-affected antibodies further suggested that a large fraction of them is uniquely affected by the Omicron variant (Figure 3A). The distribution of mutations in the previous RBD variants (Figures 1A and 1B) had allowed us to predict the identity of key binding amino acid residues within the RBD for 116 MBC-derived monoclonal antibodies among the 139 affected by at least one of the previous RBD variants in the 310 antibodies included in this analysis (Figure 3B; Sokal et al., 2021b). 98 of these 139 MBC-derived monoclonal antibodies, including most of the ones recognizing the E484, K417, and N501 receptor-binding motif (RBM) residues, appeared to be also affected in their recognition of the Omicron variant. In addition, 55 out of the 171 previously unaffected antibodies appeared to be selectively affected by the new mutated residues uniquely displayed by Omicron (Omicron-specific; Figure 3B), though we cannot

predict the role of each individual mutation in this context of multiple co-selected mutations in the Omicron RBD. The clones recognizing the Omicron-specific residues were not enriched for the recurrent and convergent antibody rearrangements observed in convalescent and vaccinated individuals (IGHV1-2, IGHV1-69, IGHV3-53, and IGHV3-66; Figure 3C) (Barnes et al., 2020). Therefore, Omicron-specific mutations appear to affect a more diverse range of VH recognizing the RBD than other VOCs and VOIs do. A few clones predicted to bind the L452 residue based on their B.1.617.1 and B.1.617.2 recognition profiles were also affected in their binding to B.1.1.529, despite the absence of this mutation in this variant. This could suggest the recognition of multiple residues (as seen for the E484/L452 and N501/K417 residues) or more complex structural changes resulting from the large number of mutations included in the Omicron’s RBD. Finally, when analyzed in the context of our previous knowledge of the neutralization potency of 163 out of the 313 monoclonal antibodies tested by BLI (Sokal et al., 2021b), the loss of affinity against Omicron RBD appeared to be mostly restricted to the potent neutralizers of the D614G SARS-CoV-2

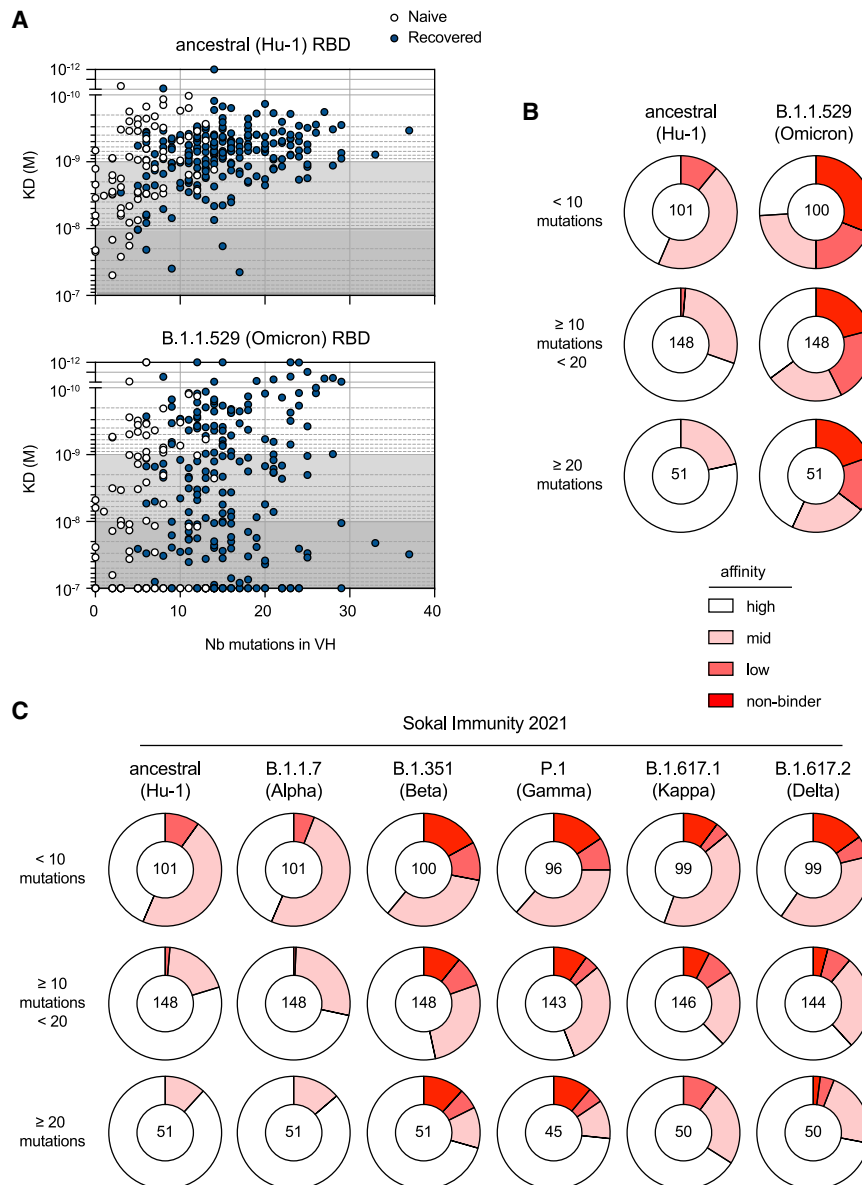


**Figure 2. Omicron RBD evades a large share of Hu-1 selected hypermutated and high-affinity memory B cell-derived antibodies**

(A) The measured KD (M) against the ancestral (Hu-1) (top panel) or B.1.1.529 (Omicron) RBD (bottom panel) versus the number of V<sub>H</sub> mutations for all the tested monoclonal antibodies from the single-cell culture supernatants of the RBD-specific MBCs isolated from the vaccinated SARS-CoV-2 recovered (n = 225) and vaccinated naive donors (n = 75) with available V<sub>H</sub> sequence from the SARS-CoV-2 recovered (dark blue) and naive (white) donors (the Spearman correlations for all sequences are as follow: V<sub>H</sub> mutation/Hu-1 KD: r = 0.3791, p < 0.0001; V<sub>H</sub> mutation/B.1.1.529 KD: r = 0.1597, p = 0.0058).

(B and C) (B) Pie charts showing the binding affinity distribution of all tested monoclonal antibodies against the ancestral (Hu-1) RBD and B.1.1.529 (Omicron) RBD variants, and (C) pie charts showing the binding affinity distribution of the same supernatants against the ancestral (Hu-1), B.1.1.7 (Alpha), B.1.351 (Beta), P.1 (Gamma), B.1.617.1 (Gamma), and B.1.617.2 (Delta) RBD variants, when available. In both cases, the monoclonal antibodies are grouped according to their overall number of mutations as follows: low (<10 mutations, upper panel), intermediate (<20 and ≥10, mid panel), or high V<sub>H</sub> mutation numbers (≥20, lower panel). All the data from (C) come from previous affinity measurements (Sokal et al., 2021b), whereas all the data in (B), including the Hu-1 RBD measurement, represent new measurements on these supernatants.

(B and C) The affinity groups are defined in Figure 1C and the numbers at the center of each pie chart indicate the total number of tested monoclonal antibodies in each group. See also Table S1.

(Figure 3D). As previously described for the Beta variants, this result highlights the selective pressure imposed on SARS-CoV-2 by such neutralizing antibodies. Similarly, the antibodies that still displayed a potent neutralization potency against the Beta SARS-CoV-2 appeared to be selectively targeted for additional loss of affinity by the Omicron-specific mutations not included in the Beta variant (Figure 3E).

**Omicron SARS-CoV-2 evades neutralization from most but not all MBC-derived monoclonal antibodies from mRNA-vaccinated individuals**

To better characterize the remaining neutralizing potential of MBC-derived antibodies against the Omicron variant, we next tested 253 supernatants in an *in vitro* focus reduction neutralization assay against authentic D614G and B.1.1.529 (Omicron) SARS-CoV-2 viruses. As previously described, a majority of

RBD-specific MBC-derived antibodies displayed some neutralization potency against the D614G SARS-CoV-2 strain in all the donor groups (Figures 4A and 4B) and all the tested individuals (Figure 4C), except in one of the 3 naive donors. These numbers were strongly reduced in all the individuals when looking at Omicron SARS-CoV-2 neutralization (Figures 4A and 4B), with notably less than 20% of potent or weak neutralizing antibodies in most vaccinated naive donors and M-CoV patients (Figure 4C). Nonetheless, we could detect potent neutralizing antibodies in 10 out of the 11 tested donors (Table S1) and neutralizing antibodies in all of them (Figure 4C). Additionally, 3 out of the 4 S-CoV patients harbored more than 20% of potent neutralizers against Omicron SARS-CoV-2. Cross-examining our neutralization data in the light of our RBD affinity measurements further confirmed a strong escape by Omicron SARS-CoV-2 from most antibodies targeting the core RBM epitopes mutated in Omicron (N501, K417, and E484) (Figure 4D). However, in line with the absence of the L452 mutation in Omicron, 6 out of the 7 identified potent neutralizing antibodies with predicted binding to this residue retained their

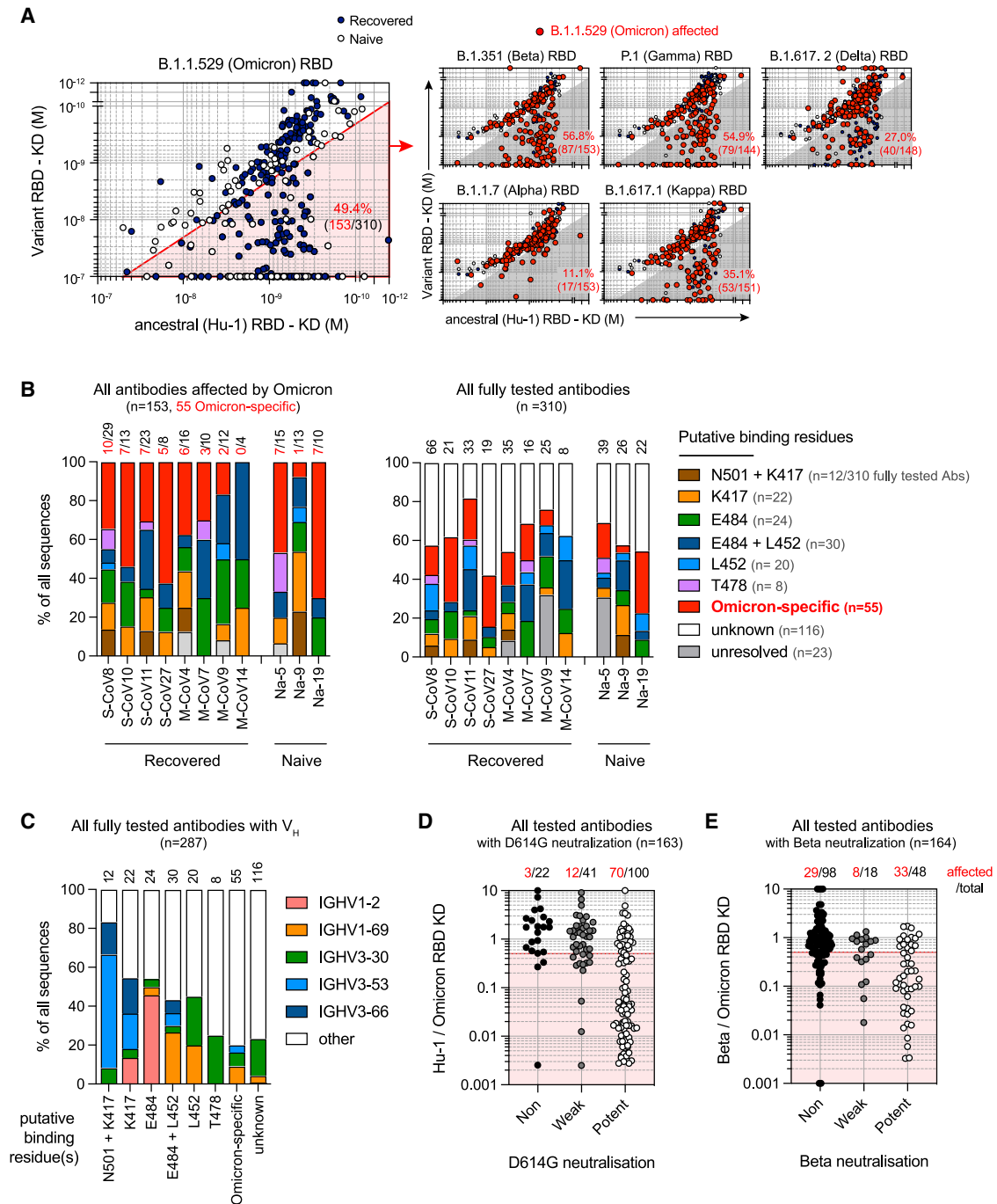


**Figure 3. Omicron-specific RBD mutations expand their overall escape of memory B cell-derived antibodies**

(A) Dot plot representing the KDs for B.1.1.529 (Omicron) RBD versus ancestral (Hu-1) RBD for all tested monoclonal antibodies from the SARS-CoV-2 recovered (dark blue dots) and naive donors (white dots). The red shaded area indicates monoclonal antibodies with at least two-fold increased KD for B.1.1.529 than for Hu-1 (termed “B.1.1.529-affected antibodies” herein) (left panel). Dot plots representing KDs against the B.1.1.7 (Alpha), B.1.351 (Beta), P.1 (Gamma), B.1.617.1 (Kappa), and B.1.617.2 (Delta) RBD versus the ancestral (Hu-1) RBD for all tested antibodies (right panels). B.1.1.529-affected antibodies are highlighted as larger size red dots (corresponding to clones present in the red sector in the left panel). The percentages indicate the proportion of B.1.1.529-affected monoclonal antibodies also affected by the indicated RBD variant (gray zone).

(B) The frequencies of antibodies targeting one of the predicted essential binding residue groups in the Omicron-affected antibodies (left panel) and in all the tested antibodies (right panel), as defined by RBD variants recognition profile in BLI, among all tested antibodies for each of the 11 individuals from whom memory B cells were assayed. The numbers of monoclonal antibodies for each donor are indicated on top of each histogram in black. The number of antibodies affected by Omicron-specific mutations is detailed in red. S-CoV, patients who recovered from severe COVID-19; M-CoV, patients who recovered from mild COVID-19; Na, patients naive from COVID-19.

(legend continued on next page)

potency against Omicron. Additionally, about one-third of the antibodies identified as binding Omicron-specific residues did retain potent neutralization despite clear affinity loss (Figures 4E and 4F). Conversely, it is important to note that none of the non or weak D614G neutralizers acquired potent neutralization potency against Omicron. Five of the 14 ultra-high Omicron binders ( $KD < 10^{-10}$  M for Omicron; Figure 2A) were included in this assay. Two out of these five were non-neutralizers of D614G SARS-CoV-2 to begin with and did not acquire any neutralization activity against Omicron SARS-CoV-2. The other three fell into a group of antibodies ( $n = 29$ ) that showed the loss of neutralization potency without any detectable reduction in RBD affinity (Figures 4E and 4F). These results are in line with our previous results of neutralization against B.1.351 (Beta) SARS-CoV-2 and most likely result from allosteric changes at the level of the whole spike imposed by mutations outside of the RBD (Sokal et al., 2021b).

## DISCUSSION

Previous analyses of the MBC repertoire elicited after mRNA vaccination in COVID-19 recovered and naive individuals had demonstrated the presence of a sizable pool of high-affinity neutralizing clones against all VOCs prior to Omicron (Cho et al., 2021; Goel et al., 2021; Sokal et al., 2021b). These data suggested that vaccine recalls would be effective at reconstituting protective levels of serum antibodies to prevent infection by VOCs. Our results suggest a strong but incomplete immune escape by the Omicron variant from specific MBCs elicited by natural infection with the D614G SARS-CoV-2 and/or vaccination with mRNA vaccine encoding the ancestral Hu-1 spike. This is consistent with the recent studies on sera collected from individuals who had received three mRNA vaccine doses (Carreño et al., 2022; Dejnirattisai et al., 2022; Garcia-Beltran et al., 2022; Gruell et al., 2022; Hoffmann et al., 2022; Planas et al., 2022), as well as with one recent study of single-cell MBCs from pooled vaccinated SARS-CoV-2-naive individuals (Kotaki et al., 2022). The reduction in the range of 4- to 18-fold in overall serum neutralizing activity against the Omicron variant as compared with the ancestral Hu-1 strain was reported in these studies, although the overall binding potential of such serum antibodies appeared less drastically reduced (Carreño et al., 2022).

Looking at the single MBC level, the unique accumulation of mutations in key amino acid residues within the RBD of the Omicron variant, either shared with previous variants or unique, resulted in a loss of affinity for close to 50% of all the MBCs analyzed in our study. The link between affinity loss and neutralization potency, however, is not as straightforward. On the one hand, a few clones with reduced binding maintained their neutralization potency and represented a large share of the

remaining potent Omicron neutralizers (11/20). On the other hand, non-affected binders were enriched in non-neutralizing antibodies against D614G SARS-CoV-2, which remained non-neutralizers against Omicron SARS-CoV-2. Additionally, many non-affected binders with weak or potent D614G neutralization potency did not display any detectable Omicron-neutralization potency, suggesting more complex allosteric effects at the level of the spike (Cerutti et al., 2022; Sokal et al., 2021b; Yin et al., 2022). Overall, of all the antibodies tested for both neutralization and affinity in our study, over 80% of the high- to mid-binder of the Hu-1 RBD displayed some neutralization potency against the D614G SARS-CoV-2 (105/131), but less than 35% of the high- to mid-binder of the Omicron RBD displayed neutralization potency against the Omicron SARS-CoV-2 (24/74). Nonetheless, Omicron-neutralizing antibodies still represented more than 10% of the anti-RBD MBC repertoire for 8 out of the 11 donors in our study and could be detected in all donors ( $5.3 \pm 3.4$ -fold reduction in the proportion of Omicron neutralizers as compared with D614G). Unlike plasma cells producing serum antibodies, MBCs are endowed with great proliferative potential and, at a rate of one division every 10–12 h, could theoretically compensate for an up to an 8-fold loss in protective clone frequency in less than 2 days. The low frequencies of the available protective MBC clones detected in our study could, therefore, still be sufficient to avoid severe forms of COVID-19, as observed in clinical reports (Nemet et al., 2022).

An important next step will be to characterize the long-term remodeling of the MBC repertoire after an Omicron breakthrough infection in vaccinated individuals and to address whether an Omicron-specific B cell response can be achieved, with the recruitment of naive B cells or the maturation of pre-existing low-affinity MBCs. Answering these questions will provide crucial information regarding the available immune protection against the Omicron or subsequent variants and allow an informed decision as to whether a vaccine boost specifically targeted against VOCs would be of interest in the near future.

## Limitations of the study

Potential limitations of our work include a limited number of subjects included in this study for in-depth MBC characterization ( $n = 11$ ). As such, the observed differences between the donor groups should be interpreted with caution, notably the slightly higher frequency of potent neutralizing antibodies detected in the severe-COVID-19 patient group. Additionally, the samples analyzed were collected early after the first vaccine boost in all individuals. The MBC repertoire of COVID-19-naive vaccinated individuals has been shown to evolve up to 6 months after the boost (Cho et al., 2021; Goel et al., 2021) and it remains to be assessed how the breadth of MBC repertoire will further evolve after an additional vaccine boost with a third dose of the ancestral Hu-1 spike mRNA vaccine (Wang et al., 2022a). Finally, our study

(C) The proportion of IGHV1-2, IGHV1-69, IGHV3-30, IGHV3-53, and IGHV3-66 usage among all the tested monoclonal antibodies with available  $V_H$  sequence and grouped based on their predicted essential binding residues, as defined in (B). The numbers of tested monoclonal antibodies from all donors are indicated on top of each histogram.

(D and E) The ratio of Hu-1 over B.1.1.529 (Omicron) RBD KD (D) or B.1.351 (Beta) over B.1.1.529 (Omicron) KD for all the monoclonal antibodies tested, grouped based on their neutralization potency against D614G (D) or B.1.351 SARS-CoV-2 (E) (refer to Sokal et al., 2021b). The numbers on top indicate the numbers of monoclonal antibodies with a [KD for Hu-1 RBD / KD for B.1.1.529 RBD] ratio  $< 0.5$  (D) or a [KD for B.1.351 / KD for B.1.1.529 RBD] ratio  $< 0.5$  (E). Values above 10 or below 0.001 were plotted on the axis. See also Table S1.

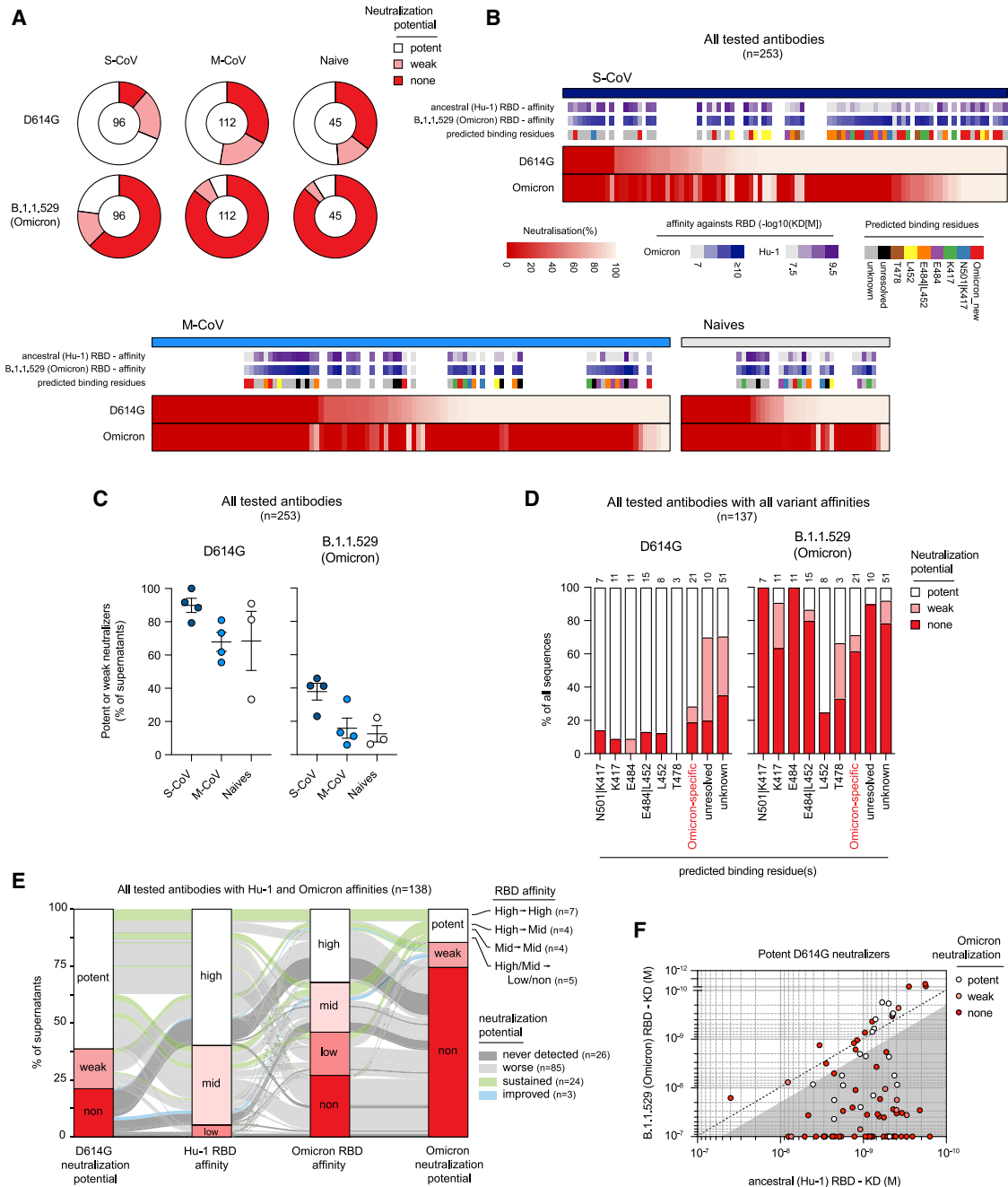


**Figure 4. The Omicron VOC evades neutralization from a large proportion of memory B cell-derived monoclonal antibodies**

(A) Pie charts showing the proportion of single-cell culture supernatants of RBD-specific MBCs isolated from SARS-CoV-2 recovered (S-CoV, n = 96; M-CoV, n = 112) and naive donors (n = 45) displaying potent, weak, or no neutralization potency (none) against D614G SARS-CoV-2 and B.1.1.529 (Omicron) SARS-CoV-2 variant. Potent neutralizers are defined as >80% neutralization at 16 nM and weak neutralizers as neutralization between 25% and 80% at 16 nM. None neutralizers are defined as neutralization <25% at 16 nM.

(B) A heatmap showing the *in vitro* neutralization of D614G SARS-CoV-2 and Omicron variant at 16 nM for all cultured supernatants tested. KD (M) against the ancestral (Hu-1) and B.1.1.529 (Omicron) RBD for tested monoclonal antibodies are represented on top along with predicted binding residues.

(C) The percentage of potent neutralizers against SARS-CoV-2 D614G or variant B.1.1.529 (Omicron) viruses among monoclonal antibodies analyzed for each donor in each group.

(D) The proportion of potent, weak, or non-D614G or B.1.1.529 (Omicron) SARS-CoV-2 neutralizers among all tested monoclonal antibodies, grouped based on their predicted binding residues, as defined in Figure 3B.

(E) A river plot connecting affinity for the ancestral (Hu-1) and B.1.1.529 (Omicron) RBD with neutralization potency for D614G and B.1.1.529 (Omicron) SARS-CoV-2. The binding and neutralizing affinity groups are defined in Figures 1C and 4A. Clones are connected with colored lines. The line colors indicate the evolution of the neutralization potency toward B.1.1.529 (Omicron) SARS-CoV-2 as follows: green indicates potent or weak clones remaining respectively potent or

(legend continued on next page)

was focused on the RBD domain of the SARS-CoV-2 spike protein, which represents the major target of neutralizing antibodies (Tong et al., 2021; Vanshylla et al., 2022). Broadly neutralizing antibodies against other domains of the trimeric spike have been described, notably against the conserved epitopes of the NTD (Wang et al., 2022b). A similar point could be made for memory T cell responses, which so far appear to be less affected by mutations selected by SARS-CoV-2 variants (Goel et al., 2021; Tarke et al., 2022).

## STAR★METHODS

Detailed methods are provided in the online version of this paper and include the following:

- KEY RESOURCES TABLE
- RESOURCE AVAILABILITY
  - Lead contact
  - Materials availability
  - Data and code availability
- EXPERIMENTAL MODEL AND SUBJECT DETAILS
  - Study participants
  - Virus strains
- METHOD DETAILS
  - Recombinant protein purification
  - Single-cell culture
  - ELISA
  - Single-cell IgH sequencing
  - Computational analyses of VDJ sequences
  - 3D representation of known mutations to the RBD surface
  - Affinity measurement using biolayer interferometry (Octet)
  - Virus neutralization assay
- QUANTIFICATION AND STATISTICAL ANALYSIS

## SUPPLEMENTAL INFORMATION

Supplemental information can be found online at <https://doi.org/10.1016/j.immuni.2022.04.002>.

## ACKNOWLEDGMENTS

We thank Garnett Kelsoe for providing the human cell culture system, together with invaluable advice; A. Boucharlat and the Chemogenomic and Biological Screening Core Facility headed by F. Agou, as well as P. England and the Molecular Biophysics Core Facility at the Institut Pasteur, Paris, France for their support during the course of this work; Sébastien Storck, Lucie Da Silva, and Sandra Weller for their advice and support; the physicians, Constance Guillaud, Raphael Lepeule, Frédéric Schlemmer, Elena Fois, Henri Guillet, Nicolas De Prost, and Pascal Lim, whose patients were included in this study; and Florence Guivel-Benhassine and Olivier Schwartz from the Institut Pasteur for providing authentic SARS-CoV-2 B.1.1.529 virus.

This work was initiated by a grant from the Agence Nationale de la Recherche and the Fondation pour la Recherche Médicale (ANR and MEMO-COV-2-FRM) and funded by the Fondation Princesse Grace, an ERC

Advanced Investigator Grant (B-response), and a grant from the French Ministry of Health (Soutien Exceptionnel à la Recherche Clinique 2022, CAPNET [Comité ad-hoc de pilotage national des essais thérapeutiques et autres recherches]). Assistance Publique – Hôpitaux de Paris (AP-HP, Département de la Recherche Clinique et du Développement) was the promotor and the sponsor of MEMO-COV-2. Work in the Unit of Structural Virology was funded by Institut Pasteur, Urgence COVID-19 Fundraising Campaign of Institut Pasteur. A.S. was supported by a Poste d'accueil from INSERM, I.F. by a fellowship from the Agence Nationale de Recherches sur le Sida et les Hépatites Virales (ANRS), M.B. by a CIFRE fellowship from the Association Nationale de la Recherche et de la Technologie (ANRT), and A.D.L.S. by a SNFMI fellowship. P.B. acknowledges funding from the French National Research Agency grant ANR-14-CE16-0011 project DROPmAbs, the Institut Carnot Pasteur Microbes et Santé (ANR 11 CARN 0017-01), the Institut Pasteur, and the Institut National de la Santé et de la Recherche Médicale (INSERM).

## AUTHOR CONTRIBUTIONS

Conceptualization, P.C., A.S., J.-C.W., C.-A.R., and M. Mahévas; data curation, P.C., A.S., M.B., G.B.-S., and I.A.; formal analysis, A.S., P.C., M.B., G.B.-S., I.A., M.B.-A., A.D.L.S., A.V., S. Fourati, and I.F.; funding acquisition, S. Fillatreau, J.-C.W., C.-A.R., and M. Mahévas; investigation, A.S., P.C., A.D.L.S., I.A., and A.V.; methodology, A.S., J.-C.W., C.-A.R., P.C., and M. Mahévas; project administration, P.C., F.C.-P., J.-C.W., C.-A.R., and M. Mahévas; resources, J.-M.P., F.N.-P., S. Fourati, E.C., M. Michel, B.G., S.G., G.M., Y.N., V.Z., P.B., F.A.R., C.-A.R., and M. Mahévas; software, P.C.; supervision, P.C., J.-C.W., C.-A.R., P.B., F.A.R., and M. Mahévas; validation, A.S., I.A., A.V., A.D.L.S., M.B., C.-A.R., P.C., and M. Mahévas; visualization, P.C., A.S., I.A., A.D.L.S., M. Mahévas; writing – original draft, P.C., A.S., J.-C.W., C.-A.R., and M. Mahévas; writing – review & editing, all authors.

## DECLARATION OF INTERESTS

Outside of the submitted work, M. Mahévas received research funds from GSK and personal fees from LFB and Amgen. J.-C.W. received consulting fees from Institut Mérieux. P.B. received consulting fees from Regeneron Pharmaceuticals. J.-M.P. received personal fees from Abbvie, Gilead, Merck, and Siemens Healthcare. F.A.R. is a member of the board of MELETIOS Therapeutics and of the Scientific Advisory Board of eureKARE.

Received: December 21, 2021

Revised: February 16, 2022

Accepted: April 4, 2022

Published: April 7, 2022

## REFERENCES

- Barnes, C.O., West, A.P., Huey-Tubman, K.E., Hoffmann, M.A.G., Sharaf, N.G., Hoffman, P.R., Koranda, N., Gristick, H.B., Gaebler, C., Muecksch, F., et al. (2020). Structures of human antibodies bound to SARS-CoV-2 spike reveal common epitopes and recurrent features of antibodies. *Cell* 182, 828–842.e16.
- Cai, Y., Zhang, J., Xiao, T., Peng, H., Sterling, S.M., Walsh, R.M., Rawson, S., Rits-Volloch, S., and Chen, B. (2020). Distinct conformational states of SARS-CoV-2 spike protein. *Science* 369, 1586–1592.
- Cameroni, E., Bowen, J.E., Rosen, L.E., Saliba, C., Zepeda, S.K., Culap, K., Pinto, D., VanBlargan, L.A., De Marco, A., di Iulio, J., et al. (2022). Broadly neutralizing antibodies overcome SARS-CoV-2 Omicron antigenic shift. *Nature* 602, 664–670.
- Carreño, J.M., Alshammery, H., Tcheou, J., Singh, G., Raskin, A.J., Kawabata, H., Sominsky, L.A., Clark, J.J., Adelsberg, D.C., Bielak, D.A., et al. (2022).

weak; light gray indicates clones with diminished neutralization potency (potent to weak, none, or weak to none); dark gray indicates clones that do not neutralize any of the 2 viruses; and blue indicates clones with improved neutralization toward B.1.1.529 (only none to weak).

(F) KD (M) for the B.1.1.529 (Omicron) RBD versus the ancestral (Hu-1) RBD for all D614G SARS-CoV-2 potent neutralizers monoclonal antibodies. The dot color indicates the neutralization potency against B.1.1.529 SARS-CoV-2 variant. The gray-shaded area highlights binding-impaired clones against the B.1.1.529 RBD variant as defined in Figure 3A. See also Table S1.

- Activity of convalescent and vaccine serum against SARS-CoV-2 Omicron. *Nature* 602, 682–688.
- Cerutti, G., Guo, Y., Liu, L., Liu, L., Zhang, Z., Luo, Y., Huang, Y., Wang, H.H., Ho, D.D., Sheng, Z., and Shapiro, L. (2022). Cryo-EM structure of the SARS-CoV-2 Omicron spike. *Cell Rep.* 38, 110428.
- Cho, A., Muecksch, F., Schaefer-Babajew, D., Wang, Z., Finkin, S., Gaebler, C., Ramos, V., Cipolla, M., Mendoza, P., Agudelo, M., et al. (2021). Anti-SARS-CoV-2 receptor-binding domain antibody evolution after mRNA vaccination. *Nature* 600, 517–522.
- Crickx, E., Chappert, P., Sokal, A., Weller, S., Azzaoui, I., Vandenberghe, A., Bonnard, G., Rossi, G., Fadeev, T., Storck, S., et al. (2021). Rituximab-resistant splenic memory B cells and newly engaged naive B cells fuel relapses in patients with immune thrombocytopenia. *Sci. Transl. Med.* 13, eabc3961.
- Dejnirattisai, W., Huo, J., Zhou, D., Zahradnik, J., Supasa, P., Liu, C., Duyvesteyn, H.M.E., Ginn, H.M., Mentzer, A.J., Tuekprakhon, A., et al. (2022). SARS-CoV-2 Omicron-B.1.1.529 leads to widespread escape from neutralizing antibody responses. *Cell* 185, 467–484.e15.
- Dugan, H.L., Stamper, C.T., Li, L., Changrob, S., Asby, N.W., Halfmann, P.J., Zheng, N.Y., Huang, M., Shaw, D.G., Cobb, M.S., et al. (2021). Profiling B cell immunodominance after SARS-CoV-2 infection reveals antibody evolution to non-neutralizing viral targets. *Immunity* 54, 1290–1303.e7.
- Gaebler, C., Wang, Z., Lorenzi, J.C.C., Muecksch, F., Finkin, S., Tokuyama, M., Cho, A., Jankovic, M., Schaefer-Babajew, D., Oliveira, T.Y., et al. (2021). Evolution of antibody immunity to SARS-CoV-2. *Nature* 591, 639–644.
- Garcia-Beltran, W.F., St Denis, K.J., Hoelzemer, A., Lam, E.C., Nitido, A.D., Sheehan, M.L., Berrios, C., Ofoman, O., Chang, C.C., Hauser, B.M., et al. (2022). mRNA-based COVID-19 vaccine boosters induce neutralizing immunity against SARS-CoV-2 Omicron variant. *Cell* 185, 457–466.e4.
- Goel, R.R., Painter, M.M., Apostolidis, S.A., Mathew, D., Meng, W., Rosenfeld, A.M., Lundgreen, K.A., Reynaldi, A., Khoury, D.S., Pattekar, A., et al. (2021). mRNA vaccines induce durable immune memory to SARS-CoV-2 and variants of concern. *Science* 374, abm0829.
- Gruell, H., Vanshylla, K., Tober-Lau, P., Hillus, D., Schommers, P., Lehmann, C., Kurth, F., Sander, L.E., and Klein, F. (2022). mRNA booster immunization elicits potent neutralizing serum activity against the SARS-CoV-2 Omicron variant. *Nat. Med.* 28, 477–480.
- Gupta, N.T., Vander Heiden, J.A., Uduman, M., Gadala-Maria, D., Yaari, G., and Kleinstein, S.H. (2015). Change-O: a toolkit for analyzing large-scale B cell immunoglobulin repertoire sequencing data. *Bioinformatics* 31, 3356–3358.
- Hoffmann, M., Krüger, N., Schulz, S., Cossmann, A., Rocha, C., Kempf, A., Nehlmeier, I., Graichen, L., Moldenhauer, A.S., Winkler, M.S., et al. (2022). The Omicron variant is highly resistant against antibody-mediated neutralization: implications for control of the COVID-19 pandemic. *Cell* 185, 447–456.e11.
- Kotaki, R., Adachi, Y., Moriyama, S., Onodera, T., Fukushi, S., Nagakura, T., Tonouchi, K., Terahara, K., Sun, L., Takano, T., et al. (2022). SARS-CoV-2 Omicron-neutralizing memory B-cells are elicited by two doses of BNT162b2 mRNA vaccine. *Sci Immunol.* eabn8590.
- Lad, L., Clancy, S., Kovalenko, M., Liu, C., Hui, T., Smith, V., and Pagratis, N. (2015). High-throughput kinetic screening of hybridomas to identify high-affinity antibodies using bio-layer interferometry. *J. Biomol. Screen.* 20, 498–507.
- Luo, X.M., Maarschalk, E., O'Connell, R.M., Wang, P., Yang, L., and Baltimore, D. (2009). Engineering human hematopoietic stem/progenitor cells to produce a broadly neutralizing anti-HIV antibody after in vitro maturation to human B lymphocytes. *Blood* 113, 1422–1431.
- Muik, A., Lui, B.G., Wallisch, A.-K., Bacher, M., Mühl, J., Reinholz, J., Ozhelvaci, O., Beckmann, N., Güimil Garcia, R. de la C., Poran, A., et al. (2022). Neutralization of SARS-CoV-2 Omicron by BNT162b2 mRNA vaccine-elicited human sera. *Science* 375, 678–680.
- Nemet, I., Kliker, L., Lustig, Y., Zuckerman, N., Erster, O., Cohen, C., Kreiss, Y., Alroy-Preis, S., Regev-Yochay, G., Mendelson, E., and Mandelboim, E. (2022). Third BNT162b2 vaccination neutralization of SARS-CoV-2 omicron infection. *N. Engl. J. Med.* 386, 492–494.
- Planas, D., Saunders, N., Maes, P., Guivel-Benhassine, F., Planchais, C., Buchrieser, J., Bolland, W.H., Porrot, F., Staropoli, I., Lemoine, F., et al. (2022). Considerable escape of SARS-CoV-2 Omicron to antibody neutralization. *Nature* 602, 671–675.
- Purtha, W.E., Tedder, T.F., Johnson, S., Bhattacharya, D., and Diamond, M.S. (2011). Memory B cells, but not long-lived plasma cells, possess antigen specificities for viral escape mutants. *J. Exp. Med.* 208, 2599–2606.
- Rodda, L.B., Netland, J., Shehata, L., Pruner, K.B., Morawski, P.A., Thouvenel, C.D., Takehara, K.K., Eggenberger, J., Hemann, E.A., Waterman, H.R., et al. (2021). Functional SARS-CoV-2-specific immune memory persists after mild COVID-19. *Cell* 184, 169–183.e17.
- Sokal, A., Barba-Spaeth, G., Fernández, I., Broketa, M., Azzaoui, I., de La Selle, A.de L., Vandenberghe, A., Fourati, S., Roeser, A., Meola, A., et al. (2021a). mRNA vaccination of naive and COVID-19-recovered individuals elicits potent memory B cells that recognize SARS-CoV-2 variants. *Immunity* 54, 2893–2907.e5.
- Sokal, A., Chappert, P., Barba-Spaeth, G., Roeser, A., Fourati, S., Azzaoui, I., Vandenberghe, A., Fernandez, I., Meola, A., Bouvier-Alias, M., et al. (2021b). Maturation and persistence of the anti-SARS-CoV-2 memory B cell response. *Cell* 184, 1201–1213.e14.
- Starr, T.N., Greaney, A.J., Dingens, A.S., and Bloom, J.D. (2021). Complete map of SARS-CoV-2 RBD mutations that escape the monoclonal antibody LY-CoV555 and its cocktail with LY-CoV016. *Cell Rep. Med.* 2, 100255.
- Tarke, A., Coelho, C.H., Zhang, Z., Dan, J.M., Yu, E.D., Methot, N., Bloom, N.I., Goodwin, B., Phillips, E., Mallal, S., et al. (2022). SARS-CoV-2 vaccination induces immunological T cell memory able to cross-recognize variants from Alpha to Omicron. *Cell* 185, 847–859.e11.
- Tiller, T., Meffre, E., Yurasov, S., Tsujii, M., Nussenzweig, M.C., and Wardemann, H. (2008). Efficient generation of monoclonal antibodies from single human B cells by single cell RT-PCR and expression vector cloning. *J. Immunol. Methods* 329, 112–124.
- Tong, P., Gautam, A., Windsor, I.W., Travers, M., Chen, Y., Garcia, N., Whiteman, N.B., McKay, L.G.A., Storm, N., Malsick, L.E., et al. (2021). Memory B cell repertoire for recognition of evolving SARS-CoV-2 spike. *Cell* 184, 4969–4980.e15.
- Vanshylla, K., Fan, C., Wunsch, M., Poopalasingam, N., Meijers, M., Kreer, C., Kleipass, F., Ruchnewitz, D., Ercanoglu, M.S., Gruell, H., et al. (2022). Discovery of ultrapotent broadly neutralizing antibodies from SARS-CoV-2 elite neutralizers. *Cell Host Microbe* 30, 69–82.e10.
- Wang, K., Jia, Z., Bao, L., Wang, L., Cao, L., Chi, H., Hu, Y., Li, Q., Zhou, Y., Jiang, Y., et al. (2022a). Memory B cell repertoire from triple vaccinees against diverse SARS-CoV-2 variants. *Nature* 603, 919–925.
- Wang, Z., Muecksch, F., Cho, A., Gaebler, C., Hoffmann, H.H., Ramos, V., Zong, S., Cipolla, M., Johnson, B., Schmidt, F., et al. (2022b). Conserved neutralizing epitopes on the N-terminal domain of variant SARS-CoV-2 spike proteins. Preprint at bioRxiv.
- Wang, Z., Schmidt, F., Weisblum, Y., Muecksch, F., Barnes, C.O., Finkin, S., Schaefer-Babajew, D., Cipolla, M., Gaebler, C., Lieberman, J.A., et al. (2021). mRNA vaccine-elicited antibodies to SARS-CoV-2 and circulating variants. *Nature* 592, 616–622.
- Weisel, F., and Shlomchik, M. (2017). Memory B cells of mice and humans. *Annu. Rev. Immunol.* 35, 255–284.
- Yin, W., Xu, Y., Xu, P., Cao, X., Wu, C., Gu, C., He, X., Wang, X., Huang, S., Yuan, Q., et al. (2022). Structures of the Omicron Spike trimer with ACE2 and an anti-Omicron antibody. *Science* 375, 1048–1053.
- Yuan, M., Huang, D., Lee, C.-C.D., Wu, N.C., Jackson, A.M., Zhu, X., Liu, H., Peng, L., van Gils, M.J., Sanders, R.W., et al. (2021). Structural and functional ramifications of antigenic drift in recent SARS-CoV-2 variants. *Science* 373, 818–823.
- Zahradnik, J., Marciano, S., Shemesh, M., Zoler, E., Harari, D., Chiaravalli, J., Meyer, B., Rudich, Y., Li, C., Marton, I., et al. (2021). SARS-CoV-2 variant prediction and antiviral drug design are enabled by RBD in vitro evolution. *Nat. Microbiol.* 6, 1188–1198.

# ARTICLE 4

## **ARTICLE 4**

### **Assessment of SARS-CoV-2 BA.1 breakthrough infection on Bmem repertoire remodeling**

As part of our ongoing collaboration with the group of Immune System Development at Institut Necker Enfants Malades (INEM) directed by Dr Matthieu Mahévas to characterize the longitudinal memory B cell response towards SARS-CoV-2 following mRNA vaccination, we sought to investigate the evolution of the memory B cell repertoire following breakthrough BA.1 infection in vaccinated individuals. The relative contribution of existing, vaccine elicited Bmem compared with de novo recruited Bmem in the months following BA.1 infection remained incompletely understood. This study sought to follow the Bmem repertoire in the months preceding and following Omicron breakthrough infection, up to 6 months. This longitudinal analysis allowed us to discern the patterns of remodeling within Bmem clonal and functional repertoires over this extended period. In the following section I have included the published manuscript (Sokal et al. 2023)<sup>131</sup> of this work.

I performed additional high throughput BLI measurements to assess the affinities of Bmem-derived monoclonal antibodies towards Omicron BA.1 RBD and several additional RBD variants. Specifically, we observed a significant increase in both the median affinities and the prevalence of potent neutralizing antibodies targeting both Hu-1 and BA.1 RBD. This observation suggests convergent clonal evolution, where Bmem populations appear to gravitate towards shared epitopes present on these two distinct RBD variants. This convergence in the immune response highlights the complex dynamics and adaptability of the Bmem repertoire in the face of evolving viral strains, shedding light on mechanisms of cross-protection and immune memory.

## Article

# SARS-CoV-2 Omicron BA.1 breakthrough infection drives late remodeling of the memory B cell repertoire in vaccinated individuals

Aurélien Sokal,<sup>1,2,3,17</sup> Giovanna Barba-Spaeth,<sup>4,17</sup> Lise Hunault,<sup>5,6,7,17</sup> Ignacio Fernández,<sup>4,17</sup> Matteo Broketa,<sup>5,6,18</sup> Annalisa Meola,<sup>4,18</sup> Slim Fourati,<sup>8,9,18</sup> Imane Azzaoui,<sup>3,10,18</sup> Alexis Vandenberghe,<sup>1,3,10,18</sup> Pauline Lagouge-Roussey,<sup>1,3,10,18</sup> Manon Broutin,<sup>1,10,18</sup> Anais Roeser,<sup>1,3</sup> Magali Bouvier-Alias,<sup>8,9</sup> Etienne Crickx,<sup>1,3,10</sup> Laetitia Languille,<sup>3</sup> Morgane Fournier,<sup>1,3</sup> Marc Michel,<sup>3</sup> Bertrand Godeau,<sup>3</sup> Sébastien Gallien,<sup>11</sup> Giovanna Melica,<sup>11</sup> Yann Nguyen,<sup>12</sup> Florence Canoui-Poitrine,<sup>13</sup> France Pirenne,<sup>9,14</sup> Jérôme Megret,<sup>15</sup> Jean-Michel Pawlotsky,<sup>8,9</sup> Simon Fillatreau,<sup>16</sup> Claude-Agnès Reynaud,<sup>1</sup> Jean-Claude Weill,<sup>1,19</sup> Félix A. Rey,<sup>4,19</sup> Pierre Bruhns,<sup>5,19</sup> Matthieu Mahévas,<sup>1,3,10,19,\*</sup> and Pascal Chappert<sup>1,10,19,20,\*</sup>

<sup>1</sup>Institut Necker Enfants Malades, INSERM U1151/CNRS UMR 8253, Action thématique incitative sur programme-Avenir Team, Auto-Immune and Immune B cells, Université Paris Cité, Université Paris Est-Créteil, Créteil, France

<sup>2</sup>Service de Médecine interne, Hôpital Beaujon, Assistance Publique-Hôpitaux de Paris (AP-HP), Université de Paris Cité, Clichy, France

<sup>3</sup>Service de Médecine Interne, Centre Hospitalier Universitaire Henri-Mondor, Assistance Publique-Hôpitaux de Paris (AP-HP), Université Paris-Est Créteil (UPEC), Créteil, France

<sup>4</sup>Institut Pasteur, Université de Paris Cité, CNRS UMR 3569, Unité de Virologie Structurale, Paris, France

<sup>5</sup>Institut Pasteur, Université de Paris Cité, INSERM UMR1222, Unit of Antibodies in Therapy and Pathology, Paris, France

<sup>6</sup>Sorbonne University, ED394, Paris, France

<sup>7</sup>Sorbonne Université, INSERM, CNRS, Centre d'Immunologie et des Maladies Infectieuses (CIMI-Paris), 75013 Paris, France

<sup>8</sup>Département de Virologie, Bactériologie, Hygiène et Mycologie-Parasitologie, Centre Hospitalier Universitaire Henri Mondor, Assistance Publique-Hôpitaux de Paris (AP-HP), Créteil, France

<sup>9</sup>INSERM U955, équipe 18. Institut Mondor de Recherche Biomédicale (IMRB), Université Paris-Est Créteil (UPEC), Créteil, France

<sup>10</sup>INSERM U955, équipe 2. Institut Mondor de Recherche Biomédicale (IMRB), Université Paris-Est Créteil (UPEC), Créteil, France

<sup>11</sup>Service de Maladies Infectieuses, Centre Hospitalier Universitaire Henri Mondor, Assistance Publique-Hôpitaux de Paris (AP-HP), Université Paris-Est Créteil (UPEC), Créteil, France

<sup>12</sup>Service de Médecine Interne, Centre Hospitalier Universitaire Cochin, Assistance Publique-Hôpitaux de Paris (AP-HP), Paris, France

<sup>13</sup>Département de Santé Publique, Unité de Recherche Clinique (URC), CEpiA (Clinical Epidemiology and Ageing), EA 7376- Institut Mondor de Recherche Biomédicale (IMRB), Centre Hospitalier Universitaire Henri-Mondor, Assistance Publique-Hôpitaux de Paris (AP-HP), Université Paris-Est Créteil (UPEC), Créteil, France

<sup>14</sup>Etablissement Français du Sang (EFS) Ile de France, Créteil, France

<sup>15</sup>Plateforme de Cytométrie en Flux, Structure Fédérative de Recherche Necker, INSERM US24-CNRS UMS3633, Paris, France

<sup>16</sup>Institut Necker Enfants Malades (INEM), INSERM U1151/CNRS UMR 8253, Université de Paris, Paris, France

<sup>17</sup>These authors contributed equally

<sup>18</sup>These authors contributed equally

<sup>19</sup>Senior author

<sup>20</sup>Lead contact

\*Correspondence: [matthieu.mahevas@aphp.fr](mailto:matthieu.mahevas@aphp.fr) (M.M.), [pascal.chappert@inserm.fr](mailto:pascal.chappert@inserm.fr) (P.C.)

<https://doi.org/10.1016/j.immuni.2023.07.007>

## SUMMARY

How infection by a viral variant showing antigenic drift impacts a preformed mature human memory B cell (MBC) repertoire remains an open question. Here, we studied the MBC response up to 6 months after SARS-CoV-2 Omicron BA.1 breakthrough infection in individuals previously vaccinated with three doses of the COVID-19 mRNA vaccine. Longitudinal analysis, using single-cell multi-omics and functional analysis of monoclonal antibodies from RBD-specific MBCs, revealed that a BA.1 breakthrough infection mostly recruited pre-existing cross-reactive MBCs with limited *de novo* response against BA.1-restricted epitopes. Reorganization of clonal hierarchy and new rounds of germinal center reactions, however, combined to maintain diversity and induce progressive maturation of the MBC repertoire against common Hu-1 and BA.1, but not BA.5-restricted, SARS-CoV-2 Spike RBD epitopes. Such remodeling was further associated with a marked improvement in overall neutralizing breadth and potency. These findings have fundamental implications for the design of future vaccination booster strategies.



## INTRODUCTION

Emergence of the severe acute respiratory syndrome coronavirus 2 (SARS-CoV-2) Omicron variant (BA.1) has marked a major antigenic shift in SARS-CoV-2 evolution.<sup>1</sup> The Spike (S) protein of SARS-CoV-2 Omicron BA.1 harbors 32 mutations as compared with the ancestral strain (Hu-1) originally identified in Wuhan. These mutations drastically impair neutralizing antibodies elicited by natural infection with the D614G SARS-CoV-2 and/or vaccination with mRNA vaccine encoding the ancestral Hu-1 S and have led to a massive wave of breakthrough infections in the early weeks of 2022 in vaccinated individuals, whether they had received 2 or 3 doses of mRNA vaccine.<sup>2–7</sup> Since, new sub-lineages, displaying additional mutations, continue to emerge, supplanting prior variants.<sup>8</sup>

Despite sizable immune escape by several SARS-CoV-2 variants, the diverse memory B cell (MBC) repertoire generated by two or three doses of mRNA vaccines has been shown to contain high-affinity neutralizing clones against all variants up to BA.1.<sup>9–11</sup> These MBCs, generated against the ancestral Hu-1 pre-fusion S encoded by the original mRNA vaccines, represent an underlying layer of immune protection associated with prevention of severe forms of COVID-19.<sup>12–16</sup> The impact of antigen imprinting in shaping the response and future B cell memory to breakthrough infection by drifted SARS-CoV-2 variants remains an open question of major importance in direct link with the current development of bivalent vaccines and rise in multiple antigenic exposures.

Upon re-infection, high-affinity cross-reactive MBCs are likely rapidly and selectively recruited from the repertoire, and MBC-derived antibodies provide a rapid protection against ongoing viral replication. When such antibodies merely mask their cognate immunodominant epitopes without effectively clearing the virus or when MBCs against specific epitopes carried by the variant strain are scarce or absent due to high antigenic distance between the original and latest strains encountered, a *de novo* naive B cell response can be initiated. These naive cells then undergo slow maturation within the germinal center (GC), resulting in the generation of new MBCs, further extending the diversity of the MBC repertoire. This point has been clearly documented in the context of influenza or SARS-CoV-2 infections<sup>15,17,18</sup> and in murine models.<sup>19</sup> Variant-specific MBCs, targeting mutated residues in the S receptor binding domain (RBD), have been detected in the context of Beta and Gamma SARS-CoV-2 primary infection,<sup>20,21</sup> suggesting that naive B cells solely specific for SARS-CoV-2 variants do exist in the repertoire. Recent reports, however, have suggested that the early response occurring in the context of Omicron BA.1 breakthrough infection or Hu-1 mRNA vaccination essentially mobilized cross-reactive clones against conserved S glycoprotein epitopes rather than recruiting novel naive B cells specific to mutated BA.1 residues.<sup>22–25</sup> This raises the question of the extent of repertoire remodeling and diversification that can occur in the context of such continued re-exposure to viral variants presenting low to moderate antigenic distance with the original strain, a key question in the design of future bivalent variant-based vaccines.

In this study, we combined single-cell multi-omics and functional analysis of several hundred naturally expressed antibodies

from RBD-specific MBCs to provide an extensive characterization of the progressive repertoire remodeling of the MBC repertoire occurring up to 6 months after Omicron BA.1 breakthrough infection in a cohort of mRNA-vaccinated individuals. BA.1 breakthrough infection almost exclusively mobilized pre-existing cross-reactive MBC clones, with limited recruitment of *de novo* BA.1-restricted responses. Nonetheless, our results demonstrate a reorganization of clonal hierarchy and new rounds of GC reaction that combine to maintain diversity and induce progressive maturation of the MBC repertoire against both Hu-1 and BA.1 SARS-CoV-2 S RBD variants.

## RESULTS

### Omicron BA.1 breakthrough infection boosts humoral and memory B cell response in triple-vaccinated individuals

To understand how the MBC repertoire elicited by vaccination is reshaped by BA.1 breakthrough infection and whether a specific response against its new epitopes occurs, we longitudinally analyzed the SARS-CoV-2-specific B cell responses in 15 individuals with no previous history of COVID-19, which were infected between end of December 2021 and end of January 2022 with Omicron BA.1, shortly after receiving a third dose of BNT162b2 mRNA vaccine (median: 32 days [13–106]). These individuals were sampled at three time points (<1, 2, and 6 months) after BA.1 breakthrough infection to fully characterize the B cell response from the early extrafollicular reaction to the late settlement of long-term memory, combining multiparameter flow cytometry analysis, single-cell RNA sequencing (scRNA-seq) and single-cell culture of S and RBD-specific B cells (Figures 1A and S1). Four of these individuals had been previously sampled after their second and/or third dose of mRNA vaccine<sup>9,26</sup> (see also Table S1). This provided us with the opportunity to decipher the selection processes occurring at the level of the MBC repertoire upon BA.1 breakthrough infection on a per-individual basis. As control, a parallel cohort of fifteen vaccinated individuals with no history of SARS-CoV-2 infection (SARS-CoV-2-naive) were also sampled at similar time points (<1, 2, and 6 months) after their third dose of mRNA vaccine.

Anti-Hu-1 and BA.1 S, RBD, and Nucleocapsid (N) IgG titers were robustly induced in all individuals after breakthrough infection (Figure 1B), with a good correlation between final anti-Hu-1 and BA.1 RBD titers in both cohorts (Figure 1C). N-specific IgG antibodies elicited after BA.1 breakthrough infection waned over the 6 months period, confirming the absence of new SARS-CoV-2 breakthrough in this cohort. The decrease in anti-RBD IgG titers over time was slightly more pronounced in vaccinated SARS-CoV-2-naive individuals than after BA.1 breakthrough infection, probably reflecting the magnitude of the initial response. In line with two recent studies,<sup>11,27</sup> plasma from uninfected patients demonstrated poor neutralizing activity against the BA.1 SARS-CoV-2 strain and progressively waning titers against the authentic D614G strain (Figures 1D and 1E). In comparison, all infected individuals rapidly displayed equally high neutralizing potential against both D614G and BA.1 SARS-CoV-2 strains. And these titers remained stable up to 6 months post infection, in line with recent observations by others.<sup>28</sup> Finally, longitudinal analyses using a flow panel that included

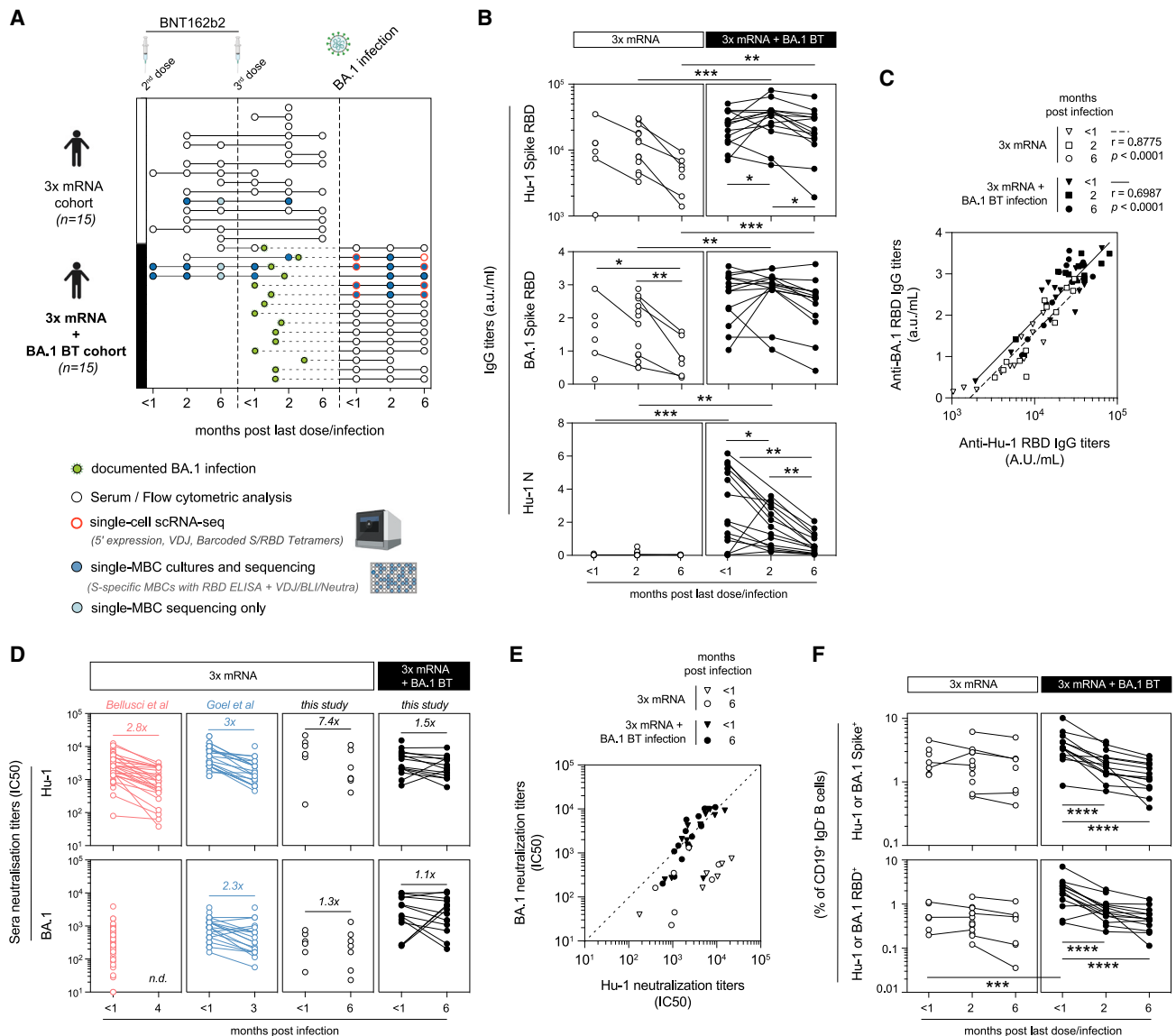


**Figure 1. Omicron BA.1 breakthrough infection boosts humoral response in triple-vaccinated individuals**

(A) Overview of cohort, sampling time points, and experimental procedures (see also Table S1 and Figure S1A for detailed sorting strategies). All donors received three doses of mRNA vaccine with or without a subsequent BA.1 breakthrough infection (3x mRNA + BA.1 BT [black dots] or 3x mRNA [white dots]). (B and C) (B) Anti-SARS-CoV-2 Hu-1 (top) or BA.1 RBD IgG titers (middle) and anti-Hu-1 Nucleocapsid (N) serum IgG titers (bottom) (a.u./mL) and (C) correlation between the anti BA.1 and Hu-1 RBD serum IgG titers at indicated time points. (D and E) (D) Half maximal inhibitory concentration ( $IC_{50}$ ) for donors' sera *in vitro* neutralization assay against authentic D614G (left) or BA.1 (right) SARS-CoV-2 virus, and (E) correlation between the anti BA.1 and D614G neutralization serum titers at indicated time points. (F) Proportion of all Hu-1 or BA.1 Spike (top) or RBD (bottom) specific memory B cells among total  $CD19^+ IgD^-$  B cells using flow cytometry on donor's peripheral blood mononuclear cells (PBMCs) at indicated time points (see also Figure S2A for detailed gating strategies). In all panels, individual donors are represented as dots, and longitudinal samplings from individual donors are connected. (B and F) Mixed model analysis with Tukey's correction for intra-group comparison and Sidak's correction for inter-group comparison. (C) Non-parametric Spearman correlation tests on pooled data from each cohort. \*\*\*\* $p < 0.0001$ , \*\*\* $p < 0.001$ , \*\* $p < 0.01$ , \* $p < 0.05$ . See also Figures S1 and S2 and Table S1.

Hu-1 and BA.1 S and RBD tetramers, demonstrated a major expansion of RBD-specific  $CD19^+ IgD^-$  B cells shortly after BA.1 breakthrough infection, more pronounced than the S-specific response and with a higher magnitude than that observed after the third mRNA vaccine in SARS-CoV-2-naive individuals (Figure 1F). Both infected and triple-vaccinated individ-

uals harbored a sizable and stable population of S and RBD-specific MBCs at the latest time point, after a contraction phase. These results show, as previously observed for SARS-CoV-2<sup>29</sup> or influenza,<sup>30</sup> that breakthrough infection in triple-vaccinated individuals induces a robust MBC and cross-neutralizing antibody response.

### BA.1 breakthrough infection mobilizes cross-reactive Spike-specific pre-existing MBCs

To characterize the fine specificity and the dynamics of the B cell response after BA.1 breakthrough infection, we first performed multiparametric fluorescence-activated cell sorting (FACS) analysis on all individuals from both cohorts using major markers of circulating B cell subpopulations (CD19, IgD, CD27, CD38, CD21, CD71 and CD11c) along with Hu-1 and BA.1 S and RBD tetramers (Figures S2A and S2B). As previously reported,<sup>23,31,32</sup> BA.1 breakthrough infection mostly mobilized B cells that displayed cross-reactivity against shared epitopes between Hu-1 and BA.1 S proteins, representing 70%–80% of all RBD-positive cells at any given time point post infection (Figure 2A; Table S2). Almost no B cells uniquely specific for BA.1 epitopes could be observed both at early time points, as previously described,<sup>23,31</sup> and at later time points when one can expect to start detecting new GC output (Figure 2A). Phenotypic analysis of CD19<sup>+</sup> IgD<sup>-</sup> switched B cell populations confirmed a massive expansion of S- and RBD-specific CD19<sup>+</sup> IgD<sup>-</sup> CD38<sup>-</sup> CD71<sup>+</sup> activated B cells (ABCs) occurring in the first couple of weeks post-BA.1 infection (Figures 2B, 2C, S2C, and S2D), together with the mobilization of CD27<sup>high</sup> CD38<sup>high</sup> antibody-secreting cells (ASCs) (Figure S2E), as previously described upon vaccination or primary infection of SARS-CoV-2 naive individuals.<sup>15,16</sup> ABCs were enriched in Hu-1/BA.1 cross-reactive cells, confirming the preferential recruitment of these cells in the context of a BA.1 breakthrough infection (Figure 2D). S- and RBD-specific atypical CD27<sup>-</sup> IgD<sup>-</sup> double-negative (DN) MBCs were also observed, but rarely in CD21<sup>-</sup> CD11c<sup>-</sup> DN2 cells (Figures 2C and S2C), a population that was previously described as a hallmark of the extrafollicular response in COVID-19.<sup>33,34</sup> After their initial expansion, the proportion of S- and RBD-specific ABCs decreased over time favoring, in a similar kinetic than observed in triple vaccinated individuals, the resting MBCs, which remain thereafter stable.

To further get access to the early ASC response, whose heterogeneous surface B cell receptor (BCR) expression prevents accurate specificity assessment, and to track potential recruitment of naive B cells to the extrafollicular response as well as repertoire and/or transcriptomic changes of the SARS-CoV-2 specific B cell response, we next performed scRNA-seq with parallel surface protein expression and immunoglobulin heavy chain (IgH) variable, diversity, and joining (VDJ) sequencing on sorted CD19<sup>+</sup> IgD<sup>-</sup> B cells at both early (<1 month) and late time points (6 months) from 4 individuals infected with BA.1 (Figure S1A). To focus on cells involved in the ongoing response, CD19<sup>+</sup> IgD<sup>-</sup> B cells were enriched in S- and/or RBD-specific B cells as well as in total ASCs (Figure S1A). Activated CD19<sup>high</sup> IgD<sup>+</sup> B cells were also sorted to track the potential mobilization of naive B cells (Figure S1A). In parallel, we sorted and single-cell cultured Hu-1 and/or BA.1 S- and RBD-specific B cells at different time points, and IgV<sub>H</sub> sequences obtained from these cells were further integrated to our scRNA-seq dataset to increase the number of identified S- and RBD-specific BCR sequences and add functional information regarding linked antibodies (Figures S1A, S1B, and S3A).

Unsupervised clustering analysis of scRNA-seq revealed 6 clusters according to their gene expression profile (Figure 2E). Among them, we distinguished CD21<sup>low</sup> CD38<sup>+</sup> CD71<sup>+</sup> ABCs, CD21<sup>-</sup> CD38<sup>-</sup> CD27<sup>-</sup> CD11c<sup>+</sup> DN2, and 2 clusters of ASCs with

both proliferative short-lived plasmablasts (PBs) and non-dividing plasma cells (PCs) based on surface protein and gene expression (Figures S2F and S2G). The remaining B cells were separated in two populations: a mixture of naive/transitional B cells and a resting MBC population (Figure 2E). At early time point after BA.1 breakthrough infection, S- and/or RBD-specific B cells mainly resided among the ABC and ASC clusters (Figures 2F and S2H), and they relocated to the resting MBC cluster at the 6 months' time point (Figure 2F). Concordant with our flow cytometry analysis, these cells were mostly cross-reactive against BA.1 and Hu-1 SARS-CoV-2 with only approximately 1.3% (14/1,075) of total specific cells analyzed only recognizing BA.1 S- or RBD-specific epitopes at any given time point.

Most of the RBD-specific B cells mobilized to the ASC and ABC responses upon BA.1 breakthrough infection harbored a high mutation load (median: 19 mutations), with less than 1% (4/546) unmutated sequences in ASCs and none in ABCs (Figure 2G; Table S3) and, overall, very limited frequencies of cells with intermediate number of mutational load (2–9 mutations). Similar results could be observed for S-specific B cells (Figures S2I–S2K). This is in stark contrast with our previous results showing that the RBD-specific ABC and ASC responses after primary infection<sup>15</sup> or 2 doses of mRNA vaccine mobilize cells with low IgV<sub>H</sub> mutations<sup>9</sup> (Figure 2G). Non-cross-reactive BA.1 RBD-specific cells appeared to display lower mutational loads (Figure 2H), but the very low number of recovered sequences prevented us from drawing any definite conclusion on this point.

Altogether, our results are consistent with a preferential recall of highly mutated pre-existing cross-reactive MBCs, massively expanding as ABCs and fueling the ASC response, with limited recruitment of naive B cells against BA.1-specific epitopes.

### BA.1 breakthrough infection remodels the MBC repertoire

One of the key questions in the context of immune imprinting relates to understanding how a secondary or tertiary antigen encounter reshapes the cognate MBC repertoire and impacts its diversity. First evidence of repertoire remodeling post-BA.1 breakthrough infection could be seen at the global S-specific repertoire level, with the proportion of RBD-specific MBCs among S-specific clones being significantly increased after BA.1 breakthrough infection (mean ± SEM of 51.8% ± 4.2% vs. 24.5% ± 3.4%;  $p < 0.0001$ ) and remaining significantly higher at 6 months as compared with individuals having solely received 3 doses of mRNA vaccine (mean ± SEM of 38.8% ± 2.9% vs. 20.2% ± 2.4%;  $p = 0.0007$ ) (Figure 3A). Further evidence of remodeling could be seen in the RBD-specific MBC repertoire at the clonal level. Longitudinal analysis of the overall RBD-specific MBC clonal diversity, reflected by Chao1 clonal richness index and Shannon entropy values showed no major loss of diversity, apart from the ASCs compartment post-BA.1 infection as expected (Figures 3B, S3A, and S3B). A sizable fraction of the RBD-specific clones was maintained over BA.1 infection (“sustained” clones) (Figure 3C), most of which being Hu-1/BA.1 cross-reactive (Figure 3D). However, in-depth analysis of the repertoire revealed marked remodeling at the clonal level, characterized by the loss of previously expanded clones, including Hu-1 RBD-specific only cells, and the emergence of new clones some of which eventually persisted over time (Figure 3C). In all longitudinally sampled individuals, sustained clones were still largely

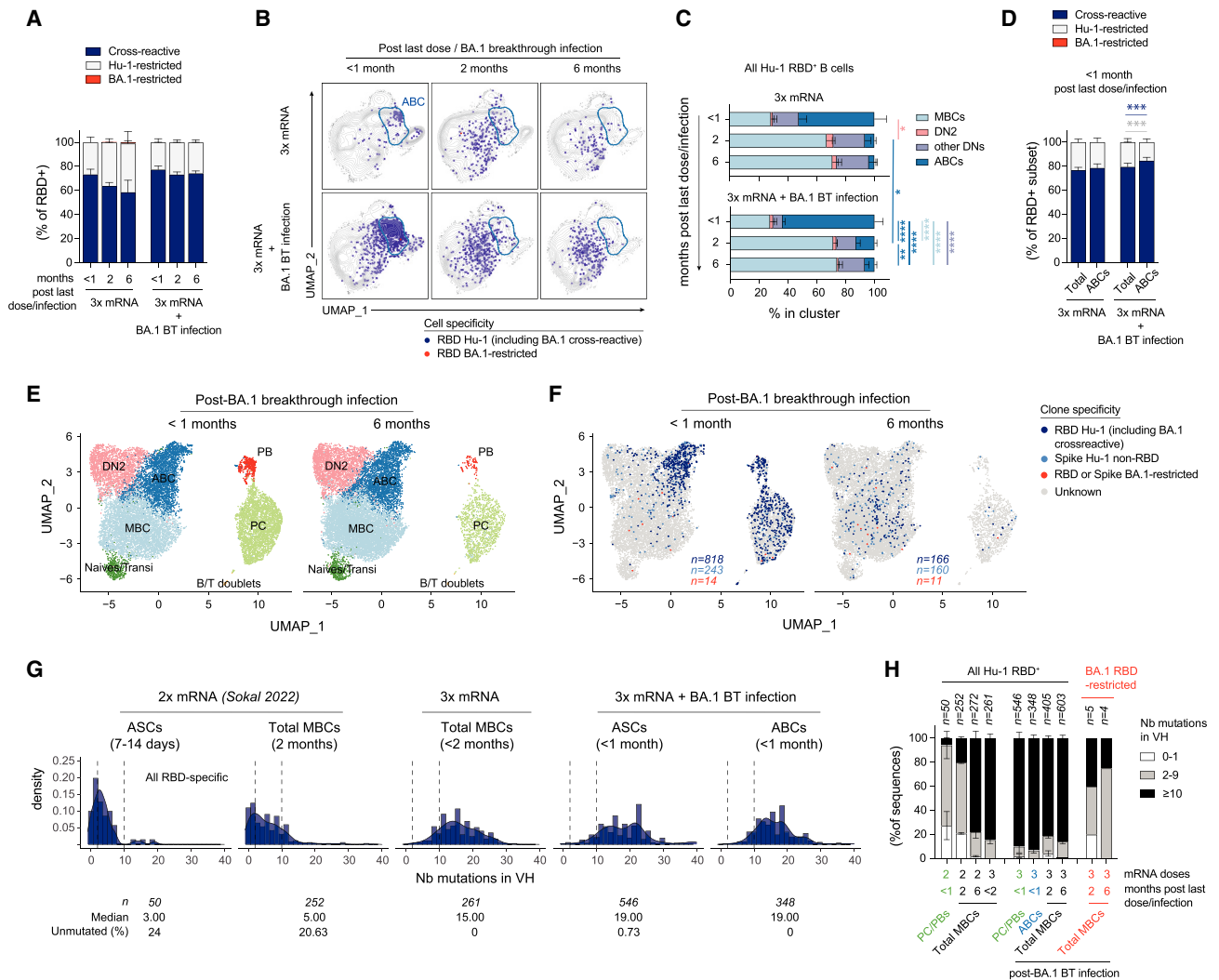


**Figure 2. BA.1 breakthrough infection-induced early response recruits Hu-1/BA.1 cross-reactive RBD-specific memory B cells**

(A–D) Flow cytometry analysis of PBMCs from donors at indicated time point after a third dose of mRNA vaccine with or without a subsequent BA.1 breakthrough infection (3x mRNA + BA.1 BT infection or 3x mRNA). (A) Frequency of SARS-CoV-2 Hu-1 and BA.1 cross-reactive (dark blue), Hu-1 (light gray), or BA.1-only (red) RBD-specific among all RBD-specific CD19<sup>+</sup> IgD<sup>-</sup> cells. (B) Uniform Manifold Approximation and Projection (UMAP) for concatenated CD19<sup>+</sup> IgD<sup>-</sup> cells from all donors analyzed by multiparametric fluorescence-activated cell sorting (FACS) analysis. RBD-specific B cells are overlaid in dark blue (Hu-1 ± BA.1 specific) or red (BA.1 only specific) dots on top of all cells. The CD71<sup>+</sup> ABC cluster is delineated by a blue line. (C) Distribution of Hu-1 RBD-specific CD19<sup>+</sup> IgD<sup>-</sup> B cells in cluster defined by manual gating strategies (see Figure S2A). (D) Mean percentage of Hu-1 and BA.1 cross-reactive (dark blue), Hu-1 (light gray), or BA.1-only (red) RBD-specific among total or CD71<sup>+</sup> (ABCs) RBD-specific CD19<sup>+</sup> IgD<sup>-</sup> B cells.

(E–H) scRNA-seq analysis of PMBCs from four donors within the 3x mRNA + BA.1 BT infection cohort. (E and F) UMAP for all VDJ-expressing cells at the <1 month (left, n = 13,644) and 6 months' time points post infection (right, n = 14,132), colored based on unsupervised clustering analysis (E) or indicated clone specificity (F). (G and H) Total number of IgV<sub>H</sub> mutations (G) and distribution in IgV<sub>H</sub> mutation groups (0–1, white; 2–9, gray; and ≥10 mutations, black) (H) for RBD-specific B cells at indicated time points post infection in indicated cell populations (2x mRNA data extracted from Sokal et al.,<sup>16</sup> antibody-secreting cells [ASCs] regroup both plasmablasts [PBs] and plasma cells [PCs]). In (G), dashed vertical lines indicate 1 and 10 mutations.

(A, C, and D) Mixed model analysis with Tukey's correction for intra-group comparison and Sidak's correction for inter-group comparison. \*\*\*\*p < 0.0001, \*\*\*p < 0.001, \*\*p < 0.01, \*p < 0.05.

See also Figure S2 and Tables S2 and S3.

represented in the MBC repertoire at 6 months (Figure 3C), with no clear reduction in the individual frequencies of these clones (Figure 3E). Germline V<sub>H</sub> gene usage in RBD-specific sequences showed no major changes after BA.1 infection relative to those found after a third dose of mRNA vaccine in our longitudinally

sampled donors (Figure 3F), albeit a progressive enrichment in IGHV1-69 gene usage, as previously described,<sup>22</sup> is to be noted.

These results suggest that the immune response against the Omicron BA.1 variant does not solely mobilize the top cross-reactive MBCs but also expands MBC clones previously found

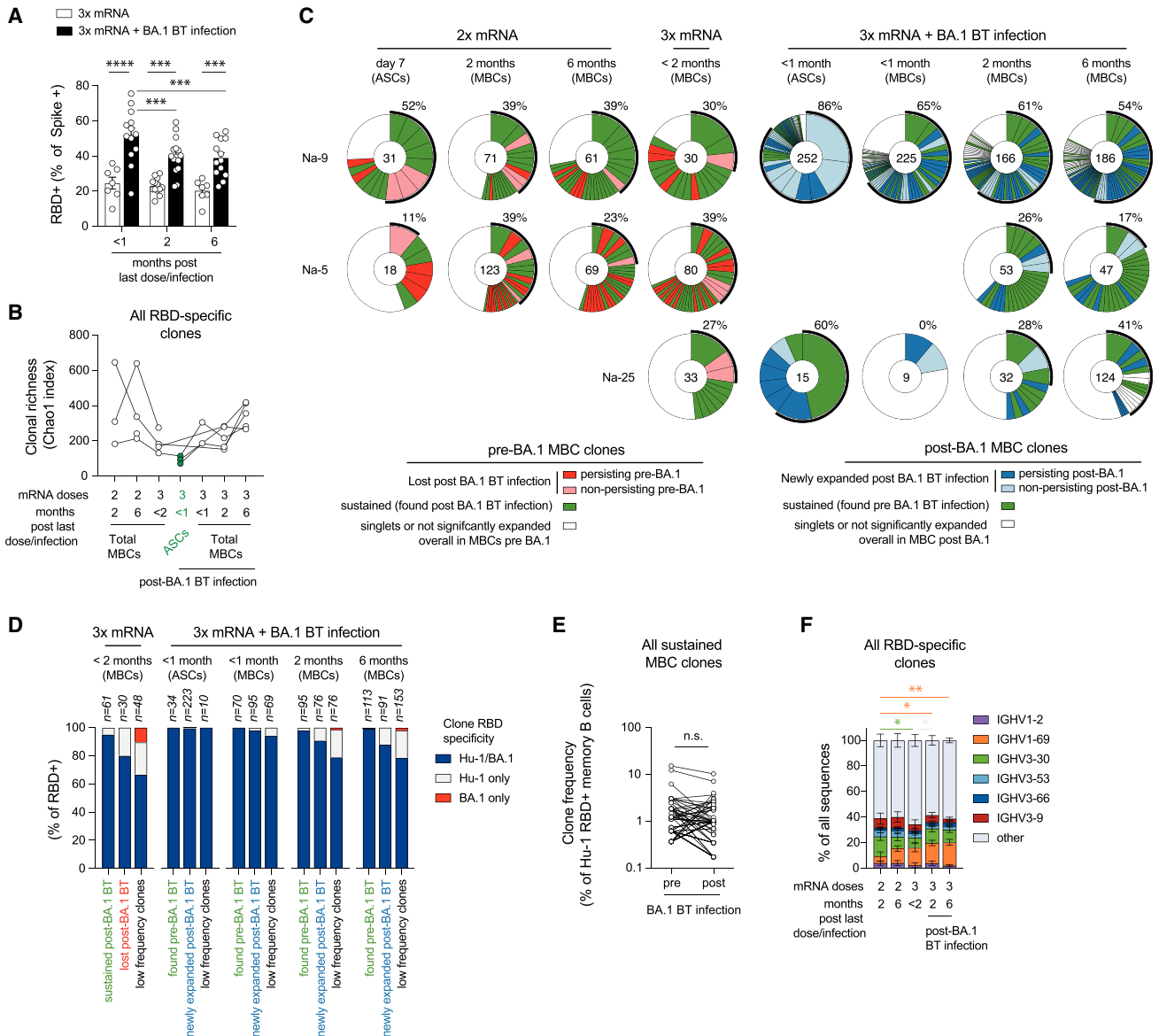


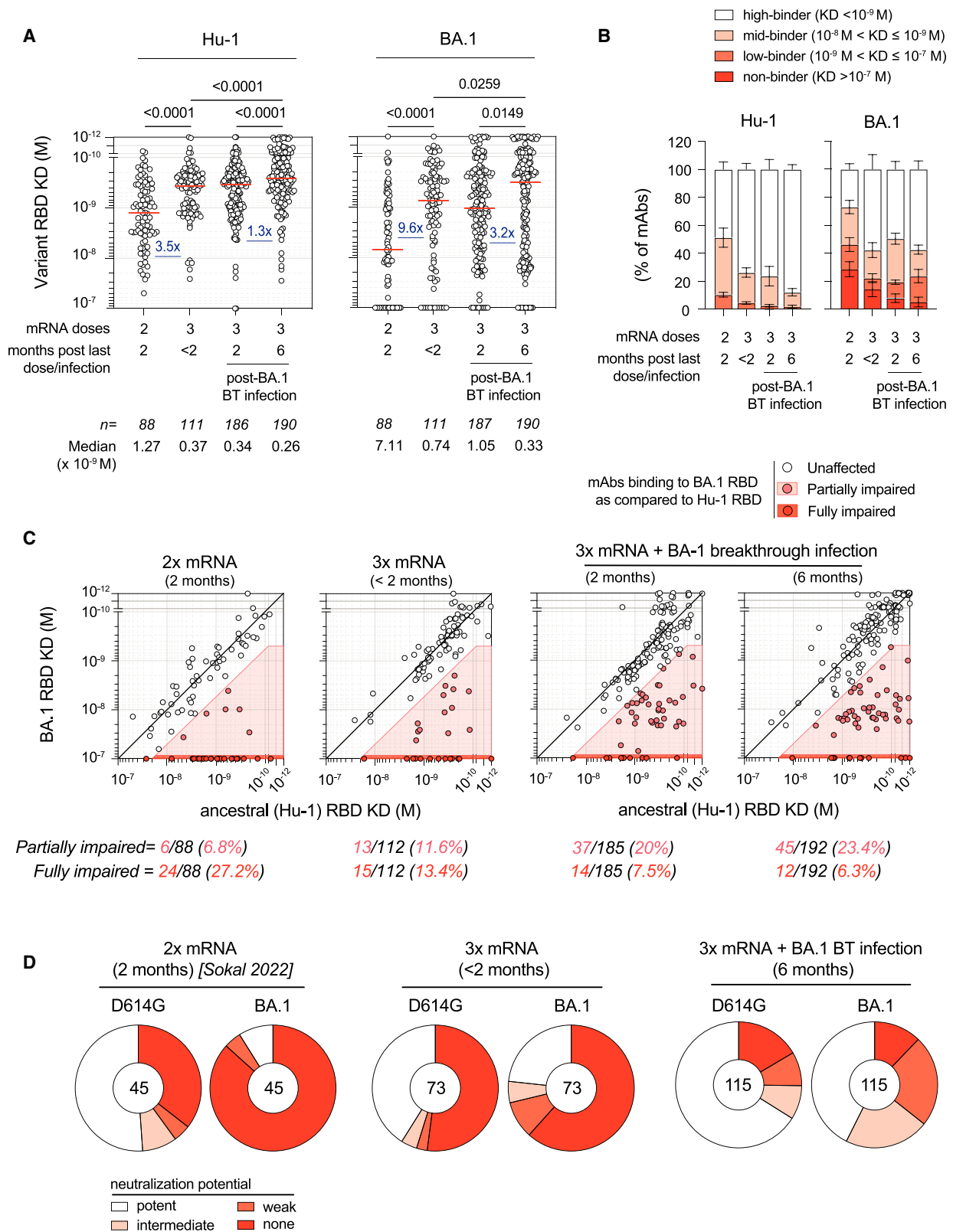
**Figure 3. BA.1 breakthrough infection induces partial remodeling of the specific memory B cell repertoire**

(A) Frequency of RBD (Hu-1 and/or BA.1) specific CD19<sup>+</sup> IgD<sup>-</sup> B cells among Spike (Hu-1 and/or BA.1) specific CD19<sup>+</sup> IgD<sup>-</sup> B cells in 3x mRNA (white) or 3x mRNA + BA.1 BT infection (black) cohorts at indicated time points.

(B–F) Repertoire analysis of RBD-specific MBCs and ASCs in individual donors from the second dose of mRNA vaccine up to 6 months after BA.1 breakthrough infection. (B) Evolution of clonal richness (Chao1 index) over time. Each line represents one individual donor. (C) Longitudinal clonal distribution in 3 donors. Slice sizes are proportional to the size of each clone. Clones found before and after BA.1 BT infection are depicted in green; expanded clones lost upon BA.1 BT infection are in light red if found at a single time point or in dark red if persisting at several time points pre-BA.1; and newly expanded clones found after BA.1 BT infection are in light blue if found at a single time point or in dark blue if found at several time points. Singletons or expanded clones whose overall frequency post-BA.1 did not reach the frequency of singletons pre-BA.1 are represented in white. Outer black semi-circular line indicates the proportion of sequences belonging to expanded clones at a given time point. The total number of sequences is indicated at the pie center. (D) Percentage of cells specific for Hu-1/BA.1, Hu-1, or BA.1 RBD among total RBD-specific cells sequenced, grouped according to their clone’s evolution upon BA.1 BT infection, as defined in (C). (E) Frequency of sustained RBD-specific clones among total RBD-specific cells sequenced at any time point pre- or post-BA.1 BT infection. (F) IgV<sub>H</sub> gene usage distribution in CD19<sup>+</sup>IgD<sup>-</sup> RBD (Hu-1 and/or BA.1) specific B cell at indicated time points.

(A and F) Mixed model analysis with Tukey’s correction. (D) Two-tailed Wilcoxon test. \*\*\*\*p < 0.0001, \*\*\*p < 0.001, \*\*p < 0.01, \*p < 0.05.

See also [Figure S3](#) and [Table S3](#).



(legend on next page)

at low frequency in the repertoire or recruits cross-reactive naive B cells (Figure 3D), maintaining in the process the overall clonal diversity and thus likely mitigating the negative impact of immune imprinting.

### BA.1 breakthrough infection drives additional affinity maturation and increased overall neutralization breadth of the MBC repertoire

To evaluate the functional consequences of the observed MBC repertoire evolution, we first assayed the affinity against Hu-1 and BA.1 RBD proteins of over 600 randomly selected monoclonal IgGs, isolated from the supernatants of single-cell cultured RBD-specific MBCs from longitudinally sampled donors pre- and post-BA.1 breakthrough infection. We detected a clear increase in affinity of the overall antibody pool against BA.1 RBD between 2 and 6 months after BA.1 infection (Figure 4A). Despite being already of high affinity against Hu-1 RBD proteins after 3 doses of mRNA vaccine—median dissociation constant ( $K_D$ ) of  $3.7 \times 10^{-10}$  M (Figure 4A) and  $73.7 \pm 7.3\%$  of tested monoclonal antibodies (mAbs) with measured affinity below 1 nM (Figure 4B)—further modest affinity increases against the Hu-1 RBD could also be observed, a trend seen in 4 out of 5 individuals (Figure S4A; Table S3). The increase in affinity against BA.1 RBD did not solely result from the selection of clones recognizing unmutated residues as the proportion of MBC-derived mAbs binding both ancestral Hu-1 and BA.1 RBD with similar affinities (labeled “unaffected,” Figures 4C and S4B) remained stable over time, representing between 60% and 70% of the overall repertoire. Instead, the increase in affinity was seen in the “affected” clones pool, with a progressive loss of the non-binder/fully impaired clones against BA.1 RBD ( $K_D > 10^{-7}$  M) up to the latest time point after BA.1 breakthrough infection (Figure 4C). This increased affinity was further paralleled by a progressive improvement in neutralization potential of the overall MBC repertoire against both D614G and BA.1 SARS-CoV-2 viruses (Figure 4D), with notably 40% of potent neutralizing antibodies (>75% at 16 nM) and a strong reduction in mAbs with no detectable neutralization potency against BA.1 SARS-CoV-2 (i.e., <25% neutralization at 16 nM) at the latest time point.

To analyze how this extended to later variants of the Omicron sublineages, we next tested affinity against BA.2 RBD, which shares most of BA.1 mutations, and BA.5 RBD, which notably contains two key additional mutations (L452R and F486V) inside immunodominant epitopes.<sup>35</sup> A similar, albeit non-significant, trend for an overall increase in affinity was observed for BA.2 RBD (Figures 5A and 5B). The median affinity of the

MBC repertoire against BA.5 RBD, on the other hand, showed the opposite trend (Figures 5A and 5B), partly driven by an increase in the frequency of partially affected clones against BA.5 over time (Figure 5C). Two by two comparisons of binding affinities between Hu-1 and BA.1, BA.2, and BA.5 RBD variants further pinpointed toward a specific increase in mAbs solely affected in their binding to BA.5 (labeled “BA.5-affected”) and thus likely targeting epitopes containing one of BA.5-specific mutations (L452R or F486V) (Figures 5D, S4C, and S4D). On the contrary, the frequency of mAbs showing weaker binding to all tested Omicron lineage RBDs (labeled “BA.1/2/5-affected”) and likely targeting one of the core Omicron lineage mutations (G339D, S375F, K417N, N440K, G446S, S477N, T478K, E484K/Q/A) remained stable over time. And we only observed a few clones affected by BA.1-specific (G446S/G496S), BA.1/BA.2 (Q493R), and BA.2/BA.5-shared (T376A/D405N/R408S) mutations. Germline  $V_H$  gene usage according to RBD binding properties did not change over time (Figure S4E) and highlighted VH1-69 as a major component of mAbs specifically targeting RBD residues mutated in BA.5, as recently shown by others.<sup>31</sup>

Although the overall frequency of broadly binding antibodies did decrease over time, they still accounted for  $44 \pm 11\%$  of all antibodies in all assayed donors 6 months after BA.1 breakthrough infection (Figures 5D and S4C). And, in line with the overall affinity maturation observed against Hu-1 and BA.1, and the fact that these antibodies likely recognize epitopes unmutated in BA.5, broadly binding antibodies also showed detectable affinity maturation against BA.5 (Figure 5E) and increased neutralization potency against all three tested SARS-CoV-2 variants (Figures 5F, S5A, and S5B). However, as previously described,<sup>9</sup> only a fraction of these broadly binding antibodies displayed intermediate or potent neutralization against all viruses, suggesting a lack of selective pressure. A similar increase in affinity and neutralization potency could be seen for BA.1/2/5-affected mAbs (Figures S5A and S5B). And this appeared to explain most of the overall increase in neutralization potency against BA.5 of the whole MBC repertoire (Figure 5F). This substantial gain of neutralization potency was equally observed for neutralizing antibodies using IGHV1-69, IGHV3-30, or IGHV3-53/66 genes, suggesting that these recurrent classes of anti-RBD antibodies can be recruited to participate in neutralization against mutated epitopes (Figures S5A and S5C).

Overall, these results demonstrate that the MBC repertoire remodeling observed following BA.1 breakthrough infection leads to an improved affinity and breadth of the MBC repertoire. Part of

### Figure 4. BA.1 breakthrough infection drives additional maturation of Hu-1/BA.1 cross-reactive RBD-specific memory B cells

(A) Dissociation constants ( $K_D$ , expressed as moles/L) measured by biolayer interferometry against Hu-1 and BA.1 RBDs for naturally expressed monoclonal antibodies randomly selected from single-cell culture supernatants of RBD-specific MBCs isolated from 6 donors, including 3 longitudinally analyzed before and after BA.1 BT infection (see Figure S4A). Numbers of tested monoclonal and median affinity per time point are indicated at the bottom of each graph.

(B) Frequencies of Hu-1 and BA.1 RBD high-binders ( $K_D < 10^{-9}$  M), mid-binders ( $10^{-9} \leq K_D < 10^{-8}$  M), low-binders ( $10^{-8} \leq K_D < 10^{-7}$  M), or non-binders ( $K_D \geq 10^{-7}$  M) among tested monoclonal antibodies at indicated time points.

(C) Measured  $K_D$ s against BA.1 versus Hu-1 RBDs for all tested monoclonal antibodies. Light and dark red shaded zones indicate partially and fully impaired BA.1-affected monoclonal antibodies, respectively (see STAR Methods). Respective frequencies are shown at the bottom of the graph (see also Figure S4B).

(D) Distribution in *in vitro* neutralization potency against authentic D614G and BA.1 SARS-CoV-2 virus for randomly selected RBD-specific monoclonal antibodies at indicated time points. Number at the center of the pie indicates the total number of tested monoclonal antibodies.

(A) Kruskal-Wallis tests with Benjamini, Krieger, and Yekutieli false discovery rate correction for multiple comparisons (q values are indicated in the figure). (B and E) Mixed model analysis with Tukey's correction. (D) Chi-squared test. \*\*\*\*p < 0.0001, \*p < 0.05.

See also Figures S4 and S5 and Table S3.

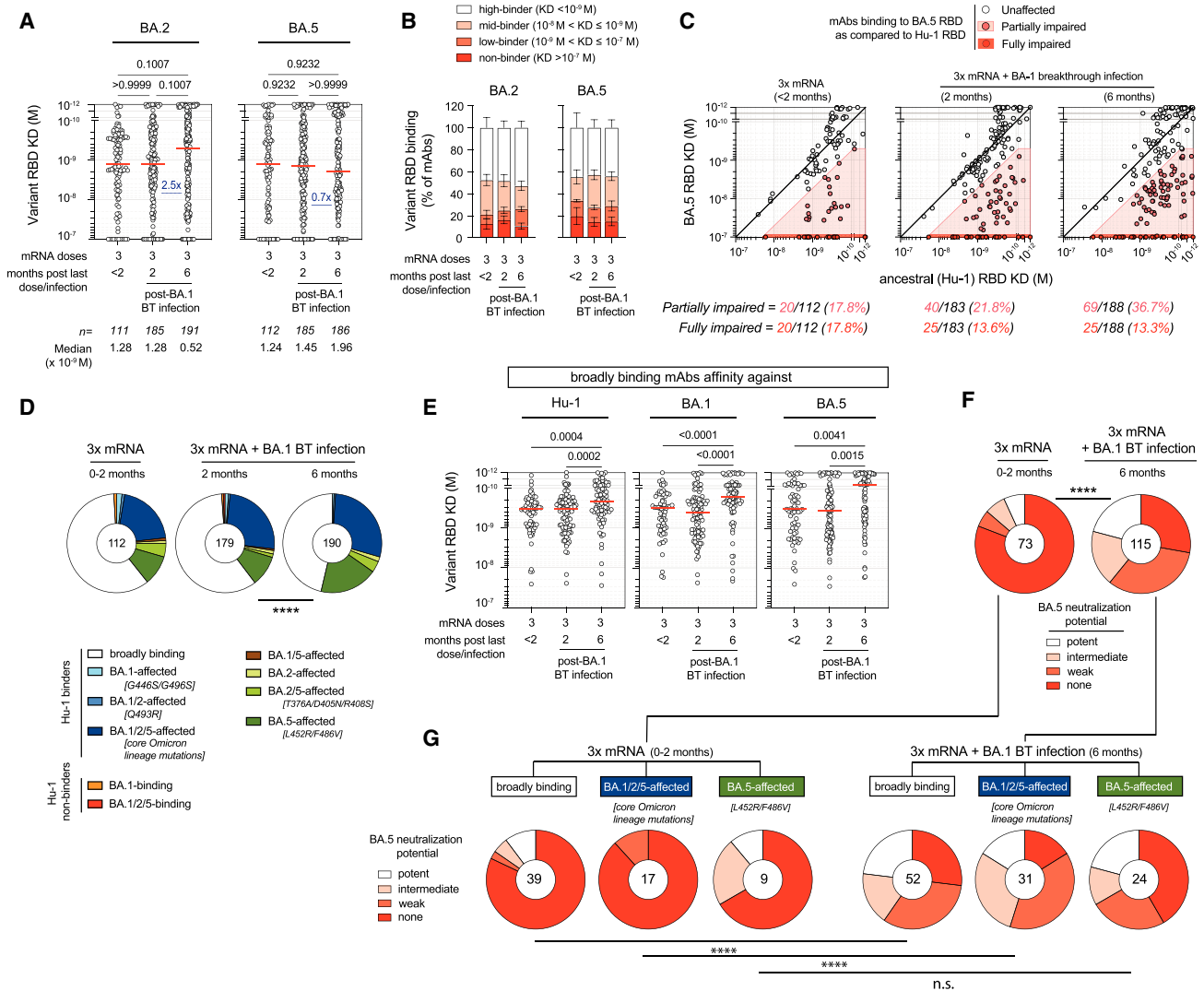


**Figure 5. BA.1 breakthrough infection broadly increases neutralization breadth of MBC-derived mAbs**

(A) Dissociation constants ( $K_D$ , expressed as moles/L) measured by biolayer interferometry against BA.2 and BA.5 RBDs for all tested monoclonal antibodies displayed in Figure 4A (see Figure S4A). Numbers of tested monoclonal and median affinity per time point are indicated at the bottom of each graph. (B) Frequencies of BA.2 and BA.5 RBD high-binders ( $K_D < 10^{-9}$  M), mid-binders ( $10^{-9} \leq K_D < 10^{-8}$  M), low-binders ( $10^{-8} \leq K_D < 10^{-7}$  M), or as non-binders ( $K_D \geq 10^{-7}$  M) among tested monoclonal antibodies at indicated time point. (C) Measured  $K_D$ s against BA.5 versus Hu-1 RBDs for all tested monoclonal antibodies. Light and dark red shaded zones indicate partially and fully impaired BA.5-affected monoclonal antibodies, respectively (see STAR Methods). Respective frequencies are shown at the bottom of the graph (see also Figure S4B). (D) Overall distribution of tested monoclonal according to their binding patterns against Hu-1, BA.1, BA.2, and BA.5 RBDs at indicated time points. (E) Measured  $K_D$  against Hu-1, BA.1, and BA.5 RBDs for broadly binding monoclonal antibodies tested in (A) at indicated time point. (F and G) Distribution in *in vitro* neutralization potency against authentic BA.5 SARS-CoV-2 virus at indicated time point for randomly selected naturally expressed monoclonal antibodies (F) or monoclonal antibodies falling in the broadly binding, BA.1/2/5-affected, and BA.5-affected groups as defined in (D) and (G). In (D), (F), and (G), numbers at the center of each pie chart indicate the total number of tested monoclonal antibodies. (A and E) Kruskal-Wallis tests with Benjamini, Krieger, and Yekutieli false discovery rate correction for multiple comparisons (q values are indicated in the figure). (D, F, and G) Chi-squared tests. \*\*\*\*p < 0.0001. See also Figures S4 and S5 and Table S3.

this comes from redirecting the response toward conserved immunodominant epitopes in BA.1, with the inherent risk that these epitopes could be mutated in later variants, as seen with BA.5. Such risk, however, is counterbalanced by a global enhancement in affinity against all epitopes included in the BA.1 RBD. This mechanism provides substantial neutralization benefit against both past and future variants sharing similar epitopes.

**Selective expansion of MBCs outside GC and additional cycles of GC maturation sequentially contribute to MBC repertoire remodeling**

Such remodeling and maturation of the MBC repertoire post-BA.1 breakthrough infection could be simply explained by the expansion of high-affinity, pre-mutated MBCs independently of any GC reaction.<sup>36</sup> Alternatively, this could also reflect a

progressive output of clones having undergone new rounds of GC reaction, as recently shown in the context of a third mRNA vaccine dose.<sup>25</sup> The first hypothesis would be expected to lead to early changes post infection, also impacting the ASC response, whereas the second would be expected to have a more progressive impact associated with the progressive output of clones from GCs.

In line with the early recruitment and proliferation of MBC clones outside of a GC reaction, we could detect an increased frequency of cells within clones bearing identical sequences in multiple donors at the earlier time points post 2<sup>nd</sup> and 3<sup>rd</sup> vaccine doses and post-BA.1 infection (Figure S6A), resulting in an overall drop in sequence diversity (Figure S6B). The diversity, however, appeared mostly restored at the 6 months' time point. A preferential recruitment of a highly mutated subpopulation of pre-existing MBC clones to the ASC compartment could also be observed when analyzing total IgV<sub>H</sub> mutations as well as replacing mutations in the heavy-chain complementarity-determining regions (CDRs) in Hu-1/BA.1 cross-reactive RBD-specific ASCs generated early after BA.1 infection (Figures 6A and S6C) and to a lesser extent in clonally related MBC clones at the same time point (Figure S6D). In parallel to the contraction of the early MBC/ASC response, longitudinal evolution in mutation profile in cross-reactive RBD-specific MBCs revealed an initial decrease in the average total number of V<sub>H</sub> mutations, seen at 2 months post-BA.1 infection (Figures 6A, S6C, and S6D). This was notably associated with an increased presence of lowly mutated cells, including 2.77% of unmutated sequences (Figure 6B). Sequences with low numbers of mutations (<10 mutations) could mostly be seen in low-frequency clones early post-BA.1 infection, thereafter, slowly transiting to the newly expanded pool (Figures 6C and 6D). Subsequently, the average number of IgV<sub>H</sub> mutations and replacing mutations in CDRs of cross-reactive MBCs significantly increased between 2 and 6 months after BA.1 infection (Figures 6A, S6B, and S6E,  $p < 0.01$ ), reaching similar mutational loads as seen early post 3<sup>rd</sup> vaccine dose or BA.1 infection.

This parallel increase in mutational load and affinity maturation observed between 2 and 6 months after BA.1 infection in the MBC repertoire in our longitudinally sampled donors suggested that naive B cells or previously generated MBCs could be recruited to newly formed or vaccine-induced persisting GCs. To investigate this point at the clonal level, we next looked at IgV<sub>H</sub> mutation number evolution in persisting clones pre- and post-BA.1 infection. Out of 22 total Hu-1/BA.1 cross-reactive RBD-specific clones with more than 7 sequences identified at least twice between the post-3<sup>rd</sup> mRNA vaccine dose time point and later time points after BA.1 breakthrough infection, 3 clones were detected to be significantly accumulating mutations over time (Figure 6E;  $p = 0.00001$ ,  $p = 0.0086$ , and  $p = 0.0203$ , respectively). These numbers, although clearly reduced as compared with the frequency of clones in evolution seen between the 2<sup>nd</sup> and 3<sup>rd</sup> vaccine dose (3 out of 4 with more than 7 sequences, Figure 6F), are in line with a similar analysis recently performed in the context of influenza vaccine recall response in which such GC response could be validated by direct staining of draining lymph nodes.<sup>18,37</sup> These clones included both sustained (clone 5,584 from donor Na-25) and newly expanded clones, in line with the fact that cells from both sustained and newly expanded/low-fre-

quency MBC clones showed a similar tendency to gain in affinity toward BA.1 RBD variant between 2 and 6 months after infection (Figure S6F). Nevertheless, we found no systematic correlation between the increase in total mutation load and affinity at the repertoire (Figure S6G) or clonal level, with notably only one out of the three clones identified as statistically increasing their overall mutational load over time after infection also increasing in affinity (Figure 6E). Differences between the two groups of clones were more marked for neutralization potency (Figure S6H). Although the majority of lost or low-frequency clones pre-BA.1 infection was non or poor-neutralizers of both the D614G and BA.1 SARS-CoV-2 viruses, newly expanded and low-frequency clones seen 6 months after BA.1 infection reached similar neutralization potency as their counterparts from sustained clones.

Overall, these analyses suggest that the MBC repertoire is dynamically reshaped by an early extra-GC expansion and subsequent contraction of a few selected highly mutated cross-reactive clones and the concomitant settlement of a more diverse pool of cells in the repertoire likely, but not necessarily exclusively, representing new GC outputs.

## DISCUSSION

Little is known about the remodeling induced by an infection by a viral variant showing antigenic drift on a repertoire of preformed mature human MBCs. Selective boosting of cross-reactive antibody specificities by prior exposures was historically coined, in the context of influenza, "original antigenic sin."<sup>38,39</sup> Studies in mice have shown that upon reinfection or re-exposure to an antigen, the MBC pool can expand outside the GCs in an affinity-dependent selective process,<sup>40</sup> differentiate in PCs, or reenter GCs to undergo affinity maturation.<sup>19,41</sup> These secondary GCs, however, mostly engage naive clones, allowing diversification against new epitopes.<sup>19,36,40,42,43</sup> Understanding how these different paths shape the recall response in humans to an antigenic variant of respiratory viruses such as SARS-CoV-2 remains an open question with fundamental implications for the design of future vaccination booster strategies.

As previously reported for influenza<sup>30</sup> and more recently SARS-CoV-2 variant breakthrough infections<sup>22,31</sup> or variant-based vaccination,<sup>25</sup> the initial ABC response following BA.1 breakthrough infection is clearly dominated by highly mutated vaccine-induced cross-reactive MBC clones eliciting broadly cross-neutralizing antibodies, a point that we could further confirm at the level of ASCs. Here, we show that this imprinting was not limited to the early extrafollicular response but persisted over time, with very few BA.1-restricted naive B cell clones recruited in *de novo* GCs. High-affinity serum antibodies elicited during the primary response have recently been demonstrated to reduce the recruitment of naive B cells to GCs during secondary responses.<sup>44</sup> Such a process, however, is epitope-specific<sup>44</sup> and, in individuals infected during the first wave of COVID-19, MBCs specific for the S of seasonal coronaviruses elicited non-neutralizing antibodies against SARS-CoV-2 that did not impair the recruitment of near-germline B cell clones recognizing novel epitopes present in SARS-CoV-2 RBD.<sup>13,16</sup> Similarly, the massive antibody response against non-neutralizing immunodominant epitopes upon a second immunization with H5N1 vaccine or HIV

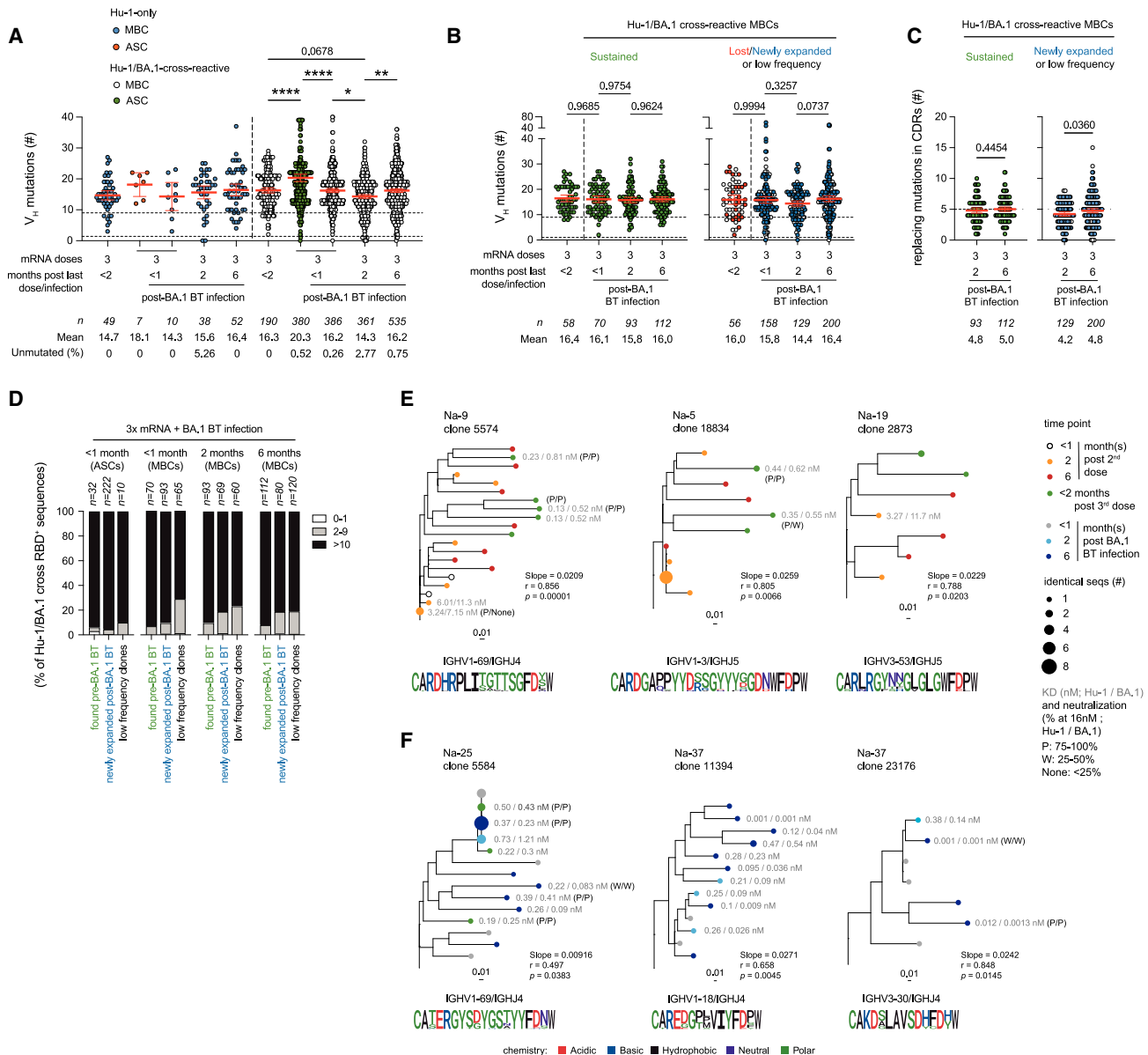


**Figure 6. MBC repertoire remodeling and maturation post-BA.1 breakthrough infection reflects successive contributions from extra-GC and GC responses together with the recruitment of low-frequency lowly mutated MBC clones**

(A) Total number of IgV<sub>H</sub> mutations in RBD-specific MBCs or ASCs, sorted according to their specificity (Hu-1 RBD-only [left, blue and red dots] versus Hu-1/BA.1 RBD cross-reactive [right, white and green dot]) at indicated time points before and after BA.1 BT infection. Mean ± SEM are shown.

(B–D) Number of total (B) or CDR3 replacing IgV<sub>H</sub> mutations (C), and (D) distribution in total number of IgV<sub>H</sub> mutations (0–1, white; 2–9, gray; and ≥ 10, black) at indicated time points in Hu-1/BA.1 cross-reactive RBD-specific MBCs, grouped according to their clone’s evolution upon BA.1 BT infection, as defined in Figure 3C.

(E and F) Phylogenetic trees for six RBD-specific clones identified as significantly evolving between 2 and 3 mRNA vaccinations (n = 3, E) and post-BA.1 BT infections (n = 3, F), scaled according to IgV<sub>H</sub> mutation frequencies. Color code and dot size reflect, respectively, time of sampling and number of identical sequences found at each time point. CDR3 (amino acids) frequency plot logos, slope for the rate of somatic mutation accumulation over time (slope), and p value (p) of the date randomization test comparing the Pearson’s correlation (r) between divergence and time in tree are shown at the bottom of each tree. Averaged (median) RBD affinity (gray) and neutralization potencies (black, : P: >75%, W: 25%–50%, and None: <25% neutralization at 16 nM) for Hu-1 (left) and BA.1 (right) are indicated on the right side of each tested monoclonal antibodies in the tree.

(A and B) ordinary one-way ANOVA with Sidak’s correction for multiple comparisons.

(C) Unpaired t tests. \*\*\*\*p < 0.0001, \*\*p < 0.01, \*p < 0.05.

See also Figure S6 and Table S3.

Env proteins masked these epitopes, thereby promoting maturation of naive B cells in GCs against a different set of non-dominant epitopes.<sup>45–47</sup> In our study, all individuals had recently received a third dose of Hu-1-pre-fusion S protein-based mRNA vaccine, but this vaccine boost did not prevent subsequent BA.1 breakthrough infection and MBC recruitment to the extrafollicular response. Omicron's antigenic distance should thus have enabled exposure of mutated epitopes of the RBD, as previously described in the context of primary infection with SARS-CoV-2 variants.<sup>21</sup> One possible explanation for the limited strain-specific response against BA.1 could be the absence of a sufficient amount of viral antigen to activate naive B cells, as the virus is rapidly cleared by neutralizing antibodies produced by newly recruited cross-reactive MBCs. Alternatively, the high initial frequency of cross-reactive MBCs, even if displaying variable affinity to mutated BA.1 RBD epitopes, may also provide them with a competitive advantage that restricts antigen accessibility to naive B cells. It remains that we did observe a late recruitment of unmutated and lowly mutated cross-reactive cells in the MBC repertoire. These cells could represent naive B cells recruited to an ongoing GC reaction.<sup>48,49</sup> This would suggest the active selection of cross-reactive B cells in the GC. Alternatively, some of these cells could also be the result of the expansion of pre-existing lowly mutated MBCs outside any GC reaction.

The absence of *de novo* recruitment of BA.1-restricted naive B cells and the parallel focus on cross-reactive MBC clones could have induced progressive reduction in overall diversity, a point we only observed transiently upon infection and mostly in the ASCs. And, although non-cross-reactive Hu-1-specific MBCs tend to be excluded from the early ABC/extra-GC response, their frequency returned to pre-BA.1 infection baseline at later time points in the response. Changes in the repertoire up to 6 months after BA.1 infection, however, were not solely restricted to the expansion and later contraction of a cross-reactive MBC response through the extra-GC response. The longitudinal tracking of RBD-specific clones revealed a more complex picture with a progressive remodeling of the MBC repertoire, refining clonal hierarchy against BA.1 epitopes, and resulting in a clear improvement in both overall affinity and neutralization breadth. Although overall functional variations were clearly more subtle than what can be detected over time in newly vaccinated individuals<sup>12–16</sup> (and this study), our results suggest new cycles of GC maturation for naive B cells and vaccine-induced MBCs following BA.1 breakthrough infection. This is in line with the recent description of a sustained GC response following a vaccine boost in double-vaccinated individuals.<sup>25</sup> Additionally, the magnitude of the GC reaction was probably underestimated in our analysis as investigating such marks in the context of a recall response in the PBMCs, with an already fully mature MBC repertoire, is clearly challenging.<sup>37</sup> Limited longitudinal sampling and overrepresentation in the early repertoire post-antigenic exposure of sequences from cells having undergone recent expansion in the extra GC response likely add up to restrict our analysis to high-frequency persisting clones. The increase in mutational load observed in low-frequency and newly expanded clones later in the response clearly suggests a key contribution of these cells to the remodeling of the MBC repertoire. Whether such initially low-frequency clones reenter GCs remains to be demonstrated. This would require direct sampling

of draining lymphoid organs. Altogether, the remodeling of the MBC repertoire upon BA.1 breakthrough infection is in line with a recent theoretical modeling study pointing toward the GC reaction during a secondary reaction as a key mechanism to reintroduce diversity in the MBC pool.<sup>36</sup> The contribution of the extra-GC expansion of MBC clones and the GCs output to remodel the MBC repertoire appears nevertheless variable from one individual to another.

Finally, our results also raise two clinically relevant points. First, breakthrough infection clearly switched the overall MBC response toward RBD epitopes. Second, post-breakthrough maturation of the MBC response could be considered to expand toward non-mutated immunodominant epitopes on the RBD. The modified pattern of immunodominance at the S level could be explained by the epitope masking of highly conserved region of the S2 domain by the pre-existing antibody response<sup>31</sup> or by differential conformational states of SARS-CoV-2 S protein between the vaccine and the virus. Whether this bears any functional relevance regarding overall protection against future infections, positive or negative, remains to be tested. The modified pattern of immunodominance at the RBD level suggests that repeated challenges with variant S proteins may simply increase the selective advantage of specific amino-acid substitutions, as exemplified here for the L452Q/R mutation responsible for part of the immune escape potential of the BA.5 strain from IGHV1-69 and IGHV3-9 class of antibodies.<sup>31,50</sup> In terms of vaccination, it suggests that further strategies to extend the immune response beyond the conserved RBD epitopes will be needed to favor diversity and cope with future antigenic drifts of the SARS-CoV-2.

Collectively, these data show that although BA.1 breakthrough infection induces a cross-reactive extra-GC expansion, the clonal diversity is maintained by the GCs' output to remodel and improve neutralization potency and breadth of the MBC repertoire.

### Limitations of the study

Potential limitations of our work include the limited number of subjects that could be included in this study for in-depth MBC characterization as well as the sparse sampling that could be achieved for some of these donors at some time points. This may have introduced some bias in clonal representation. As such, the extent of observed clonal remodeling and affinity maturation should be interpreted with caution, notably in donors for which the number of analyzable sequences was low, potentially affecting the labeling of clones as “lost,” “sustained,” or “newly expanded” and limiting the contribution of individual donors to the overall pool of tested mAbs. To limit such biases, we have attempted to select similar number of clones per donor when testing affinities and neutralization and to display individual donor data in [Figures S1–S6](#). All patients studied were infected with BA.1 early after their third vaccine boost (see [Figure 1A](#); [Table S1B](#)), as has been the case for a sizable fraction of early Omicron breakthrough infections. In this setting, mRNA vaccine-induced residual GCs driven by the Hu-1 pre-fusion S were recently activated.<sup>25</sup> As we were not able to perform direct longitudinal comparisons with non-infected individuals having solely received 3 doses of mRNA vaccine, we cannot exclude that part of the observed clonal remodeling would have occurred in non-infected individuals. It also remains to be investigated whether such a situation, with two closely related antigens being presented

concomitantly as currently implemented in bivalent vaccines, might favor the selection of cross-reactive MBCs and affinity maturation against both antigens. Affinity maturation was only observed against the BA.1 RBD in a recent preprint analyzing MBCs following a similar BA.1 breakthrough infection in individuals mostly remote from their second mRNA vaccine dose.

## STAR★METHODS

Detailed methods are provided in the online version of this paper and include the following:

- KEY RESOURCES TABLE
- RESOURCE AVAILABILITY
  - Lead Contact
  - Materials Availability
  - Data and Code Availability
- EXPERIMENTAL MODEL AND SUBJECT DETAILS
  - Study participants
  - Virus strains
- METHOD DETAILS
  - Anti-RBD (S) and -N SARS-CoV-2 antibodies assay
  - Recombinant protein purification
  - Flow cytometry and cell sorting
  - Single-cell culture
  - ELISA
  - Single-cell RNA-seq library preparation and sequencing
  - Single-cell IgH sequencing
  - Single-cell gene expression analysis
  - Computational analyses of VDJ sequences
  - Affinity measurement using biolayer interferometry (Octet)
  - Virus neutralization assay
- QUANTIFICATION AND STATISTICAL ANALYSIS
- ADDITIONAL RESOURCES

## SUPPLEMENTAL INFORMATION

Supplemental information can be found online at <https://doi.org/10.1016/j.immuni.2023.07.007>.

## ACKNOWLEDGMENTS

We thank Garnett Kelsoe (Duke University, Durham, NC, USA) for providing us with the human cell culture system, together with invaluable advice. We thank all the physicians, Constance Guillaud, Raphael Lepeule, Frédéric Schlemmer, Elena Fois, Henri Guillet, Nicolas De Prost, Sarah Feray, and Pascal Lim, whose patients were included in this study. Funding: this study has been labeled as a National Research Priority by the National Orientation Committee for Therapeutic Trials and other research on COVID-19 (CAPNET). The investigators would like to acknowledge ANRS|Emerging Infectious Diseases for their scientific support, the French Ministry of Health and Prevention, the French Ministry of Higher Education, Research, and Innovation, and the Fondation Princesse Grace for their funding and support. Assistance Publique – Hôpitaux de Paris (AP-HP, Département de la Recherche Clinique et du Développement) was the promotor and sponsor of MEMO-COV-2. Work in the Unit of Structural Virology was funded by the Institut Pasteur, Urgence COVID-19 Fundraising Campaign of Institut Pasteur. P.B. acknowledges funding from the Institut Pasteur and the Institut National de la Santé et de la Recherche Médicale (INSERM). A.S. was supported by a Poste d'accueil from INSERM.

## AUTHOR CONTRIBUTIONS

Conceptualization, A.S., G.B.-S., J.-C.W., F.A.R., P.B., M. Mahévas, and P.C.; data curation, A.S., L.H., M. Broketa, G.B.-S., I.F., I.A., L.L., and P.C.; formal analysis, A.S., P.C., L.H., M. Broutin, G.B.-S., I.A., A.R., M.B.-A., S. Fourati, A.V., and I.F.; funding acquisition, J.-C.W., C.-A.R., S. Fillatreau, P.B., P.C., and M. Mahévas; investigation, A.S., L.H., I.A., P.L.-R., M.F., J.M., and A.V.; methodology, A.S., J.-C.W., F.A.R., P.B., M. Mahévas, and P.C.; project administration, P.C. and M. Mahévas; resources, I.F., J.-M.P., F.P., S. Fourati, E.C., M. Michel, B.G., S.G., G.M., Y.N., P.B., F.A.R., and M. Mahévas; software, P.C.; supervision, J.-C.W., P.B., F.A.R., P.C., and M. Mahévas; validation, A.S., A.V., M. Broketa, P.C., and M. Mahévas; visualization, A.S., M. Broutin, I.A., M. Mahévas, and P.C.; writing – original draft, A.S., M. Mahévas, and P.C.; writing – review & editing, all authors.

## DECLARATION OF INTERESTS

Outside of the submitted work, M. Mahévas received research funds from GSK and personal fees from LFB and Amgen. J.-C.W. received consulting fees from Institut Mérieux. P.B. received consulting fees from Regeneron Pharmaceuticals.

Received: January 27, 2023

Revised: May 12, 2023

Accepted: July 6, 2023

Published: August 4, 2023

## REFERENCES

1. van der Straten, K., Guerra, D., van Gils, M.J., Bontjer, I., Caniels, T.G., van Willigen, H.D.G., Wynberg, E., Poniman, M., Burger, J.A., Bouhuijs, J.H., et al. (2022). Antigenic cartography using sera from sequence-confirmed SARS-CoV-2 variants of concern infections reveals antigenic divergence of Omicron. *Immunity* 55, 1725–1731.e4. <https://doi.org/10.1016/j.immuni.2022.07.018>.
2. Dejnirattisai, W., Huo, J., Zhou, D., Zahradnik, J., Supasa, P., Liu, C., Duyvesteyn, H.M.E., Ginn, H.M., Mentzer, A.J., Tuekprakhon, A., et al. (2022). SARS-CoV-2 Omicron-B.1.1.529 leads to widespread escape from neutralizing antibody responses. *Cell* 185, 467–484.e15. <https://doi.org/10.1016/j.cell.2021.12.046>.
3. Garcia-Beltran, W.F., Lam, E.C., St. Denis, K., Nitido, A.D., Garcia, Z.H., Hauser, B.M., Feldman, J., Pavlovic, M.N., Gregory, D.J., Poznansky, M.C., et al. (2021). Multiple SARS-CoV-2 variants escape neutralization by vaccine-induced humoral immunity. *Cell* 184, 2372–2383.e9. <https://doi.org/10.1016/j.cell.2021.03.013>.
4. Muik, A., Lui, B.G., Wallisch, A.-K., Bacher, M., Mühl, J., Reinholz, J., Ozhelvaci, O., Beckmann, N., de la Güimil Garcia, R., Poran, A., et al. (2022). Neutralization of SARS-CoV-2 Omicron by BNT162b2 mRNA vaccine-elicited human sera. *Science* 375, 678–680. <https://doi.org/10.1126/science.abn7591>.
5. Cameroni, E., Bowen, J.E., Rosen, L.E., Saliba, C., Zepeda, S.K., Culap, K., Pinto, D., VanBlargan, L.A., De Marco, A., di Iulio, J., et al. (2022). Broadly neutralizing antibodies overcome SARS-CoV-2 Omicron antigenic shift. *Nature* 602, 664–670. <https://doi.org/10.1038/s41586-021-04386-2>.
6. Planas, D., Saunders, N., Maes, P., Guivel-Benhassine, F., Planchais, C., Buchrieser, J., Bolland, W.H., Porrot, F., Staropoli, I., Lemoine, F., et al. (2022). Considerable escape of SARS-CoV-2 Omicron to antibody neutralization. *Nature* 602, 671–675. <https://doi.org/10.1038/s41586-021-04389-z>.
7. Carreño, J.M., Alshammary, H., Tcheou, J., Singh, G., Raskin, A.J., Kawabata, H., Sominsky, L.A., Clark, J.J., Adelsberg, D.C., Bielak, D.A., et al. (2022). Activity of convalescent and vaccine serum against SARS-CoV-2 Omicron. *Nature* 602, 682–688. <https://doi.org/10.1038/s41586-022-04399-5>.
8. Planas, D., Bruel, T., Staropoli, I., Guivel-Benhassine, F., Porrot, F., Maes, P., Grzelak, L., Prot, M., Mougari, S., Planchais, C., et al. (2023). Resistance of Omicron subvariants BA.2.75.2, BA.4.6, and BQ.1.1 to

- neutralizing antibodies. *Nat. Commun.* 14, 824. <https://doi.org/10.1038/s41467-023-36561-6>.
9. Sokal, A., Broketa, M., Barba-Spaeth, G., Meola, A., Fernández, I., Fourati, S., Azzaoui, I., de La Selle, A., Vandenberghe, A., Roeser, A., et al. (2022). Analysis of mRNA vaccination-elicited RBD-specific memory B cells reveals strong but incomplete immune escape of the SARS-CoV-2 Omicron variant. *Immunity* 55, 1096–1104.e4. <https://doi.org/10.1016/j.immuni.2022.04.002>.
  10. Wang, Z., Muecksch, F., Cho, A., Gaebler, C., Hoffmann, H.H., Ramos, V., Zong, S., Cipolla, M., Johnson, B., Schmidt, F., et al. (2022). Analysis of memory B cells identifies conserved neutralizing epitopes on the N-terminal domain of variant SARS-CoV-2 spike proteins. *Immunity* 55, 998–1012.e8. <https://doi.org/10.1016/j.immuni.2022.04.003>.
  11. Goel, R.R., Painter, M.M., Lundgreen, K.A., Apostolidis, S.A., Baxter, A.E., Giles, J.R., Mathew, D., Pattekar, A., Reynaldi, A., Khoury, D.S., et al. (2022). Efficient recall of Omicron-reactive B cell memory after a third dose of SARS-CoV-2 mRNA vaccine. *Cell* 185, 1875–1887.e8. <https://doi.org/10.1016/j.cell.2022.04.009>.
  12. Dugan, H.L., Stamper, C.T., Li, L., Changrob, S., Asby, N.W., Halfmann, P.J., Zheng, N.Y., Huang, M., Shaw, D.G., Cobb, M.S., et al. (2021). Profiling B cell immunodominance after SARS-CoV-2 infection reveals antibody evolution to non-neutralizing viral targets. *Immunity* 54, 1290–1303.e7. <https://doi.org/10.1016/j.immuni.2021.05.001>.
  13. Gaebler, C., Wang, Z., Lorenzi, J.C.C., Muecksch, F., Finkin, S., Tokuyama, M., Cho, A., Jankovic, M., Schaefer-Babajew, D., Oliveira, T.Y., et al. (2021). Evolution of antibody immunity to SARS-CoV-2. *Nature* 591, 639–644. <https://doi.org/10.1038/s41586-021-03207-w>.
  14. Rodda, L.B., Netland, J., Shehata, L., Pruner, K.B., Morawski, P.A., Thouvenel, C.D., Takehara, K.K., Eggenberger, J., Hemann, E.A., Waterman, H.R., et al. (2021). Functional SARS-CoV-2-specific immune memory persists after mild COVID-19. *Cell* 184, 169–183.e17. <https://doi.org/10.1016/j.cell.2020.11.029>.
  15. Sokal, A., Chappert, P., Barba-Spaeth, G., Roeser, A., Fourati, S., Azzaoui, I., Vandenberghe, A., Fernandez, I., Meola, A., Bouvier-Alias, M., et al. (2021). Maturation and persistence of the anti-SARS-CoV-2 memory B cell response. *Cell* 184, 1201–1213.e14. <https://doi.org/10.1016/j.cell.2021.01.050>.
  16. Sokal, A., Barba-Spaeth, G., Fernández, I., Broketa, M., Azzaoui, I., de La Selle, A., Vandenberghe, A., Fourati, S., Roeser, A., Meola, A., et al. (2021). mRNA vaccination of naive and COVID-19-recovered individuals elicits potent memory B cells that recognize SARS-CoV-2 variants. *Immunity* 54, 2893–2907.e5. <https://doi.org/10.1016/j.immuni.2021.09.011>.
  17. Koutsakos, M., and Ellebedy, A.H. (2023). Immunological imprinting: understanding COVID-19. *Immunity* 56, 909–913. <https://doi.org/10.1016/j.immuni.2023.04.012>.
  18. Turner, J.S., Zhou, J.Q., Han, J., Schmitz, A.J., Rizk, A.A., Alsoussi, W.B., Lei, T., Amor, M., McIntire, K.M., Meade, P., et al. (2020). Human germinal centres engage memory and naive B cells after influenza vaccination. *Nature* 586, 127–132. <https://doi.org/10.1038/s41586-020-2711-0>.
  19. Victora, G.D., and Nussenzweig, M.C. (2022). Germinal centers. *Annu. Rev. Immunol.* 40, 413–442. <https://doi.org/10.1146/annurev-immunol-120419-022408>.
  20. Evans, J.P., Zeng, C., Qu, P., Faraone, J., Zheng, Y.M., Carlin, C., Bednash, J.S., Zhou, T., Lozanski, G., Mallampalli, R., et al. (2022). Neutralization of SARS-CoV-2 Omicron sub-lineages BA.1, BA.1.1, and BA.2. *Cell Host Microbe* 30, 1093–1102.e3. <https://doi.org/10.1016/j.chom.2022.04.014>.
  21. Agudelo, M., Muecksch, F., Schaefer-Babajew, D., Cho, A., DaSilva, J., Bednarski, E., Ramos, V., Oliveira, T.Y., Cipolla, M., Gazumyan, A., et al. (2022). Plasma and memory antibody responses to Gamma SARS-CoV-2 provide limited cross-protection to other variants. *J. Exp. Med.* 219, e20220367. <https://doi.org/10.1084/jem.20220367>.
  22. Kaku, C.I., Starr, T.N., Zhou, P., Dugan, H.L., Khalifé, P., Song, G., Champney, E.R., Mielcarz, D.W., Geoghegan, J.C., Burton, D.R., et al. (2023). Evolution of antibody immunity following Omicron BA.1 breakthrough infection. *Nat. Commun.* 14, 2751. <https://doi.org/10.1038/s41467-023-38345-4>.
  23. Quandt, J., Muik, A., Salisch, N., Lui, B.G., Lutz, S., Krüger, K., Wallisch, A.K., Adams-Quack, P., Bacher, M., Finlayson, A., et al. (2022). Omicron BA.1 breakthrough infection drives cross-variant neutralization and memory B cell formation against conserved epitopes. *Sci. Immunol.* 7, eabq2427. <https://doi.org/10.1126/sciimmunol.abq2427>.
  24. Muik, A., Lui, B.G., Bacher, M., Wallisch, A.K., Toker, A., Finlayson, A., Krüger, K., Ozhelvaci, O., Grikscheit, K., Hoehl, S., et al. (2022). Omicron BA.2 breakthrough infection enhances cross-neutralization of BA.2.12.1 and BA.4/BA.5. *Sci. Immunol.* 7, eade2283. <https://doi.org/10.1126/sciimmunol.ade2283>.
  25. Alsoussi, W.B., Malladi, S.K., Zhou, J.Q., Liu, Z., Ying, B., Kim, W., Schmitz, A.J., Lei, T., Horvath, S.C., Sturtz, A.J., et al. (2023). SARS-CoV-2 Omicron boosting induces de novo B cell response in humans. *Nature* 617, 592–598. <https://doi.org/10.1038/s41586-023-06025-4>.
  26. Sokal, A., Bastard, P., Chappert, P., Barba-Spaeth, G., Fourati, S., Vandenberghe, A., Lagouge-Roussey, P., Meyts, I., Gervais, A., Bouvier-Alias, M., et al. (2023). Human type I IFN deficiency does not impair B cell response to SARS-CoV-2 mRNA vaccination. *J. Exp. Med.* 220, e20220258. <https://doi.org/10.1084/jem.20220258>.
  27. Bellusci, L., Golding, H., and Khurana, S. (2023). Therapeutic potential of convalescent plasma and hyperimmune immunoglobulins against SARS-CoV-2 BQ.1, BQ.1.1, and XBB variants. *J. Clin. Invest.* 133, e168583. <https://doi.org/10.1172/JCI168583>.
  28. Lee, W.S., Tan, H.-X., Reynaldi, A., Esterbauer, R., Koutsakos, M., Nguyen, J., Amarasena, T., Kent, H.E., Aggarwal, A., Turville, S.G., et al. (2023). Durable reprogramming of neutralising antibody responses following breakthrough Omicron infection. Preprint at medRxiv. <https://doi.org/10.1101/2023.02.19.23286159>.
  29. Park, Y.J., Pinto, D., Walls, A.C., Liu, Z., De Marco, A., Benigni, F., Zatta, F., Silacci-Fregni, C., Bassi, J., Sprouse, K.R., et al. (2022). Imprinted antibody responses against SARS-CoV-2 Omicron sublineages. *Science* 378, 619–627. <https://doi.org/10.1126/science.adc9127>.
  30. Dugan, H.L., Guthmiller, J.J., Arevalo, P., Huang, M., Chen, Y.Q., Neu, K.E., Henry, C., Zheng, N.Y., Lan, L.Y.-L., Tepora, M.E., et al. (2020). Preexisting immunity shapes distinct antibody landscapes after influenza virus infection and vaccination in humans. *Sci. Transl. Med.* 12, eabd3601. <https://doi.org/10.1126/scitranslmed.abd3601>.
  31. Kaku, C.I., Bergeron, A.J., Ahlm, C., Normark, J., Sakharkar, M., Forsell, M.N.E., and Walker, L.M. (2022). Recall of preexisting cross-reactive B cell memory after Omicron BA.1 breakthrough infection. *Sci. Immunol.* 7, eabq3511. <https://doi.org/10.1126/sciimmunol.abq3511>.
  32. Wang, Z., Zhou, P., Muecksch, F., Cho, A., Ben Tanfous, T., Canis, M., Witte, L., Johnson, B., Raspe, R., Schmidt, F., et al. (2022). Memory B cell responses to Omicron subvariants after SARS-CoV-2 mRNA breakthrough infection in humans. *J. Exp. Med.* 219, e20221006. <https://doi.org/10.1084/jem.20221006>.
  33. Woodruff, M.C., Ramonell, R.P., Haddad, N.S., Anam, F.A., Rudolph, M.E., Walker, T.A., Truong, A.D., Dixit, A.N., Han, J.E., Cabrera-Mora, M., et al. (2022). Dysregulated naive B cells and de novo autoreactivity in severe COVID-19. *Nature* 611, 139–147. <https://doi.org/10.1038/s41586-022-05273-0>.
  34. Woodruff, M.C., Ramonell, R.P., Nguyen, D.C., Cashman, K.S., Saini, A.S., Haddad, N.S., Ley, A.M., Kyu, S., Howell, J.C., Ozturk, T., et al. (2020). Extrafollicular B cell responses correlate with neutralizing antibodies and morbidity in COVID-19. *Nat. Immunol.* 21, 1506–1516. <https://doi.org/10.1038/s41590-020-00814-z>.
  35. Tuekprakhon, A., Nutalai, R., Djokaite-Guraliuc, A., Zhou, D., Ginn, H.M., Selvaraj, M., Liu, C., Mentzer, A.J., Supasa, P., Duyvesteyn, H.M.E., et al. (2022). Antibody escape of SARS-CoV-2 Omicron BA.4 and BA.5 from vaccine and BA.1 serum. *Cell* 185, 2422–2433.e13. <https://doi.org/10.1016/j.cell.2022.06.005>.
  36. Van Beek, M., Nussenzweig, M.C., and Chakraborty, A.K. (2022). Two complementary features of humoral immune memory confer protection

- against the same or variant antigens. *Proc. Natl. Acad. Sci. USA* 119. e2205598119. <https://doi.org/10.1073/pnas.2205598119>.
37. Hoehn, K.B., Turner, J.S., Miller, F.I., Jiang, R., Pybus, O.G., Ellebedy, A.H., and Kleinstein, S.H. (2021). Human B cell lineages associated with germinal centers following influenza vaccination are measurably evolving. *eLife* 10, e70873. <https://doi.org/10.7554/eLife.70873>.
  38. Monto, A.S., Malosh, R.E., Petrie, J.G., and Martin, E.T. (2017). The doctrine of original antigenic sin: separating good from evil. *J. Infect. Dis.* 215, 1782–1788. <https://doi.org/10.1093/infdis/jix173>.
  39. Francis, T. (1953). On the doctrine of original antigenic sin. *Proc. Am. Philos. Soc.* 572–578.
  40. Shlomchik, M.J. (2018). Do memory B cells form secondary germinal centers? Yes and no. *Cold Spring Harb. Perspect. Biol.* 10, a029405. <https://doi.org/10.1101/cshperspect.a029405>.
  41. Shlomchik, M.J., and Weisel, F. (2012). Germinal center selection and the development of memory B and plasma cells. *Immunol. Rev.* 247, 52–63. <https://doi.org/10.1111/j.1600-065X.2012.01124.x>.
  42. Mesin, L., Schiepers, A., Ersching, J., Barbulescu, A., Cavazzoni, C.B., Angelini, A., Okada, T., Kurosaki, T., and Victora, G.D. (2020). Restricted clonality and limited germinal center reentry characterize memory B cell reactivation by boosting. *Cell* 180, 92–106.e11. <https://doi.org/10.1016/j.cell.2019.11.032>.
  43. Pape, K.A., Taylor, J.J., Maul, R.W., Gearhart, P.J., and Jenkins, M.K. (2011). Different B cell populations mediate early and late memory during an endogenous immune response. *Science* 331, 1203–1207. <https://doi.org/10.1126/science.1201730>.
  44. Tas, J.M.J., Koo, J.H., Lin, Y.C., Xie, Z., Steichen, J.M., Jackson, A.M., Hauser, B.M., Wang, X., Cottrell, C.A., Torres, J.L., et al. (2022). Antibodies from primary humoral responses modulate the recruitment of naive B cells during secondary responses. *Immunity* 55, 1856–1871.e6. <https://doi.org/10.1016/j.immuni.2022.07.020>.
  45. Cirelli, K.M., Carnathan, D.G., Nogal, B., Martin, J.T., Rodriguez, O.L., Upadhyay, A.A., Enemuoh, C.A., Gebru, E.H., Choe, Y., Viviano, F., et al. (2019). Slow delivery immunization enhances HIV neutralizing antibody and germinal center responses via modulation of immunodominance. *Cell* 177, 1153–1171.e28. <https://doi.org/10.1016/j.cell.2019.04.012>.
  46. Ellebedy, A.H., Nachbagauer, R., Jackson, K.J.L., Dai, Y.N., Han, J., Alsoussi, W.B., Davis, C.W., Stadlbauer, D., Roupheal, N., Chromikova, V., et al. (2020). Adjuvanted H5N1 influenza vaccine enhances both cross-reactive memory B cell and strain-specific naive B cell responses in humans. *Proc. Natl. Acad. Sci. USA* 117, 17957–17964. <https://doi.org/10.1073/pnas.1906613117>.
  47. Lee, J.H., Sutton, H.J., Cottrell, C.A., Phung, I., Ozorowski, G., Sewall, L.M., Nedellec, R., Nakao, C., Silva, M., Richey, S.T., et al. (2022). Long-primed germinal centres with enduring affinity maturation and clonal migration. *Nature* 609, 998–1004. <https://doi.org/10.1038/s41586-022-05216-9>.
  48. de Carvalho, R.V.H., Ersching, J., Barbulescu, A., Hobbs, A., Castro, T.B.R., Mesin, L., Jacobsen, J.T., Phillips, B.K., Hoffmann, H.H., Parsa, R., et al. (2023). Clonal replacement sustains long-lived germinal centers primed by respiratory viruses. *Cell* 186, 131–146.e13. <https://doi.org/10.1016/j.cell.2022.11.031>.
  49. Hägglöf, T., Cipolla, M., Loewe, M., Chen, S.T., Mesin, L., Hartweg, H., ElTanbouly, M.A., Cho, A., Gazumyan, A., Ramos, V., et al. (2023). Continuous germinal center invasion contributes to the diversity of the immune response. *Cell* 186, 147–161.e15. <https://doi.org/10.1016/j.cell.2022.11.032>.
  50. Pushparaj, P., Nicoletto, A., Sheward, D.J., Das, H., Castro Dopico, X., Perez Vidakovics, L., Hanke, L., Chernyshev, M., Narang, S., Kim, S., et al. (2023). Immunoglobulin germline gene polymorphisms influence the function of SARS-CoV-2 neutralizing antibodies. *Immunity* 56, 193–206.e7. <https://doi.org/10.1016/j.immuni.2022.12.005>.
  51. Bruel, T., Stéfic, K., Nguyen, Y., Toniutti, D., Staropoli, I., Porrot, F., Guivel-Benhassine, F., Bolland, W.H., Planas, D., Hadjadj, J., et al. (2022). Longitudinal analysis of serum neutralization of SARS-CoV-2 Omicron BA.2, BA.4, and BA.5 in patients receiving monoclonal antibodies. *Cell Rep. Med.* 3, 100850. <https://doi.org/10.1016/j.xcrm.2022.100850>.
  52. Hsieh, C.L., Goldsmith, J.A., Schaub, J.M., DiVenere, A.M., Kuo, H.C., Javanmardi, K., Le, K.C., Wrapp, D., Lee, A.G., Liu, Y., et al. (2020). Structure-based design of prefusion-stabilized SARS-CoV-2 spikes. *Science* 369, 1501–1505. <https://doi.org/10.1126/science.abd0826>.
  53. Crickx, E., Chappert, P., Sokal, A., Weller, S., Azzaoui, I., Vandenberghe, A., Bonnard, G., Rossi, G., Fadeev, T., Storck, S., et al. (2021). Rituximab-resistant splenic memory B cells and newly engaged naive B cells fuel relapses in patients with immune thrombocytopenia. *Sci. Transl. Med.* 13. <https://doi.org/10.1126/scitranslmed.abc3961>.
  54. Luo, X.M., Maarschalk, E., O’Connell, R.M., Wang, P., Yang, L., and Baltimore, D. (2009). Engineering human hematopoietic stem/progenitor cells to produce a broadly neutralizing anti-HIV antibody after in vitro maturation to human B lymphocytes. *Blood* 113, 1422–1431. <https://doi.org/10.1182/blood-2008-09-177139>.
  55. Tiller, T., Meffre, E., Yurasov, S., Tsuiji, M., Nussenzweig, M.C., and Wardemann, H. (2008). Efficient generation of monoclonal antibodies from single human B cells by single cell RT-PCR and expression vector cloning. *J. Immunol. Methods* 329, 112–124. <https://doi.org/10.1016/j.jim.2007.09.017>.
  56. Hao, Y., Hao, S., Andersen-Nissen, E., Mauck, W.M., Zheng, S., Butler, A., Lee, M.J., Wilk, A.J., Darby, C., Zager, M., et al. (2021). Integrated analysis of multimodal single-cell data. *Cell* 184, 3573–3587.e29. <https://doi.org/10.1016/j.cell.2021.04.048>.
  57. Hafemeister, C., and Satija, R. (2019). Normalization and variance stabilization of single-cell RNA-seq data using regularized negative binomial regression. *Genome Biol.* 20, 296. <https://doi.org/10.1186/s13059-019-1874-1>.
  58. Korsunsky, I., Millard, N., Fan, J., Slowikowski, K., Zhang, F., Wei, K., Baglaenko, Y., Brenner, M., Loh, P.R., and Raychaudhuri, S. (2019). Fast, sensitive and accurate integration of single-cell data with Harmony. *Nat. Methods* 16, 1289–1296. <https://doi.org/10.1038/s41592-019-0619-0>.
  59. Gupta, N.T., Vander Heiden, J.A., Uduman, M., Gadala-Maria, D., Yaari, G., and Kleinstein, S.H. (2015). Change-O: a toolkit for analyzing large-scale B cell immunoglobulin repertoire sequencing data. *Bioinformatics* 31, 3356–3358. <https://doi.org/10.1093/bioinformatics/btv359>.
  60. Hoehn, K.B., Pybus, O.G., and Kleinstein, S.H. (2022). Phylogenetic analysis of migration, differentiation, and class switching in B cells. *PLoS Comput. Biol.* 18, e1009885. <https://doi.org/10.1371/journal.pcbi.1009885>.
  61. Lad, L., Clancy, S., Kovalenko, M., Liu, C., Hui, T., Smith, V., and Pagratis, N. (2015). High-throughput kinetic screening of hybridomas to identify high-affinity antibodies using bio-layer interferometry. *J. Biomol. Screen* 20, 498–507. <https://doi.org/10.1177/1087057114560123>.

# **ONGOING PROJECT**

## **ONGOING PROJECT**

### **DropPick: Isolation of cell-of-interest from DropMap**

#### **DropMap microfluidic assay**

The DropMap microfluidic technique is a method used to analyze the functionality of individual cells with high throughput and single-cell resolution (Figure 10)<sup>128,132</sup>. It employs droplet microfluidics to encapsulate individual cells in picoliter water-in-oil droplets. This technology enables the generation of millions of single data points within a short amount of time, typically for between  $10^4$  to  $10^6$  individual cells. The compartmentalization of cells into small volumes (40 pL) allows for the analysis of cellular functionality without interference from other cells. The small volume within each droplet minimizes dilution, resulting in a measurable concentration of the secreted molecule in a short period. This accelerates analyses and assay run time, while also easing cell handling and reducing bias due to the shorter timeframe. The ability to analyze multiple samples per day further increases throughput and resolution of the immune reaction. Various assays that measure cellular functionality have been successfully integrated using the DropMap technology, enabling the quantification of functions of a variety of immune cells, including B-cells, T-cells, neutrophils, monocytes, cell lines, and cancer cells.

#### **Linking phenotype to genotype with DropMap**

DropMap is currently unparalleled in its ability to characterize functional diversity of the ASC pool in a single assay, particularly regarding affinity, with the nearest alternatives requiring combinations of FACS, scRNAseq, cloning, and ELISA or BLI. Despite the apparent advantages, DropMap does not offer any method for genotyping the ASCs identified, leaving immense amounts of data unutilized and many answers unobtainable. There are many questions that could be answered by analyzing DropMap-identified ASCs with FACS and scRNAseq. As a technique that directly measures antibody secretion as opposed to inferring secretion from other expressed markers, DropMap is uniquely positioned to inform how the functional subgroups within the ASC pool (high, medium, low levels of affinity and/or secretion rate) relate to populations of developing or differentiated ASCs identified by FACS and mass cytometry. Additionally, studies of ASC clonality and VDJ diversity require the complicated procedure of cloning, re-expression, and kinetic binding measurements if affinity is sought to be related to ASC genotype.

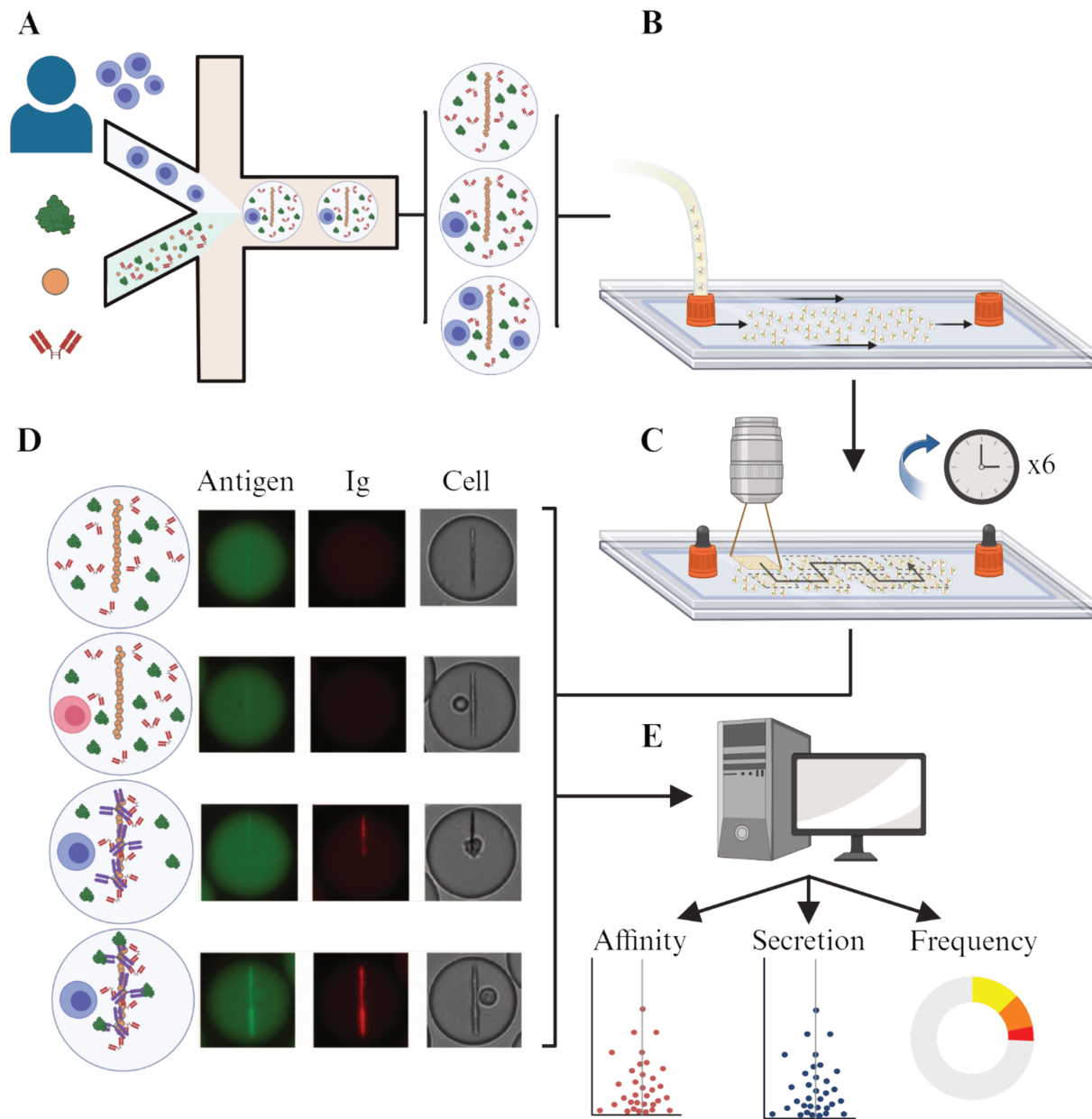


Figure 10 Overview of DropMap assay. (A) Cells isolated from patients are encapsulated into water-in-oil droplets along with antigen (green), magnetic nanobeads (orange), and anti-Ig F(ab')<sub>2</sub> (red). (B) Droplets are flowed into a horizontal glass chamber and immobilized. (C) The chamber is imaged over 45 minutes with 6 intermediary acquisitions. (D) Depending on the nature of the droplet and encapsulated cell, secreted Ig will be captured on the surface of the nanobeads. Anti-Ig F(ab')<sub>2</sub> binds bead-captured Ig, proportionally increasing the fluorescent signal along the beads' surface (row 3 and 4). If the secreted Ig is specific towards the assayed antigen, antigen is bound by capture Ig and the corresponding fluorescent signal is similarly increased relative to the amount of secreted Ig and its affinity (row 4). If the droplet is empty (row 1) or contains a non-Ig-secreting cell (row 2), no changes in fluorescence are observed. (E) Images from the experiment are analyzed to quantify fluorescence relocation to beads over time, from which Ig secretion and affinity for antigen is calculated.

Similarly, many scRNAseq techniques are limited by the incomplete gating strategies available during FACS. We therefore sought to evolve the DropMap technique into a novel technique where ASCs are capable of being labelled, recovered, and sorted for analysis with other techniques.

We have named this new assay DropPick, and it would allow for simultaneous deep-functional assessment and sorting/identification of ASCs, a technical capability not yet available and much needed. The potential to perform cytometry or molecular assays on ASC populations of varying affinities for their antigen or Ig secretion rates is highly valuable. Moreover, the ability to sequence and clone identified high-affinity antibodies within this framework would be a breakthrough in current mAb development, accelerating development and reducing costs. The improvements we propose are not necessarily rooted in the introduction of a new metric related to secretion, affinity, surface marker expression, or genotyping. These parameters can already be measured using existing methods. Instead, the focus of DropPick is to overcome the throughput limit imposed when performing functional characterization secondary to molecular assays. This is achieved by reimagining the conventional process flow, often likened to a pyramid, through which cells are passed for analysis. In this inverted pyramid model, affinity is determined first<sup>116</sup>. This approach capitalizes on the fact that the antibody is already being expressed by its own ASC, avoiding cloning and re-expression related costs, labor, and delay. Following this initial determination of affinity, a population of interest can then be identified. This could include antigen-specific cells or ASCs with either high or low affinity or Ig secretion, which can subsequently be visualized using FACS for isolation or phenotyping.

Microfluidic devices have long been used for sorting cells and subcellular structures, given the ability for cell measurement and manipulation at the cellular scale. Microfluidic microchannel sorters may be found as passive systems where primarily the morphological characteristics of cells are used as well as active techniques that use acoustophoresis, dielectrophoresis, or optophoresis to pull/push the measured cell away when it is identified to be within defined thresholds<sup>133</sup>. Alternatively, numerous microfluidic devices have been developed that hold cells within microwells for functional assessment at high throughput<sup>134</sup>; cells of interest are capable of being directly recovered for further culture or analyses via micromanipulation<sup>135,136</sup>.

The technical challenge to be overcome with the recovery of cells of interest identified using DropMap is the current inability to directly extract the droplet of interest and its cell. When a cell

of interest is normally detected within a flow channel of a microfluidic device, a temporal “coordinate” can be communicated to the sorting mechanism such that the droplet or cell may be sorted. There is usually no variability in the position or speed of the cells or droplets within the channel, simplifying the complexity of sorting to a single variable of the time between detection and arrival at the site of sorting; after empirically optimizing sort parameters, active sorting with microfluidic flow channels is highly efficient and robust<sup>137</sup>. DropMap is unusual from most microfluidic techniques by horizontally immobilizing droplets, which is a necessity to achieve linked measurements overtime in droplets and obtain key functional kinetics; the commonly pursued alternative is to immobilize cells within microwells. Therefore, droplets identified to contain cells of interest are only known by their spatial coordinates and not temporal coordinates, preventing droplet sorting using existing techniques. When recovering droplets from the observation chamber, restarting the flow within the chamber would move the cells of interest from their known coordinates and become again lost within the sea of irrelevant droplets. The DropMap assay is also contained within a glass chamber, removing possibility of isolation via micromanipulation.

A unique marker must therefore be applied to the cells of interest, such that cells are still identifiable once their spatial coordinates are lost during recovery. This presents the further technical challenge of labelling cells already within their droplets and encased within the glass observation chamber. Two approaches are foreseeable to apply a label, either an intrinsic process in which the functional property of interest itself triggers or accelerates labelling or an extrinsic process where a physical agent causes labelling; in this case light would be suitable due to the limitation of the glass chamber blocking most other physical stimuli. Although intrinsic methods for ASC “self” labelling have been used with success in flow cytometry<sup>138,139</sup>, it is difficult to imagine how this may be adapted for labelling based on affinity; additionally, such a technique could only effectively create a binary distinction, without the resolution to define at will ranges within which to apply the label.

We therefore pursued the use of photoactivable cell labelling dyes suggested by our collaborator Dr Jean Baudry (ESPCI, Paris) as this strategy fulfills both criteria of being applicable to all cells irrespective of their nature and using light as the extrinsic stimulus for labelling. The rationale for this approach is to imbue all cells entering the assay with the potential to be labelled, but to only

activate the label within a defined population of cells (Figure 11). The use of fluorescence for labelling also affords the added benefit of readily integrating with the numerous systems already available for cell isolation based on fluorescence, namely FACS and active microfluidic sorters.

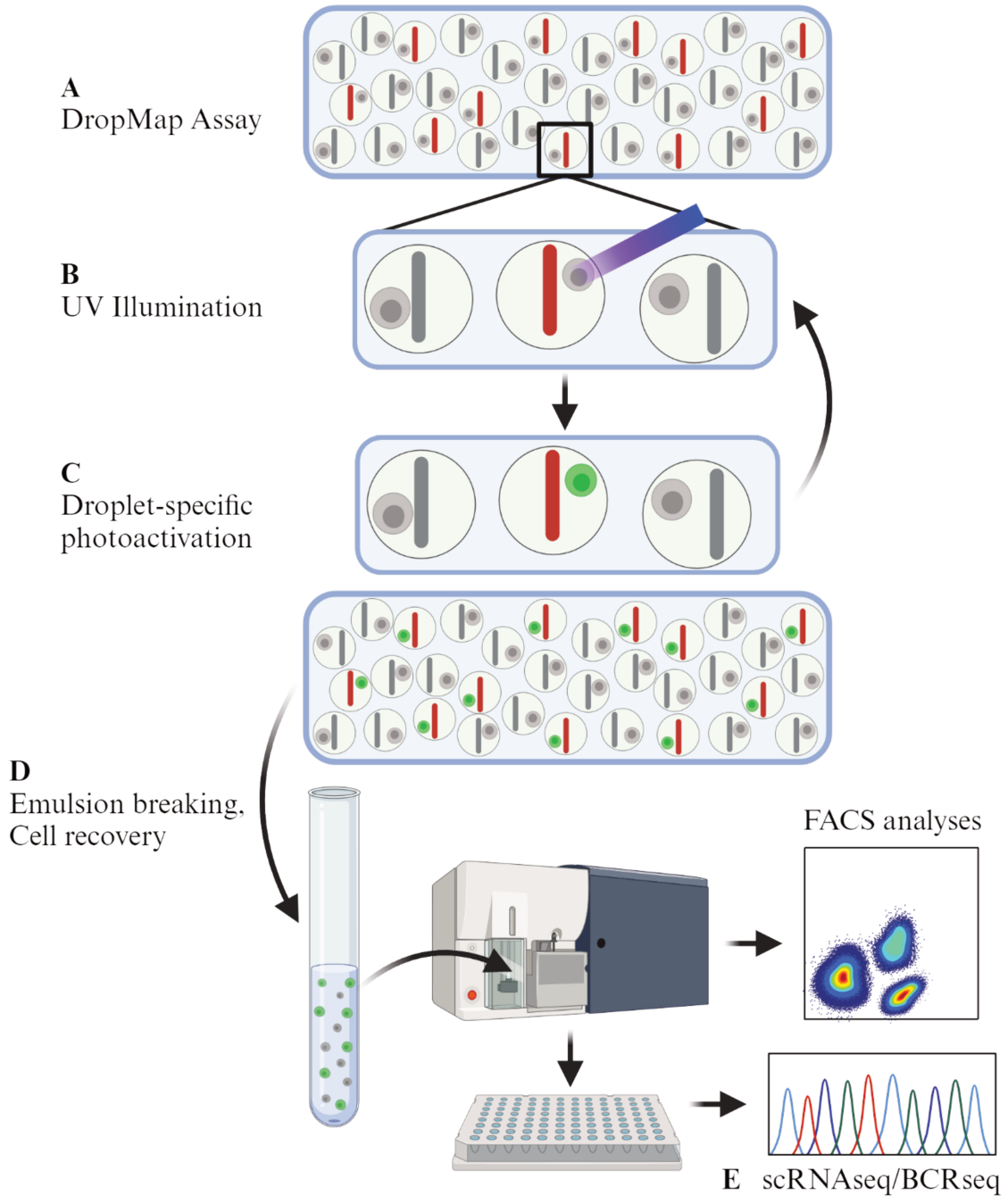


Figure 11 DropPick Pipeline. (A) Following the classical DropMap assay, cells of interest are illuminated with localized UV radiation. (B) CMNB-CFSE is then photoactivated and fluoresces in the CFSE channel.

(C) Droplets are then recovered from the observation chamber, the emulsion is broken, and cells are resuspended in suitable FACS buffer. (D) Cells are single sorted based on CFSE-fluorescence into wells containing lysis buffer. (E) scPCR to identify VH and VL of cells of interest.

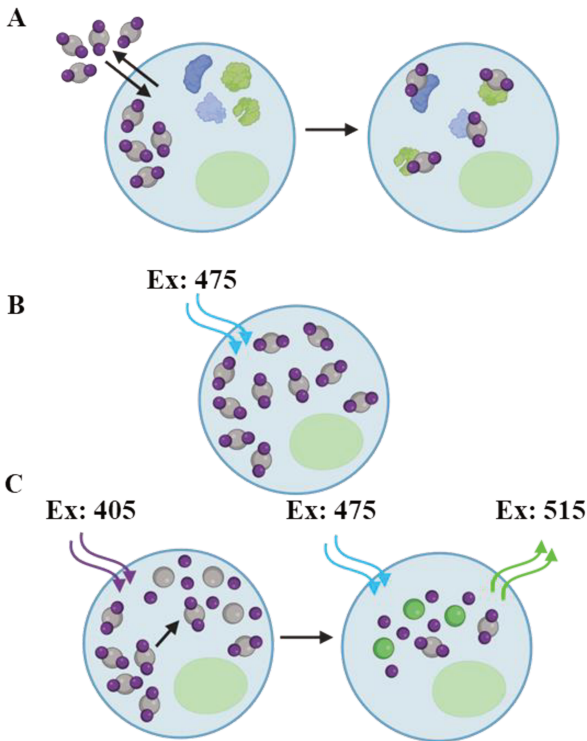
The realization of DropPick using photoactivable dyes can be divided into 3 stages: the incorporation of the photoactivable dye in existing DropMap workflows, the development of the technical capability to systematically uncage and thereby label defined cells, and the recovery of cells from DropMap and isolation using existing sorting technology. We present here the technical development of a targeted photoactivation platform and preliminary results on recovery of a population of interest using FACS.

### **Validation of photoactivable dye for DropPick**

Photoactivatable fluorescent dyes are a unique class of dyes that remain non-fluorescent when excited by light corresponding to their excitation wavelength unless the dye has been first uncaged<sup>140</sup>. The principle behind these dyes is that part of the dye structure is photosensitive, and specific wavelengths of light irradiation changes their molecular structure, allowing the dye to switch from a non-fluorescent state to a fluorescent state<sup>141</sup>. One of the major advantages of photoactivatable dyes is their ability to provide high spatial precision. Experimenters can selectively activate and visualize fluorescence in specific regions or subcellular structures, enabling the study of dynamic cellular processes at a fine scale. These dyes have been used in various applications such as super-resolution microscopy (PALM), single molecule tracking, and live cell imaging<sup>142,143</sup>. Despite their usefulness in microscopy, photoactivable dyes have limited applicability to other techniques and few dyes are commercially available.

We opted to use the photoactivatable dye CMNB-CFSE, a decision influenced by its prior application in droplet microfluidics<sup>144</sup>, its well documented use in lymphocytes<sup>145</sup> and preliminary data obtained by the group of Dr Jean Baudry (Patent # 11396017). Carboxyfluorescein succinimidyl ester (CFSE) is a fluorescent dye (ex498-em517) used for cell tracing that gained popularity in the measurement of cell proliferation. The mechanism of CFSE labelling involves passive diffusion across the cell membrane, after which it covalently binds to intracellular proteins. This covalent binding ensures the dye's retention within cells for extended periods and across multiple cell divisions. The CMNB cage is sensitive to wavelengths between approximately 350-420nm and when exposed to light within this wavelength range is removed, thereby allowing

CFSE to fluoresce in response to excitation (Figure 12). This unique property of CMNB-CFSE makes it an invaluable tool in biological studies, allowing for precise control over the timing and



location of fluorescence activation.  
 Figure 12 Mechanism of CMNB-CFSE labelling and uncaging. (A) CMNB-CFSE is capable of diffusing across the cell membrane, where the dye covalently attaches to intracellular proteins. (B) CMNB-caging group prevents fluorescence when molecules are exposed to excitation wavelength. (C) Initial illumination with UV-violet wavelength removes CMNB-cage from CFSE, allowing for excitation and emission at standard wavelength.

We show that uncaging of CMNB-CFSE alone in solution increases fluorescence linearly as a function of total illumination time, with minimal background signal (Figure 13A). We investigated the compatibility of the CMNB-CFSE dye with the DropMap assay by following the manufacturer guidelines for CFSE labelling to load human PBMCs with CMNB-CFSE. The droplet encapsulation of CMNB-CFSE labelled PBMCs showed no signs of immediate interaction with assay reagents, sensitivity to mechanical stresses of encapsulation, or additional difficulty in sample preparation.

We found maximal uncaging of cell-bound dye was achievable within 10 seconds of UV illumination (Figure 13B). Future illumination programs were limited to 5 seconds to minimize collateral uncaging of nearby cells. An added complexity to the DropMap assay caused by incorporation of CMNB-CFSE into cells is the necessity to manipulate under darkened conditions (Figure 13D-E). Exposure of CMNB-CFSE labelled PBMCs to ambient light conditions yielded an observable increase in background fluorescence of most cells after only 30 minutes. For all work

shown hereafter, cells were prepared and DropMap assays were performed in a room equipped with UV-safe LED lamps emitting only wavelengths between 620nm and 650nm.

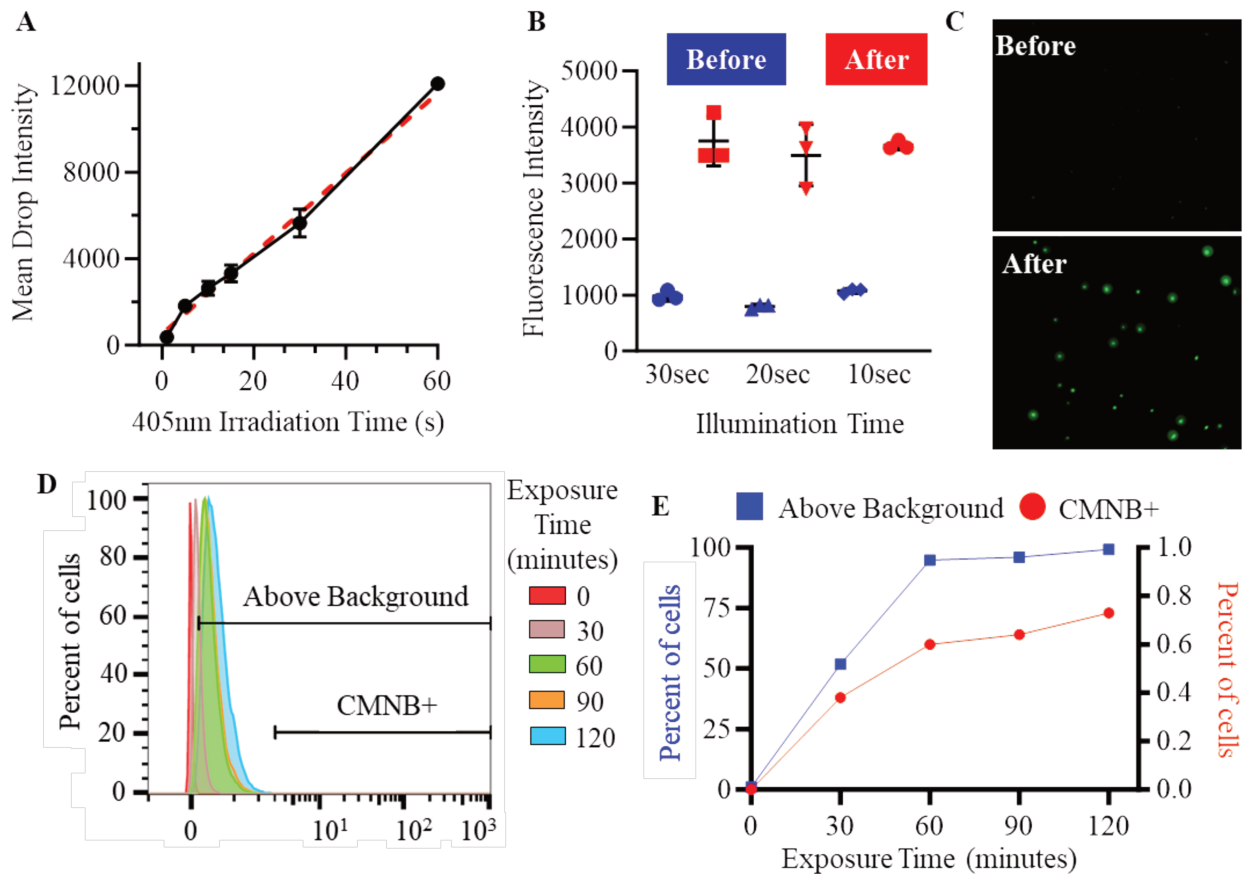


Figure 13 Evaluation of CMNB-CFSE photoactivatable dye. (A) Mean fluorescence intensity of droplets containing 100nM solution of CMNB-CFSE in DropMap assay buffer, following increasing durations of illumination with 365nm light, n=247 droplets. (B) Mean fluorescence intensity of encapsulated PBMCs labelled with 10uM CMNB-CFSE followed by illumination by 365nm light for indicated interval, n=3 experiments with mean fluorescence intensity of 50 cells given per experiment. (C) Before and after images of droplet field with 10uM CMNB-CFSE labelled PBMCs in CFSE fluorescence channel during UV illumination. (D-E) CMNB-CFSE labelled PBMCs were left at 4°C without covering, subject to exposure to overhead laboratory lighting. CFSE fluorescence was measured by flow cytometry (MACSQuant 16, Miltenyi) after 30-minute intervals, showing increases in the number of cells above background (greater than MFI of unexposed) and CMNB<sup>+</sup> (signal greater than prior to exposure/photoactivation).

We also investigated whether exposure of cells to CMNB-CFSE altered their behavior with the DropMap assay, namely decreased cell viability or any changes to Ig secretion rates. CFSE and other cell permeable dyes have been previously demonstrated to be cytotoxic and alter physiology<sup>146</sup>. We compared the effects of CMNB-CFSE on both human PBMCs and a human hybridoma cell line, as much of the reported CFSE toxicity was related to cell proliferation and activation state. CMNB-CFSE labelled cells were sorted by FACS into a human IgG ELISPOT

assay to determine the proportion of IgG secreting cells between samples. We found that CMNB-CFSE labelling caused a significant increase in the observable proportion of IgG-SCs among PBMCs and no effect on the number of IgG<sup>+</sup> spots among SA13 cells (Figure 14). It is unclear whether the unexpected increase in IgG<sup>+</sup> spots among CMNB-labelled PBMCs is attributable to an increased activation of nascent IgG-SCs or was caused by increased removal of irrelevant cell types; notably, cell viability as measured by 7-AAD was similar across all samples tested (>95%). We assessed the individual IgG secretion rates of CMNB-CFSE labelled cells using DropMap and found minor but significant changes in both samples tested; CMNB-labelled PBMCs showed a slightly decreased average IgG secretion rate whereas CMNB-labelled SA13 hybridomas on average secreted more IgG (Figure 14E).

We established the capacity for CMNB-CFSE labelled cells to participate in the DropMap assay and be successfully photoactivated. However, a key requirement for DropPick is to achieve discrete photoactivation, specifically illuminating only cells of interest with minimal influence on nearby cells. We found the optimal system for restricting incoming light to be a combination of a higher magnification objective to limit the field of view to a smaller area of the observation chamber, paired with closure of an internal diaphragm of the microscope (Figure 15A). The resulting width of the focused light reaching the observation chamber is approximately 50um, although a small degree of scattering is observable beyond the limit of the droplet (Figure 15B); this represents both light scattered internally by the droplet and cell as well as the limitation of our widefield microscope system.

We applied this restricted illumination protocol to a DropMap chamber prepared with CMNB-labelled SA13 hybridomas. Droplets targeted with 5 seconds of UV illumination showed strong photoactivation of their contained cell with minimal collateral illumination or activation of surrounding droplets (Figure 15C-D). Photoactivated cells showed a high degree of fluorescence and were significantly increased compared to background and non-targeted cells, which should enable sorting of target cells based on green fluorescence. Illuminating droplets for longer than 5 seconds did not yield higher photoactivation as we had observed previously.

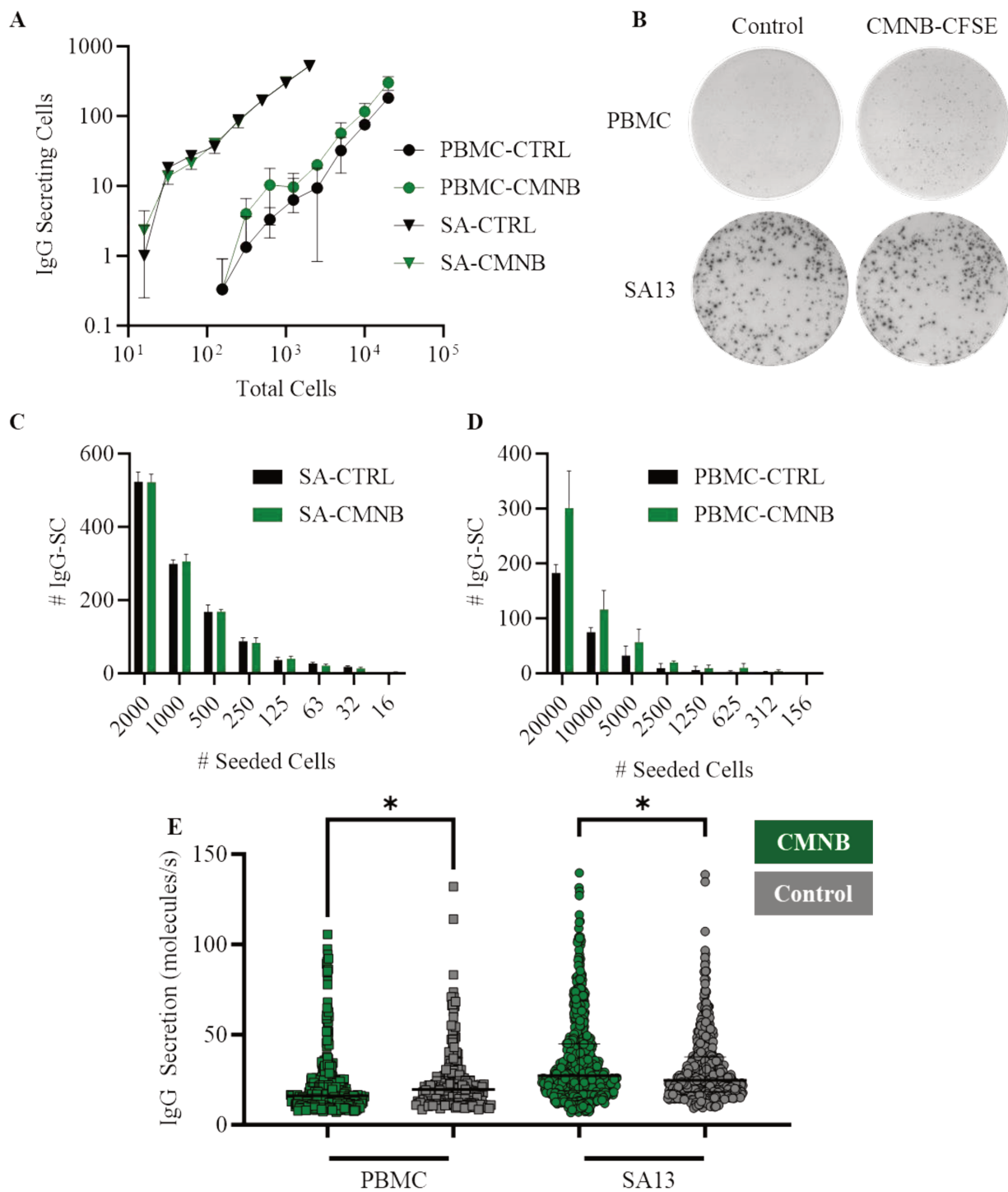


Figure 14 Effects of CMNB-CFSE on ASC proportion and IgG secretion rate. (A-D) CMNB-CFSE labelled (green) or control (black) PBMCs or SA-13 human hybridomas were sorted by FACS into human IgG ELISPOT, n=3 wells per condition. (A) IgG+ spots per well at various densities of cell seeding show linear increase in IgG-SC. (B) Representative images from ELISPOT showing well with highest seeded number of CMNB-CFSE labelled (right) or control (left) samples of PBMCs (top) or SA-13 (bottom) cells. (C) SA-13 cell showed no difference between CMNB-CFSE labelling. (D) CMNB-CFSE labelled PBMC samples produced fewer IgG-SCs compared to unlabeled.

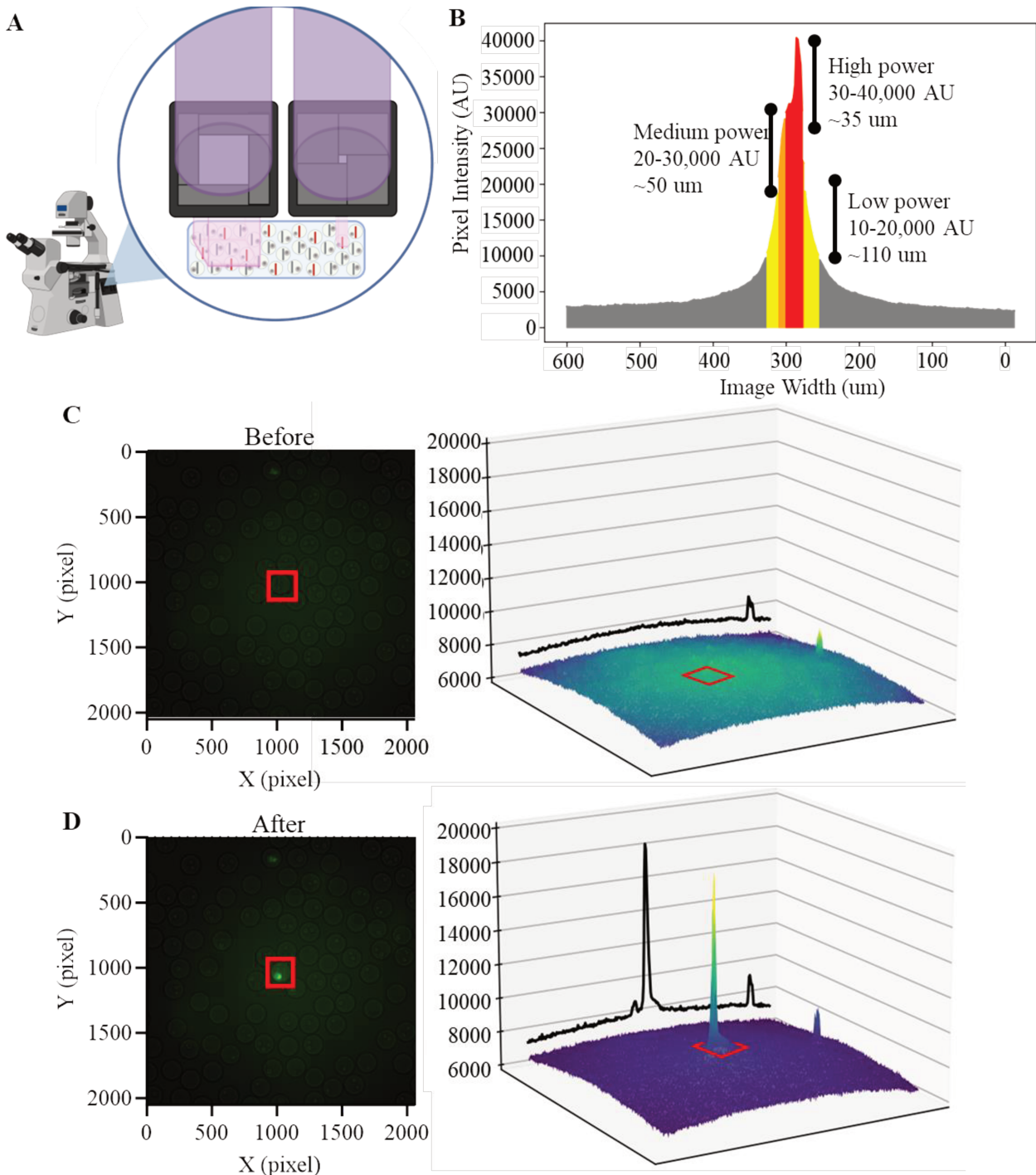


Figure 15 Diaphragm closure for single droplet illumination. (A) The light path of a scientific microscope with a diaphragm to restrict incoming light. Closure of this diaphragm to its lower limit restricts light reaching the DropMap chamber to a ~50um wide square. (B) Projection of pixel intensity value from image of UV illumination of droplet. (C-D, left) Encapsulated CMNB-CFSE labeled SA13 cells are shown in microscope image with brightfield and corresponding fluorescence channel overlaid, either (C) before or (D) after 5 seconds of UV illumination. Red boxes indicate the area of targeted illumination. (C-D, right) Graphical representation of fluorescence channel shown in 3D, with x and y axes corresponding to pixel location and z axis height denoting pixel intensity.

We have primarily developed DropPick for use on *ex vivo* cells from humans and standard mouse models, to which a cell permeable photoactivable label must be added to integrate with the DropPick workflow. However, there are cases without the need for photoactivable dyes where our system may also be readily applicable. Photoactivatable and photoswitchable proteins are another class of biological tool that have also seen extensive use in not only microscopy but also in *in vivo* studies<sup>147,148</sup>. Photoactivatable fluorescent proteins are frequently preferred to photoactivatable dyes due to their comparative lack of toxicity and ability to label cells *in vivo* through stable transgenic expression. We sought to validate our protocol of discrete photoactivation for a photosensitive protein model to demonstrate the complete versatility of this workflow for targeted cell recovery. We obtained splenocytes from the Vav-H2B-Dendra2 mouse, in which the histone protein H2B is fused to the green-to-red photoconvertible protein Dendra2 and expressed in lymphocytes via the Vav promoter<sup>149</sup>. A photoconversion model has the notable difference to photoactivatable dyes where only cells expressing the protein can be labelled and the capacity for photoconversion and thereby labeling is intrinsic to the level of transgene expression by the cell; as a result, the fluorescence intensity of photoconverted cells may vary depending on factors influencing expression and is difficult to control. Using our platform, targeted UV illumination of Vav-H2B-Dendra2 splenocytes in a DropMap preparation resulted in strong, discrete photoactivation of the cell of interest in the conversion channel (Figure 16). Notably, the Vav-H2B-Dendra2 preparation shows a higher degree of background activation when comparing the field of view prior to illumination with that of the various photoactivatable dyes. This background activation is likely the result of a short exposure to ambient lighting during spleen isolation and processing, highlighting the importance of manipulation in a controlled environment or haste when UV exposure is unavoidable. Nonetheless, the photoconverted cell is easily distinguishable with an intensity far above background.

Here we have validated the use of a photoactivatable dye and a photoconvertible protein within the DropMap system. We show that dye labelled cells are reliably capable of near total photoactivation within a short period and yield a significant increase in cellular fluorescence. Labelling of cells with photoactivatable dyes does not prohibit the DropMap assay from assessing ASCs, although minor effects should be noted and the DropPick system is perhaps less reflective of physiological conditions. We developed a simple yet effective means of delivering targeted

illumination for dye or protein uncaging within droplets of interest that results in minimal collateral activation.

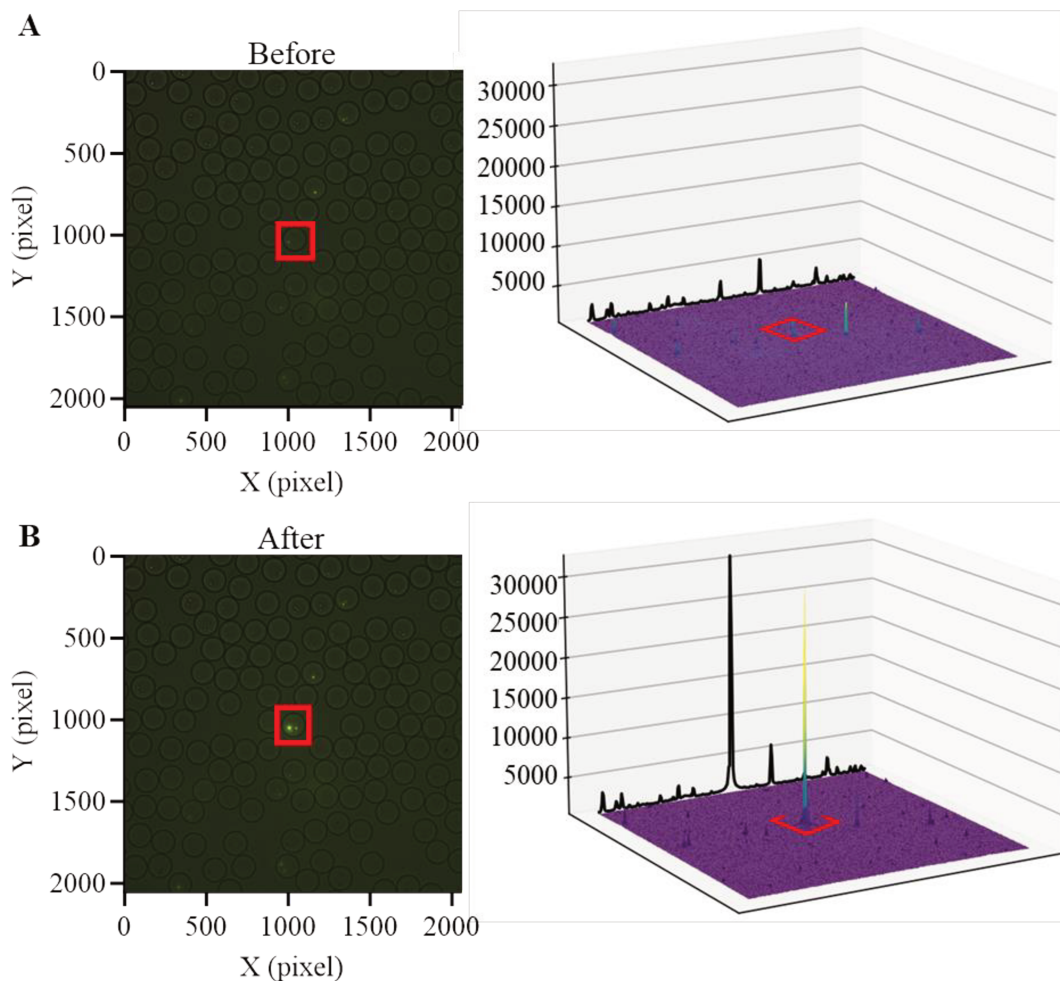


Figure 16 Discrete photoconversion of Vav-H2B-Dendra2 splenocyte via DropPick.

### Development of fully automated uncaging protocol

We have shown that cells loaded with photoactivable dyes or proteins are capable of being used in the DropMap assay and that specific cells within droplets may be photoactivated. However, for the goal of DropPick to offer an integrated solution for selecting populations of interest from DropMap, cell “picking” must be performed in an automated manner. Individual targeting of droplets by the experimenter is untenable for reasons of accuracy and ease of use. Additionally, if large numbers of cells require targeting, manual control is not feasible. The realization of an automated control protocol for DropPick therefore incorporates two solutions, first an acceleration

and automation of the existing DropMap analyses to find and determine droplets of interest to be targeted and secondly the direct control of microscope utilities to perform discrete illumination without user input.

## **Evolving DropMap Analyses**

The growth of microfluidic techniques for single cell assays has rapidly expanded the available throughput in immunology research. However, with the increasing complexity and volume of data generated by microfluidic systems, there is a growing need for big data analysis and robust analysis protocols. These protocols should be capable of handling large volumes of data, detecting patterns, and making accurate predictions. Furthermore, they should be reproducible and easy to use to ensure consistency across different studies.

DropMap is a data intensive technique and regularly generates 30GBs per acquisition. The analyses of DropMap can be divided into two phases, a “primary” analysis of the microscopy images from the assay and a “secondary” analysis to validate and translate the measurements of the primary analysis into affinities, secretion rates, and cell frequencies. The primary analysis identifies for each droplet its centroid coordinates, radius, whole droplet fluorescence intensity, beadline fluorescence intensity, and the ratio of the beadline intensity over the whole droplet intensity (relocation ratio). To support the implementation of DropPick during the secondary analysis, we developed an automated analysis framework for DropMap offering significant increases to analysis throughput and robustness (Figure 17). I decided to develop an automated secondary analysis solution using the Python coding language due to its open-source availability and existing image analysis modules. A necessary element for an automated analysis solution is to offer straightforward and simple means of selecting data to be analyzed and how it should be treated. I created a graphical user interface allowing the user to adjust the analysis parameters and types of analysis to be performed, with no programming knowledge required. Following user data selection, the proceeding steps occur automatically without user direction.

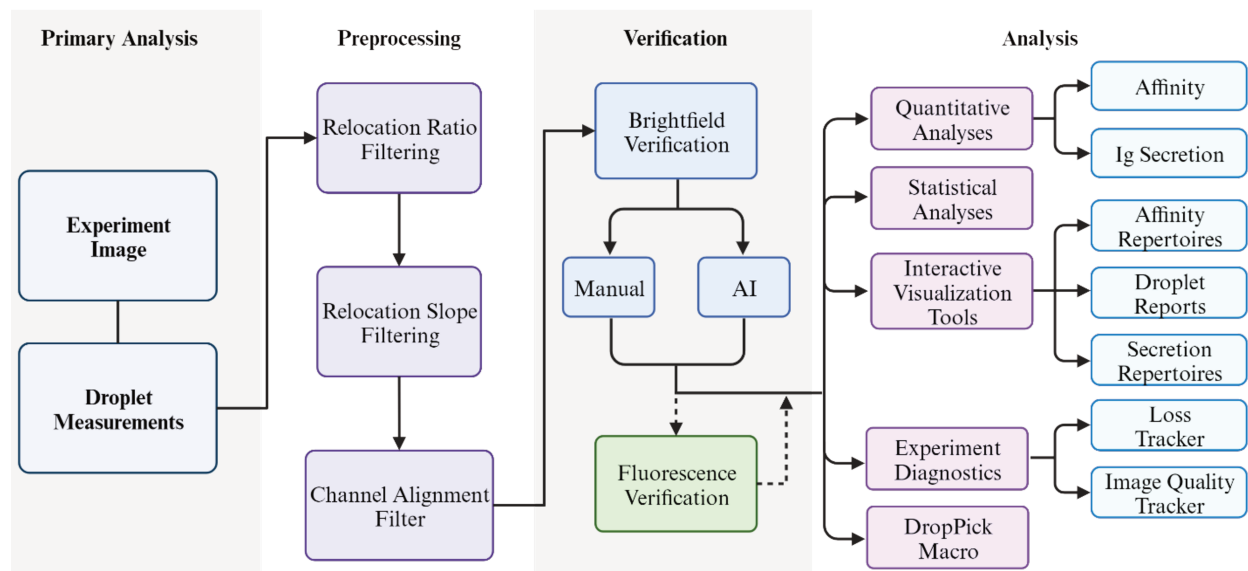


Figure 17 Workflow of Python DropMap Analysis

After selecting the experiment to be analyzed, preprocessing is performed on measured relocation values to remove droplets with no detectable Ig secretion; for more details, see the methods below. Droplets that pass the various thresholds of their relocation ratios and slope are now considered to putatively contain ASC. These droplets must now be validated to be free of aggregates and to contain single cells (Figure 18). To overcome the previous challenge of droplet classification, Angga Prima (Microfluidic engineer in the lab) and myself developed a machine learning solution using the ResNet 50 model, for which we are finalizing a manuscript (**refer to Article 5 - manuscript in preparation**). To briefly summarize, we utilized a training dataset of 70,000 droplet images, classified as empty, single cell, or multiple cell droplets. With the help of an undergraduate student, Thibault Vanhoucke, we applied a convolution to images before model training and evaluation that eliminates vertical contours, essentially removing droplet elements with prolonged vertical orientations, namely the headline. We demonstrate high accuracy classification of droplets according to their cell contents, enabling unsupervised droplet validation during secondary DropMap analysis. In addition to the cell count and abnormalities visible in the brightfield channel, droplet validation must also include verification of the absence of fluorescent abnormalities in the antibody capture channel. This is most often the result of a memory B cell in the droplet, to which the IgG detection reagent also relocates and gives the appearance of headline-like relocation (Figure 18). To address this problem, we have also begun to implement fluorescence

body detection and bounding box measurements to flag likely artifactual objects. However, additional testing to determine thresholds is required before allowing for unsupervised exclusion.

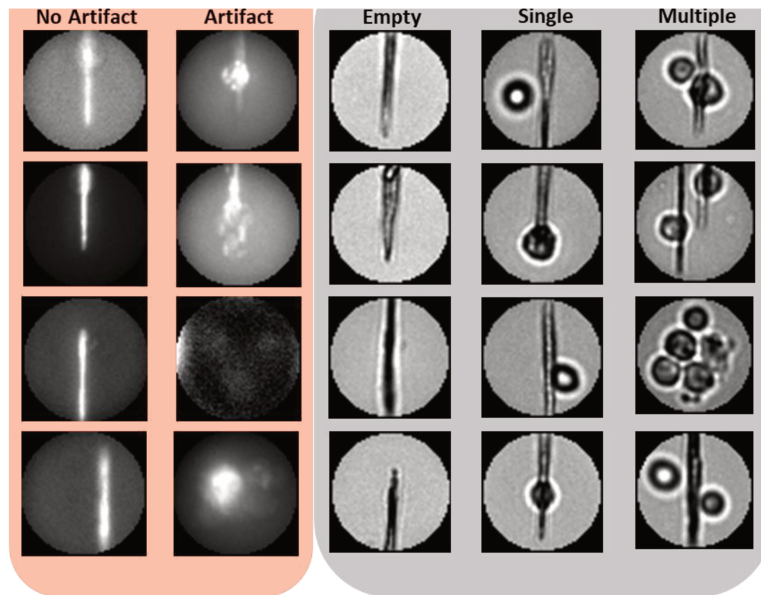


Figure 18 Example images of droplets from DropMap in either the Ig fluorescent (left, red) or brightfield (right, grey) channels, showing the diversity of cellular and beadline presentations. Fluorescent channels may contain bright artifacts due to cell surface Ig or aggregates.

Droplets passing both image-based validation steps have been verified as ASC-containing droplets. The relocation ratio slope represents the amount of antigen captured relative to the amount of antibody present and is the value used in tandem with the antigen-specific reference curve to determine affinity, consistent with previous analyses. Several key final metrics offered by DropMap are also the frequency of ASCs among the cell population assayed (e.g., PBMCs, enriched B cells), the frequency of antigen-specific ASC among all ASC, and the proportions of various affinity ranges among antigen-specific ASC or all ASC. These are now offered in a standardized format with each analysis for all antigens included in the assay. We also decided to improve the precision of antibody secretion rate estimation, the details of which can be found in the methods below.

A final key aspect lacking from previous analyses was a means to readily visualize and interpret analyzed data, without the need for the user to manually generate figures. At the end of the automated analysis, a report is generated for each verified ASC-droplet, showing the droplet in all

image channels at all timepoints as well as the relocation ratio graphs for each antigen-fluorescence channel (Figure 19).

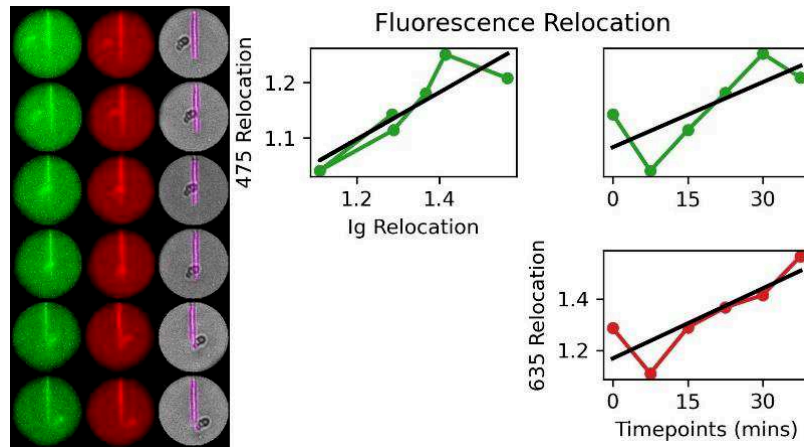


Figure 19 Droplet report generated by automated secondary analysis.

To further facilitate analysis, we have created an interactive user interface with the ability to view the full affinity ranges from analyzed samples and the report for any droplet within the final dataset (Figure 20). The following analysis workflow is capable of being applied to a single image or to groups of images by batch processing, to enable reanalysis of the whole dataset using different thresholds, affinity referencing equations, verification models, etc.

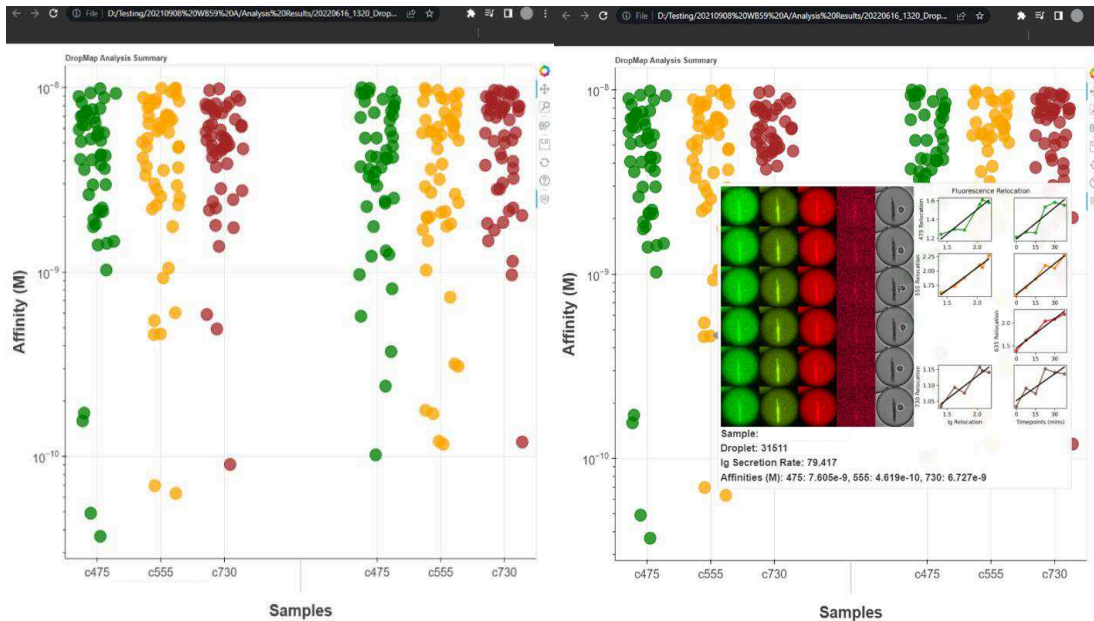


Figure 20 Interactive data viewer for automated DropMap analyses. Affinity data are presented for each antigen channel and sample from analysis, available to view with any HTML compatible viewer or web

browser. Plot area is user interactive with ability to zoom, gate on, and pan across data points. Hovering the cursor over data point yields a tooltip panel (right) showing corresponding droplet report, droplet number, Ig secretion rate, and affinities in antigen channels.

Globally, all the calculations and validation offered by this automated analysis are performed within 10-20 seconds depending on the number of putative ASC-containing droplets. This represents a significant (~200 fold) improvement over previous analyses that would require between 30 and 60 minutes due to manual data arrangement and verification required and was not capable of generating figures and reports for each droplet. With this automated analysis program, we provide a solution that offers vastly improved ease of use, precision, throughput, and reproducibility. All previous concerns regarding the historical method of analysis are thereby addressed and this program may also act as a means for increased adoption of DropMap by other research groups. Importantly, DropPick may proceed immediately following the end of data acquisition to allow for a rapid, integrated workflow.

### **Automated illumination for droplet photoactivation**

Targeted droplet illumination must be performed in an unsupervised and automated procedure to achieve a sufficient speed of illumination and high fidelity photoactivation. Manual stage movement between droplets is inefficient and prone to excessive movement that may shift droplets as well as being unfeasible when large numbers of cells require illumination. The control software for the Nikon Ti2-E microscope on which DropMap has been performed supports macro functionality, with functions available for stage, laser shutter, mirror wheel, and camera control; I therefore developed a means of procedurally generating a macro function during DropMap analysis to perform the stages of illumination for each droplet. This illumination macro is automatically generated for the experimenter following the secondary analysis program outlined in the previous section.

Prior to movement of the microscope stage, the coordinates of each droplet to be illuminated are calculated from the original assay image. A pathfinding algorithm is then applied to order the list of converted target coordinates according to the path between points that minimizes the distance of stage travel (Figure 21), lowering the likelihood of excessive stage movements that may cause droplet shift and mistargeting and the time needed for these illuminations.

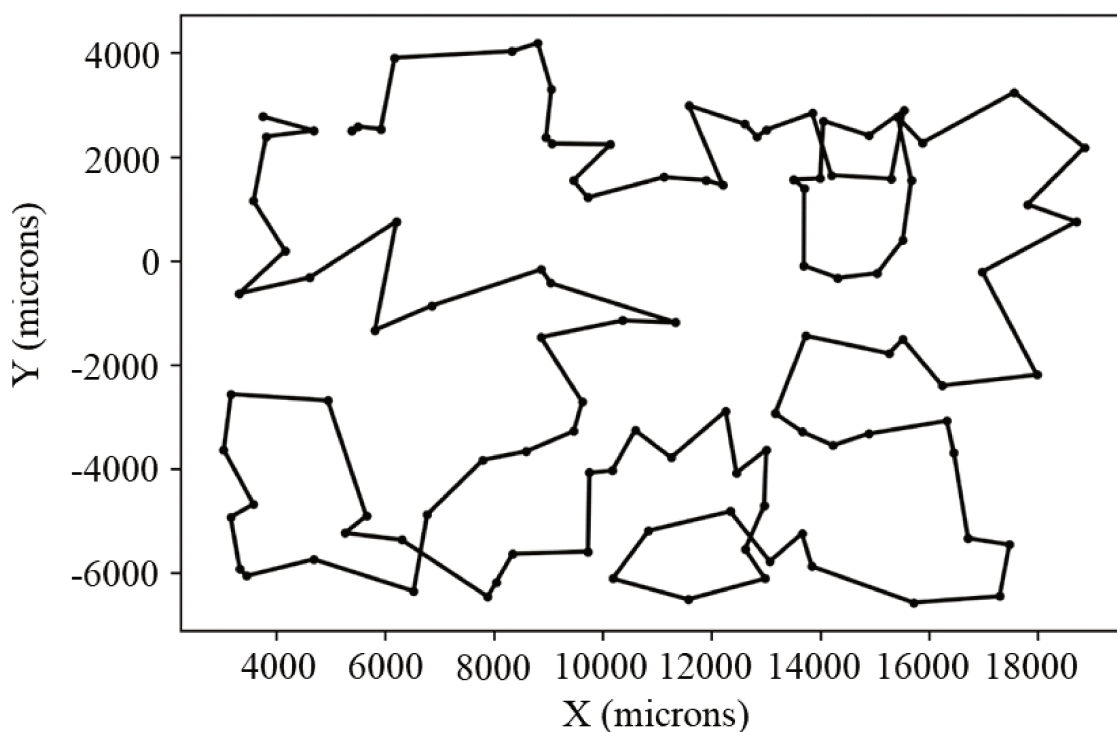


Figure 21 Example path of DropPick illumination program. Each point represents a droplet to be illuminated and lines represent the path to be travelled by the microscope stage following the pathfinding algorithm.

An additional component I have implemented to the unsupervised illumination protocol is an auto-centering feature after each stage movement to a new droplet (Figure 22). Droplet size irregularity, droplet packing density, and chamber non-uniformity can all lead to varying degrees of droplet movement during the 15-20 minutes required for analysis between the end of the DropMap experiment and the start of DropPick illumination. In these cases, there is a chance the target cell is no longer well situated within the area of illumination or that a non-target droplet may now be partially within the illumination area. This auto-centering feature thereby corrects for minor errors from coordinate miscalculation or movement to achieve perfect droplet centering; additional details are described in the methods. During testing we found near all initial movements to correctly center on the target droplet with high accuracy (>95% within 5  $\mu\text{m}$  of target droplet center).

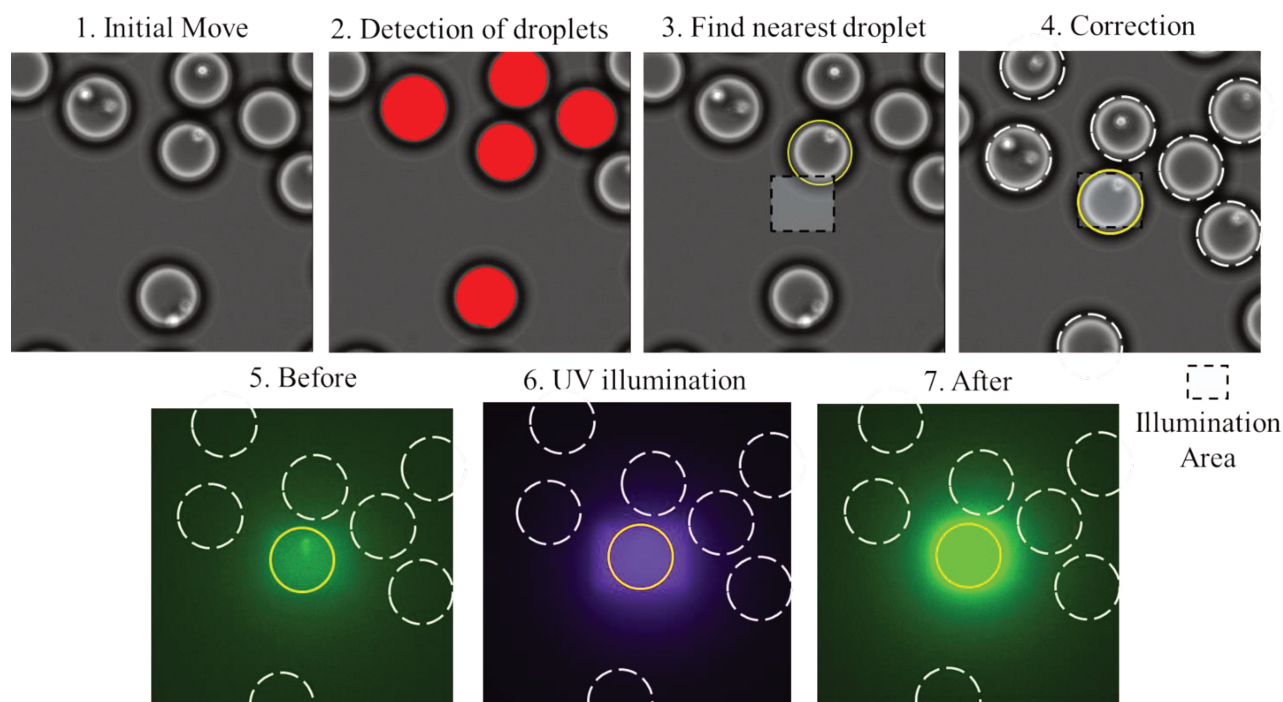


Figure 22 Overview of targeted droplet illumination procedure. Following the DropMap assay, a macro function is generated to direct droplet illumination without user input for each droplet. The illumination steps include: 1. Movement of the microscope stage to the theoretical droplet position calculated using the DropMap assay image. 2. Droplets near the theoretical droplet position are detected. 3. Identification of the droplet currently nearest to the theoretical position of the target droplet for illumination (dotted box), assuming excessive movement has not occurred. 4. To obtain optimal illumination specificity and efficiency, an autocorrection protocol is used to ensure the area of illumination is situated on the center of the target droplet: this makes the microscope stage move to align the center of the illumination area with the center of the target droplet. 5. A control image is acquired in the CMNB-CFSE fluorescence channel (FITC). 6. The droplet is illuminated with 365nm light (violet) for a user defined duration. 7. A control image is acquired to verify significant CMNB-CFSE photoactivation of the target droplet, but not of the surrounding droplets.

The final component of automated illumination program includes the recording of images for all intermediary steps during photoactivation (Figure 22): the initial movement of the stage to the calculated target position, the potential correction to center the illumination area on the target droplet, the fluorescence channel of the label prior to UV illumination, and the same channel after photoactivation. These images are joined together to form a comprehensive “receipt” of photoactivation for each droplet targeted to validate successful labelling and aid in troubleshooting potential targeting or labelling issues (Figure 23).

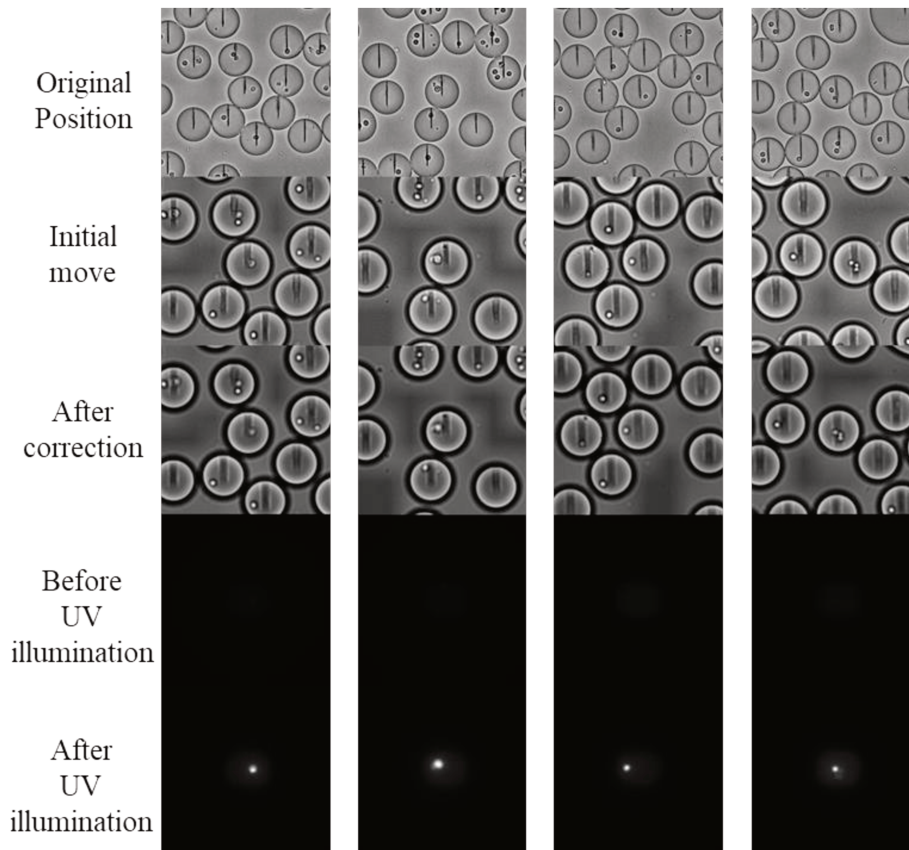


Figure 23 Record-keeping of droplet illumination and photoactivation. Images show four example “receipts” of stages during automated illumination program on CMNB-CFSE labeled PBMCs. The “original position” shows the field of view centered over the target droplet. The microscope stage first moves to the calculated position of the target droplet (initial move). The autocorrection feature then may slightly adjust the stage ( $<20\mu\text{m}$ ) to center more precisely over the droplet nearest the expected target position (after correction). The field of view in the reporter fluorescence channel is recorded before and after the UV illumination period (before/after UV illumination). The original position, initial move, and after correction images show the brightfield channel. The before and after UV illumination images show the reporter fluorescence channel (FITC). The rightmost image shows an example of a strong correction.

This automated illumination program for targeted droplet photoactivation therefore consists of 4 stages: translation of the coordinates from the DropMap experiment, calculation of an optimal beaming path, illumination of the targeted droplet with an autocorrection for optimal alignment, and record-keeping of the full illumination process to validate program efficacy. The automated illumination proceeds at a current rate of approximately 4 droplets per minute, assuming a 5 second illumination time per droplet; this rate can be increased to 6-7 droplets per second by forgoing the autocorrection and reporter channel checking features of the full program, at a slight cost to targeting accuracy and the potential for verification.

## Visualizing DropPick photoactivated cells by FACS

We have thus validated the process to imbue cells with the ability to be labelled within the DropMap system and the technical capacity to direct photoactivation to the precise droplet population of interest. The remaining component essential to realizing DropPick is the visualization and isolation of photoactivated cells by FACS. We evaluated beaming efficiency by performing a DropMap assay on photoactivatable dye labeled PBMCs, including assay reagents, the droplet encapsulation process, and the incubation delay to observe Ig secretion. The target population for illumination and photoactivation was defined by droplets containing single IgG secreting cells, of which the activation program was limited to 100 droplets. We found that between 60-70% of photoactivated CMNB-CFSE labeled cells were able to be reliably visualized by FACS following recovery from the DropMap chamber and droplet emulsion (Figure 24).

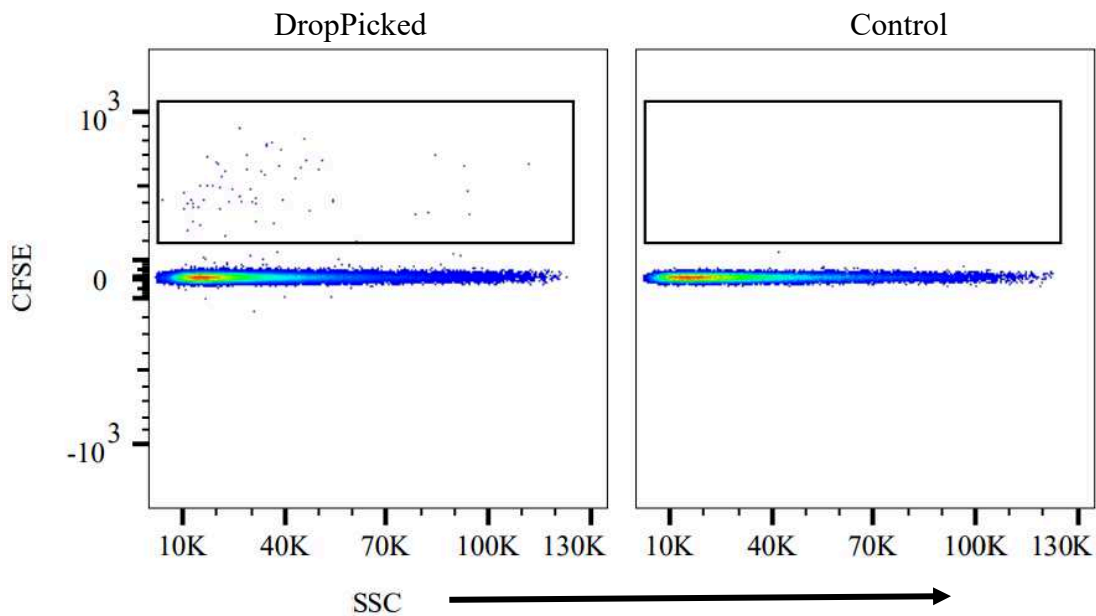


Figure 24 Visualizing CMNB-CFSE labeled PBMCs photoactivated by DropPick. The DropMap assay was performed on CMNB-CFSE labeled PBMCs to identify IgG-secreting cells (IgG-SCs), of which 100 IgG-SCs containing droplets were subjected to targeted illumination. Cells were recovered from DropMap by breaking the emulsion with an anti-static electric field. Samples were assessed using the BD ARIA III FACS machine, and gated by standard lymphocyte, doublet exclusion, and live/dead gates. Gate shown identifies photoactivated CMNB-CFSE cells, 62 cells in the DropPicked sample and none in the control sample. Representative of 3 replicate experiments.

We similarly evaluated splenocytes from mice that express a photoconvertible protein (Dendra2) to ensure that our approach is not limited to CMNB-CFSE labeled cells. We used the Vav-H2B-Dendra2 transgenic mouse model that expresses a fusion protein of histone H2B and Dendra2

(H2B-Dendra2) under the control of the hematopoietic Vav promoter<sup>149</sup> to assess whether a photoconverted population may be visualized by FACS. A sample was prepared with 200 droplets containing single cells targeted for photoconversion. Visualization by FACS revealed an efficiency of approximately 65% (131/200) for detection of cells with clear photoconversion and strong fluorescence-switched signal compared to a control sample (Figure 25); notably, an additional weakly photoconverted population was evident in the sample with photoconversion, possibly resulting from collateral activation of non-target H2B-Dendra2 expressing cells. A unique dynamic was apparent with the converted reporter fluorescence (Dendra-Red) intensity being dependent on the intensity of the unconverted form of the reporter (Dendra-Green).

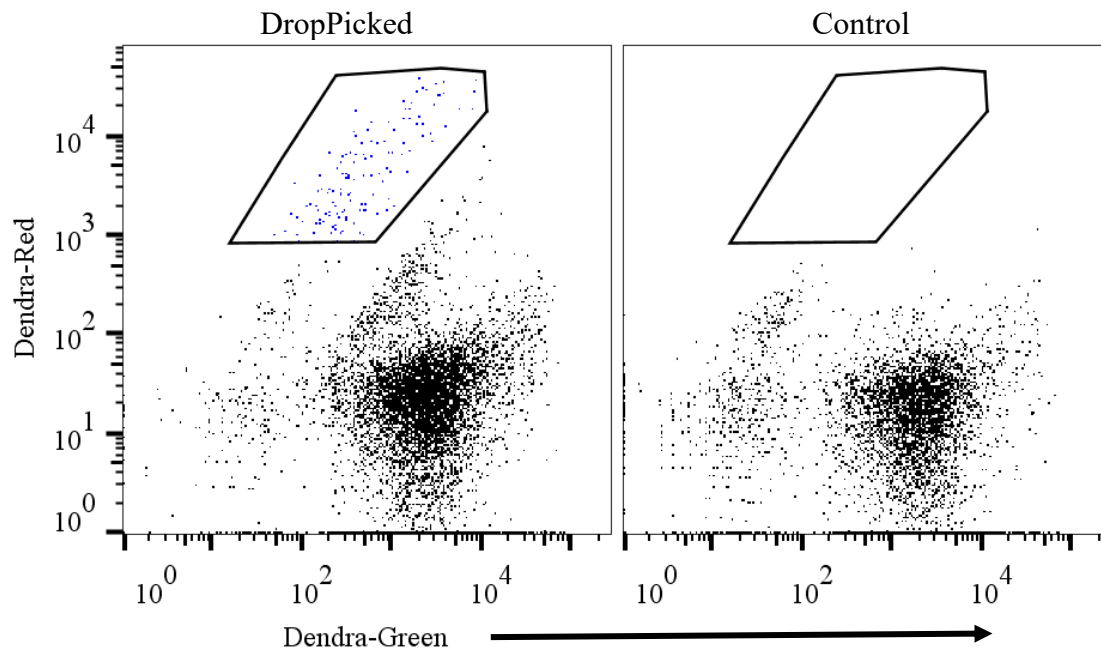


Figure 25 Visualizing photoconverted Vav-H2B-Dendra2 splenocytes by FACS. The mouse IgG DropMap assay was performed on splenocytes from Vav-H2B-Dendra2 mice to identify IgG-secreting cells (IgG-SCs), of which 200 IgG-SCs containing droplets were subjected to targeted illumination. Cells were recovered from DropMap by breaking the emulsion with an anti-static electric field. Samples were assessed using the BD ARIA III FACS machine and gated by standard lymphocyte and doublet exclusion gates. The gate shown identifies photoactivated H2B-Dendra2 cells, 131 cells in the DropPicked sample and none in the control sample.

## Discussion and Perspectives for DropPick

We show here a platform for the labelling of cells of interest within a droplet microfluidic assay, DropMap, and have laid the groundwork for demonstrating successful recovery of cells via FACS.

Nonetheless, there are several aspects of photoactivated cell recovery that still require optimization and validation.

CFSE labeling as a means of measuring the total protein content of a cell has been previously shown to directly correlate with both the forward- and side-scatter signals of flow cytometry<sup>150</sup>. We therefore hypothesized that visualizing DropPicked cells using the photoactivatable dye signal against either the forward- or side-scatter signals would yield a distinct population with a diagonal appearance on which to more easily gate. However, we did not observe a diagonal population of photoactivated cells, suggesting either alternative labeling behavior in PBMCs compared to the cell line for which the correlation was previously shown or additional sources of fluorescence influencing the population shape in FACS. Currently, labeling via targeted photoactivation yields fluorescent signals still significantly weaker compared to cells labeled with the native, noncaged dye format. DropPick development is ongoing to optimize the gating strategy to visualize photoactivated cells as well as the signal-to-noise ratio achieved by photoactivation, with the goal of producing a more discrete photoactivated population for confident gating.

An additional aspect of visualizing DropPicked cells that warrants further optimization is the consistent observation of fewer cells by cytometry than were originally photoactivated with approximately 30-40% of cells lost. Using the photoactivation recording functionality we incorporated into the automated targeting program, we can confirm that a lack of successful droplet targeting or cell photoactivation is exceptionally rare and likely not a cause of cell loss. We suspect that the majority of cell loss occurs during transfer from the DropMap chamber to the flow cytometer and hypothesize 2 possible sources. The first possible source is the incomplete coalescence of droplets into a singular aqueous phase, which may leave some cells in their original droplets that are not visible within a flow cytometer. To address this, we will investigate longer and/or more vigorous electrostatic force application to ensure 100% coalescence. Secondly, there remains the possibility for incomplete droplet transfer from the observation chamber to the collection tube prior to droplet coalescence. We are in the process of prototyping adaptors with threaded connections to remove this source of loss. Despite the potential for procedural improvements, there will likely remain at least 10-15% of cells lost due to cell doublet formation as well as the adherence of cells to the recovery and cytometry tubing walls.

Our approach to developing the DropPick workflow has consistently been to co-opt and adapt existing capabilities of the microscopy platform currently utilized for the DropMap assay. While adaptation is beneficial for promoting assay flexibility and the ease of adoption, it should be noted that additional performance improvements can be envisioned with a more purpose-built system. The most notable area for improvement would be a solution for targeted illumination of the droplet of interest. The restriction of the area of illumination using a diaphragm within the light path yields a satisfactorily discrete, but nonetheless partially diffuse, profile of illumination (Figure X). Illumination during testing of photoactivation therefore occasionally results in minor but noticeable collateral photoactivation of cells in droplets in the immediate vicinity of the target droplet. Targeted illumination modules are available for most existing microscope systems, offering both digital micromirror devices to direct light precisely to areas within the optical field with nanomolar precision as well as dedicated light sources with higher precision, using lasers instead of lamps. Confocal microscopes offer another solution with inherently less diffuse illumination and spatial control, although a confocal microscope has never been tested for use with DropMap. However, these technical approaches bring the significant disadvantages of increased maintenance needs and decreased imaging speed and relative ease of use. Ultimately, if collateral “bystander” photoactivation appears to be a significant problem hindering accurate cell recovery or visualization by DropPick in the future, additional fidelity and performance should be readily attainable through the adjustments outlined.

Beyond the potential for improvement regarding the intensity of the photoactivated fluorescence signal and the robustness of visualizing photoactivated cells by FACS, several important experimental milestones are currently being pursued to demonstrate the full efficacy of the DropPick workflow. We are currently performing extensive testing of how our ASC recovery pipeline may be integrated with existing protocols for surface marker phenotyping, functional assays (ELISPOT), and single cell VDJ sequencing. We will determine and optimize the feasibility of adding classical B cell or ASC FACS staining panels, such as the OMIP-43<sup>151</sup> panel, to cells collected following recovery from DropMap to maximize the analysis depth of the photoactivated cells of interest. However, the use of photoactivatable dyes alongside multiple other fluorophores in flow cytometry is not described in the relevant literature. The translation of our photoactivation platform into a cohesive workflow to obtain VDJ genes sequences from the isolated ASCs is the

other primary goal of DropPick and we are in the process of validating accurate and robust genotyping of the photoactivated population.

We aim to confirm our ability to visualize photoactivated cells by performing DropPick on a combination of the DB (ATCC CRL-2289) cell line with another B cell lymphoblast cell line, ARH-77 (ATCC CRL-1621). DB cells express high levels of IgG on their surface, whereas ARH-77 secrete IgG and have little/no IgG expression on their surface. Photoactivated droplets will be chosen from droplets with IgG secretion as detected by the standard DropMap assay, to identify ARH-77 cells; the photoactivated population should therefore not include any IgG high/positive cells. Confirmation of the “photoactivated” population in FACS corresponding to the targeted population will be followed by recovery and BCRseq of cells with known VDJ sequences. A tetanus-toxoid (TT) specific DropMap assay will be performed on mixed suspensions of DB, ARH77, and SA13 (ATCC HB-8501) cell lines, followed by specific targeting of each cell line depending on the observed presence or lack of IgG secretion or specificity towards TT. SA13 is a human hybridoma that is specific to TT. The heterogeneous cell sample replicates the mixture of non-Ig-secreting, non-specific Ig-secreting, and antigen-specific Ig secreting cells that would be expected from an ex vivo sample, while allowing for the precise VDJ sequence of each of the 3 populations to be known. This allows for determination of both the accuracy of photoactivated cell sorting, as the sorted clonotype should exclusively belong to the targeted secretion phenotype, and the precision of the single cell BCRseq method utilized, particularly in terms of sequence fidelity and CDR3 length. The goal of these experiments will be to demonstrate the specific and robust scBCRseq of each targeted cell line with no contamination from the non-targeted cell lines.

We ultimately plan to use DropPick to select ASCs from the spleen, bone marrow and blood of an immune thrombocytopenia (ITP) patient that we have studied previously (Canales-Herrerias et al, *J Clin Invest* 2022)<sup>152</sup> and that displayed high numbers of high-affinity anti-GPIIbIIIa plasma cells and plasmablasts. Photoactivated cells will be isolated by FACS for BCRseq and re-expressed as fully human IgG1. Their specificity and affinity towards GPIIbIIIa will be assessed by BLI, and their clonal relationship examined. The aim is to demonstrate the clonal relationship between high-affinity anti-GPIIbIIIa ASC from different anatomical locations within the same individual. This investigation would also provide rare antibody sequences for an autoimmune context where little is known about the autoreactive repertoire responsible for pathology. DropPick is well adapted to

address this problem, as the visualization of antigen-specific B cells using traditional antigen-based labelling and FACS isolation has proven impossible for the antigens primarily targeted by autoreactive cells during ITP. Indeed, staining of memory B cells with fluorescently labeled platelet antigen is unsuccessful as these cells are probably covered by platelet debris, fragments or antigens in circulation in this disease.

### **Improvements to DropMap analyses**

At the inception of the DropMap technique, secondary analysis was performed with Excel (Microsoft) for its ease of use and the ability to readily identify problems or patterns visually. From all droplets quantified during the primary analysis, droplets likely containing ASC were identified based on a minimum relocation slope in the antibody detection fluorescence channel. These putative ASC containing droplets must then be visually screened by the experimenter. Several circumstances may often produce false positive signals. These scenarios include “cellular accumulation of fluorescence, pixel errors, insufficiently long beadlines or dust particles” (Eyer *et al*, 2017)<sup>132</sup>. Additionally, droplets must be verified to only contain a single cell, instead of no cell or multiple cells. A reliance on the experimenter for inclusion of each individual data point is problematic, due to the potential for bias during selection and difficulty maintaining consistency between replicate experiments, assay models, experimenters, and research groups. Experimenters are also cognizant of the nature of a given sample and may unconsciously vary the stringency by which they subjectively judge droplets. Overall, the original process for secondary DropMap analysis using Excel required a high degree of user supervision and all steps required manual transfer of datapoints.

The limitations imposed by visual droplet verification and manual data analysis using Excel prevent DropMap users from quickly producing results from experiments, which may be crucial for guiding the next steps in investigation. A dependence on manual analysis also contributes to the bespoke nature of DropMap and acts as a barrier towards more widespread adoption of the technique. Robust analyses performed using a publicly available program lend additional credibility to the analyses and technique. Finally, such heavily supervised analysis also inherently limits the scale and throughput of DropMap. Several hundred droplets may require verification within an image and usually several images are analyzed at once, cumulating in long analysis times.

The analysis module we have developed has addressed these concerns regarding analysis speed, accuracy, and reproducibility. The implementation of a user interface and pre-generation of figures and dataset visualizations should also reduce the barrier to entry for new users of DropMap and by extension DropPick.

### **Conclusion**

The realization of DropPick to address specific shortcomings in current ASC affinity measurement throughput when BCR sequences are needed represents a multifaceted endeavor that has encompassed three distinct stages. First, we have validated the integration of photoactivable dyes into the existing DropMap workflows, establishing a foundational framework for subsequent phases. The second stage has achieved the development of the technical capacity required to systematically uncage and, in turn, label specific cells of interest within the droplets under examination. Finally, we are in the process of fully validating the recovery of the labeled cells from the DropMap assay and their subsequent isolation, which is achieved through the utilization of pre-existing sorting technology. The implementation of an automated control protocol for DropPick has consisted of two technical solutions. The first solution involves the acceleration and automation of the existing DropMap analyses, streamlining the process of identifying and characterizing droplets of interest that are to be precisely targeted. This enhancement not only expedites the workflow but also minimizes potential sources of error, thereby contributing to the overall efficiency and reliability of both DropMap and DropPick. The second solution within this approach pertains to the direct control of microscope utilities, enabling the system to autonomously execute discrete illumination processes without the need for constant user intervention. This feature not only significantly reduces the demands on experimenters but also enhances the precision and consistency of the photoactivation process, thereby ensuring the accuracy of target cell recovery.

## Methods

### Data processing during automated analyses

All droplets are filtered on several criteria prior to determining the slope of antibody relocation, the first criteria being consistent with previous Excel analyses as well as two novel criteria we have introduced. First, the maximal Ig relocation ratio must be greater than that corresponding to a known low concentration of Ig (approximately 1nM of Ig). This filter removes droplets that do not demonstrate at any timepoint an Ig capture at least equivalent to the lower detection limit of the assay. Secondly, the difference between the Ig relocation ratio at the first and last timepoints must be greater than half of the relocation ratio difference between droplets containing assay buffer alone and the previous threshold described. This filter removes droplets that do not demonstrate a significant change in Ig capture during the assay. Third, any droplets with a relocation ratio less than 1 at any timepoint are excluded, as a relocation ratio  $< 1$  indicates incorrect beadline detection or droplet movement during acquisition. These latter two filters largely do not affect the size or character of the final dataset, as excluded droplets would be removed during later analysis steps, but implementing these filters significantly reduces analysis time and the verification workload.

The relocation slope is then determined by a least-squares linear regression, treating measured relocation ratios as y values and timepoints (minutes) as x values. Droplets with a regression  $R^2$  below the user defined threshold ( $\sim 0.7$ ) are excluded from downstream analysis. We decided to include this additional threshold as there are numerous scenarios in which the calculation of relocation slope using linear regression may be skewed or inappropriate. For example, if there is a significant change in the relocation ratio at a single timepoint, the slope calculated can be skewed towards the deflection (Figure 26). This would result in the over or underestimation of the relocation slope, as well as potential inclusion of non-ASC containing droplets. Several other patterns are conceivable where a comparable relocation slope may be calculated, but a linear regression fitting is fundamentally inappropriate (Figure 26). A robust method for the filtering of droplets during DropMap analysis must therefore include a minimum threshold for the  $R^2$  associated with the linear regression fitting and a significance test for the application of a linear regression to the relocation ratio trend. We have found that filtering of droplets based on  $R^2$  also significantly reduces the number of false positive droplets that must be removed during verification with minimal impact on true ASC-containing droplets; droplets

containing sources of false signal or that move during acquisition are more prone to non-linear relocation ratio profiles. This exclusion results in a reduced workload and analysis time during both manual and automated droplet verification approaches.

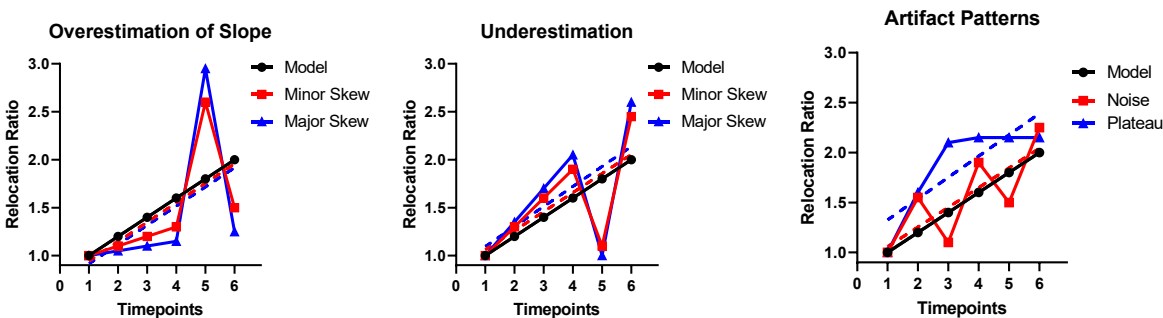


Figure 26 Scenarios potentially skewing relocation slope fitting. Hypothetical scenarios in which outlying datapoints or data patterns may skew a linear regression fitting. A model relocation ratio trend (black) is shown, with slope=0.2 and  $R^2=1$ . Alternative skew scenarios are shown in red and blue that yield near identical slope values as the model line (black), but with  $R^2$  values of 0.4-0.6.

Droplets passing these thresholds of relocation ratio and relocation ratio regression are then generated as images for verification of cell count and lack of artifact. Images are either shown to the user for verification or passed to a trained ResNet-50 classification model. Droplets identified as containing single cells then have Ig affinity and secretion rate calculated as previously described.

The Ig secretion rate is calculated using a reference curve consisting of known in-droplet antibody concentrations to translate the change in beadline relocation ratio into the change of in-droplet Ab molarity (e.g. +0.5 relocation ratio = +3nM in-droplet Ab concentration). The mean molarity change over the time course of the experiment is converted to moles (molecules) and finally adjusted to molecules per second according to the assay duration. To this calculation, we included an additional compensation for variations in individual droplet volumes. The average droplet volume of 40pL was assumed for all droplets during secretion estimation, for which a 1nM in-droplet IgG concentration corresponds to 24089 IgG molecules (Figure 27A). However, droplets may vary in size approximately +/- 3pL, which in turn means that 1nM in-droplet IgG may range from ~22500-25500. We therefore find the volume for each droplet using its radius (r) determined by the primary analysis using the equation in Figure 27B. Each droplet's determined volume is then used to calculate its secretion rate for additional estimation precision.

(A)

*molecules = droplet molarity (M) \* droplet volume(L) \* Avogadro's Constant*

(B)

$$V = 2\pi h(r - h)^2 + \pi^2 h^2 \left[ r - h \left( 1 - \frac{3}{4\pi} \right) \right]$$

Figure 27 Equations for Ig secretion calculation. (A) Calculation of number of molecules given droplet volume and molarity. (B) Equation to calculate volume of flattened sphere, “h” is considered as half of the observation chamber height (from Boitard L, et al. 2012).

### **Cell labelling with CMNB-CFSE**

Cells are washed twice with PBS by centrifugation at 300g for 5 min. Following the second wash, cells were resuspended in 1ml of CMNB-CFSE staining (10nM CMNB-CFSE in PBS) and left for 10 min at room temperature. Following the incubation, MACS buffer is added to fill the remaining tube capacity and the cells are washed twice with MACS by centrifugation at 300g for 5 min.

### **Droplet illumination and auto-correction**

The stage is first moved to the coordinates calculated. A brightfield image is taken and droplets are detected using the contrast-based “Spot Detection” native-function of NIS Elements; the camera focus in brightfield is offset during illumination to create prominent dark circles around droplets for more robust detection. The distances of detected droplet centers from the image center are measured and if the nearest droplet center is calculated as being more than 5 $\mu$ m and less than 25 $\mu$ m, the stage is moved to the coordinates of this nearest droplet. The rationale for 5 $\mu$ m constraint is to prevent moving the stage when it is not necessary for optimal beaming. For the 25 $\mu$ m constraint, the stage should not be moved as this signifies 2 possible negative outcomes. The target droplet may already be within the illumination area but was undetected and the “nearest” detected droplet is a non-target droplet, in which case movement would cause illumination of a non-intended droplet. Alternatively, due to excess movement there may be no droplet center within 25 $\mu$ m of the image center, in which case the lack of a droplet is advantageous as a non-target droplet would not be illuminated and the stage should not move.

It is worth noting that in >95% of cases, the original movement of the stage to the calculated coordinates centers the image within <5 $\mu$ m of the intended droplet center. This feature is only used

in a minority of cases to achieve optimal illumination. Additionally, in the rare cases where a non-target droplet has moved within the calculated coordinates of the target droplet, the non-target droplet would be illuminated regardless of the auto-centering feature and so this correction does not introduce new artifacts.

### **Emulsion breaking and cell recovery.**

The observation chamber is removed from the imaging apparatus and fitted with nanoport adapters (F-333NX, IDEX). The observation chamber is then inverted, and the outlet port is positioned above a 200ul low-binding pipette tip (Rainin), which is held vertically and plugged at its narrow end using a custom-made PDMS insert. The inlet port of the observation chamber is attached to a neMESYS syringe pump (Cetoni) and HFE7500 oil is flowed at 1000ul/h to empty the observation chamber. Once all droplets have been transferred to the 200ul pipette tip, an anti-static instrument (Zerostat Anti-Static Gun) is placed against the wall of the pipette tip at the level of the aqueous (droplet) to oil phase interface. The anti-static instrument is triggered for a minimum of 50 cycles until all droplets have coalesced into a single large droplet. A compatible pipette is attached to the pipette tip and the PDMS insert is removed. Next, the pipette is positioned above an empty 1.5-ml Eppendorf tube and the pipette volume adjustment knob is carefully turned to extrude the oil. When as much oil has been removed as possible without perturbing the coalesced aqueous phase, the aqueous phase is transferred into the appropriate tube and buffer for following analyses.

# **ARTICLE 5**

**(in preparation)**

# Deep learning enabled label-free microfluidic droplet classification for single cell functional assays

## Authors

Thibault Vanhoucke<sup>1,2</sup>, Angga Perima<sup>1</sup>, Lorenzo Zolfanelli<sup>1,3</sup>, Pierre Bruhns<sup>1</sup>, Matteo Broketa<sup>1,2,4,\*</sup>

## Affiliations

<sup>1</sup>Institut Pasteur, Université Paris Cité, INSERM UMR1222, Antibodies in Therapy and Pathology, 75015 Paris, France.

<sup>2</sup>Sorbonne Université, College Doctoral; Paris, France.

<sup>3</sup>Laboratoire de Colloïdes et Matériaux Divisés, École Supérieure de Physique et de Chimie Industrielles de la Ville de Paris, Université Paris Sciences et Lettres, CNRS UMR8231, Paris, France

<sup>4</sup>Diaccurate SA, F-75003 Paris, France

\*: corresponding author.

## ABSTRACT

Droplet-based microfluidics (DBMF) techniques coupled to microscopy allow for the characterization of cells at the single-cell scale. However, such techniques generate substantial amounts of data and microscopy images that must be analyzed. Droplets on these images usually need to be classified depending on the number of cells they contain. This verification, when visually carried out by the experimenter image-per-image, is time-consuming and impractical for analysis of many assays or when an assay yields many putative droplets of interest. Machine learning models have already been developed to classify cell-containing droplets within microscopy images, but not in the context of assays in which non-cellular structures are present inside the droplet in addition to cells. Here we develop a deep learning model using the neural network ResNet-50 that can be applied to functional droplet-based microfluidic assays to classify droplets according to the number of cells they contain with >90% accuracy in a very short time. This model also performs high accuracy classification of droplets containing cells alone and can accommodate several different cell types, for generalization to a broader array of DBMF applications.

## INTRODUCTION

Droplet-based microfluidics (DBMF) have been a breakthrough in the realm of biological research, having been applied to molecular analyses and single cell analyses, particularly in the field of immunology. DBMF assays offer significantly improved throughput and parallelization while also minimizing reagent usage by miniaturizing the traditional well-plate format. Despite the apparent improvements offered by the adaptation of existing assays into DBMF formats for single cell characterization, there is a technical limitation imposed by the nature of current droplet generation methods. The encapsulation of cells into droplets follows Poisson distribution patterns of in droplet cell numbers and is an inherently heterogeneous process<sup>1</sup>. For DBMF methods to achieve true single cell resolution, final analysis of single cells may be achieved by a high cellular dilution factor prior to encapsulation or a means of sorting for single-cell/-object droplets following encapsulation. Various methods have implemented single cell sorting either as a physical droplet isolation step using dielectrophoresis, a piezoelectric actuator, or a solenoid actuator<sup>2</sup> or alternatively as an analytical filter applied during data analysis<sup>3,4</sup>; both approaches have recently begun to be driven using single cell content classifications made by machine learning algorithms.

Machine learning has seen considerable growth in recent years regarding its technical capabilities as well as its ease of applicability and robustness. Due to their successful application in image classification tasks and increased accessibility, Convolutional Neural Network (CNN) architectures have paved the way for the exploitation of deep learning methods in biotechnology. CNNs can directly extract information from input images: they are implemented as a deep series of convolutional layers, where at each convolutional layer a sliding filter is applied to the input image to produce an activation map of the detected features. Layer after layer this information is progressively pooled and simplified to obtain, at the last output layer, a categorical classification for the input image. The fact that all the model parameters can be learned directly from the data, using a set of manually classified training images, simplifies the application and exploitation of these architectures.

Various machine learning models have been developed to address the needs of those working on microfluidics. Microfluidic devices and the experimental procedures they are

employed under are now able to be artificially designed by machine learning, as well as the analysis of droplets for classification and sorting<sup>4</sup>. Deep learning methods offer considerable improvement when handling structured data types, namely images within the context of DBMF. The availability of numerous publicly available deep learning solutions offers researchers means to automatically identify droplets containing single cells and extract biophysical feature data, increasing the throughput and breadth of analyses<sup>5</sup>. CNNs have been used for high throughput sorting of droplets according to the number of objects they contain with the added functionality to distinguish mixtures of in-droplet objects, such as a cell and bead mixture<sup>6</sup>. Another method of droplet classification recently demonstrated the classification of various cell types despite having visually similar presentations when manually analyzed<sup>7</sup>.

Parallel to the application of machine learning to DBMF, another emerging field of DBMF has been in-droplet secretion assays for single cell functional characterization<sup>8,9</sup>. These techniques often utilize microbeads<sup>10</sup>, rods<sup>11</sup>, or nanoparticles<sup>12</sup> as surfaces for assay reactions or reagent and analyte capture. The detection of secreted analytes by surface capture is the basis for several widely used techniques in biomedical research<sup>8,13</sup>, namely ELISA and ELISPOT or FLISA and FLUOROSPOT depending on whether detection is enzyme or fluorophore-based, respectively. Single cell DBMF secretion assays will likely become increasingly common given the increased throughput and parallelization afforded by such techniques, as has been seen with DBMF techniques for single cell molecular characterization compared to their well plate-based predecessors<sup>14</sup>. The additional data that may be extracted from the images gathered during DBMF techniques, such as cell morphology or motility, also allows one to address unexplored aspects of functional heterogeneity.

The presence of non-cellular structures within the droplet represents an additional challenge during analyses where cellular features require identification. Cell detection and quantification during image analyses has been extensively addressed and numerous informatic packages are available to incorporate into image analysis pipelines<sup>15,16</sup>. Cell detection is commonly performed using fluorescent surface markers when possible or detection in the brightfield channel when label-free conditions are necessary. However, during DBMF secretion assays the included analyte capture surface (beads or rods) will introduce its own fluorescent signals or brightfield distortions. Analyses of single cell DBMF secretion assays that use non-cellular capture surfaces

have largely been limited by a need for manual droplet verification or experimental restrictions. A requirement for manual droplet verification by the experimenter represents a significant analysis bottleneck, is less robust when applied over larger datasets, and reduces comparability of results between studies.

In this article we describe a deep learning solution using ResNet-50 for label-free droplet classification that is resistant to vertical non-cellular structures within the droplet. We used a droplet image dataset from a previous publication using the DropMap DBMF system, which utilizes paramagnetic beads to form a large immunoassay capture surface in the center of droplets. Our trained model is capable of classifying droplets as containing zero, one, or multiple cells to allow for automated analyses of DBMF secretion assays. This work addresses a gap in the current capabilities of machine learning-enabled image analyses to accommodate non-cellular structures that can obscure or mimic cells.

## RESULTS

### Conventional object recognition for cell detection

Conventional image analyses for cell detection use image processing algorithms such as morphological or thresholding-based transformation to identify objects within images and are preferred due to their relative simplicity and robustness<sup>17,18</sup>. The detection of cells from microscopy images is well established and several approaches are readily available through standard bioinformatic analysis packages<sup>19–21</sup>. We therefore initially sought to use conventional object recognition to address the need for determining the number of cells within droplets.

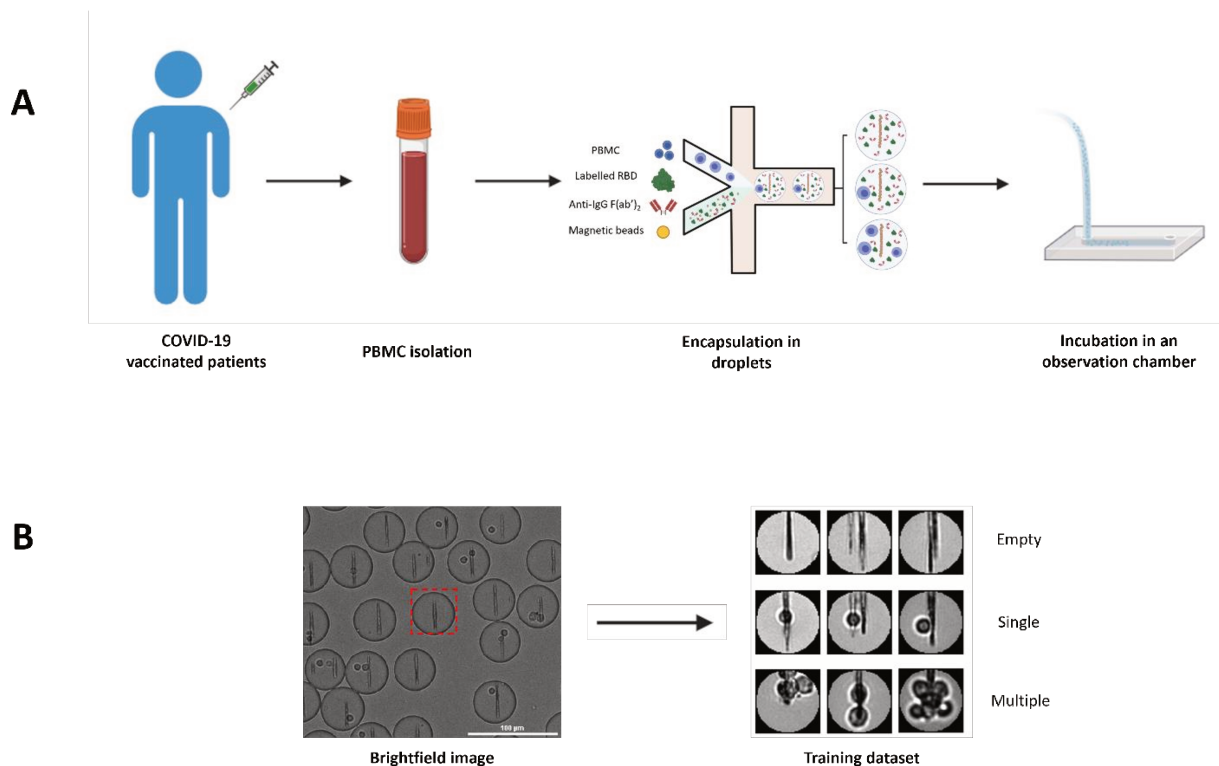


Figure 1. (A) PBMCs were isolated from COVID-19 vaccinated patient blood and injected into a microfluidic chip together with a mixture of anti-human-IgG-VHH-coated paramagnetic nanobeads, fluorescent antigen (recombinant SARS-CoV-2 Spike Receptor Binding Domain) and fluorescent anti-human IgG F(ab')<sub>2</sub>. The mix of cells and reagents was encapsulated in droplets using flow focusing technique. The produced droplets were introduced and immobilized in an observation chamber. A magnetic field generated by two magnets was applied to the chamber so that the nanobeads form a vertical line. (B) Brightfield images of the chamber were acquired with an optical microscope. Images of each droplet were cropped (red square) and manually sorted into 3 populations (empty droplets, single cell droplets, and multiple cell droplets).

To evaluate the performance of conventional methods we generated three classifications of droplet images as either empty, containing a single cell, or containing multiple cells, through sorting of randomly selected droplet images. Each classification contained 1,000 brightfield droplet images, gathered from previously published experiments (Figure 1)<sup>22</sup>. We also generated three similar image datasets of droplets containing cells only to compare the accuracy of conventional methods in the presence or the absence of nanobeads. For each dataset we tested three common cell detection methods for their ability to classify droplets according to the number of cells they contained: Hough transform<sup>23,24</sup>, Maximally Stable Extremal Regions (MSER) algorithm<sup>16,25</sup>, and segmentation algorithm<sup>26</sup> (Supplementary Figure 2).

Table 1. Classification accuracy of empty droplets, droplets containing a single cell and droplets containing multiple cells obtained with conventional methods (Hough transform, MSER algorithm, segmentation algorithm, in presence or absence of nanobeads in the droplets. The scores were calculated with 1,000 images for each condition.

Classification Dataset	Detection Method	Classification Accuracy (%)		
		Empty	Single cell	Multiple cell
Cells only	Hough transform	100	85	20
	MSER algorithm	99	21	26
	Segmentation algorithm	100	83	34
Cells with beads	Hough transform	99	31	4
	MSER algorithm	68	38	42
	Segmentation algorithm	99	62	42

When classifying droplets containing cells only, all tested methods achieve accuracy above 99% for empty droplets (Table 1). The accuracy for single-cell (multiple-cell) droplets is 85%, 21% and 83% (20%, 26% and 34%) for Hough transform, MSER algorithm and segmentation algorithm, respectively. When nanobeads are present within the droplets, the scores tend to either stay similar or decrease for most conditions. The accuracy for single-cell droplets is 31%, 38% and 62% for Hough transform, MSER algorithm and segmentation algorithm, respectively.

Overall conventional cell detection methods perform poorly to accurately quantify the number of cells in a droplet, especially when the droplet contains nanobeads, despite their proven accuracy and robustness in other applications. This is most likely explained by partial occlusion of the cells by the vertical line formed by the nanobeads (hereafter named *beadline*) (Supplementary Figure 2). Traditional cell detection methods usually require a defined border between the cell and other cells or environmental elements. In this context, occlusion of cells by the beads disrupts the cell border within the image, as well as often the cell's measured "circularity", causing cells to erroneously be excluded from detection. Additionally, the *beadline* itself occasionally presents with morphological irregularities that may be detected as a cell, further obfuscating detection. We therefore sought to use machine learning to find a more reliable method to classify droplets based on the number of cells they contain.

## **Deep Learning**

ResNet-50 is a 50-layer CNN architecture introduced in 2015, designed to address the problem of vanishing gradients in very deep neural networks, which can make it difficult for the network to learn and make accurate predictions<sup>27</sup>. ResNet-50 is based on the residual learning framework, which involves adding "shortcut connections" that allow information to flow directly from one layer to another while bypassing one or more intermediate layers. ResNet-50 models are typically trained using mini-batch stochastic gradient descent, which involves randomly selecting a subset of the training data (a "mini-batch") and using it to update the network's weights. Overall, ResNet-50 is a powerful CNN architecture that has been shown to achieve state-of-the-art performance on a variety of domains including microfluidics<sup>28,29</sup>.

Before training the neural network, we manually generated two training datasets (with or without nanobeads in the droplets) each containing three categories (empty, single-cell and multiple-cell). Each category was composed of 2,500 and 16,000 images for the datasets with and without *beadlines*, respectively. We then assessed the performances of ten model replicates for each dataset. Each replicate was tested with the images used to evaluate the accuracy of conventional methods. When trained and tested with droplets containing cells only, ResNet-50 reached accuracy scores above 99% for each category (Table 2). When trained and tested with droplets containing cells and *beadlines*, the accuracy for single-cell droplets dropped to 55%, whereas the accuracy for

empty and multiple-cell droplets remained above 90%. When trained with droplets containing cells and beadlines (cells only) and tested with droplets containing cells only (cells and beadlines) overall accuracy scores were lower compared to the other conditions, which was expected. The presence of the beadline within droplets likely represented an obstacle to classification. The potential for nearby droplets to also introduce image distortion at the edges of the droplet image also likely affected the model. We therefore implemented a pre-processing method for removing information irrelevant to classification, such as the beadline and droplet borders, while also emphasizing meaningful information, which in this case represented the cells.

Table 2. Classification accuracy of empty droplets, droplets containing a single cell and droplets containing multiple cells obtained with machine learning models (ResNet-50), in presence or absence of nanobeads in the droplets. The scores were calculated with 1,000 images for each condition.

Classification Dataset	Detection Method	Classification Accuracy (%)		
		Empty	Single cell	Multiple cell
Cells only	ResNet-50 (cell trained)	100	99	99
	ResNet-50 (cell + bead trained)	100	72	97
Cells with beads	ResNet-50 (cell trained)	71	59	81
	ResNet-50 (cell + bead trained)	100	55	92

## Image Preprocessing

Image pre-processing is composed here of four steps. First, a convolution using a Prewitt operator kernel<sup>30</sup> is applied to remove the beadline and other vertical structures (Figure 2a). This causes the image background to be uniformly grey, whereas horizontal edges are either white or black; this difference is due to the asymmetry of the Prewitt operator. Then, a sigmoidal filter is applied to enhance the segregation between the background and the contours (Figure 2b). All images are then resized, and pixel values are harmonized by applying an affine transformation (Figure 2c). Finally, droplet borders are removed by applying a circular binary mask, in which the central circle radius is several pixels less than that of the droplet (Figure 2d).

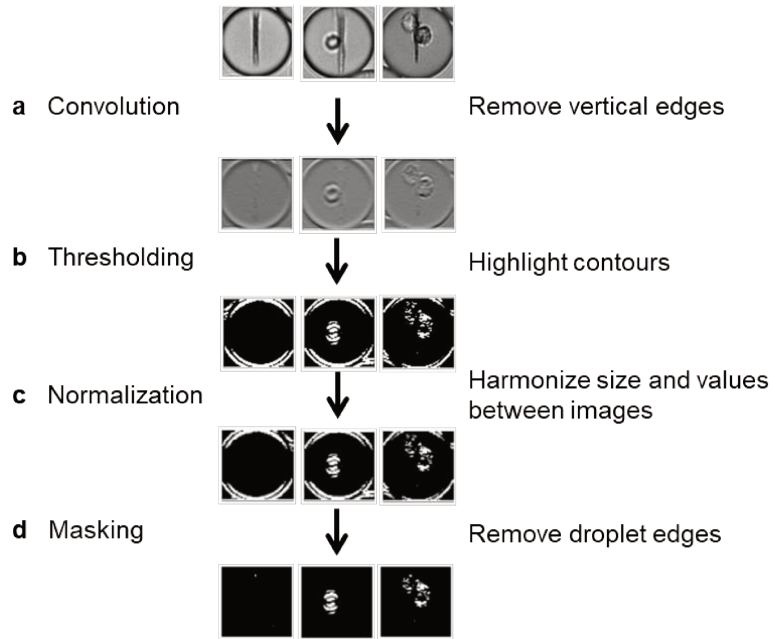
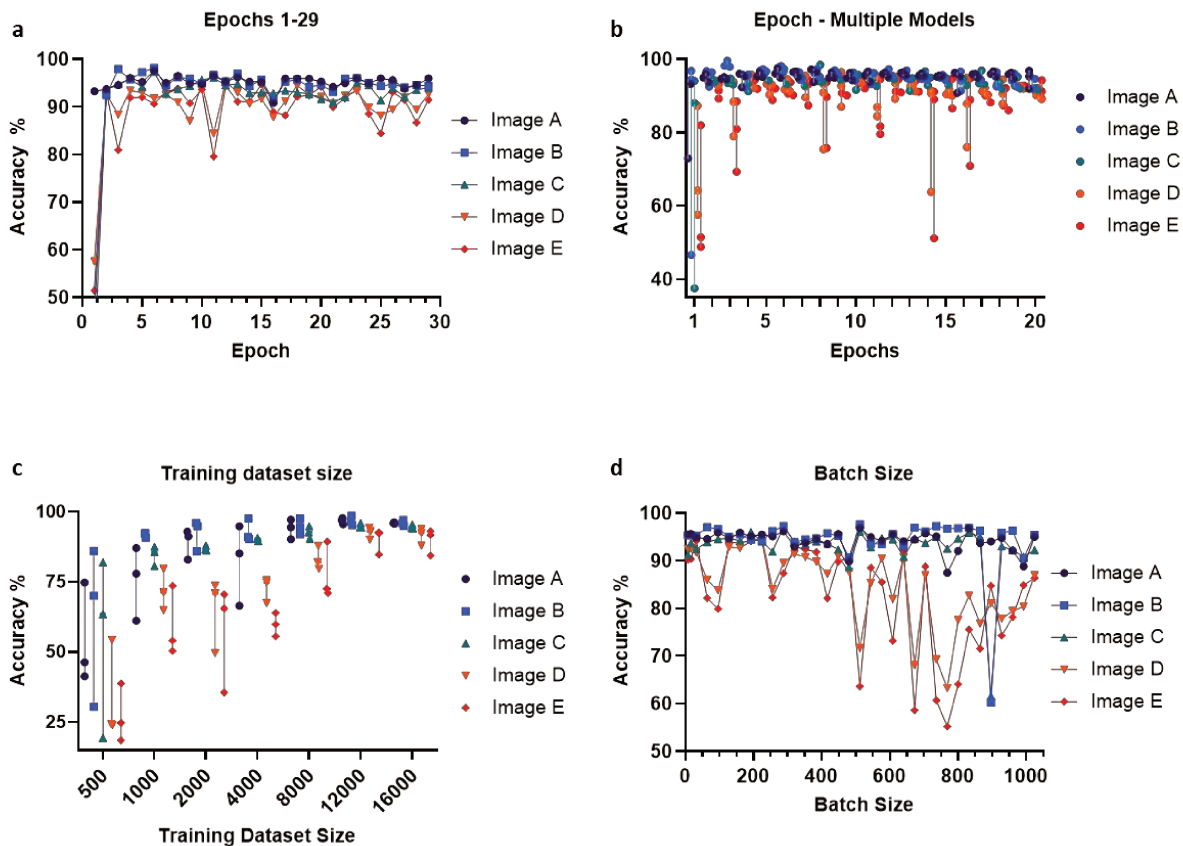


Figure 2. Flow Chart of proposed preprocessing method. (a) A horizontal-edge-detecting convolution using Prewitt operator removes the beadline and other vertical structures. (b) A sigmoidal threshold is applied to create firm segregation between the detected edges and the uniform grey. (c) Images are resized to create uniform input for model training. (d) The droplet edges are removed by applying a circular black mask, whose radius is slightly lower than the half-width of the image.

## Model Performance

We set out to optimize various training parameters, including the dataset size, the number of epochs, and the batch size. The training datasets again contained 3 classes of images, empty droplets, or no cells (empty), droplets with only a single cell (single), or droplets with multiple cells or clear aggregates (multiple). Accuracy was tested on droplet images across 5 independent experiments (300 images per experiment, 1,500 images in total) to investigate potential performance variability (Figure 3).



**Figure 3** – Adjustment of epochs number, training dataset size (per class) and batch size. The values of these parameters were optimized by evaluating validation accuracy using data from five independent experiments (Images A-E). For each image, three hundred droplets were used to measure the accuracy. Prediction precision was calculated using either one (a,d) or three (b,c) trained models per parameter value. The default values for the parameters are training dataset size = 16,000 images per class, epochs number = 12 and batch size = 64.

As expected, the performance of the model improves as the training dataset increases, with the accuracy reaching a plateau around 12,000 images per class (Figure 3c). Concerning the number of epochs, an abrupt increase in accuracy was observed for the first several epochs, followed by a plateau and a trend to decrease after 10 epochs, corresponding to the onset of overfitting (Figure 3a). Large batch sizes led to irregular performances, as the model likely became unable to converge quickly enough; the optimal and most stable accuracies were obtained with batch sizes between 128 and 200 (Figure 3b). From these observations, we proceeded to train a final model using 16,000 images per class to train the final model, and the gradient descent was performed using 6 epochs and a batch size of 160.

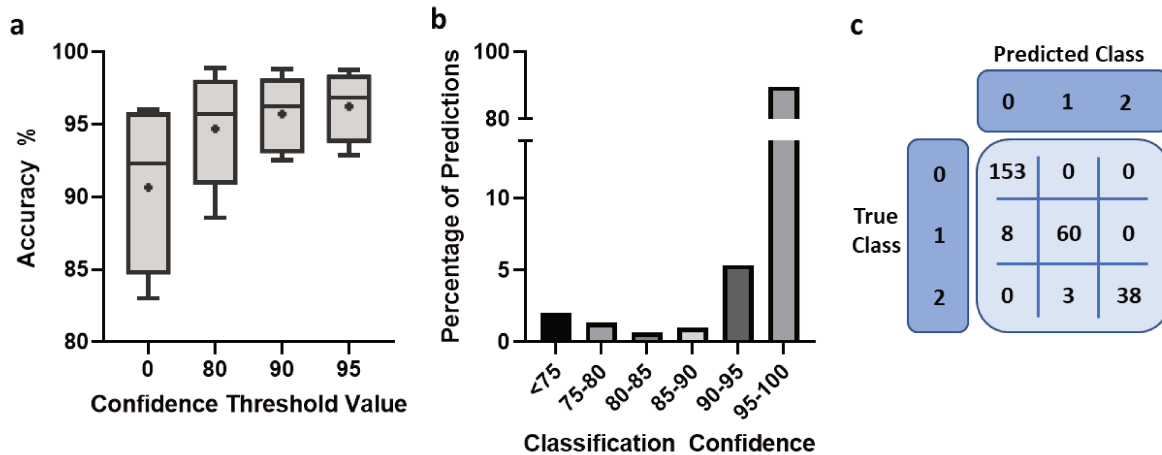


**Figure 4** Model performance after training. (a) Accuracy of model predictions under different conditions of confidence restriction,  $n=5$  and “+” indicates mean. (b) Bar chart representing the proportion of predictions against the classification confidence of the trained model. (c) Representative confusion matrix used to assess model performance.

We used the same 5 image datasets to further assess performance of the final model in representative conditions for applied experiment analysis. The model demonstrates a high degree of accuracy, over 90% in all images analyzed (Figure 4a-b). Moreover, imposing a confidence threshold to only include the most reliable predictions led to an increase of accuracy and reduced variability between experiments. This confidence threshold for classification exclusion did not result in notable amounts of data loss, 2% or 5% of all predictions when a threshold of 75 or 90 was applied, respectively (Figure 4b). We further investigated model performance through the confusion matrices of classifications to better understand the nature of errors made by the model (Figure 4c). The model appears minorly skewed towards under-detection of cells, with the number of cells in the droplet being underestimated when classification is incorrect. We also investigated the applicability of this model with pre-processing to droplet contexts that do not have a non-cellular structure present. When assessing droplets containing PBMCs alone, the model was 99% accurate in identifying droplets containing single cells (). Our findings demonstrate the model can perform cell content classification of droplets both with and without non-cellular structures present.

## DISCUSSION

In the process of optimizing and automatizing our existing DBMF data analyses, which relied heavily on manual discrimination of droplet images, we faced limitations of classical image analysis approaches aimed at detecting cells in the absence of other structures that may hide part or the entirety of the cell. We explored the possibility of using a well-established machine learning classification approach based on the CNN ResNet-50. We demonstrate high accuracy classification under our assay conditions where magnetic nanoparticles form a column (termed *beadline*) within the droplet that often occludes or mimics the shape of cells. Introducing an additional pre-processing module that was specific to the morphological properties of these images – the presence of vertically aligned linear structures – significantly improved the model training performance and the accuracy of the results.

In most known approaches to machine learning for image classification, minimal pre-processing is applied to the datasets or generic data normalization transformations are used with the aim of improving the numerical stability and the convergence time of the models<sup>31</sup>. In our scenario we show that adding an application-specific pre-processing step can be highly beneficial, guided by previous-knowledge-based assumptions on which image features do not carry any useful information for the classification. Other DBMF techniques that use non-cellular objects whose morphology is sufficiently different from cells<sup>32</sup> may benefit from adding a custom filter at the start of any image-based machine learning pipeline.

It is noteworthy that our full pipeline produced an improvement in results also for droplets that do not contain any *beadline*. In this case, the application of the circular mask before feeding the images in the neural network may have played a significant role in masking disturbances that could arise from surrounding droplets. This can be expected as CNNs alone are inherently local and insensitive to global (non-local) patterns<sup>33,34</sup>, and might advocate for the integration of non-local layers in networks used to analyze structured images. Our implementation of ResNet-50 for droplet classification offers a simple, robust solution for other investigators seeking to implement cell number classification into their DBMF analysis workflows.

We applied our approach to the classification of droplet images coming from a stationary experiment, in which droplets were immobilized in a horizontal-plane imaging chamber. However, the sole element needed to perform this classification is a bright-field image of the droplet. This

classification method may also be applied to images from flowed DBMF systems, in which the images of single flowing droplets can be captured using a high-speed camera<sup>35</sup>. In such cases, the ability to quickly perform an automated classification could be used to directly trigger sorting decisions in real-time. Despite the availability of image flow cytometry and cell sorting, commercially available systems only allow for a limited set information from the image to be used to gate and sort cells<sup>36</sup>; being able to feed the image through a pre-trained neural network and sort the droplets according to the output holds the potential of improving existing workflows in droplet-based assays where the recovery of rare or difficult-to-detect populations is required.

The application of deep learning methods to make “live” sorting decisions poses significant barriers, especially in fast high-throughput setups where all the computations must be done with strict and reproducible timing. We believe that the increasing performance of currently available workstations and acquisition hardware, coupled with the smart design of synchronized acquisition setups<sup>6</sup> will make AI-assisted sorting a valuable tool for DBMF. Our work to implement machine learning for droplet cell number classification in a context with in-droplet structures to measure secretion significantly improves the throughput of such single cell assays as well as the scope of machine learning use for DBMF.

## Bibliography

1. Moon, S. J., Ceyhan, E., Gurkan, U. A. & Demirci, U. Statistical modeling of single target cell encapsulation. *PLoS One* **6**, (2011).
2. Murphy, T. W., Zhang, Q., Naler, L. B., Ma, S. & Lu, C. Analyst CRITICAL REVIEW Recent advances in the use of microfluidic technologies for single cell analysis. *Cite this: Analyst* **143**, 60 (2018).
3. Sesen, M. & Whyte, G. Image-Based Single Cell Sorting Automation in Droplet Microfluidics. *Sci Rep* **10**, (2020).
4. Srikanth, S., Dubey, S. K., Javed, A. & Goel, S. Droplet based microfluidics integrated with machine learning. (2021) doi:10.1016/j.sna.2021.113096.
5. Soldati, G. *et al.* Microfluidic droplets content classification and analysis through convolutional neural networks in a liquid biopsy workflow. *Am J Transl Res* **10**, 4004–4016 (2018).
6. Anagnostidis, V. *et al.* Lab on a Chip Deep learning guided image-based droplet sorting for on-demand selection and analysis of single cells and 3D cell cultures †. **20**, 889 (2020).
7. Chen, C. L. *et al.* Deep Learning in Label-free Cell Classification. *Sci Rep* **6**, 21471 (2016).
8. Bucheli, O. T. M., Sigvaldadóttir, I. & Eyer, K. Measuring single-cell protein secretion in immunology: Technologies, advances, and applications. *Eur J Immunol* **51**, 1334–1347 (2021).
9. Broketa, M. & Bruhns, P. Single-Cell Technologies for the Study of Antibody-Secreting Cells. *Front Immunol* **12**, (2022).
10. Konry, T., Dominguez-Villar, M., Baecher-Allan, C., Hafler, D. A. & Yarmush, M. L. Droplet-based microfluidic platforms for single T cell secretion analysis of IL-10 cytokine. *Biosens Bioelectron* **26**, 2707–2710 (2011).
11. Wei, S. C., Hsu, M. N. & Chen, C. H. Plasmonic droplet screen for single-cell secretion analysis. *Biosens Bioelectron* **144**, 111639 (2019).
12. Eyer, K. *et al.* Single-cell deep phenotyping of IgG-secreting cells for high-resolution immune monitoring. *Nat Biotechnol* **35**, 977–982 (2017).
13. Janetzki, S., Rueger, M. & Dillenbeck, T. Stepping up ELISpot: Multi-Level Analysis in FluoroSpot Assays. *Cells* **3**, (2014).
14. Sánchez Barea, J., Lee, J. & Kang, D.-K. Recent Advances in Droplet-based Microfluidic Technologies for Biochemistry and Molecular Biology. *Micromachines (Basel)* **10**, (2019).
15. Maddalena, L., Antonelli, L., Albu, A., Hada, A. & Guarracino, M. R. Artificial Intelligence for Cell Segmentation, Event Detection, and Tracking for Label-Free Microscopy Imaging. *Algorithms* **15**, 313 (2022).
16. Buggenthin, F. *et al.* An automatic method for robust and fast cell detection in bright field images from high-throughput microscopy. *BMC Bioinformatics* **14**, 297 (2013).

17. Gao, H., Kwong, S., Yang, J. & Cao, J. Particle swarm optimization based on intermediate disturbance strategy algorithm and its application in multi-threshold image segmentation. *Inf Sci (N Y)* **250**, 82–112 (2013).
18. Macfarlane, F. *et al.* Robust Object Detection in Colour Images Using a Multivariate Percentage Occupancy Hit-or-Miss Transform. *Mathematical Morphology - Theory and Applications* **5**, 128–152 (2021).
19. Cuevas, E., Díaz, M., Manzanares, M., Zaldivar, D. & Perez-Cisneros, M. An Improved Computer Vision Method for White Blood Cells Detection. *Comput Math Methods Med* **2013**, 1–14 (2013).
20. Li, K. *et al.* Computer vision tracking of stemness. in *2008 5th IEEE International Symposium on Biomedical Imaging: From Nano to Macro* 847–850 (IEEE, 2008). doi:10.1109/ISBI.2008.4541129.
21. Markovic, S. *et al.* A computer vision approach to rare cell in vivo fluorescence flow cytometry. *Cytometry Part A* **83**, 1113–1123 (2013).
22. Broketa, M. *et al.* Qualitative monitoring of SARS-CoV-2 mRNA vaccination in humans using droplet microfluidics. *JCI Insight* **8**, (2023).
23. Djekoune, A. O., Messaoudi, K. & Amara, K. Incremental circle hough transform: An improved method for circle detection. *Optik (Stuttg)* **133**, 17–31 (2017).
24. Ioannou, D., Huda, W. & Laine, A. F. Circle recognition through a 2D Hough Transform and radius histogramming. *Image Vis Comput* **17**, 15–26 (1999).
25. Zhang, X., Bian, H., Cai, Y., Zhang, K. & Li, H. An improved tongue image segmentation algorithm based on Deeplabv3+ framework. *IET Image Process* **16**, 1473–1485 (2022).
26. Rosenfeld, N., Young, J. W., Alon, U., Swain, P. S. & Elowitz, M. B. Gene Regulation at the Single-Cell Level. *Science (1979)* **307**, 1962–1965 (2005).
27. He, K., Zhang, X., Ren, S. & Sun, J. Deep residual learning for image recognition. in *Proceedings of the IEEE Computer Society Conference on Computer Vision and Pattern Recognition* vols 2016-December (2016).
28. Praljak, N. *et al.* Integrating deep learning with microfluidics for biophysical classification of sickle red blood cells adhered to laminin. *PLoS Comput Biol* **17**, e1008946 (2021).
29. Sahaai, M. B., Jothilakshmi, G. R., Ravikumar, D., Prasath, R. & Singh, S. ResNet-50 based deep neural network using transfer learning for brain tumor classification. in 20014 (2022). doi:10.1063/5.0082328.
30. Baareh, A. K. M., Al-Jarrah, A., Smadi, A. M. & Shakah, G. H. Performance Evaluation of Edge Detection Using Sobel, Homogeneity and Prewitt Algorithms. *Journal of Software Engineering and Applications* **11**, 537–551 (2018).
31. Shanker, M., Hu, M. Y. & Hung, M. S. Effect of data standardization on neural network training. *Omega (Westport)* **24**, 385–397 (1996).
32. Ding, R. *et al.* Rapid isolation of antigen-specific B-cells using droplet microfluidics. *RSC Adv* **10**, (2020).

33. Song, H., Zhou, Y., Jiang, Z., Guo, X. & Yang, Z. ResNet with Global and Local Image Features, Stacked Pooling Block, for Semantic Segmentation. in *2018 IEEE/CIC International Conference on Communications in China (ICCC)* 79–83 (IEEE, 2018). doi:10.1109/ICCCChina.2018.8641146.
34. Wang, X., Girshick, R., Gupta, A. & He, K. Non-local Neural Networks. in *2018 IEEE/CVF Conference on Computer Vision and Pattern Recognition* 7794–7803 (IEEE, 2018). doi:10.1109/CVPR.2018.00813.
35. Gérard, A. *et al.* High-throughput single-cell activity-based screening and sequencing of antibodies using droplet microfluidics. *Nat Biotechnol* **38**, (2020).
36. Holzner, G. *et al.* High-throughput multiparametric imaging flow cytometry: toward diffraction-limited sub-cellular detection and monitoring of sub-cellular processes. *Cell Rep* **34**, (2021).
37. Rosenfeld, N., Young, J. W., Alon, U., Swain, P. S. & Elowitz, M. B. Gene Regulation at the Single-Cell Level. *Science (1979)* **307**, 1962–1965 (2005).
38. Buggenthin, F. *et al.* An automatic method for robust and fast cell detection in bright field images from high-throughput microscopy. *BMC Bioinformatics* **14**, 297 (2013).

## **Methods**

### **Cell preparation**

PBMCs were prepared as previously described (COVID Paper). Briefly, density gradient centrifugation (Ficoll-Paque Plus, 17-1440-03, GE Healthcare) was used to isolate PBMCs from venous blood samples. CD3<sup>-</sup> cells were enriched by negative selection using anti-CD3 microbeads (Miltenyi Biotec) according to manufacturer protocol.

The DB (ATCC, CRL-2289) cell line was cultured according to supplier guidelines, using RPMI-1640 Medium, supplemented with 10% fetal bovine serum.

All cell types were prepared prior to encapsulation in the same method. Cells were washed twice using PBS (Gibco, 14190-094) with 0.2% bovine serum albumin and 2 mM EDTA, then filtered through a 40- $\mu$ m cell strainer to remove aggregates. Cells were finally resuspended in assay buffer consisting of RPMI-1640 (without phenol red) supplemented with 0.1% Pluronic F68 (Gibco, 24040032), 25 mM HEPES pH 7.4, 5% KnockOut™ serum replacement (Thermo Fisher, 10828010), 0.5% human serum albumin (Sigma Aldrich, A9731).

### **Wafer production**

The wafer for chip production was fabricated using soft lithography technique. Wafers were spin-coated with SU-8 2035 (MicroChem) using 3000rpm for 30 seconds, then heated for pre-baking at 65°C for 5 minutes, followed by 95°C for 3 minutes. Afterwards, using MJB-4 (SUSS MicroTec), wafers were exposed to UV light (365nm) for 16 seconds. Subsequently, wafers were heated for post-baking at 65°C for 3 minutes and 95°C for 1 minutes then followed by developing to remove the SU-8 resin residue for 2 minutes at 100rpm. The thickness was measured using a DEKTAK profilometer (Bruker) to ensure ~40 $\mu$ m of thickness.

### **Chip production**

A mix of Sylgard 184 (Dow, 1317318) prepared at a 10:1 mix ratio was poured onto the wafer covered on its rear by round aluminium foil to create a mould. Subsequently, a desiccator was used to remove bubbles and incubated in an oven at 65°C for 2 hours. Afterwards, the foil mould and wafer were removed, appropriate holes were punched with a 0.75mm biopsy puncher, and the cured PDMS was plasma bonded with glass slide 75mm x 50mm (Corning, 2947-75x50). The microfluidic chips were then silanized using 5% v/v solution of 1H,1H,2H,2H-Perfluorododecyltrichlorosilane (Sigma, 729965) in HFE7500 oil (3M, B40045191).

### **Droplet formation**

Droplet were produced by mixing two aqueous phases. Phase 1 consisted of a cell suspension (30E6 cells/ml) flowed at 70 $\mu$ L/h and phase 2 consisted of assay buffer flowed at 70 $\mu$ L/h, with or without paramagnetic nanobeads as indicated. The oil phase consisted of 2% v/v solution of Perfluorosurfactant (RAN-Biotechnologies, 008-FluoroSurfactant) in HFE 7500 oil, with a flow rate of 600 $\mu$ L/h to obtain a final droplet volume of ~40pL.

### **Computing**

Computation was done with a Windows 10, 64-bit operating system using an AMD 3990X 4.3 GHz processor with 64 GB RAM and GeForce RTX 3080. All image data was stored and read from a local M.2 NVME SSD drive. Scripts were written in Python 3.7.11 utilizing the Tensorflow 2.5.0 library. Scripts used in this work are available as ESI.

### **Image acquisition**

An inverted microscope with a motorized stage (Nikon, Ti2-Eclipse) was used to acquire droplet images with a high-speed CMOS camera (Orca Flash 4.0, Hamamatsu) at room temperature. Images were acquired through a 10x objective (NA 0.45). The whole of the droplet chamber was acquired as an array of 9x9 individual images stitched together to form a single image. Image acquisition was done every 7.5 over 37.5 min (6 measurements in total). Duplicates were systematically acquired for every sample, with each replicate being the filling of the DropMap 2D chamber with a novel droplet population. Images were stored in the nd2 file format.

### **Datasets**

Droplets were identified as previously described (COVID Paper), based on circle detection by Hough transformation.  $X$  images were randomly selected from  $X$  total images available from the previous study (COVID Paper), representing  $Y$  different patients. Droplet images for model training were taken from the brightfield channel of the original nd2 format image, centered on the droplet, and cropped to the diameter of the droplet. Images were saved in the TIF file format. Droplet images were randomly generated without prior measurement or filtering based on droplet contents. Images for the creation of the validation datasets were selected amongst those images not included in the training dataset. Droplet images were visually classified by the authors according to number of cells inside of the droplets.

### **Image preprocessing**

The droplet image is either loaded from a tif file into a Python 3.7.11 environment using scikit-image v0.19.2 during training or cropped directly from the nd2 file according to measured position and diameter. Then, the image undergoes either a minimal or a more sophisticated preprocessing. In the latter, the image is convolved using a Prewitt operator kernel, with the `convolve2d` function from the `scipy.signal` package. Image contours are then highlighted using a sigmoid filter. The image is resized to dimensions of 55 x 55 pixels using the `resize` function without anti-aliasing from `skimage.transform` package. The pixel values are then normalized using the full in16 value range. A circular mask with a 5-pixel radius reduction compared to the image half-width is applied to the image to occlude the area outside of the droplet. When minimally preprocessed, the image is resized to dimensions of 55 x 55 pixels using the `resize` function without anti-aliasing from `skimage.transform`. Pixel values are then normalized. Images are finally all passed to the model as an array of  $(n, 55, 55)$  with  $n$  representing the number of images to be classified.

### **Convolutional neural network implementation**

Droplet images were separated into three classes: “Empty/0”, if the droplet contained no cell, “Single/1”, if one cell is within the droplet, and “Multiple/2”, if two or more cells are inside the droplet.

We used Keras module of the TensorFlow v2.5 library in Python 3.7.11 to define a ResNet-50 model (<https://arxiv.org/abs/1512.03385>). Images were converted resized to a uniform dimension of 55 x 55 pixels. Categorical crossentropy was used to compute loss during training. The learning rate was set to 0.001 during training. Hyper-parameters were incrementally increased to determine optimal values. Final model training was performed using 6 epochs and a batch size of 160. The training-set contained 95% of all labelled images with the remaining 5% used for the validation-set. The model used to classify droplets containing only cells was trained with 12 epochs, batches of 30 images and 2500 training images for each class.

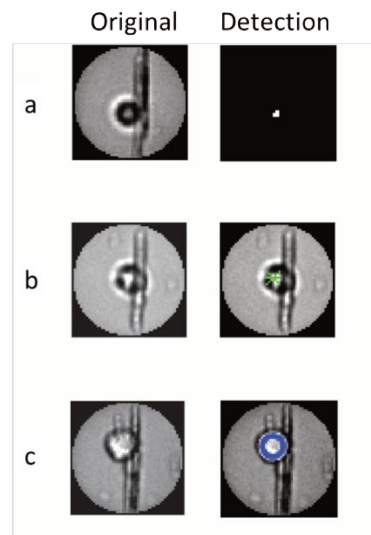
### **Computer-vision-based methods implementation**

Scripts for conventional object recognition were run in Matlab 2021a. Rosenfeld method was performed using the script previously published<sup>37</sup>, run with a ‘dilatation’ parameter of 15 instead of 7, to allow for the unique and unintended nature of our dataset.

Morphological shape algorithm method is similar with the method published by Buggenthin and colleagues<sup>38</sup>. On this method, we detect first the edge, adding mask to the image, create linear structuring elements, dilating the image, filling the holes, eroding the images, then find the image centroid. Number of cell was determined based on how many image centroid were calculated.

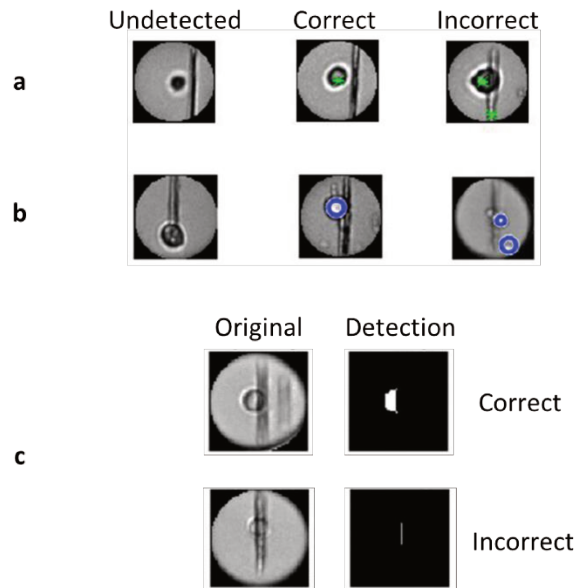
## Supplementary Information

### Supplementary Figure 1



Supplementary Figure 1. Cell detection in droplets containing aligned beads using various methods: (a) Maximally stable extremal regions (MSER) algorithm, (b) segmentation algorithm, or (c) Hough transform.

### Supplementary Figure 2



Supplementary Figure 2. Examples of incorrect cell detection due to non-cellular structure, using a (a) segmentation algorithm, (b) Hough transform, or (c) maximally stable extremal regions (MSER) algorithm.

# ARTICLE 6

## ARTICLE 6

### **Characterizing autoreactive ASCs in multiple organs during primary ITP**

In addition to my work on SARS-CoV2 and microfluidic development, I collaborated on another ongoing project within our group to characterize autoreactive ASCs in patients with primary immune thrombocytopenia (ITP). This work was a collaboration between the group of Immune System Development at Institut Necker Enfants Malades (INEM) directed by Dr Matthieu Mahévas and a former post-doc of our laboratory, Dr Pablo Canales-Herrerias, that had been submitted to *J Clin Invest* and came back with requests from the reviewers. I was asked to contribute at this stage to help with the revisions of the manuscript for acceptance.

ITP is an autoimmune disorder characterized by a low platelet count, leading to an increased risk of bleeding. Autoreactive B cells play a crucial role in the pathogenesis of ITP by producing autoantibodies that bind to antigens on the surface of platelets, marking them for destruction by the immune system. This results in a decrease in the number of circulating platelets, leading to the symptoms associated with ITP such as easy bruising, bleeding gums, and, in severe cases, internal bleeding. The exact mechanisms leading to the development of these autoreactive B cells in ITP are not fully understood. However, it is believed that both genetic and environmental factors contribute to their development. Some individuals may have a genetic predisposition that makes their B cells more likely to become autoreactive under certain conditions. Environmental triggers such as infections or exposure to certain drugs may also play a role. Given the central role of autoreactive B cells in ITP, many treatment strategies aim to reduce their numbers or inhibit their activity. These include immunosuppressive drugs, which reduce the overall activity of the immune system, and targeted therapies such as splenectomy or B cell depletion via immunotherapy.

The goal of this project was to functionally characterize autoreactive ASCs in ITP patients and determine the distributions of autoreactive ASCs and their affinities between different immune compartments of the spleen, bone marrow, and blood. We also investigated the effect of novel treatment on autoreactive ASCs. My contribution to this work involved using the DropMap assay to characterize additional patients and to compare the affinity and secretion rate repertoires

between frozen samples and how this may influence assay results. Our work demonstrated the efficacy of DropMap to study ASCs in an autoimmune context and provided valuable new functional insights on ASCs in ITP.

# High-affinity autoreactive plasma cells disseminate through multiple organs in patients with immune thrombocytopenic purpura

Pablo Canales-Herrerias,<sup>1,2,3</sup> Etienne Crickx,<sup>4,5</sup> Matteo Broketa,<sup>1,6,7</sup> Aurélien Sokal,<sup>4</sup> Guilhem Chenon,<sup>2</sup> Imane Azzaoui,<sup>5,8</sup> Alexis Vandenberghe,<sup>5,8</sup> Angga Perima,<sup>1</sup> Bruno Iannascoli,<sup>1</sup> Odile Richard-Le Goff,<sup>1</sup> Carlos Castrillon,<sup>1</sup> Guillaume Mottet,<sup>1</sup> Delphine Sterlin,<sup>1</sup> Ailsa Robbins,<sup>9</sup> Marc Michel,<sup>10,11</sup> Patrick England,<sup>12</sup> Gael A. Millot,<sup>13</sup> Klaus Eyer,<sup>14</sup> Jean Baudry,<sup>2</sup> Matthieu Mahevas,<sup>4,5,11</sup> and Pierre Bruhns<sup>1,11</sup>

<sup>1</sup>Institut Pasteur, Université Paris Cité, INSERM UMR1222, Unit of Antibodies in Therapy and Pathology, Paris, France. <sup>2</sup>Laboratoire Colloïdes et Matériaux Divisés (LCMD), ESPCI Paris, PSL Research University, CNRS UMR8231 Chimie Biologie Innovation, Paris, France. <sup>3</sup>École Doctorale Frontières du Vivant (FdV), Centre de Recherches Interdisciplinaires, Paris, France. <sup>4</sup>Institut Necker-Enfants Malades, INSERM U1151/CNRS UMS8253, Université Paris Descartes, Sorbonne Paris Cité, Paris, France. <sup>5</sup>Service de Médecine Interne, Centre national de référence des cytopénies auto-immunes de l'adulte, Hôpital Henri Mondor, Assistance Publique Hôpitaux de Paris (AP-HP), Université Paris Est Créteil, Créteil, France. <sup>6</sup>Diacurate SA, Paris, France. <sup>7</sup>Sorbonne University, ED394, Paris, France. <sup>8</sup>INSERM U955, Université Paris Est Créteil (UPEC), Créteil, France. <sup>9</sup>Department of Internal Medicine, Infectious Diseases, and Clinical Immunology, Robert Debré Hospital, Reims University Hospitals, Reims, France. <sup>10</sup>Centre Hospitalier Universitaire Henri-Mondor, Université Paris Est Créteil, Créteil, France. <sup>11</sup>Paris Est Créteil University UPEC, Assistance Publique-Hôpitaux de Paris (AP-HP), Henri Mondor Hospital, Fédération Hospitalo-Universitaire TRUE InnovaTive theRapy for immUne disorders, Créteil, France. <sup>12</sup>Plateforme de Biophysique Moléculaire, Institut Pasteur, CNRS UMR3528, Paris, France. <sup>13</sup>Hub Bioinformatique et Biostatistique – DBC, Institut Pasteur, Paris, France. <sup>14</sup>Laboratory for Functional Immune Repertoire Analysis, Institute of Pharmaceutical Sciences, ETH Zurich, Zurich, Switzerland.

**The major therapeutic goal for immune thrombocytopenic purpura (ITP) is to restore normal platelet counts using drugs to promote platelet production or by interfering with mechanisms responsible for platelet destruction. Eighty percent of patients with ITP possess anti-integrin  $\alpha$ IIb $\beta$ 3 IgG autoantibodies that cause platelet opsonization and phagocytosis. The spleen is considered the primary site of autoantibody production by autoreactive B cells and platelet destruction. The immediate failure in approximately 50% of patients to recover a normal platelet count after anti-CD20 rituximab-mediated B cell depletion and splenectomy suggests that autoreactive, rituximab-resistant, IgG-secreting B cells (IgG-SCs) reside in other anatomical compartments. We analyzed more than 3,300 single IgG-SCs from spleen, bone marrow, and/or blood of 27 patients with ITP, revealing high interindividual variability in affinity for  $\alpha$ IIb $\beta$ 3, with variations over 3 logs. IgG-SC dissemination and range of affinities were, however, similar for each patient. Longitudinal analysis of autoreactive IgG-SCs upon treatment with the anti-CD38 mAb daratumumab demonstrated variable outcomes, from complete remission to failure with persistence of high-affinity anti- $\alpha$ IIb $\beta$ 3 IgG-SCs in the bone marrow. This study demonstrates the existence and dissemination of high-affinity autoreactive plasma cells in multiple anatomical compartments of patients with ITP that may cause the failure of current therapies.**

## Introduction

Immune thrombocytopenic purpura (ITP) is an immune disorder characterized by a strong autoimmune response against platelet autoantigens that causes platelet destruction (1). Clinical manifestations often present as mild bleeding on the skin or mucosal surfaces, but can also include life-threatening internal bleeding

episodes in more severe cases (2, 3). The hallmark of ITP is the presence of anti-platelet antibodies, which contributes to the accelerated destruction of platelets by mechanisms that include FcR-mediated phagocytosis by macrophages, and inhibition of new platelet generation by megakaryocytes. Autoantibodies against platelets are predominantly of the IgG isotype (4), with IgG1 being the most prevalent subclass (5). Although several platelet surface proteins are known to be targeted by autoantibodies, namely the CD42 complex (GPIb/IX/V), integrin  $\alpha$ 2 $\beta$ 1 (GPIa/IIa), and GPVI (6), the integrin  $\alpha$ IIb $\beta$ 3 complex (GPIIb/IIIa) has long been known as the dominant autoantigen in ITP, with anti-integrin  $\alpha$ IIb $\beta$ 3 antibodies found in 60% to 90% of patients (6–8).

The spleen plays a major role in the pathophysiology of ITP (9), and splenectomy remains the most effective and curative therapy (10). Indeed, autoreactive anti- $\alpha$ IIb $\beta$ 3-secreting cells arise from germinal center reactions located in the spleen of patients with ITP. Germinal center expansion results from T follicular helper

**Authorship note:** JB, M Mahevas, and PB are co-senior authors.

**Conflict of interest:** KE and JB have filed patents (WO/2016/159182 and WO/2010/007307) on the DropMap technology, and the inventors may receive payments related to exploitation of these under their employer's rewards-to-inventors scheme. M Mahevas received research funds from GSK and consulting fees from LFB and Amgen. PB received consulting fees from Regeneron Pharmaceuticals.

**Copyright:** © 2022, Canales-Herrerias et al. This is an open access article published under the terms of the Creative Commons Attribution 4.0 International License.

**Submitted:** July 27, 2021; **Accepted:** April 28, 2022; **Published:** June 15, 2022.

**Reference information:** *J Clin Invest.* 2022;132(12):e153580.

<https://doi.org/10.1172/JCI153580>.

cell activation (11) and reduced Treg cell numbers (12). Pathogenic anti- $\alpha$ IIB $\beta$ 3 antibody-secreting cells can be detected by ELISpot in the spleen and blood of patients with ITP (9, 13, 14). In this prototypic antibody-mediated autoimmune disease, B cell depletion using rituximab (anti-CD20 mAb) is widely used, with up to 60% of patients having a short-term complete response (15), 40% achieving durable responses (6–12 months), and only 20% to 30% achieving a long-term response (5 years; refs. 16, 17). Paradoxically, B cell depletion therapy stimulates an adaptation of splenic short-lived plasma cells that leads to their reprogramming into long-lived spleen cells in patients with ITP, explaining in part primary failure of rituximab (13). Furthermore, relapse of ITP after B cell depletion therapy with rituximab usually occurs during B cell lymphopoiesis (more than 6 months after treatment), corresponding to the reinitiation of an autoimmune B cell response. We recently demonstrated that rituximab-resistant memory B cells directly contributed to ITP relapses by enabling autoreactive germinal centers along with the recruitment of naive B cells and leading to anti- $\alpha$ IIB $\beta$ 3 secretion by newly formed antibody-secreting cells (ASCs) (18).

In a T cell-dependent response such as ITP, ASCs arise from germinal centers or memory B cells and egress the spleen as short-lived ASCs to circulate in the blood, with some maturing into long-lived plasma cells in the bone marrow. The longevity of ASCs is not primarily cell intrinsic but largely depends on signals provided by their microenvironment (19–21). Despite their fundamental role, a major impediment to studying heterogeneity of autoimmune ASCs is the difficulty in assessing the specificity of such cells that express no or relatively few immunoglobulins at their surface. In order to decipher the exact contribution of different subsets of anti- $\alpha$ IIB $\beta$ 3 ASCs to the pathogeny in different organs and in different clinical situations, we performed herein a high-throughput phenotypic analysis of these autoreactive human IgG-secreting cells (IgG-SCs) at single-cell level, comparing patients with ITP and healthy donors. We describe a 3-log repertoire of affinities of anti- $\alpha$ IIB $\beta$ 3 IgG autoantibodies secreted from freshly isolated spleen, bone marrow, and blood. The proportion of autoreactive cells among IgG-SCs was highly correlated between the spleen and the 2 other compartments, and very-high-affinity anti- $\alpha$ IIB $\beta$ 3 IgG-SCs were detected in all 3 compartments. A longitudinal analysis of autoreactive IgG-SCs in 3 patients refractory to approved treatments who were administered the anti-CD38 mAb daratumumab demonstrated interindividual variability in the targeting of high-affinity anti- $\alpha$ IIB $\beta$ 3 IgG-SCs. These studies identify the large repertoire of anti- $\alpha$ IIB $\beta$ 3 affinities in patients with ITP and demonstrate the existence and dissemination of high-affinity autoreactive ASCs to the bone marrow of patients with ITP that may be the underlying cause of failure of current therapies.

## Results

*Single-cell bioassay allows phenotypic characterization of autoreactive ASCs.* In order to directly characterize the secretion rate, specificity, and affinity for  $\alpha$ IIB $\beta$ 3 of IgG secreted by autoreactive plasma cells and plasmablasts, collectively termed ASCs hereafter, without the need to sort, clone, or re-express antibodies, we adapted a single-cell bioassay in microfluidic droplets (termed “DropMap”) that we have described previously (22, 23). In this assay, mononuclear cells from the spleen, bone marrow, or blood of patients

and fluorescent bioassay reagents are coencapsulated in droplets, immobilized within an observation chamber, and imaged over 1 hour by time-lapse fluorescence imaging. Magnetic beads in each droplet form a line (beadline) under a magnetic field to serve as a physical surface for a double-fluorescent sandwich ELISA, revealing IgG secretion from the cell and specificity of that IgG for  $\alpha$ IIB $\beta$ 3 (Figure 1A). The time-resolved fluorescence signals allow for estimation of IgG secretion rates and affinity for  $\alpha$ IIB $\beta$ 3 of the secreted IgG by using calibration curves generated with monoclonal anti- $\alpha$ IIB $\beta$ 3 IgG of known affinity ( $K_D$ ). The anti- $\alpha$ IIB $\beta$ 3 reference curve, generated using 9 anti- $\alpha$ IIB $\beta$ 3 IgG mAbs of various affinities, allows for measurements over 2 logs of affinities, i.e.,  $2.5 \times 10^{-10} \leq K_D \leq 5 \times 10^{-8}$  M (Figure 1B). Therefore herein, IgG interacting with  $\alpha$ IIB $\beta$ 3 at a calculated  $K_D$  below  $5 \times 10^{-8}$  M was considered binding, i.e., anti- $\alpha$ IIB $\beta$ 3 IgG antibodies, and the cells secreting such IgG were termed “ $\alpha$ IIB $\beta$ 3-reactive ASCs.”

As an example, samples from the spleen, bone marrow, and blood were obtained at the time of splenectomy from 1 patient (patient “F”; 73-year-old male) who was splenectomized 8 months after the last rituximab infusion due to treatment failure (Figure 1, C–E). All data from these samples were acquired in duplicate on the same day with high reproducibility in total and autoreactive IgG-SC detection per replicate (Supplemental Figure 1; supplemental material available online with this article; <https://doi.org/10.1172/JCI153580DS1>). For each organ we analyzed 5,000–9,000 single cells in total, and found IgG-SCs represented 0.55%, 0.41%, and 1.26% of the mononuclear cell pool in the spleen, bone marrow, and blood, respectively. IgG-SCs from the 3 organs displayed a similar range (5–500 molecules per second [IgG/s]) and median values (approximately 50 IgG/s) of IgG secretion (Figure 1C). Within the IgG-SC pool of all 3 organs, a fraction secreted anti- $\alpha$ IIB $\beta$ 3 IgG antibodies with  $K_D$  values in the  $5 \times 10^{-8}$  M to  $1 \times 10^{-10}$  M range that we categorized into low-affinity ( $50 \text{ nM} \leq K_D \leq 10 \text{ nM}$ ), medium-affinity ( $10 \text{ nM} < K_D \leq 1 \text{ nM}$ ), and high-affinity ( $K_D < 1 \text{ nM}$ )  $\alpha$ IIB $\beta$ 3-reactive IgG-SCs to facilitate subsequent analyses (Figure 1D). In this patient, the spleen contained IgG-SCs with significantly higher affinities for  $\alpha$ IIB $\beta$ 3 as compared with the blood, and the proportion of  $\alpha$ IIB $\beta$ 3-reactive cells among IgG-secreting cells was 25% in the spleen, 20% in the bone marrow, and 12% in the blood, with high-affinity antibodies detected only in the spleen (Figure 1E).

*High interindividual variability of autoreactive ASC presence and affinity in spleen, bone marrow, and blood of patients with ITP.* Our cohort included 25 patients diagnosed with chronic or acute ITP, with a median age of 51 years (ranging 21–79 years), to investigate the anatomical distribution, affinity, and secretion rate of anti- $\alpha$ IIB $\beta$ 3 IgG-SCs. Clinical characteristics are presented in Table 1. Eight patients (8 of 18) achieved complete response after splenectomy, with a follow-up of 14 to 24 months, while 10 patients (10 of 18) had no significant increase in platelet counts after splenectomy. A bone marrow aspirate was also performed in 7 of 18 patients in addition to the programmed splenectomy. We also analyzed bone marrow and blood from 9 patients with ITP that were not splenectomized (Table 1), and 21 healthy donors (no immune disease) as controls for spleen, bone marrow, or blood samples. For every sample, we analyzed an average of 50,000 to 100,000 droplets in total, representing an average of 10,000 to 27,000 single mononuclear cells containing

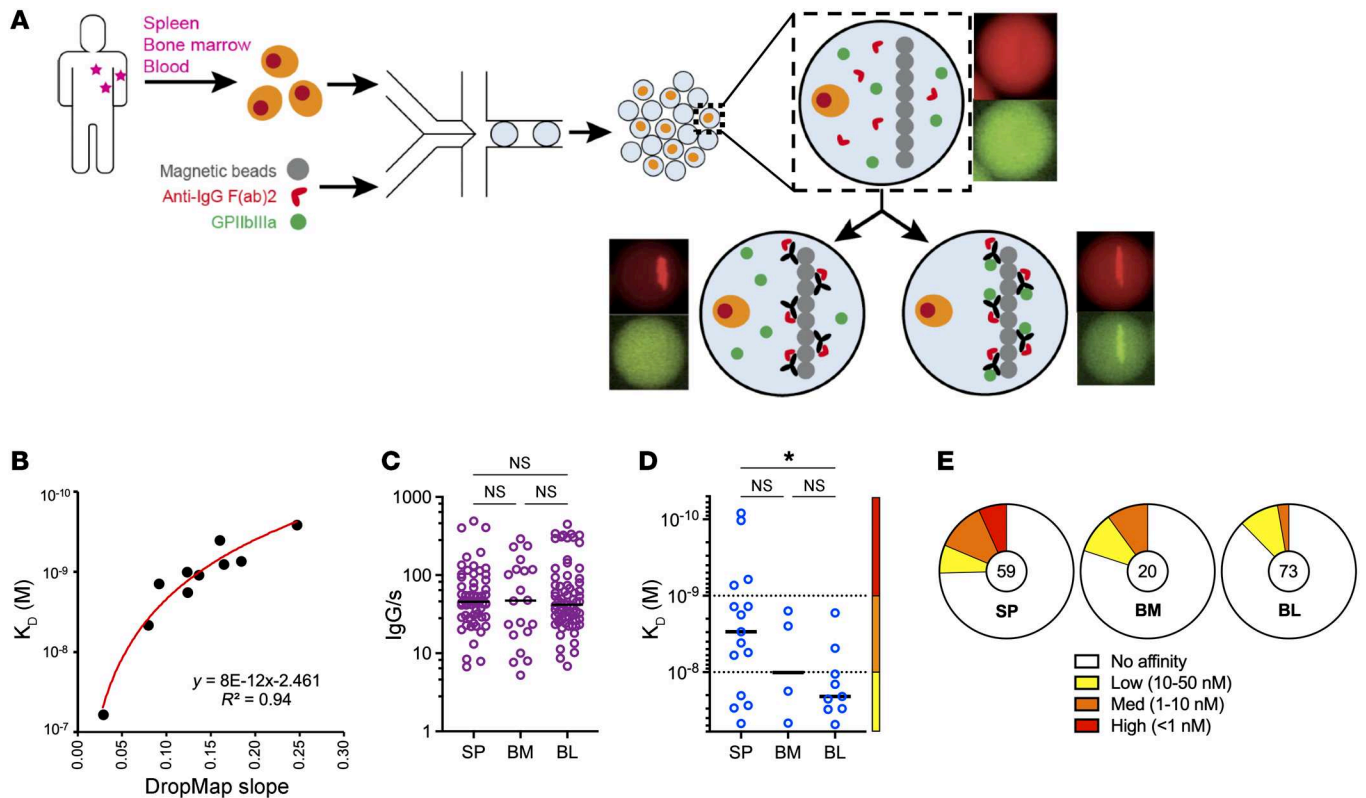


**Figure 1. Single-cell analyses reveal  $\alpha$ IIb $\beta$ 3 affinity and secretion rate from IgG-SCs. (A)** Schematic of the DropMap pipeline. Single mononuclear cells are encapsulated in droplets, together with magnetic beads coated with anti- $\kappa$  light chain nanobody (VHH) and fluorescently labeled anti-IgG F(ab)<sub>2</sub>-Alexa Fluor 647 (red) and  $\alpha$ IIb $\beta$ 3-Alexa Fluor 488 (green). Droplets are immobilized in the chip, exposed to a magnetic field to induce beads to form a beadline, and imaged over time. **(B)**  $\alpha$ IIb $\beta$ 3 affinity reference curve generated using anti- $\alpha$ IIb $\beta$ 3 mAbs with known  $K_D$  and values obtained from DropMap experiments using these mAbs. **(C-E)** DropMap analysis of spleen (SP), bone marrow (BM), and blood (BL) samples from patient F at the time of splenectomy. **(C)** IgG secretion rate. **(D)** Affinity for  $\alpha$ IIb $\beta$ 3 ( $K_D$ ) classified into high (red), medium (orange), and low (yellow) affinity, with dotted lines separating these categories. **(E)** Distribution of IgG-SCs into low (yellow), medium (orange), and high (red) affinity binders to  $\alpha$ IIb $\beta$ 3 or nonbinders (white), with total IgG-SC numbers indicated. **(C and D)** Single-cell values and medians are plotted. \* $P < 0.05$  using Welch's  $t$  test and multiple-testing  $P$ -value adjustment. NS, not significant. See Supplemental Table 2 for further details.

0.01%–5% IgG-SCs (Supplemental Figure 2). Compared with the detection of anti- $\alpha$ IIb $\beta$ 3 IgG-SCs by ELISpot, DropMap was far more sensitive (Supplemental Figure 3A).

We first analyzed the global IgG-SC response per organ for all patients and healthy donors and found that among mononuclear cells, 0.01% to 5% had detectable levels of IgG secretion, with a wide range of IgG secretion rates (1–713 IgG/s) (Figure 2A and Supplemental Figure 2C). In healthy donors, IgG secretion rates were not significantly different between the spleen, blood, and bone marrow. However, in patients with ITP the IgG secretion rates in the bone marrow were significantly higher than in spleen and blood. Unexpectedly, splenic IgG-SCs showed significantly (2.5-fold) lower secretion rates in patients with ITP compared with healthy donors, with median values of 46 IgG/s and 116 IgG/s, respectively. Similar findings were observed for IgG-SCs from peripheral blood, with a 2-fold lower secretion rate in patients with ITP (median 37 IgG/s) compared with healthy donors (74 IgG/s). However, IgG-SCs in the bone marrow had similar secretion rates between patients with ITP and healthy donors (median 60 and 59 IgG/s, respectively) (Figure 2A). In all 3 compartments, the top approximately 20% highest IgG producers were responsible for approximately 50% of the total amount of secreted IgG (Supplemental Figure 3, B and C).

Similar to the first patient we analyzed as a proof of concept (Figure 1, C–E), we identified IgG-SCs with affinity in the  $5 \times 10^{-8}$  M to  $5 \times 10^{-11}$  M range for  $\alpha$ IIb $\beta$ 3 in pooled data from all 3 anatomical sites of patients with ITP, but also in significantly fewer numbers in pooled data from healthy donors in the  $5 \times 10^{-8}$  M to  $5 \times 10^{-9}$  M range (Figure 2B). Only patients with ITP had IgG-SCs with very high estimated affinity ( $K_D$  below  $10^{-10}$  M), mathematically extrapolated from values outside the boundaries of the reference curve presented in Figure 1B. A weak (low  $R$  value) but significant positive correlation was found between  $K_D$  and secretion rate using the pooled data, suggesting that high-affinity autoreactive ASCs tend to secrete less than low-affinity autoreactive ASCs (Supplemental Figure 3, D–F). No correlation, however, was found between time elapsed since the end of rituximab treatment and either secretion rate or affinity in any compartment analyzed (Supplemental Figure 4). Only a fraction (8%–13%) of IgG-SCs showed cross-binding to  $\alpha$ IIb $\beta$ 3 and antigens used for polyreactivity testing (keyhole limpet hemocyanin [KLH] and insulin; ref. 24) with poor affinity (10–50 nM), as expected from IgG-secreting plasma cells (25), and increased affinity for  $\alpha$ IIb $\beta$ 3 did not increase affinity for these other antigens (Supplemental Figure 5). These results demonstrate that approximately 90% of the IgG-SCs with reactivity for  $\alpha$ IIb $\beta$ 3 analyzed herein are not polyreactive. The

**Table 1. Characteristics of patients with ITP**

Patient ID	Sex	Age	ITP duration (months)	Clinical pattern	RTX (months from last infusion)	RTX efficacy	Current therapy	Past treatment history	Splenectomy outcome
G	F	22	240	Chronic	41	CR <sup>a</sup>	TPO-RA, CS, IVIG	CS, IVIG, RTX, TPO-RA	CR
J	M	24	45	Chronic	1 <sup>b</sup>	Failure <sup>b</sup>	Vinblastine, tacrolimus	CS, IVIG, OFA, TPO-RA, MMF, tacrolimus	CR
K	F	50	37	Chronic	–	–	TPO-RA	CS, IVIG, TPO-RA	CR
O	M	36	43	Chronic	32	Failure	CS, IVIG	CS, IVIG, RTX, TPO-RA, dapsone, danatrol	CR
Q	M	37	6	Persistent	2	Failure	TPO-RA, CS, IVIG, AZA	CS, IVIG, RTX, TPO-RA, AZA	CR
AI	F	79	396	Chronic	2	Failure	CS, IVIG, TPO-RA	CS, IVIG, TPO-RA	CR
AM	M	75	192	Chronic	108	Failure	CS (3 days) <sup>c</sup> and TPO-RA	CS, IVIG, TPO-RA	CR
AG	F	55	>24	Chronic	12	Response, relapse	– <sup>d</sup>	CS, IVIG, TPO-RA	CR
B	F	60	36	Chronic	8	Failure	TPO-RA, CS, IVIG	CS, IVIG, RTX, TPO-RA, dapsone	Failure
F	M	73	12	Chronic	8	Failure	TPO-RA, MMF, IVIG	CS, IVIG, RTX, TPO-RA, AZA	Failure
H	F	21	30	Chronic	7	Failure	TPO-RA, IVIG	CS, IVIG, RTX, TPO-RA	Failure
I	M	22	36	Chronic	–	–	–	CS, TPO-RA	Failure
M	M	70	17	Chronic	4	Failure	CS	CS, IVIG, RTX, TPO-RA	Failure
N	M	33	192	Chronic	12	Partial response	CS, IVIG, vincristine	CS, IVIG, TPO-RA, RTX, vincristine, dapsone, MMF	Failure
R	M	31	7	Persistent	5	Failure	IVIG, MMF, TPO-RA	CS, IVIG, RTX, TPO-RA, MMF	Failure
S	M	26	7	Persistent	4	Failure	CS, IVIG	CS, IVIG, RTX, TPO-RA, MMF	Failure
T (D3)	F	20	174	Chronic	10	Failure	Daratumumab	CS, IVIG, RTX, TPO-RA, MMF, dapsone, splenectomy	Failure
D1	M	34	95	Chronic	3	Failure	Daratumumab	CS, IVIG, RTX, TPO-RA, MMF, CSA, HCQ, splenectomy	Failure
AC	F	68	24	Chronic	–	–	TPO-RA	CS, TPO-RA	–
AD	M	65	0	Acute	–	–	No	–	–
AE	F	30	156	Chronic	1	Failure	RTX (1 month)	CS, IVIG, vincristine, RTX, TPO-RA, chemotherapy and autologous stem cell transplantation 14 years before current sample (Hodgkin disease)	–
AF	F	77	0	Acute	–	–	No	–	–
AH	F	72	0	Acute	–	–	CS (1 day)	CS (1 day) <sup>c</sup>	–
AJ	F	77	12	Chronic	9	Failure	MMF	CS, IVIG, TPO-RA, RTX, CSA, MMF	–
AK	F	66	1	Acute	–	–	CS (3 days)	CS (3 days) <sup>c</sup>	–
AL	M	51	>24	Chronic	12	Response, relapse	TPO-RA	CS, IVIG, TPO-RA	–
D2	F	35	128	Chronic	98	Failure	Daratumumab	CS, IVIG, RTX, TPO-RA, MMF, CSA, AZA, EDX	–
R-406	F	77	7	Persistent	–	CR	CS	CS, TPO-RA, dapsone	–
R-429	M	74	3	Persistent	–	CR	CS, IVIG	CS, IVIG	–
R-367	M	75	4	Persistent	–	CR	CS, IVIG	CS, IVIG	–
R-387	F	78	2	Newly diagnosed	–	CR	TPO-RA, CSA	CS, IVIG, TPO-RA, CSA	–

<sup>a</sup>Duration unknown. <sup>b</sup>Patient J received anti-CD20 mAb ofatumumab instead of rituximab. <sup>c</sup>Duration of some drug treatments for some patients are indicated in parenthesis. <sup>d</sup>Splenectomy performed 1 month after rituximab arrest. RTX, rituximab; OFA, ofatumumab; CR, complete response; –, none or not administered; TPO-RA, thrombopoietin receptor agonist; CS, corticosteroids; IVIG, intravenous immunoglobulins; AZA, azathioprine; MMF, mycophenolate mofetil; HCQ = Hydroxychloroquine; CSA = Cyclosporine; EDX = Endoxan (Cyclophosphamide).

overall median affinity of anti- $\alpha$ IIB $\beta$ 3 IgG-SCs from pooled patients with ITP was identical (~8 nM) between the 3 anatomical compartments (Figure 2B). The same result was found for anti- $\alpha$ IIB $\beta$ 3 IgG-SCs of pooled healthy donors, with a significantly lower median affinity (~23 nM) (Figure 2B). The proportion of autoreactive IgG-SCs among mononuclear cells was 10-fold, 5-fold, and 3-fold higher in patients with ITP than healthy donors in the spleen, bone marrow, and blood, respectively (Figure 2C). Healthy donors harbored 65% to 75% low-affinity and relatively few high-affinity IgG-SCs, whereas patients with ITP harbored 37% to 46% medium affinity and 11%

to 16% high-affinity IgG-SCs in the 3 anatomical compartments analyzed. Compared with healthy donors, patients with ITP secrete IgG at a lower rate but with a higher proportion of medium- and high-affinity anti- $\alpha$ IIB $\beta$ 3 specificities in spleen, bone marrow, and blood. These results suggest a role for high-affinity autoantibodies secreted from different anatomical locations in the pathogenesis of ITP.

With the majority of the patients in our cohort being refractory to various therapies, including B cell depletion and splenectomy, we wondered whether patients achieving complete response to rituximab therapy would demonstrate a reduction/disappearance of

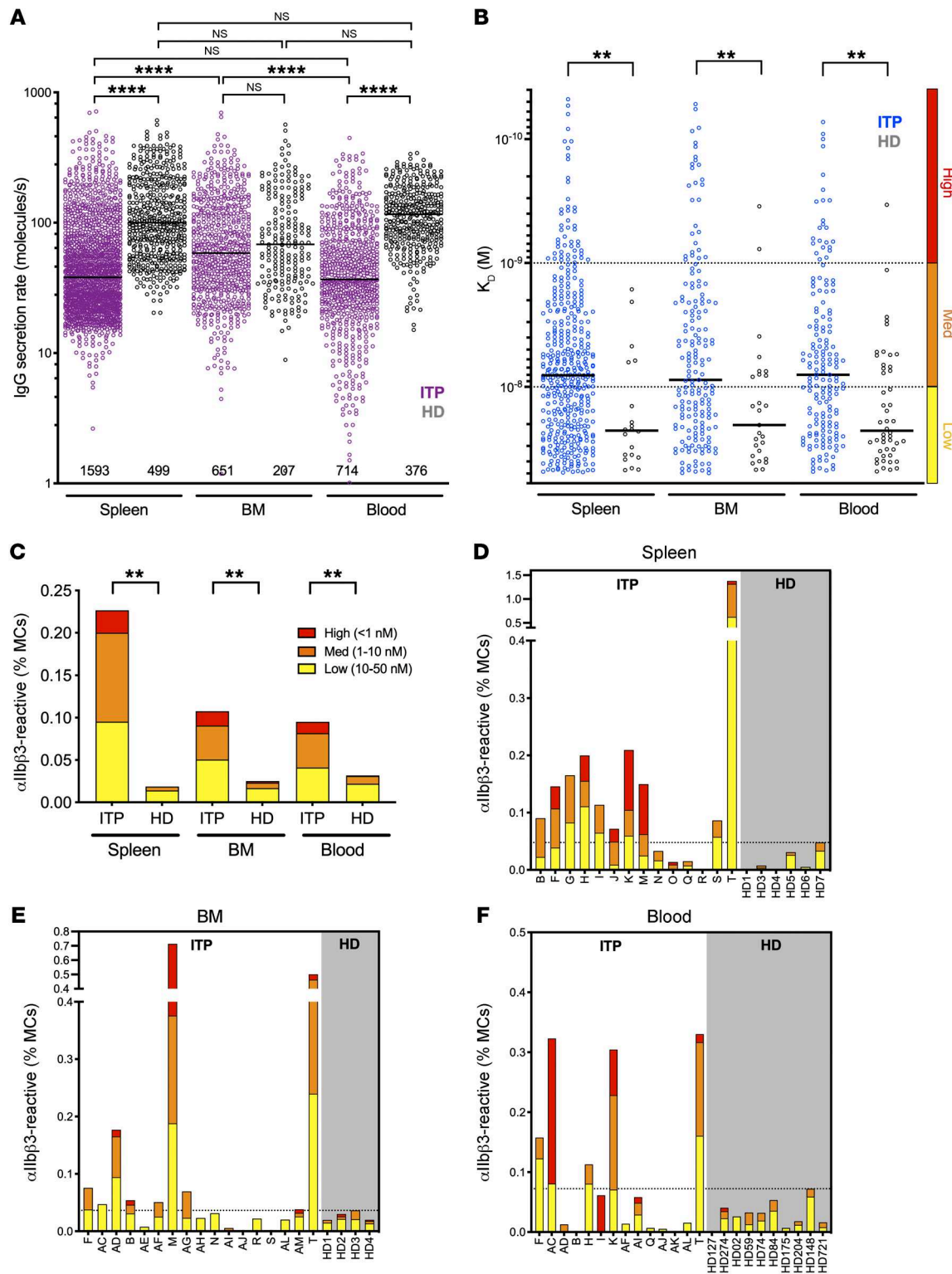


**Figure 2. Autoreactive ASCs with high and low affinity are present in the spleen, blood, and bone marrow (BM) of patients with ITP.** (A) IgG secretion rate and (B) affinity for  $\alpha$ IIb $\beta$ 3 of single ASCs from pooled data of patients with ITP and healthy donors (HD) for spleen (ITP,  $n = 14$ ; HD,  $n = 6$ ), BM (ITP,  $n = 17$ ; HD,  $n = 4$ ), and blood (ITP,  $n = 14$ ; HD,  $n = 10$ ). Single-cell values and medians are plotted. Total numbers of IgG-SCs analyzed per compartment are indicated in A. In B, affinities are classified into high (red), medium (orange), and low (yellow) affinity, with dotted lines separating these categories. (C) Frequency of  $\alpha$ IIb $\beta$ 3-reactive IgG-SCs among mononuclear cells (MCs) classified into high, medium, and low affinity from patients (ITP) and HD according to B. (D–F) Frequency of  $\alpha$ IIb $\beta$ 3-reactive IgG-SCs among MCs classified into high, medium, and low affinity represented for individual patients (ITP) and HD for (D) spleen, (E) BM, and (F) blood. (D–F) The dotted line marks the highest frequency found in an HD. \*\* $P < 0.01$ ; \*\*\*\* $P < 0.0001$  using post hoc contrast analysis after linear (A and B) or logistic (C) modeling and multiple-testing  $P$ -value adjustment. NS, not significant. See Supplemental Table 2 for further details.

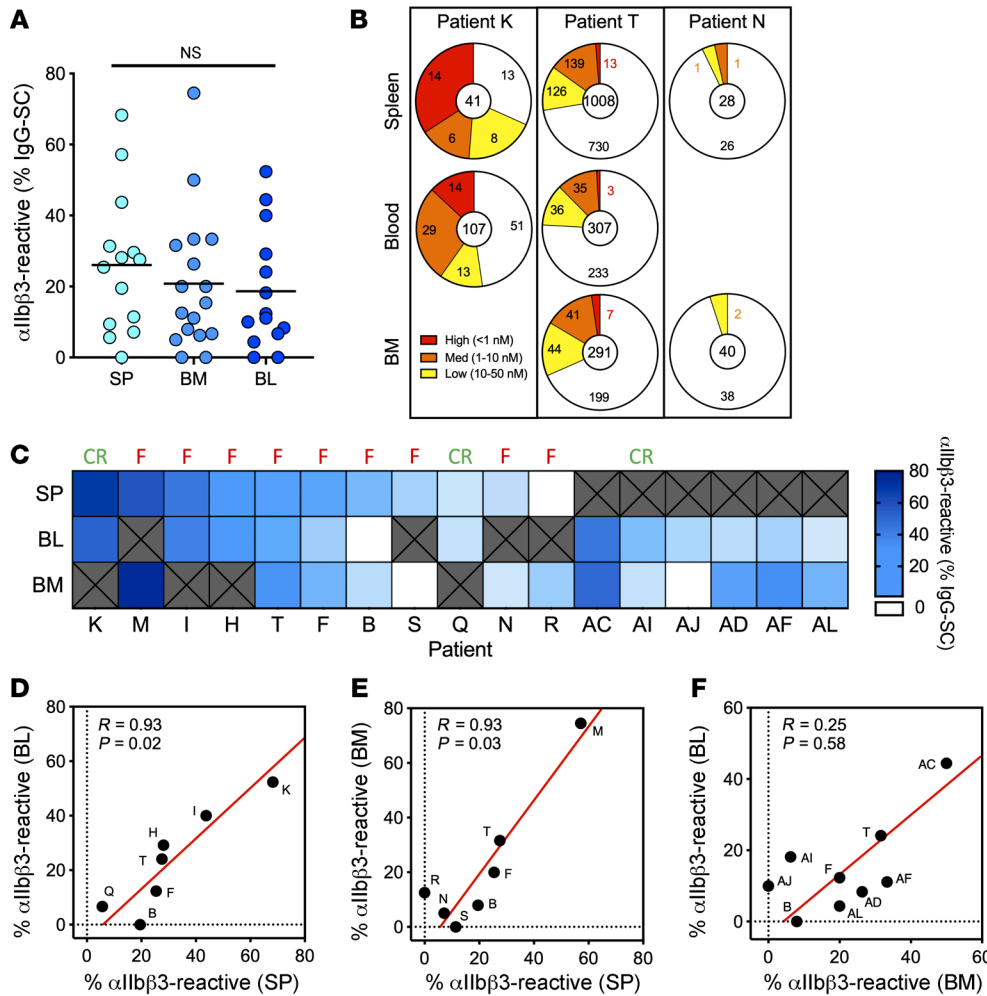


**Figure 3. Paired organs demonstrate a comparable autoantibody response.** (A) Frequency of  $\alpha$ IIb $\beta$ 3-reactive IgG-SCs among total IgG-SCs in the spleen (SP), bone marrow (BM), and blood (BL) from individual patients with ITP. Each dot represents an individual. Values are pooled data from 2 replicates. NS, not significant using Welch's *t* test and multiple-testing *P*-value adjustment. See Supplemental Table 2 for further details. (B) Distribution of IgG-SCs into low (yellow), medium (orange), and high (red) affinity binders to  $\alpha$ IIb $\beta$ 3 or nonbinders (white), with total IgG-SC numbers indicated, for paired samples of patients K, T, and N. (C) Heatmap of the frequency of  $\alpha$ IIb $\beta$ 3-reactive cells among IgG-SCs per patient, ordered from most frequent to less frequent in spleen for patients with a spleen sample, and ordered from most frequent to less frequent in blood for patients without a spleen sample. White boxes indicate undetectable reactivity for  $\alpha$ IIb $\beta$ 3, and "X" indicate absence of samples. Result of splenectomy is indicated: complete remission (CR) or failure (F). (D-F) Pearson's correlation analysis of data from C; scatterplots compare the frequency of  $\alpha$ IIb $\beta$ 3-reactive cells among paired organs. *R* and adjusted *P* values are indicated. Red line indicates the reduced major axis.

the high-affinity anti- $\alpha$ IIb $\beta$ 3 IgG-SC population after treatment. We retrospectively analyzed frozen PBMC samples of 4 responder ITP patients collected 1 week before the first and 3 months after the last rituximab infusion. Seventy-five percent (3 of 4) patients displayed 3 times or greater less total IgG-SCs after rituximab treatment, with nevertheless a nonsignificant trend for the group (Supplemental Figure 6A). IgG secretion rates were, however, significantly higher after treatment (Supplemental Figure 6B), reminiscent of the higher secretion rate of blood IgG-SCs in healthy donors compared with patients with ITP (Figure 2A). All 4 responder patients had very low initial frequencies of  $\alpha$ IIb $\beta$ 3-specific IgG-SCs in circulation (mean 0.016% among PBMCs), with approximately 10-fold reduction in 2 patients and no major variation in the 2 other patients (Supplemental Figure 6C). Nevertheless, high-affinity autoreactive IgG-SCs disappeared after treatment in these patients in remission (Supplemental Figure 6D), supporting our hypothesis on the role for high-affinity ASCs in the pathogenesis of ITP. We then grouped the patients from our main cohort by rituximab responsiveness and compared them in terms of  $\alpha$ IIb $\beta$ 3 reactivity. Even though the number of responding patients in our cohort was very limited, we observed a tendency toward lower affinity for  $\alpha$ IIb $\beta$ 3 in rituximab-responding patients as compared with rituximab-failure patients (Supplemental Figure 6E), whereas no difference was observed in the frequency of autoreactive ASCs (Supplemental Figure 6F).

We found varying proportions of autoreactive IgG-SCs among mononuclear cells between patients with ITP, and within anatomical compartments of a given patient (Figure 2, D-F). This finding may rely on the heterogeneity of therapeutic regimens and intrinsic cell heterogeneity of each anatomical compartment. Nevertheless, 71% (10 of 14) of spleen samples, but only 41% (7 of 17) of bone marrow and 36% (5 of 14) of blood samples harbored more autoreactive IgG-SCs in patients with ITP compared with the highest value found in healthy control samples. Fifty percent (7 of 14) of the patients with ITP harbored high-affinity anti- $\alpha$ IIb $\beta$ 3 IgG-SCs in the spleen, compared with 29% (5 of 17) and 36% (5 of 14) in the bone marrow and blood, respectively. No such cell could be detected in spleens from healthy donors, and only once in blood and twice in bone marrow at very low numbers. Thus, most patients with ITP displayed a robust anti- $\alpha$ IIb $\beta$ 3 response in the spleen that underlies the central role of this organ in ITP.

*Comparable autoantibody responses in paired organs.* In order to compare the autoantibody response in different immune sites from the same patient with ITP, we obtained paired samples, either taken at the time of splenectomy (spleen + bone marrow and/or blood) or at the time of bone marrow collection (bone marrow + blood). On average, 20% to 25% of IgG-SCs were  $\alpha$ IIb $\beta$ 3 specific in the 3 compartments, with some patients presenting with a robust autoreactive response of up to 75% of auto-

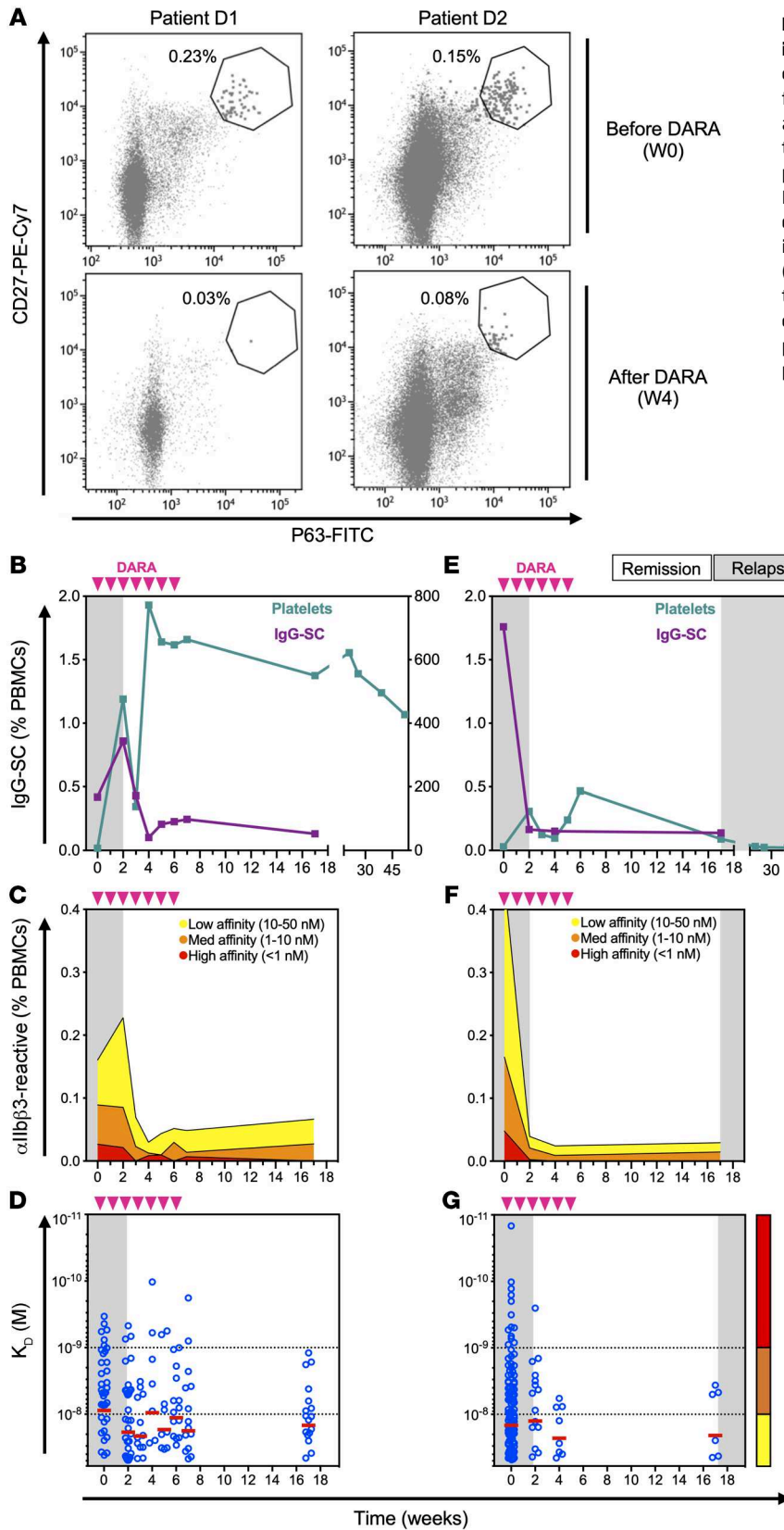


**Figure 4. Anti-CD38 therapy depletes pathogenic ASCs in patients with ITP.** (A) Flow cytometric identification of circulating CD27<sup>+</sup>P63<sup>+</sup> plasmablasts/plasma cells from patients D1 and D2 before (top panel) and 4 weeks after (bottom panel) the start of daratumumab (DARA) treatment. (B–G) Kinetic follow-up of patient D1 (B–D) and patient D2 (E–G) blood samples for (B and E) frequency of IgG-SCs among PBMCs and platelet levels. (C and F) Frequency of  $\alpha$ IIB $\beta$ 3-reactive IgG-SCs among PBMCs classified into high (red), medium (orange), and low (yellow) affinity. (D and G) Affinity for  $\alpha$ IIB $\beta$ 3 of single IgG-SCs. Displayed on the background is time spent in clinical remission (white) or relapse (gray). Daratumumab infusions are indicated by pink arrows. Single-cell affinity values and medians are plotted in D and G.

a robust anti- $\alpha$ IIB $\beta$ 3 response, with greater than 50% autoreactive IgG-SCs distributed among high-, medium-, and low-affinity IgG-SCs in both spleen and blood; patient T displayed large numbers of IgG-SCs, with approximately 25% autoreactive IgG-SCs largely predominated by low- and medium-affinity IgG-SCs in all 3 compartments; and patient N displayed low numbers of IgG-SCs, with approximately 5% autoreactive IgG-SCs (Figure 3B). Generally, in the cohort of paired samples, patients harboring a large proportion of  $\alpha$ IIB $\beta$ 3-reactive IgG-SCs among all IgG-SCs in one compartment also did so in the other one or two compartments (Figure 3C). For the 7 patients for whom splenectomy failed to induce clinical remission and a bone marrow sample was available (patients M, T, F, B, S, N, and R), anti- $\alpha$ IIB $\beta$ 3 IgG-SCs were present in the bone marrow the day of splenectomy, except for patient S. This suggests that the autoreactive bone marrow ASC population is responsible for the sustained disease observed after splenectomy in these patients.

Proportions of  $\alpha$ IIB $\beta$ 3-reactive IgG-SCs correlated well between spleen and blood ( $R > 0.9$ ;  $P = 0.02$ ) and spleen and bone marrow ( $R > 0.9$ ;  $P = 0.03$ ), but did not correlate between bone marrow and blood ( $R = 0.25$ ;  $P = 0.58$ ) (Figure 3, D–F). Despite the heterogeneity of clinical

reactive IgG-SCs among all IgG-SCs (Figure 3A). Distribution of affinities for IIB $\beta$ 3 was similar within compartments of individual patients, as exemplified in Figure 3B (refer to Supplemental Figure 7 for all paired samples). For example, patient K displayed

situations and treatment history among patients in this cohort, the spleen appears to determine the extent of the autoreactive response, likely by providing the other compartments with autoreactive IgG-SCs. Our results suggest that the autoreactive-IgG

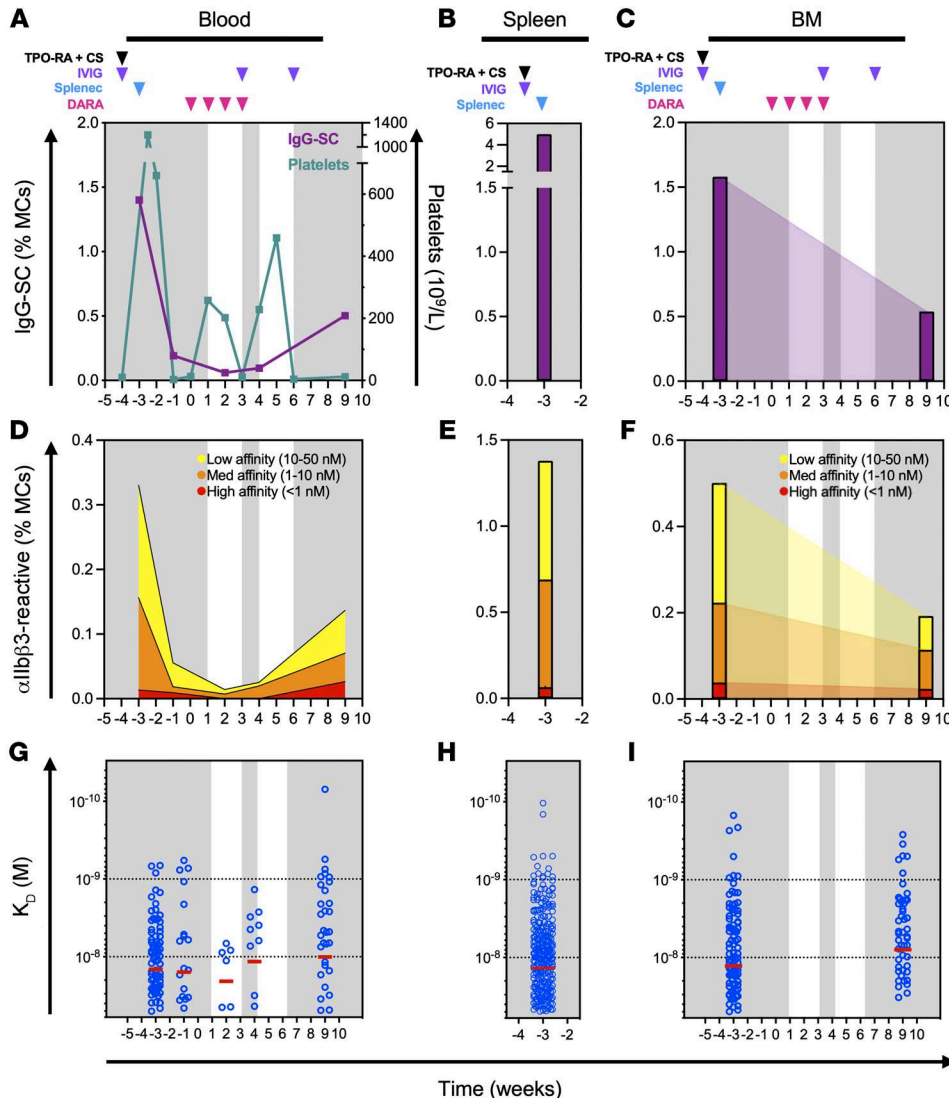


**Figure 5. Failure of anti-CD38 treatment is associated with persistence of pathogenic ASCs.** Kinetic follow-up of patient T. Displayed on the background is time spent in clinical remission (white) or relapse (gray). Drug infusions are indicated by arrows: thrombopoietin receptor agonist and cyclosporin (TPO-RA + CS; black), intravenous immunoglobulin (IVIG; purple), and daratumumab (DARA; pink). The time of splenectomy is indicated by a blue arrow. (A–C) Frequency over time of IgG-SCs among mononuclear cells (MCs) in (A) blood with platelet levels indicated, (B) spleen, and (C) bone marrow (BM). (D–F) Frequency over time of  $\alpha$ IIb $\beta$ 3-reactive IgG-SCs among MCs in (D) blood, (E) spleen, and (F) BM classified into high, medium, and low affinity. (G–I) Affinity over time for  $\alpha$ IIb $\beta$ 3 of single IgG-SCs in (G) blood, (H) spleen, and (I) BM. Single-cell affinity values (blue dots) and medians (red lines) are plotted.

response in patients with ITP disseminates through multiple organs, resulting in IgG-SC populations with similar ranges of anti- $\alpha$ IIb $\beta$ 3 affinity and proportion among IgG-SCs.

**Kinetic follow-up of anti-CD38 therapy with daratumumab in patients with ITP.** The autoreactive IgG-SCs in patients with chronic ITP that are refractory to conventional therapies (rituximab and/or splenectomy) can be theoretically eliminated using the anti-CD38 mAb daratumumab that was developed to target malignant plasma cells (26). We therefore analyzed 3 patients who received off-label (compassionate use) daratumumab for severe chronic refractory ITP. After 3 infusions, daratumumab led to an 89% reduction in circulating CD27<sup>+</sup>P63<sup>+</sup> plasmablasts and plasma cells (27), identified by flow cytometry (Figure 4A and Supplemental Figure 8).

Patient D1 (34-year-old male) had been splenectomized 9 years prior to daratumumab therapy, but continued to experience skin and/or mucosal bleedings because of low platelet counts (<30 × 10<sup>9</sup>/L) despite receiving several immunosuppressant drugs (including rituximab, mycophenolate mofetil, and cyclosporin) and thrombopoietin receptor agonist (TPO-RA).

He received 7 daratumumab infusions at 16 mg/kg per week without other treatment except oral dexamethasone (20 mg) before each infusion and achieved a complete response lasting now over 1 year (defined by platelet count >100 × 10<sup>9</sup>/L) (Figure 4B). After a short increase in total IgG-SC (Figure 4B) and anti- $\alpha$ IIb $\beta$ 3 IgG-SC (Figure 4C) numbers in blood, these proportions dropped 2- to 3-fold and remained low for at least 10 weeks after the last daratumumab infusion. Remarkably, whereas low-affinity IgG-SCs remained at a third of their initial level, high-affinity IgG-SCs became undetectable a few weeks after the end of the treatment (Figure 4, C and D).

Patient D2 (35-year-old female) had not been splenectomized and received her last rituximab infusion 8 years before receiving weekly daratumumab (without other treatment except 20 mg dexamethasone orally before each infusion) for 6 weeks. This resulted in a transient complete response lasting 17 weeks before relapse. Total IgG-SC (Figure 4E) and anti- $\alpha$ IIb $\beta$ 3 IgG-SC numbers in blood nevertheless dropped approximately 10-fold following daratumumab infusions, again with the disappearance of high-affinity IgG-SCs (Figure 4, F–G). Overall, both patients

responded similarly to daratumumab therapy in terms of depletion of IgG-SCs, both total and  $\alpha$ Ib $\beta$ 3 specific, and elimination of high-affinity anti- $\alpha$ Ib $\beta$ 3 IgG-SCs from circulation.

These results emphasize that daratumumab therapy targets ASCs in patients with ITP and suggest that the depletion of these cells, which include the autoreactive population, could be related to clinical improvement.

*Spleen-independent reappearance of high-affinity anti- $\alpha$ Ib $\beta$ 3 ASCs after daratumumab.* Patient T (20-year-old female) had ITP requiring splenectomy 10 months after rituximab, and then daratumumab therapy for refractory disease, allowing a sequential follow-up after these interventions. After splenectomy, IgG-SC and anti- $\alpha$ Ib $\beta$ 3 IgG-SC numbers in blood dropped 7- and 4-fold, respectively (Figure 5, A and D), supporting the spleen as an important source of IgG-SCs in circulation (21, 28). On the day of splenectomy, high numbers of IgG-SCs were found among mononuclear cells in the blood (1.4%), bone marrow (1.6%), and spleen (5%) (Figure 5, A–C), i.e., 7-fold higher than the ITP spleen with the highest numbers we had analyzed before (Supplemental Figure 2). Among IgG-SCs, 27%, 32%, and 24% were  $\alpha$ Ib $\beta$ 3 specific, including high-affinity IgG-SCs, in the spleen, bone marrow, and blood, respectively, demonstrating a relatively homogeneous distribution of autoreactive IgG-SCs across all 3 compartments (Figure 5, D–I). Daratumumab treatment started 3 weeks after splenectomy induced a transient increase in platelet counts (Figure 5A), associated with a decrease in total IgG-SC and anti- $\alpha$ Ib $\beta$ 3 IgG-SC numbers (Figure 5D), and led to a disappearance of high-affinity IgG-SCs (Figure 5G). Daratumumab was discontinued after 4 infusions because of relapse and an increase in total IgG-SCs, anti- $\alpha$ Ib $\beta$ 3 IgG-SCs, and high-affinity IgG-SCs in the blood was observed after 5 weeks (Figure 5, A, D, and G). This reappearance of autoreactive, high-affinity IgG-SCs in circulation occurred after splenectomy, suggesting autoreactive B cell reservoirs were present in other anatomical compartments or re-emergence of autoreactivity from naive B cells in secondary lymphoid organs (e.g., lymph nodes) (18). Remarkably, whereas bone marrow IgG-SCs (Figure 5C) and anti- $\alpha$ Ib $\beta$ 3 IgG-SCs (Figure 5F) were reduced 2.5- to 3-fold compared with their content before splenectomy and daratumumab treatment, high-affinity IgG-SCs could be readily detected in the bone marrow 5 weeks later with a similar distribution (Figure 5I). These bone marrow-resistant autoreactive high-affinity IgG-SCs identified after multiple therapies could correspond to daratumumab-resistant ASCs, and/or to newly immigrating ASCs generated in another compartment that remains to be identified.

## Discussion

This study represents the first characterization to our knowledge of ASCs in humans in terms of their anatomical distribution, antibody secretion, and affinity for their target autoantigen, including both patients with autoimmune disease and healthy donors. It demonstrates the dissemination of autoreactive IgG-SCs among the spleen, blood, and bone marrow from patients with ITP. Rates of IgG secretion per cell were very diverse, with a tendency for secretion to decrease with decreasing affinity values for  $\alpha$ Ib $\beta$ 3, but globally similar between IgG-SCs from the spleen and blood

and dissimilar from IgG-SCs from the bone marrow. Whereas affinities for the platelet autoantigen  $\alpha$ Ib $\beta$ 3 varied over 3 logs, the median affinity and range of affinities were strikingly similar between the 3 compartments, suggesting a common origin. In addition, the proportion of autoreactive IgG-SCs closely correlated between spleen and blood, and spleen and bone marrow, supportive of the spleen being the source of autoreactive IgG-SCs and the dominant tissue in this disease (9). The persistence of autoreactive ASCs in the bone marrow after failure of anti-CD20 B cell depletion, splenectomy, and anti-CD38 therapy represents a new layer of complexity and target for ITP therapy.

Chronic ITP is the most common hematologic indication for splenectomy (29), making this major secondary lymphoid organ accessible for research.  $\alpha$ Ib $\beta$ 3-reactive memory B cells (13, 18) and IgG-SCs (plasma cells) were identified in the spleen of patients with ITP, as well as increased  $\alpha$ Ib $\beta$ 3-reactive effector T cell (9) and reduced Treg (12) numbers compared with healthy controls. The stage of B cell development at which tolerance to platelet antigens breaks down remains to be determined. The identification in small numbers of anti- $\alpha$ Ib $\beta$ 3 IgG-SCs in all healthy donors in this work supports the hypothesis of a low-level autoreactivity against platelets in healthy individuals. This is in agreement with the low frequency (~13%) of self-reactive IgG-secreting plasma cells found in healthy donors after sorting of CD138<sup>+</sup>CD27<sup>+</sup>CD38<sup>+</sup> cells and in vitro expression of their IgG (25). As the abundance of anti- $\alpha$ Ib $\beta$ 3 IgG-SCs is low, with poor affinity and IgG secretion rates, the amount and overall affinity of circulating platelet autoantibodies may be insufficient in these healthy donors to have a meaningful impact on platelet numbers, but may represent a biomarker for future evolution into ITP.

In ITP, breakdown of tolerance to platelets leads to the generation of anti- $\alpha$ Ib $\beta$ 3 ASC clones that are a hallmark of germinal center autoreactive B cell generation (11, 13, 18). We provided here a comprehensive view of affinity-matured autoreactive ASCs in different compartments that possess a broad range of affinities, including high-affinity binders. Autoantibodies with affinities for cytokines as high as  $3 \times 10^{-14}$  M have been reported to develop in patients with autoimmune polyendocrine syndrome type 1 (APS-1, also known as autoimmune polyendocrinopathy–candidiasis–ectodermal dystrophy [APECED]) (30). Whether antibody affinities for the extremely abundant antigen  $\alpha$ Ib $\beta$ 3 could reach such values remains speculative and may certainly require an extreme defect in tolerance. Remarkably, anti- $\alpha$ Ib $\beta$ 3 subnanomolar affinities could be identified from IgG-SCs in spleen, blood, and bone marrow in similar distributions in some individuals. The magnitude of the response in the spleen correlated with that of the blood and bone marrow, with a strong decrease in circulating IgG-SCs after splenectomy, highlighting the role of this organ in the generation of IgG-SCs that are released to the bloodstream. Supportive of this notion, a correlation in the number of  $\alpha$ Ib $\beta$ 3-reactive IgG-SCs between spleen and blood from patients with ITP that responded to splenectomy was reported previously using ELISpot (9).

Only 1 case report previously identified anti- $\alpha$ Ib $\beta$ 3 in the bone marrow of 1 ITP patient using ELISpot (31). Our study identified anti- $\alpha$ Ib $\beta$ 3 IgG-SCs in the bone marrow in 40% of patients with ITP in similar or higher proportions among mononuclear cells than in the spleen. In a direct comparison, the sensitivity of

DropMap was overall higher than ELISpot. In this study, we found the frequency of autoreactive IgG-SCs among mononuclear cells to be around 0.1%, which is 10 times higher than what was previously described using ELISpot (9). This may be due to the inherent higher sensitivity of fluorescent bioassays compared with chromogenic assays, or to the necessity of IgG-SCs to secrete over longer periods of time for ELISpot (hours) than for DropMap (45 minutes). The bone marrow is thought to be the main niche for survival of long-lived ASCs, so the presence of autoreactive IgG-SCs in this compartment could be correlated to long-term autoantibody production and, in turn, with the maintenance of chronic disease (reviewed in ref. 32). Our results constitute one of the first direct findings to our knowledge of autoreactive plasma cell populations in human autoimmunity (33), supported also by similar findings in mouse autoimmunity models of vasculitis (34), lupus (35–38), and encephalomyelitis (39). The establishment of long-lived ASCs in the bone marrow could also have important implications for treatment of ITP and other B cell-dependent autoimmune disorders: first, this population could sustain autoantibody levels following splenectomy, which may be sufficient to affect clinical manifestations; and second, long-lived ASCs in the bone marrow have been observed to be resistant to immunosuppressive agents (36) and to B cell-targeted therapies, such as anti-CD20 or anti-BAFF antibodies (32, 39), which may partly explain therapeutic failures.

In this context, targeting ASCs with anti-CD38 appeared to be a very promising option. This work reports anti-CD38 daratumumab off-label use in 3 patients with refractory chronic ITP, a treatment that has been proposed for autoimmune cytopenia following bone marrow transplantation (40, 41). Similar to our results, daratumumab therapy gave drastically different clinical outcomes, from complete remission to failure of therapy (41). The bone marrow is probably responsible for immediate failures of splenectomy by harboring sufficient autoreactive ASCs for effective platelet destruction. However, targeting autoreactive ASCs may prove difficult, as bone marrow cells have been reported in mouse models to be rather resistant to therapeutic antibody depletion (42, 43). Similarly, we showed that autoreactive ASCs persisted in the bone marrow of a patient with no response to daratumumab, providing a possible explanation for treatment resistance. Another patient achieved complete remission after daratumumab but relapsed several weeks later, suggesting that a lymphoid organ was perhaps able to generate new autoreactive ASCs. The lymphoid organ responsible may have been lymph nodes in splenectomized patient T (Figure 5) and the spleen (and perhaps also lymph nodes) in patient D2 who received daratumumab but had not been splenectomized (Figure 4, E–G). Understanding the reasons for such variability in clinical responses to B cell depletion therapy will require more investigation, particularly as we describe here in a relatively homogeneous dissemination of IgG-SCs among spleen, blood, and bone marrow of patients with ITP.

Our work also has several limitations, mostly inherent to human studies. Patients had varying clinical histories and received treatments that probably affected the ASC pool. However, long-term corticosteroids and/or immunosuppressant drugs are not commonly given for ITP in France, and we took advantage of the various therapeutic sequences, including splenectomy and daratumumab, to study ASC dissemination in humans. Our

assay focused on IgG and  $\alpha$ IIB $\beta$ 3, as previous studies showed that anti- $\alpha$ IIB $\beta$ 3 IgGs were predominant autoantibodies in ITP (4, 5). We cannot, however, exclude the possibility that some patients had a response of another isotype or directed against other, less common, platelet antigens (e.g., CD42 complex [GPIb/IX/V] and integrin  $\alpha$ 2 $\beta$ 1 [GPIa/IIa]; ref. 44). ASCs are also rare among mononuclear cells, and in some patients described here only few  $\alpha$ IIB $\beta$ 3-reactive cells could be identified that limit broad extrapolations on autoreactive ASCs. Our method of analysis proved nevertheless more sensitive than conventional assays (i.e., ELISpot), which allowed us to investigate secretion rate and affinity for  $\alpha$ IIB $\beta$ 3 for more than 3,300 freshly isolated ex vivo IgG-SCs.

This work extends (45–48) our knowledge of autoreactive IgG-SCs in human ITP. We demonstrate the homogeneous dissemination of platelet autoreactive ASCs into multiple anatomical compartments that could explain splenectomy failure in some patients. A wide range of affinities for the major ITP autoantigen  $\alpha$ IIB $\beta$ 3 were identified, with very high affinities reminiscent of affinities found in other systemic autoimmune diseases. Anti-CD38 daratumumab therapy allowed us to demonstrate the crucial contribution of ASCs in ITP, and to point toward a compartment other than the spleen that may serve in some patients as a source to reconstitute autoreactive ASC pools in circulation and in the bone marrow.

## Methods

### ITP patients and controls

All patients included in this study were adults (>18 years old) and were diagnosed with ITP according to international guidelines (10). Patients with underlying immunodeficiencies, hepatitis C virus or human immunodeficiency virus infection, lymphoproliferative disorders, and defined systemic lupus erythematosus ( $\geq$ 4 American Rheumatism Association criteria) were excluded. Patients had acute (<3 months), persistent (3–12 months), or chronic (>12 months) ITP. According to these guidelines, a bone marrow smear biopsy was performed in patients over 60 years old to exclude myelodysplastic syndromes. Complete response to splenectomy was defined by a platelet count over  $100 \times 10^9/L$  and the absence of bleeding, partial response was defined by a platelet count over  $30 \times 10^9/L$  and below  $100 \times 10^9/L$  and at least doubling values from baseline, and failure by a platelet count under  $30 \times 10^9/L$  or use of salvage therapy after 1 month. Relapsing patients were defined as those that initially had a complete response, but then had a drop in the platelet count, below  $30 \times 10^9/L$ , as well as a medical intervention by the treating physician. Healthy controls were individuals with no autoimmune disease or lymphoma. Control spleen samples were obtained from organ donors that died from stroke or head trauma. Control bone marrow aspirate samples were taken from healthy organ transplantation donors and were obtained from the Pitié-Salpêtrière Hospital (AP-HP). Control blood samples were obtained from the French Blood Establishment (EFS).

### Sample processing

Splenic tissue was obtained from splenectomy and maintained at 4°C for transportation to the laboratory. Splenic tissue fragments were homogenized using a dissociator (gentleMACS, Miltenyi Biotec), and cell suspensions were subsequently filtered and diluted in RPMI-1640 (Invitrogen). Ficoll density gradient (Ficoll Paque Plus, GE Health-

care) centrifugation at 300 *g* for 20 minutes with no brake was used to obtain mononuclear cells. Bone marrow cells were obtained from bone marrow aspiration and immediately placed in sodium heparin tubes (BD) for transportation to the lab at room temperature. Bone marrow cells were then dissociated by flushing thoroughly through a syringe needle and diluted in RPMI-1640, before processing by Ficoll density gradient to obtain mononuclear cells. Blood was obtained in sodium heparin tubes and transported at room temperature. After dilution in RPMI-1640, blood was processed by Ficoll density gradient. After isolation, mononuclear cells from all organs were resuspended in RPMI-1640 supplemented with 10% HyClone FBS (Thermo Fisher Scientific) and 1% penicillin/streptomycin (Thermo Fisher Scientific). From this point on, cell suspensions were maintained on ice. All experiments were performed within 12 hours from sample collection, except for PBMCs from 4 patients with nonrefractory ITP that were analyzed from frozen samples. Although these 4 samples had been frozen for storage, their frequencies of IgG-SCs (mean 0.27% among PBMCs) were comparable to those found on average in fresh PBMCs from the rest of the cohort.

#### Aqueous phase I: preparation of cells for droplet compartmentalization

Cell suspensions were centrifuged (300*g*, 5 minutes) and resuspended twice using MACS buffer consisting of PBS pH 7.2, 0.2% bovine serum albumin, and 2 mM EDTA. After each resuspension, cells were filtered through a 40- $\mu$ m cell strainer to eliminate aggregates. Cells were then spun (300*g*, 5 minutes) and resuspended in DropMap buffer, which consisted of RPMI-1640 (without phenol red) supplemented with 0.1% Pluronic F68, 25 mM HEPES pH 7.4, 5% KnockOut serum replacement (all Thermo Fisher Scientific), and 0.5% human serum albumin (Sigma-Aldrich). Cell number in the suspension was adjusted to achieve a  $\lambda$  (mean number of cells per droplet) of approximately 0.3. For calibration curves, IgG mAbs were diluted in DropMap buffer.

#### Aqueous phase II: preparation of beads and bioassay reagents

Paramagnetic nanoparticles (Bio-Ademabeads Streptavidin plus 300 nm, Ademtech) were washed with Dulbecco's PBS with calcium and magnesium (DPBS++, Thermo Fisher Scientific). The nanoparticles were resuspended in DPBS++ containing 1  $\mu$ M biotin-labeled anti-human  $\kappa$  light chain (Ig $\kappa$ ) (CaptureSelect, Thermo Fisher Scientific), and incubated 20 minutes at room temperature. After another wash with DPBS++, nanoparticles were resuspended in 5% Pluronic F127 (Thermo Fisher Scientific) and incubated 20 minutes at room temperature. The nanoparticles were washed again and resuspended in DropMap buffer containing fluorescent reporter proteins at a final concentration of 1.25 mg/mL beads. Reporter proteins were Alexa Fluor 647-labeled F(ab')<sub>2</sub> fragment of rabbit anti-human IgG Fc-specific (Jackson ImmunoResearch) used at 75 nM final in-droplet concentration and Alexa Fluor 488-labeled (Thermo Fisher Scientific)  $\alpha$ Ib $\beta$ 3 (purified protein, Enzyme Research) used at 30 nM final in-droplet concentration.

#### Droplet production and collection

Droplets were generated using hydrodynamic flow-focusing on a microfluidic chip as described previously (22). The wafer master of an SU-8 photoresist layer (MicroChem) with approximately 40  $\mu$ m thickness was manufactured using soft lithography (49) and microfluidic chips were fabricated using polydimethylsiloxane (Sylgard; ref. 22).

The continuous phase consisted of 2% (wt/wt) 008 Fluorosurfactant (RAN Biotechnologies) in Novec HFE7500 fluorinated oil (3M). Aqueous phases I and II were coflowed and partitioned into droplets. The flow rate of aqueous phases I and II was 70  $\mu$ L/h, whereas that of oil was 600  $\mu$ L/h in order to achieve monodisperse droplets of approximately 40 pL volume. Newly generated droplets were directly injected into the DropMap 2D chamber system (22) and mounted on a fluorescence microscope (Ti Eclipse, Nikon). The emulsion was exposed to a magnetic field, forcing the nanoparticles inside each droplet to form an elongated aggregate termed a "beadline."

#### Data acquisition

Images were acquired using a Nikon inverted microscope with a motorized stage (Ti Eclipse). Excitation light was provided by a light-emitting diode (LED) source (SOLA light source, Lumencor Inc.). Fluorescence for the specific channels was recorded using appropriate bandpass filters and camera settings (Orca Flash 4.0, Hamamatsu) at room temperature and ambient oxygen concentration. Images were acquired using a 10 $\times$  objective (NA 0.45). An array of 10  $\times$  10 images was acquired for each replicate, every 7.5 minutes in all channels over 37.5 minutes (6 measurements total). Duplicates or triplicates were systematically acquired for every sample, with each replicate being the filling of the DropMap 2D chamber with a different droplet population acquired over time on a 10  $\times$  10 image array.

#### Image analysis and calculations

Images were analyzed using a custom-made MatLab script (MathWorks) that identifies each droplet and the beadline within each droplet. Fluorescence values associated with the beadline were extracted as well as the mean fluorescence of the entire droplet except the beadline (background fluorescence). A value of fluorescence relocation for each droplet at each time point was calculated, i.e., fluorescence value of the beadline divided by the fluorescence value of the background. Data were exported to Excel (Microsoft) and sorted for droplets showing an increase in relocation of the anti-IgG reporter fluorescence (Alexa Fluor 647) over time and above a threshold of Alexa Fluor 647 relocation greater than 1.5. The sorted droplets were visually controlled for the presence of a single cell within the droplet, for droplet movement between image acquisitions, absence of fluorescent particles other than the beadline (e.g., Alexa Fluor 647-anti-IgG or Alexa Fluor 488- $\alpha$ Ib $\beta$ 3 protein aggregates, cell debris) and undesired aggregation of fluorescent reporters on the cell surface inside the droplet. IgG secretion rate and dissociation constant ( $K_D$ ) were estimated as described previously (22).

*Estimation of IgG concentration within each droplet.* A calibration curve for the estimation of IgG concentration was obtained by preparing droplet populations containing all bioassay reagents except cells that were replaced by a range of concentrations of monoclonal IgG1 (one concentration per droplet population). Images were acquired exactly 3 minutes after the droplets were immobilized in the DropMap chamber for each IgG concentration, and fluorescence relocation calculated. The calibration curve was subsequently used to estimate the IgG concentration and secretion rate (IgG/s) for each time interval, and the mean secretion rate was calculated by averaging the values of all intervals.

*Estimation of  $K_D$  for  $\alpha$ Ib $\beta$ 3 within each droplet.* A calibration curve was obtained by defining relocation values for both anti-IgG (Alexa Fluor 647) and  $\alpha$ Ib $\beta$ 3 (Alexa Fluor 488) for a collection of 10 anti-

$\alpha$ Ib $\beta$ 3 mAbs (listed in Supplemental Table 3) with a range of  $K_D$  over 1 log as defined using bio-layer interferometry (ForteBio). Droplet populations were generated for different concentrations of each mAb to be analyzed by the DropMap bioassay. A curve was defined by plotting the relocation from the anti-IgG (Alexa Fluor 647) against relocation of  $\alpha$ Ib $\beta$ 3 (Alexa Fluor 488), and the slope of the resulting line was calculated and termed the “DropMap slope.” The calibration curve was defined by the linear relationship between  $K_D$  for  $\alpha$ Ib $\beta$ 3 and the DropMap slope of each mAb, and allowed to extract a  $K_D$  value for each DropMap slope value calculated from a droplet containing an IgG-SC of unknown affinity for  $\alpha$ Ib $\beta$ 3.

#### Affinity determination of mAbs

Bio-layer interferometry measurements were performed using anti-human IgG sensors in an Octet system (ForteBio). Anti- $\alpha$ Ib $\beta$ 3 mAbs (10  $\mu$ g/mL) were captured on the sensors for 10 minutes. Equilibrium dissociation constants ( $K_D$ ) were determined by monitoring over 85 minutes the association between the immobilized antibodies and  $\alpha$ Ib $\beta$ 3 in solution in duplicate for 7 concentrations of antigen (200, 100, 50, 25, 12.5, 6.25, and 3.13 nM). An irrelevant IgG mAb was used as negative control to subtract the background signal. Data analysis was performed using the Octet Analysis software (ForteBio), and  $K_D$  values were calculated by steady-state analysis.

#### Flow cytometry

Fresh PBMCs were isolated from venous blood samples via standard density gradient centrifugation. For surface staining, cells were washed and resuspended at  $2 \times 10^6$  in 100  $\mu$ L PBS with 2% FBS and incubated with Zombie Violet fixable viability dye (BioLegend) and an antibody cocktail for 25 minutes at 4°C in the dark. Following surface staining, cells were fixed/permeabilized for 30 minutes at 4°C in the dark with an eBioscience FoxP3 transcription factor buffer kit and incubated with antibodies recognizing intracellular targets for 30 minutes at 4°C in the dark. Samples were acquired on an LSR Fortessa (BD Biosciences). Data were analyzed with Kaluza software (Beckman Coulter). A list of antibodies used in this panel can be found in Supplemental Table 1 and the detailed gating strategy is depicted in Supplemental Figure 8.

#### ELISpot

Anti- $\alpha$ Ib $\beta$ 3 ELISpot assays were performed as previously described (13). Briefly, KLH (2.5  $\mu$ g/mL), goat anti-human Ig polyvalent antibody (10  $\mu$ g/mL; Invitrogen), or purified  $\alpha$ Ib $\beta$ 3 (15  $\mu$ g/mL; Stago) was coated in PBS and 0.05% CaCl<sub>2</sub> in multiscreen 96-well filter plates (MSIP54510, Millipore) with overnight incubation at 4°C.

Then,  $1 \times 10^6$  splenocytes were serially diluted in culture medium (RPMI-1640 supplemented with 10% HyClone FBS and 1% penicillin/streptomycin) in triplicate before transferring to ELISpot plates and incubated overnight at 37°C with 5% CO<sub>2</sub>. Cells were removed and the ELISpot plate was incubated for 4 hours at 4°C with biotinylated goat anti-human IgG Fc (Invitrogen), followed by incubation for 1 hour at room temperature with horseradish peroxidase-conjugated (HRP-conjugated) avidin (Vector Laboratories). HRP activity was further revealed using 3-amino-9-ethylcarbazole (BD Biosciences) for 8 minutes at room temperature in the dark. Spots were enumerated in each well with an ELISpot reader using AID software v3.5 (AutoImmun Diagnostika).

#### Statistics

The R environment v4.0.5 was used for all the analyses (50). Data were neither averaged nor normalized prior to analyses. Response variables were log<sub>2</sub> converted for better adjustment to linear models. Data were fitted to a linear (quantitative response) or logistic (qualitative response) model that includes the variables of interest, i.e., group (healthy donor or ITP classes) and sample type (SP, BL or BM classes), plus the patient variable nested into the group variable. Group and sample type interaction was added in the model related to Figure 2A because of the post hoc inter-variable contrast comparisons. Otherwise, it was removed from the models when the effect was not significant. Age and sex covariates were not incorporated, as their effects were already represented by the patient variable. Mixed models using the lmer() function of the lme4 package were used in order to consider the effect of patient and patient-group interaction as random. ANOVAs were performed with the Anova() function of the car package. Type 3 sum of squares was applied because of unbalanced designs. Two-by-two effect comparisons (contrast comparisons) were performed with the emmeans() function of the emmeans package. Unequal variance *t* test (Welch's test) was used in bivariate designs, i.e., when data were analyzed on a single patient (Figure 1) or in the presence of a single value per patient (Figure 3A). In Figure 3, D-F, Pearson's correlation test was performed after removal of zero values, log<sub>2</sub> transformation, and residuals checking of the linear regression carried out in both ways. Statistical significance was set to a *P* value of 0.05 or less. In each figure, type I error was controlled by correcting the *P* values according to the Benjamini & Hochberg method [“BH” option in the p.adjust() function of R]. Results are detailed in Supplemental Table 2.

#### Study approval

This study was conducted in compliance with the Declaration of Helsinki principles and was approved by the Agence de la Biomédecine and the Institutional Review Boards Comité de Protection des Personnes (CPP) Ile-de-France IX (patients with ITP) and Ile-de-France II (healthy donor spleens). All patients with ITP provided written informed consent before the collection of samples.

#### Author contributions

PCH, KE, JB, M Mahevas, and PB designed the experiments. PCH, EC, MB, AS, GC, IA, AV, AP, BI, ORL, CC, GM, AR, and DS carried out the investigations. PCH, MB, PE, GAM, KE, JB, M Mahevas, and PB conducted formal analyses of the data. PCH and PB wrote the original draft of the manuscript. PCH, EC, MB, AS, GC, IA, AV, AP, BI, ORL, CC, GM, DS, AR, M Michel, PE, GAM, KE, JB, M Mahevas, and PB reviewed and edited the manuscript.

#### Acknowledgments

The authors acknowledge Laetitia Languille for the coordination of patient recruitment at Hôpital Henri Mondor, Créteil, France, and Maxime Moulard (BioCytex, Marseille, France) and Habib Boukerche (Faculté de Médecine René Laënnec, Lyon, France) for their gifts of anti- $\alpha$ Ib $\beta$ 3 (GPIIbIIIa) mAb clones. PCH was supported partly by a stipend from the Pasteur - Paris University (PPU) International PhD program, and by a fellowship from the French Fondation pour la Recherche Médicale (FRM). MB is the

recipient of a CIFRE PhD fellowship. CC was supported by CONCYTEC, Peru. PB acknowledges funding from the French National Research Agency grants ANR-18-CE15-0001 project Autoimmuni-B and ANR-14-CE16-0011 project DROPmAbs, funding by the Institut Carnot Pasteur Microbes et Santé, the Institut Pasteur, and the Institut National de la Santé et de la Recherche Médicale (INSERM). KE acknowledges funding from the Branco Weiss Fellowship (Society in Science) and the European Research Council (ERC) (grant agreement 80336). JB acknowledges funding from

the French government through BPIFrance under the frame “Programme d’Investissements d’Avenir” (CELLIGO Project), the “Institut Pierre-Gilles de Gennes” through the laboratoire d’excellence, and “Investissements d’avenir” programs ANR-10-IDEX-0001-02 PSL, ANR-10-EQPX-34, and ANR-10-LABX-31.

Address correspondence to: Pierre Bruhns, Institut Pasteur, 25 rue du Dr Roux, 75015 Paris, France. Phone: 33.14.5688629; Email: pierre.bruhns@pasteur.fr.

- Audia S, et al. Pathogenesis of immune thrombocytopenia. *Autoimmun Rev.* 2017;16(6):620–632.
- Arnold DM. Bleeding complications in immune thrombocytopenia. *Hematology Am Soc Hematol Educ Program.* 2015;2015:237–242.
- Neunert C, et al. Severe bleeding events in adults and children with primary immune thrombocytopenia: a systematic review. *J Thromb Haemost.* 2015;13(3):457–464.
- He R, et al. Spectrum of Ig classes, specificities, and titers of serum antiglycoproteins in chronic idiopathic thrombocytopenic purpura. *Blood.* 1994;83(4):1024–1032.
- Chan H, et al. The IgG subclasses of platelet-associated autoantibodies directed against platelet glycoproteins IIb/IIIa in patients with idiopathic thrombocytopenic purpura. *Br J Haematol.* 2003;122(5):818–824.
- Swinkels M, et al. Emerging concepts in immune thrombocytopenia. *Front Immunol.* 2018;9:880.
- McMillan R, et al. Platelet-associated and plasma anti-glycoprotein autoantibodies in chronic ITP. *Blood.* 1987;70(4):1040–1045.
- Al-Samkari H, et al. A modern reassessment of glycoprotein-specific direct platelet autoantibody testing in immune thrombocytopenia. *Blood Adv.* 2020;4(1):9–18.
- Kuwana M, et al. Spleen is a primary site for activation of platelet-reactive T and B cells in patients with immune thrombocytopenic purpura. *J Immunol.* 2002;168(7):3675–3682.
- Neunert C, et al. American Society of Hematology 2019 guidelines for immune thrombocytopenia. *Blood Adv.* 2019;3(23):3829–3866.
- Audia S, et al. Splenic TFH expansion participates in B-cell differentiation and antiplatelet-antibody production during immune thrombocytopenia. *Blood.* 2014;124(18):2858–2866.
- Audia S, et al. Immunologic effects of rituximab on the human spleen in immune thrombocytopenia. *Blood.* 2011;118(16):4394–4400.
- Mahevas M, et al. B cell depletion in immune thrombocytopenia reveals splenic long-lived plasma cells. *J Clin Invest.* 2013;123(1):432–442.
- Kuwana M, et al. Detection of circulating B cells producing anti-GPIIb autoantibodies in patients with immune thrombocytopenia. *PLoS One.* 2014;9(1):e86943.
- Arnold DM, et al. Systematic review: efficacy and safety of rituximab for adults with idiopathic thrombocytopenic purpura. *Ann Intern Med.* 2007;146(1):25–33.
- Deshayes S, et al. Long-term safety and efficacy of rituximab in 248 adults with immune thrombocytopenia: results at 5 years from the French prospective registry ITP-ritux. *Am J Hematol.* 2019;94(12):1314–1324.
- Tjonnfjord E, et al. Long-term outcomes of patients treated with rituximab as second-line treatment for adult immune thrombocytopenia - Follow-up of the RITP study. *Br J Haematol.* 2020;191(3):460–465.
- Crickx E, et al. Rituximab-resistant splenic memory B cells and newly engaged naive B cells fuel relapses in patients with immune thrombocytopenia. *Sci Transl Med.* 2021;13(589):eabc3961.
- Nutt SL, et al. The generation of antibody-secreting plasma cells. *Nat Rev Immunol.* 2015;15(3):160–171.
- Lindquist RL, et al. In the right place, at the right time: spatiotemporal conditions determining plasma cell survival and function. *Front Immunol.* 2019;10:788.
- Chang HD, et al. Pathogenic memory plasma cells in autoimmunity. *Curr Opin Immunol.* 2019;61:86–91.
- Eyer K, et al. Single-cell deep phenotyping of IgG-secreting cells for high-resolution immune monitoring. *Nat Biotechnol.* 2017;35(10):977–982.
- Bounab Y, et al. Dynamic single-cell phenotyping of immune cells using the microfluidic platform DropMap. *Nat Protoc.* 2020;15(9):2920–2955.
- Tiller T, et al. Autoreactivity in human IgG<sup>+</sup> memory B cells. *Immunity.* 2007;26(2):205–213.
- Scheid JF, et al. Differential regulation of self-reactivity discriminates between IgG<sup>+</sup> human circulating memory B cells and bone marrow plasma cells. *Proc Natl Acad Sci U S A.* 2011;108(44):18044–18048.
- Costello C. An update on the role of daratumumab in the treatment of multiple myeloma. *Ther Adv Hematol.* 2017;8(1):28–37.
- Mizuta S, et al. VS38 as a promising CD38 substitute antibody for flow cytometric detection of plasma cells in the daratumumab era. *Int J Hematol.* 2019;110(3):322–330.
- Fink K. Origin and function of circulating plasmablasts during acute viral infections. *Front Immunol.* 2012;3:78.
- Schwartz SI. Role of splenectomy in hematologic disorders. *World J Surg.* 1996;20(9):1156–1159.
- Meyer S, et al. AIRE-deficient patients harbor unique high-affinity disease-ameliorating autoantibodies. *Cell.* 2016;166(3):582–595.
- Kuwana M, et al. The role of autoantibody-producing plasma cells in immune thrombocytopenic purpura refractory to rituximab. *Am J Hematol.* 2007;82(9):846–848.
- Hiepe F, Radbruch A. Plasma cells as an innovative target in autoimmune disease with renal manifestations. *Nat Rev Nephrol.* 2016;12(4):232–240.
- Alexander T, et al. The proteasome inhibitor bortezomib depletes plasma cells and ameliorates clinical manifestations of refractory systemic lupus erythematosus. *Ann Rheum Dis.* 2015;74(7):1474–1478.
- Bontscho J, et al. Myeloperoxidase-specific plasma cell depletion by bortezomib protects from anti-neutrophil cytoplasmic autoantibodies-induced glomerulonephritis. *J Am Soc Nephrol.* 2011;22(2):336–348.
- Espeli M, et al. Local renal autoantibody production in lupus nephritis. *J Am Soc Nephrol.* 2011;22(2):296–305.
- Mumtaz IM, et al. Bone marrow of NZB/W mice is the major site for plasma cells resistant to dexamethasone and cyclophosphamide: implications for the treatment of autoimmunity. *J Autoimmun.* 2012;39(3):180–188.
- Taddeo A, et al. Long-lived plasma cells are early and constantly generated in New Zealand Black/New Zealand White F1 mice and their therapeutic depletion requires a combined targeting of autoreactive plasma cells and their precursors. *Arthritis Res Ther.* 2015;17:39.
- Suurmond J, et al. Loss of an IgG plasma cell checkpoint in patients with lupus. *J Allergy Clin Immunol.* 2019;143(4):1586–1597.
- Chen D, et al. Autoreactive CD19<sup>+</sup>CD20<sup>-</sup> plasma cells contribute to disease severity of experimental autoimmune encephalomyelitis. *J Immunol.* 2016;196(4):1541–1549.
- Even-Or E, et al. Successful treatment with daratumumab for post-HSCT refractory hemolytic anemia. *Pediatr Blood Cancer.* 2020;67(1):e28010.
- Drinouk L, et al. Daratumumab therapy for post-HSCT immune-mediated cytopenia: experiences from two pediatric cases and review of literature. *Mol Cell Pediatr.* 2021;8(1):5.
- Lux A, et al. A humanized mouse identifies the bone marrow as a niche with low therapeutic IgG activity. *Cell Rep.* 2014;7(1):236–248.
- Grandjean CL, et al. Imaging the mechanisms of anti-CD20 therapy in vivo uncovers spatiotemporal bottlenecks in antibody-dependent phagocytosis. *Sci Adv.* 2021;7(8):eabd6167.
- Cines DB, McMillan R. Pathogenesis of chronic immune thrombocytopenic purpura. *Curr Opin Hematol.* 2007;14(5):511–514.
- Chaturvedi S, et al. Splenectomy for immune

- thrombocytopenia: down but not out. *Blood*. 2018;131(11):1172-1182.
46. Cooper N, Ghanima W. Immune thrombocytopenia. *N Engl J Med*. 2019;381(10):945-955.
47. Crickx E, et al. Anti-CD20-mediated B-cell depletion in autoimmune diseases: successes, failures and future perspectives. *Kidney Int*. 2020;97(5):885-893.
48. Audia S, Bonnotte B. Emerging therapies in immune thrombocytopenia. *J Clin Med*. 2021;10(5):1004.
49. Mazutis L, et al. Single-cell analysis and sorting using droplet-based microfluidics. *Nat Protoc*. 2013;8(5):870-891.
50. R: A language and environment for statistical computing. Version 4.2.0. R Foundation for Statistical Computing; 2022. <https://www.R-project.org/>.

# **GENERAL DISCUSSION**

## GENERAL DISCUSSION

### Emerging patterns from human DropMap affinity repertoires

Our use of DropMap to monitor the ASC response following mRNA vaccination against SARS-CoV2 is the second application of this microfluidic technique for broad ASC monitoring in humans<sup>128</sup>. The first use of DropMap in humans was in the autoimmune context of immune thrombocytopenia<sup>152</sup>. These immunological contexts and representative antigens are distinct in their underlying pathology and the understood mechanisms by which they promote ASC differentiation. Despite this, it is apparent across these two published studies as well as ongoing works that low to medium affinity antibodies are the norm amongst circulating ASCs and their affinity repertoires globally resemble pyramids with stronger affinities at their peak. DropMap is limited in its ability to resolve affinities below 50-100nM, which still contains many antibodies of physiological relevance. This emerging trend between our studies provides two major points to consider in the ongoing discussion surrounding affinity and B cell differentiation.

Across both of our studies we have surprisingly observed low affinity ASCs in contexts we did not classically expect such cells to be generated in frequencies that could be reliably detected. Healthy control donors without any clinical manifestations of ITP symptoms would frequently possess low numbers of ASCs with weak affinities towards platelet glycoproteins<sup>152</sup>. This observation of apparently auto-reactive, anti-platelet IgG-SCs in multiple anatomical compartments, especially the bone marrow, strongly suggests that these ASCs are not transiently or spontaneously activated<sup>153</sup>. Whether these cells were polyreactive and had been generated during an earlier immune response or generated by other means is unclear. Additionally, our study on SARS-CoV2 mRNA vaccination found that some individuals with no known prior exposure to SARS-CoV2 possessed rare, low affinity RBD-targeting IgG-SCs in circulation.

The shared trait among these observed non-canonical ASCs is their low affinities, which may highlight a potential flaw in current antigen-specific B cell identification methods. DropMap's approach capitalizes on measuring the binding equilibrium between secreted antibodies and antigens in a constant, confined volume<sup>132</sup>. In contrast, many B cell studies rely on labeling with fluorophore-conjugated antigens, followed by visualization or flow cytometry-based sorting after centrifugation-based washing<sup>154,155</sup>. Unlike the commercial monoclonal antibodies used in staining that are selected for higher affinities towards their targets, the affinity of unknown BCRs towards

the antigen remains uncertain. Typically taking 30-45 minutes, or potentially longer, the interval between sample washing and analysis for flow cytometry contrasts with the brief periods (3-15 minutes) used for dissociation in kinetic affinity assays such as BLI or SPR, underscoring the risk of antigen label dissociation during this waiting period. It is therefore possible that current flow cytometry methods introduce a procedural affinity threshold during antigen-specific B cell classification, which excludes B cells with lower affinity antibodies, at least those with higher dissociation rates, but may still be physiologically relevant. It is unclear to what extent our current understanding of B cells and ASCs may be biased by the omission of lower affinity or avidity. It has been reported in a model of scFv yeast display that antigen-based sorting for fluorescein-specific cells still produced a broad repertoire of affinities between  $10^{-5}$  and  $10^{-10}$ ; however, this study lacked validation by BLI or SPR<sup>156</sup>. The issue of antigen-specific B cell exclusion due to antigen-label sorting has been discussed by investigators as both a caveat to their presented findings<sup>42</sup> and as a core principle of the study itself<sup>122</sup>, with the full extent of the effect unknown and no clear resolution to the limitation proposed. A key novelty of the study published by Viant et al<sup>122</sup> in 2020 regarding affinity and B cell fates was the emphasis on unbiased assessment of B cells without antigen-sorting.

We were able to perform in 2021 a limited but valuable experiment to investigate this potential artifact, using DropMap to assess affinity repertoires. To determine if antigen-sorting of B cells produced a different affinity repertoire and potentially omitted weaker affinity cells, we sorted by FACS memory B cells into an ASC-differentiation culture system as described previously<sup>129</sup>; from the same sample, a portion of cells was sorted based on RBD-binding (RBD<sup>+</sup> Bmem) and another was sorted irrespective of RBD signal (Bmem) (Figure 28). We also prepared samples with either 120 or 60 total possible clones, by sorting that number of cell per well, to compare the potential for sampling bias. When these Bmem-derived ASCs were assessed by DropMap, we found the median affinity among RBD-specific cells from the RBD<sup>+</sup> Bmem samples to be approximately 4 times better than that of the non-antigen-sorted Bmem sample; high-to-medium affinity clones were still observed among non-antigen-sorted Bmem. It should be noted that this demonstration is only supported by 2 technical replicates, no biological replicates, and no confirmation by a more robust method for affinity measurement (BLI or SPR). Additionally, the expansion of clones within the Bmem-to-ASC culture system does not necessarily reflect the *in vivo* repertoire. Nonetheless this data suggests that antigen sorting may underrepresent lower affinity clones. It would be interesting

to perform additional controlled comparisons of the various methods for identifying and isolating antigen-specific B cells to perhaps identify potential artifacts relating to the measured clonal and functional repertoires. The insight gained may provide answers to how the differing conclusions regarding B cell affinity repertoires may be reconciled or explained by technical differences.

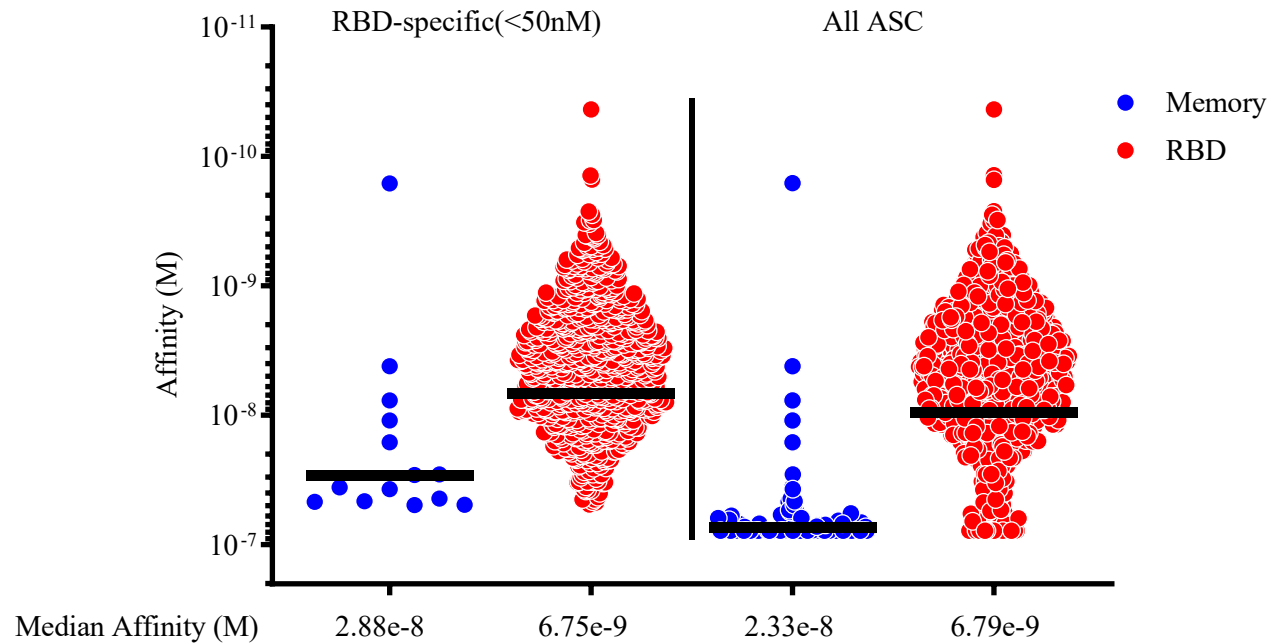


Figure 28 Comparison of affinity repertoires after antigen-based sorting. Affinity measured by DropMap towards SARS-CoV-2 Spike RBD of ASCs derived from Bmem in vitro, either (red) sorted specifically for RBD<sup>+</sup> Bmem as assessed by fluorescent antigen-labelling or (blue) nonspecifically to include any Bmem irrespective of antigen binding. Left: (RBD-specific) data represented with a  $\geq 50$ nM cut-off. Right: (All ASC) data represented without restriction (calibration equation limits KD conversion to maximum of  $\sim 98$ nM).

Another interesting and non-classical feature of the ASC response that has emerged from our studies using DropMap is the transient appearance of higher affinity plasmablasts. The original description of the DropMap technique featured a characterization of affinity repertoire evolution in a mouse model of TT immunization<sup>132</sup>, with frequent spleen and bone marrow sampling for up to 49 days. Consistent with our study on human SARS-CoV2 vaccination, we found that the appearance of high affinity plasmablasts was mostly limited to the peak of antigen-specific plasmablasts emergence (Figure 29). These data diminish the notion of the B cell response collectively moving towards higher affinities as the immune response progresses, relating the appearance of high affinity ASCs to the overall magnitude of antigen-specific ASC differentiation. Interestingly, this may further reinforce the notion of stochasticity in plasmablast generation within

the GC. During influenza infection in mice, Mathew et al (2021) found plasmablast clonal diversity to be low after week 1, highest at the end of week 2, and then decreasing by the end of week 4<sup>42</sup>; this kinetic of ASC clonal diversity follows our own affinity repertoire data during immunization in mice and humans. These findings are contradictory to our current understanding of B cell response kinetics, with the source of plasmablasts during T-dependent responses beginning as extrafollicular naïve B cells and Bmem that is soon joined by GC-derived plasmablasts, which are considered to have higher affinities that continue to increase as the GC reaction progresses. A reconciliation of these two observations could be explained by a relatively limited duration of the GC reaction, in which the appearance of higher affinity clones via affinity maturation only shortly precedes the diminishing of B cell proliferation. The diminishing of high affinity clones may be further driven by naïve B cells continuously joining the GC reaction and introducing non-affinity matured clones<sup>157</sup>; the proportion of late entry B cells was reported to be up to 30% of the germinal center participants, which may greatly outpace and overshadow high affinity clones emerging by affinity maturation.

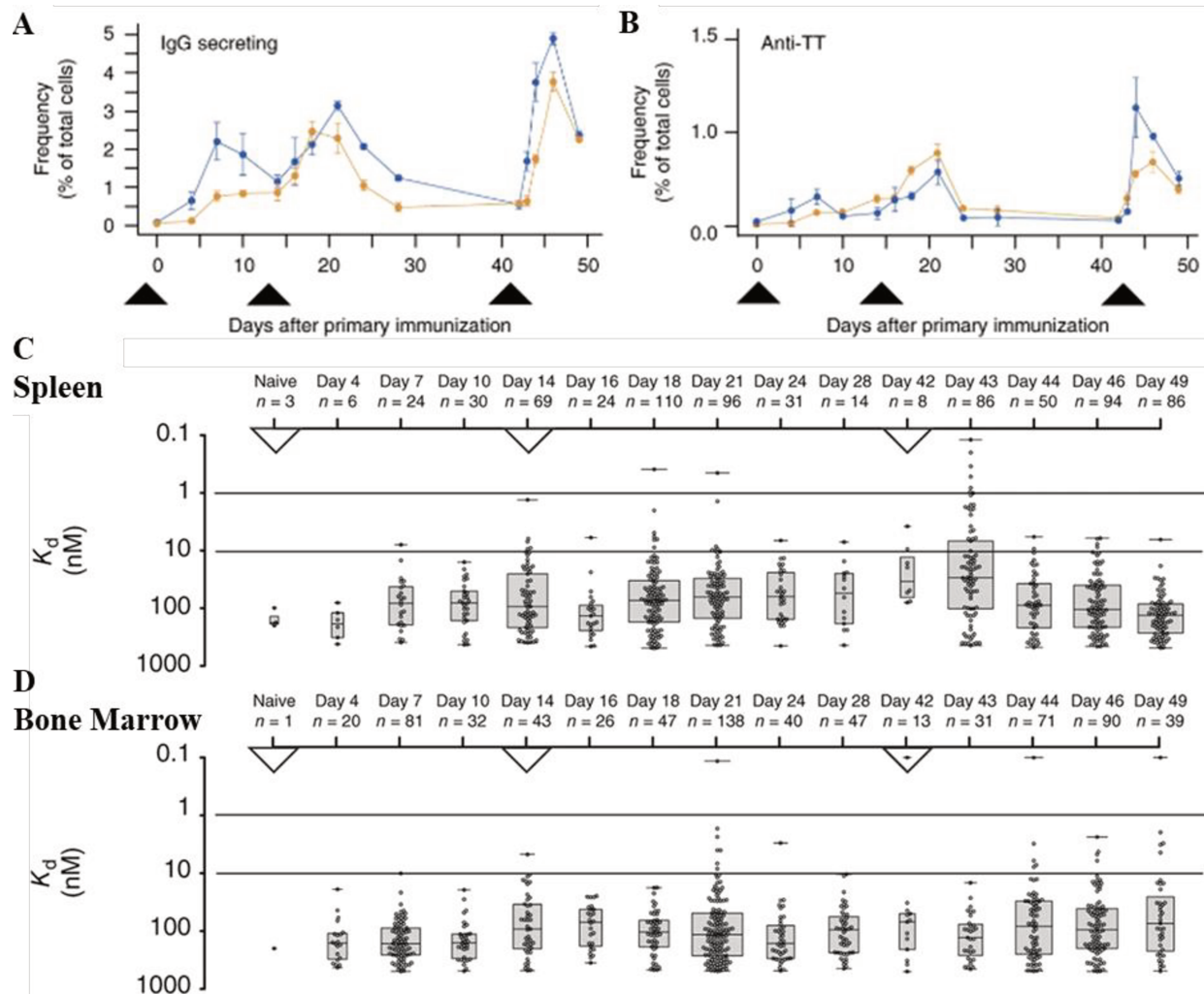


Figure 29 Kinetics of ASC response during immunization with TT in mice (From Eyer et al, 2016)<sup>132</sup>. (A-B) Frequencies of (A) total IgG-secreting cells or (B) TT-specific IGG secreting cells in cell suspensions obtained from the spleen (orange) and bone marrow (blue) of TT-immunized mice,  $n = 3$  mice per timepoint. Time points of immunization are indicated by black triangles below the x-axes. (C-D) Affinity repertoires of the (C) spleen ( $n = 731$  among 318,695 cells analyzed) and (D) bone marrow ( $n = 719$  among 272,899 cells analyzed) of TT-immunized mice,  $n = 3$  mice per timepoint, each dot represents a single IgG-secreting cell. Boxes show median and interquartile range. Horizontal lines indicate high- ( $<10$  nM) and very-high affinities ( $<1$  nM) for the TT antigen.

While it is valuable to consider the possible implications of our findings, it is also important to consider how our observations align with existing models from others in the field regarding B cell affinity. Returning to the debate outlined in the introduction, our studies using DropMap to assess ASC affinity repertoires lend additional support to the notion that ASCs may have a broad range of affinities, in agreement with the findings of Mathew et al<sup>42</sup> and Neumeier et al<sup>124</sup>. This simultaneously puts our findings in opposition to those studies that report a predominance of high affinity clones among ASCs. The observation of low affinity ASCs being predominant is also

difficult to reconcile with current understandings of the role of the BCR and affinity in ASC differentiation, which commonly considers obtaining medium to high affinity as a threshold. It is unclear to what degree these differences are attributable to technical differences during B cell selection, sorting, and the single cell affinity measurement method or biological differences in the samples assayed and the nature of the elicited immune response being studied. It would be valuable to continue our investigations into ASC affinity repertoires with DropPick, allowing for the clonal relationships between Bmem and ASC to be characterized; this could help to address the major outstanding question of Bmem and ASC clonal overlap between higher and lower affinities.

It is similarly relevant to consider our own measurements of the affinity repertoires within the Bmem compartment using BLI on in vitro culture supernatants<sup>129-131</sup>. It is important to note that these measurements were performed on antigen-specific Bmem as determined and sorted according to antigen-based labelling, for which the potential influencing factors have been already discussed. During our studies on Bmem and SARS-CoV-2, we have reliably found that the Bmem compartment contains affinity repertoires with median affinities at least as high or higher than those we have measured by DropMap in any of our studies using the technique. There is the key factor that each affinity measurement modality will reflect its own inherent artifact arising from the sensitivity of the measurement and the variability of how binding analytes are handled<sup>158</sup>; KD determinations can vary both in consistency and absolute value depending on the technology used. Therefore, it is not worthwhile to directly compare these affinity repertoires of Bmem and ASCs measured using BLI or DropMap, respectively. It is certainly possible that by measuring both B cell populations using the same techniques, including ASC-derived antibodies with BLI or Bmem-derived antibodies by DropMap (Figure 28), we may observe the same hierarchy of affinities between these populations.

However, one finding of our DropMap study that is incongruent with our Bmem investigations<sup>129,130</sup> is the lack of significant difference between naïve and previously infected individuals in either the magnitude of the ASC response or the affinity repertoire. Irrespective of the particularities of specific affinity measurement methods, significant variation between populations assessed by the same technique would be expected to be conserved when assayed by a similar technique. We demonstrated prior to the boost dose in recovered vaccinees a median VH mutation rate in Bmem over twice as that of Bmem from naïve vaccinees 2 months post-boost

dose<sup>129</sup>. The increased mutation rate is indicative of increased affinity maturation and our BLI measurements confirmed this hypothesis with a significantly increased median affinity among recovered-vaccinee Bmem compared to those from naïve vaccinees; a significant correlation between the number of VH mutations and the measured KD further reinforces this relationship. With the clear presence of mature, high affinity Bmem in individuals with prior SARS-CoV-2 exposure<sup>129,159</sup>, we could hypothesize that the ASC response in recovered vaccinees would yield a stronger ASC response, with at least an improved median affinity; following vaccination, Bmem from the prior infection can encounter antigen and rapidly generate plasmablasts, expressing antibodies that have already undergone somatic hypermutation, which we have shown ourselves to improve affinity. Therefore, our observations by DropMap for a lack of significant difference between naïve and recovered vaccinees<sup>128</sup> is puzzling. The previously mentioned influence of using different affinity measurement methods is not applicable in this case, as both recovered and naïve vaccinee-derived ASCs are measured by DropMap.

It is difficult at this point to fully integrate our collective findings from DropMap into the ongoing discussion surrounding affinity and ASC responses, as described during the introduction. Despite its advantages in affinity measurement throughput, DropMap lacks the key ability to distinguish between the evolution and the emergence of B cell clones, which is a crucial distinction to make when considering the influence of affinity maturation, memory B cells, and the germinal center reaction in the potential explanations for variation in ASC affinity. A major motivation for the development of DropPick has been to bridge this gap in our functional characterization capabilities and the clonal repertoire dynamics revealed by single cell BCR sequencing methods.

## **Open Source and Standardized Microfluidics**

DropPick offers insight into newly imaginable futures for a wide arsenal of existing assays. The workflow we demonstrate is highly flexible and independent of one specific machine or protocol. Any microscope or alternative system for imaging that is equipped with an adjustable diaphragm for incoming light and the capability to run user defined macros could be adapted as a platform for such targeted illumination. Furthermore, the method of applying our label to specify cells of interest is neither proprietary nor dependent on a specific means of extraction downstream, but rather makes use of fluorophore photoactivation that offers many opportunities. Both soluble photoactivatable dyes and numerous photo-switchable and photo-activatable protein families are

well described in the literature and available commercially. Finally, once cells of interest have been labelled and recovered, it is foreseeable to pass the sample through any type of cell sorter to be used for a wide array of downstream applications.

Microfluidic solutions to address assay needs are currently largely divided between two sources. Many options are largely bespoke systems used by small communities of researchers and require key components to be handmade and/or operated by specialized engineers<sup>160</sup>. The solutions offered by academic groups are well documented and transparent with their design and methods but are difficult to readily incorporate by other researchers without microfluidic backgrounds. Alternatively, microfluidic assays are frequently offered as complex ecosystems of kits and machines only available from a unique supplier. Globally, microfluidic assay kits are more accessible options for those seeking the throughput and fidelity advantages offered by microfluidics, but are globally more expensive, making them out of reach to many<sup>161,162</sup>. Proprietary workflows are often not completely transparent, which makes it difficult for researchers to understand how they work, validate results, or develop new applications, and the lack of customization limits the flexibility and versatility of these assays. Finally, their development and innovation are ultimately driven by the needs of the commercial provider, which may not always be aligned with those of researchers.

The ability to readily exchange consumables, reagents, and machines is a core principle of assay development and technical innovation, allowing for researchers to conceive of new or better ways to answer novel questions. Cross-compatibility and the freedom to exchange components between manufacturers or even intended use-cases is common in many techniques. It is commonplace for protocols to adopt machines or reagents from different sources to best suit individual needs; a true inclusion by natural selection that steers labs and research fields towards reproducible and robust results.

How exactly this cross-compatible future might materialize is difficult to predict exactly. The building of a strong and invested community of scientists and engineers who are interested in open-source microfluidics is critical<sup>163</sup>. Engagement with the industry partners who manufacture microfluidic devices and reagents will be required to achieve widespread feasibility for new groups to implement functional microfluidic assays. Placing an emphasis during project and funding planning to develop open-source hardware and software platforms for microfluidic assays can help

to increase the accessibility and usability of these technologies. At a minimum, multi-step workflows should ensure that the sample itself being assessed can be transferred to different applications after manipulation steps. Additional steps may include the standardization of consumable dimensions to allow for compatibility with existing platforms and avoiding a dependence on proprietary proteins or chemical pathways with the option for researchers to substitute and test their own reagents.

DropPick as a concept of first performing a single cell functional assay, followed by sorting cells of interest, and then finally sequencing, has only scratched the surface of what perhaps is possible. We have described only one specific combination of these specific steps: DropMap as a functional assay to find cells of interest, traditional isolation by FACS, and a well-based PCR to amplify antibody encoding RNAs from B cells. Improved efficiency or novel applications may be achieved by exchanging any of these steps with other assays or machines, particularly scRNAseq workflows. I hope that our demonstration of this workflow may be informative to other groups seeking to pair their existing microfluidic or imaging-based assays with other downstream assays.

# BIBLIOGRAPHY

**BIBLIOGRAPHY**

1. Frangione, B. & Milstein, C. Disulphide bridges of immunoglobulin G1 heavy chains. *Nature* **216**, 939–941 (1967).
2. Liu, H. & May, K. Disulfide bond structures of IgG molecules: Structural variations, chemical modifications and possible impacts to stability and biological function. *MAbs* **4**, 17 (2012).
3. Bowen, A. & Casadevall, A. The Role of the Constant Region in Antibody-Antigen Interactions: Redefining the Modular Model of Immunoglobulin Structure. *Structural Biology in Immunology: Structure and Function of Novel Molecules of Immunologic Importance* 145–170 (2018) doi:10.1016/B978-0-12-803369-2.00006-1.
4. Janda, A., Bowen, A., Greenspan, N. S. & Casadevall, A. Ig constant region effects on variable region structure and function. *Front Microbiol* **7**, 22 (2016).
5. Briney, B., Inderbitzin, A., Joyce, C. & Burton, D. R. Commonality despite exceptional diversity in the baseline human antibody repertoire. *Nature* **566**, 393–397 (2019).
6. Chi, X., Li, Y. & Qiu, X. V(D)J recombination, somatic hypermutation and class switch recombination of immunoglobulins: mechanism and regulation. *Immunology* **160**, 233–247 (2020).
7. Jackson, K. J. L. *et al.* Divergent human populations show extensive shared IGK rearrangements in peripheral blood B cells. *Immunogenetics* **64**, 3–14 (2012).
8. Hoi, K. H. & Ippolito, G. C. Intrinsic bias and public rearrangements in the human immunoglobulin V $\lambda$  light chain repertoire. *Genes & Immunity* **2013 14:4** **14**, 271–276 (2013).
9. Sajadi, M. M. *et al.*  $\lambda$  Light Chain Bias Associated With Enhanced Binding and Function of Anti-HIV Env Glycoprotein Antibodies. *J Infect Dis* **213**, 156 (2016).
10. Wu, Y. & Song, H. A Comparative and Comprehensive Review of Antibody Applications in the Treatment of Lung Disease. *Life* **2022, Vol. 12, Page 130** **12**, 130 (2022).
11. Stavnezer, J., Guikema, J. E. J. & Schrader, C. E. Mechanism and Regulation of Class Switch Recombination. *Annu Rev Immunol* **26**, 261 (2008).
12. Stavnezer, J. & Schrader, C. E. IgH Chain Class Switch Recombination: Mechanism and Regulation. *The Journal of Immunology* **193**, (2014).
13. Vidarsson, G., Dekkers, G. & Rispen, T. IgG subclasses and allotypes: From structure to effector functions. *Front Immunol* **5**, (2014).
14. Gutzeit, C., Chen, K. & Cerutti, A. The enigmatic function of IgD: some answers at last. *European Journal of Immunology* vol. 48 Preprint at <https://doi.org/10.1002/eji.201646547> (2018).
15. Koelsch, K. *et al.* Mature B cells class switched to IgD are autoreactive in healthy individuals. *Journal of Clinical Investigation* **117**, (2007).
16. Wienands, J. & Engels, N. The memory function of the B cell antigen receptor. *Curr Top Microbiol Immunol* **393**, 107–121 (2015).

## References

17. Kunik, V., Peters, B. & Ofran, Y. Structural consensus among antibodies defines the antigen binding site. *PLoS Comput Biol* **8**, (2012).
18. Tsuchiya, Y. & Mizuguchi, K. The diversity of H3 loops determines the antigen-binding tendencies of antibody CDR loops. *Protein Science* **25**, (2016).
19. Cooper, M. D., Peterson, R. D. A. & Good, R. A. Delineation of the Thymic and Bursal Lymphoid Systems in the Chicken. *Nature* *1965* **205**:4967 **205**, 143–146 (1965).
20. Miller, J. F. & Mitchell, G. F. Cell to cell interaction in the immune response. I. Hemolysin-forming cells in neonatally thymectomized mice reconstituted with thymus or thoracic duct lymphocytes. *J Exp Med* **128**, 801–820 (1968).
21. Lebien, T. W. & Tedder, T. F. B lymphocytes: How they develop and function. *Blood* **112**, (2008).
22. Herzog, S., Reth, M. & Jumaa, H. Regulation of B-cell proliferation and differentiation by pre-B-cell receptor signalling. *Nature Reviews Immunology* vol. 9 Preprint at <https://doi.org/10.1038/nri2491> (2009).
23. Melchers, F. Checkpoints that control B cell development. *J Clin Invest* **125**, 2203–2210 (2015).
24. Liu, X., Shen, S. & Manser, T. Influence of B Cell Antigen Receptor Expression Level on Pathways of B Cell Tolerance Induction. *The Journal of Immunology* **182**, 398–407 (2009).
25. Allman, D. & Pillai, S. Peripheral B cell subsets. *Curr Opin Immunol* **20**, 149 (2008).
26. Allman, D., Wilmore, J. R. & Gaudette, B. T. The continuing story of T-cell independent antibodies. *Immunological Reviews* vol. 288 Preprint at <https://doi.org/10.1111/imr.12754> (2019).
27. Bouvet, J. P. & Dighiero, G. Cross-reactivity and polyreactivity: the two sides of a coin. *Immunol Today* **21**, 411–412 (2000).
28. Baumgarth, N. *et al.* B-1 and B-2 cell-derived immunoglobulin M antibodies are nonredundant components of the protective response to influenza virus infection. *J Exp Med* **192**, 271–280 (2000).
29. Smith, F. L. & Baumgarth, N. B-1 Cell Responses to Infections. *Curr Opin Immunol* **57**, 23 (2019).
30. Akkaya, M., Kwak, K. & Pierce, S. K. B cell memory: building two walls of protection against pathogens. *Nature Reviews Immunology* *2019* **20**:4 **20**, 229–238 (2019).
31. Cyster, J. G. & Allen, C. D. C. B Cell Responses: Cell Interaction Dynamics and Decisions. *Cell* **177**, 524–540 (2019).
32. Racine, R., Chatterjee, M. & Winslow, G. M. CD11c Expression Identifies a Population of Extrafollicular Antigen-Specific Splenic Plasmablasts Responsible for CD4 T-Independent Antibody Responses during Intracellular Bacterial Infection. *J Immunol* **181**, 1375 (2008).
33. MacLennan, I. C. M. *et al.* Extrafollicular antibody responses. *Immunol Rev* **194**, 8–18 (2003).
34. Elsner, R. A. & Shlomchik, M. J. Germinal Center and Extrafollicular B Cell Responses in vaccination, immunity and autoimmunity. *Immunity* **53**, 1136 (2020).

## References

35. Faro, J., von Haefen, B., Gardner, R. & Faro, E. A Sensitivity Analysis Comparison of Three Models for the Dynamics of Germinal Centers. *Front Immunol* **10**, (2019).
36. Victora, G. D. & Nussenzweig, M. C. Germinal Centers. <https://doi.org/10.1146/annurev-immunol-020711-075032> **30**, 429–457 (2012).
37. Tolar, P. Cytoskeletal control of B cell responses to antigens. *Nat Rev Immunol* **17**, 621–634 (2017).
38. Natkanski, E. *et al.* B cells use mechanical energy to discriminate antigen affinities. *Science* **340**, 1587–1590 (2013).
39. Kwak, K. *et al.* Intrinsic properties of human germinal center B cells set antigen affinity thresholds. *Sci Immunol* **3**, (2018).
40. Victora, G. D. *et al.* Germinal Center Dynamics Revealed by Multiphoton Microscopy with a Photoactivatable Fluorescent Reporter. *Cell* **143**, 592–605 (2010).
41. Weisel, F. J., Zuccarino-Catania, G. V., Chikina, M. & Shlomchik, M. J. A Temporal Switch in the Germinal Center Determines Differential Output of Memory B and Plasma Cells. *Immunity* **44**, 116–130 (2016).
42. Mathew, N. R. *et al.* Single-cell BCR and transcriptome analysis after influenza infection reveals spatiotemporal dynamics of antigen-specific B cells. *Cell Rep* **35**, (2021).
43. Tellier, J. & Nutt, S. L. Plasma cells: The programming of an antibody-secreting machine. *European Journal of Immunology* vol. 49 Preprint at <https://doi.org/10.1002/eji.201847517> (2019).
44. Schebesta, A. *et al.* Transcription factor Pax5 activates the chromatin of key genes involved in B cell signaling, adhesion, migration, and immune function. *Immunity* **27**, 49–63 (2007).
45. Ochiai, K., Muto, A., Tanaka, H., Takahashi, S. & Igarashi, K. Regulation of the plasma cell transcription factor Blimp-1 gene by Bach2 and Bcl6. *Int Immunol* **20**, 453–460 (2008).
46. Tellier, J. & Nutt, S. L. Standing out from the crowd: How to identify plasma cells. *European Journal of Immunology* vol. 47 Preprint at <https://doi.org/10.1002/eji.201747168> (2017).
47. Nutt, S. L., Hodgkin, P. D., Tarlinton, D. M. & Corcoran, L. M. The generation of antibody-secreting plasma cells. *Nat Rev Immunol* **15**, (2015).
48. Robinson, E. *et al.* A System for In Vitro Generation of Mature Murine Plasma Cells Uncovers Differential Blimp-1/Prdm1 Promoter Usage. *The Journal of Immunology* **208**, 514–525 (2022).
49. Arumugakani, G. *et al.* Early Emergence of CD19-Negative Human Antibody-Secreting Cells at the Plasmablast to Plasma Cell Transition. *J Immunol* **198**, 4618–4628 (2017).
50. Todd, D. J. *et al.* XBP1 governs late events in plasma cell differentiation and is not required for antigen-specific memory B cell development. *J Exp Med* **206**, 2151 (2009).
51. Taubenheim, N. *et al.* High rate of antibody secretion is not integral to plasma cell differentiation as revealed by XBP-1 deficiency. *J Immunol* **189**, 3328–3338 (2012).

## References

52. Hasbold, J., Corcoran, L. M., Tarlinton, D. M., Tangye, S. G. & Hodgkin, P. D. Evidence from the generation of immunoglobulin G-secreting cells that stochastic mechanisms regulate lymphocyte differentiation. *Nature Immunology* 2004 5:1 5, 55–63 (2003).
53. Hasbold, J., Lyons, A. B., Kehry, M. R. & Hodgkin, P. D. Cell division number regulates IgG1 and IgE switching of B cells following stimulation by CD40 ligand and IL-4. doi:10.1002/(SICI)1521-4141(199803)28:03.
54. Gitlin, A. D., Shulman, Z. & Nussenzweig, M. C. Clonal selection in the germinal centre by regulated proliferation and hypermutation. *Nature* 2014 509:7502 509, 637–640 (2014).
55. Phan, T. G. *et al.* High affinity germinal center B cells are actively selected into the plasma cell compartment. *J Exp Med* 203, 2419–2424 (2006).
56. Ise, W. *et al.* T Follicular Helper Cell-Germinal Center B Cell Interaction Strength Regulates Entry into Plasma Cell or Recycling Germinal Center Cell Fate. *Immunity* 48, 702-715.e4 (2018).
57. Li, X. *et al.* Cbl Ubiquitin Ligases Control B Cell Exit from the Germinal-Center Reaction. *Immunity* 48, 530-541.e6 (2018).
58. Barnett, B. E. *et al.* Asymmetric B cell division in the germinal center reaction. *Science* 335, 342–344 (2012).
59. Sze, D. M. Y., Toellner, K. M., De Vinuesa, C. G., Taylor, D. R. & MacLennan, I. C. M. Intrinsic constraint on plasmablast growth and extrinsic limits of plasma cell survival. *J Exp Med* 192, 813–821 (2000).
60. Duffy, K. R. & Hodgkin, P. D. Intracellular competition for fates in the immune system. *Trends Cell Biol* 22, 457–464 (2012).
61. Duffy, K. R. *et al.* Activation-induced B cell fates are selected by intracellular stochastic competition. *Science* 335, 338–341 (2012).
62. Fairfax, K. A. *et al.* Different kinetics of blimp-1 induction in B cell subsets revealed by reporter gene. *J Immunol* 178, 4104–4111 (2007).
63. Kometani, K. *et al.* Repression of the Transcription Factor Bach2 Contributes to Predisposition of IgG1 Memory B Cells toward Plasma Cell Differentiation. *Immunity* 39, 136–147 (2013).
64. Weisel, F. J. *et al.* Germinal center B cells selectively oxidize fatty acids for energy while conducting minimal glycolysis. *Nat Immunol* 21, 331–342 (2020).
65. Boothby, M. R., Brookens, S. K., Raybuck, A. L. & Cho, S. H. Supplying the trip to antibody production—nutrients, signaling, and the programming of cellular metabolism in the mature B lineage. *Cellular & Molecular Immunology* 2021 19:3 19, 352–369 (2021).
66. Woodruff, M. C. *et al.* Extrafollicular B cell responses correlate with neutralizing antibodies and morbidity in COVID-19. *Nature Immunology* 2020 21:12 21, 1506–1516 (2020).
67. Serrán, M. G. *et al.* Extrafollicular Plasmablasts Present in the Acute Phase of Infections Express High Levels of PD-L1 and Are Able to Limit T Cell Response. *Front Immunol* 13, 828734 (2022).

## References

68. Jenks, S. A. *et al.* Distinct Effector B Cells Induced by Unregulated Toll-like Receptor 7 Contribute to Pathogenic Responses in Systemic Lupus Erythematosus. *Immunity* **49**, 725-739.e6 (2018).
69. Di Niro, R. *et al.* Salmonella Infection Drives Promiscuous B Cell Activation Followed by Extrafollicular Affinity Maturation. *Immunity* **43**, 120–131 (2015).
70. Trivedi, N. *et al.* Liver Is a Generative Site for the B Cell Response to Ehrlichia muris. *Immunity* **51**, 1088-1101.e5 (2019).
71. Sang, A. *et al.* Activation of rheumatoid factor-specific B cells is antigen dependent and occurs preferentially outside of germinal centers in the lupus-prone NZM2410 mouse model. *J Immunol* **193**, 1609–1621 (2014).
72. Männe, C. *et al.* Salmonella SiiE prevents an efficient humoral immune memory by interfering with IgG<sup>+</sup> plasma cell persistence in the bone marrow. *Proc Natl Acad Sci U S A* **116**, 7425–7430 (2019).
73. Kabashima, K. *et al.* Plasma cell S1P1 expression determines secondary lymphoid organ retention versus bone marrow tropism. *J Exp Med* **203**, 2683–2690 (2006).
74. Odendahl, M. *et al.* Generation of migratory antigen-specific plasma blasts and mobilization of resident plasma cells in a secondary immune response. *Blood* **105**, 1614–1621 (2005).
75. Rouers, A. *et al.* CD27<sup>hi</sup>CD38<sup>hi</sup> plasmablasts are activated B cells of mixed origin with distinct function. *iScience* **24**, (2021).
76. Hargreaves, D. C. *et al.* A coordinated change in chemokine responsiveness guides plasma cell movements. *J Exp Med* **194**, 45–56 (2001).
77. Tokoyoda, K., Egawa, T., Sugiyama, T., Choi, B. II & Nagasawa, T. Cellular niches controlling B lymphocyte behavior within bone marrow during development. *Immunity* **20**, 707–718 (2004).
78. Bonaud, A. *et al.* Transinteractome analysis reveals distinct niche requirements for isotype-based plasma cell subsets in the bone marrow. *Eur J Immunol* **0**, 2250334 (2023).
79. Chu, V. T. & Berek, C. Immunization induces activation of bone marrow eosinophils required for plasma cell survival. *Eur J Immunol* **42**, (2012).
80. Haberland, K. *et al.* Eosinophils are not essential for maintenance of murine plasma cells in the bone marrow. *Eur J Immunol* **48**, (2018).
81. Bortnick, A., Chernova, I., Spencer, S. P. & Allman, D. No strict requirement for eosinophils for bone marrow plasma cell survival. *Eur J Immunol* **48**, (2018).
82. Chu, V. T. *et al.* Eosinophils are required for the maintenance of plasma cells in the bone marrow. *Nature Immunology* **2011 12:2** **12**, 151–159 (2011).
83. Benet, Z., Jing, Z. & Fooksman, D. R. Plasma cell dynamics in the bone marrow niche. *Cell Rep* **34**, (2021).
84. Nera, K. P., Kyläniemi, M. K. & Lassila, O. Regulation of B Cell to Plasma Cell Transition within the Follicular B Cell Response. *Scand J Immunol* **82**, 225–234 (2015).

## References

85. Carter, M. J., Mitchell, R. M., Sauteur, P. M. M., Kelly, D. F. & Trück, J. The antibody-secreting cell response to infection: Kinetics and clinical applications. *Frontiers in Immunology* vol. 8 Preprint at <https://doi.org/10.3389/fimmu.2017.00630> (2017).
86. Huang, A. T. *et al.* A systematic review of antibody mediated immunity to coronaviruses: kinetics, correlates of protection, and association with severity. *Nature Communications* 2020 11:1 **11**, 1–16 (2020).
87. Wrammert, J. *et al.* Rapid and Massive Virus-Specific Plasmablast Responses during Acute Dengue Virus Infection in Humans. *J Virol* **86**, 2911–2918 (2012).
88. Lee, F. E.-H. *et al.* Circulating Human Antibody-Secreting Cells during Vaccinations and Respiratory Viral Infections Are Characterized by High Specificity and Lack of Bystander Effect. *The Journal of Immunology* **186**, 5514–5521 (2011).
89. Amanat, F. *et al.* SARS-CoV-2 mRNA vaccination induces functionally diverse antibodies to NTD, RBD, and S2. *Cell* **184**, (2021).
90. Lee, F. E.-H. *et al.* Circulating Human Antibody-Secreting Cells during Vaccinations and Respiratory Viral Infections Are Characterized by High Specificity and Lack of Bystander Effect. *The Journal of Immunology* **186**, 5514–5521 (2011).
91. Goel, R. R. *et al.* Distinct antibody and memory B cell responses in SARSCoV-2 naïve and recovered individuals following mRNA vaccination. *Sci Immunol* **6**, 1–19 (2021).
92. Blanchard-Rohner, G., Pulickal, A. S., Jol-van Der Zijde, C. M., Snape, M. D. & Pollard, A. J. Appearance of peripheral blood plasma cells and memory B cells in a primary and secondary immune response in humans. *Blood* **114**, 4998–5002 (2009).
93. Galipeau, Y., Greig, M., Liu, G., Driedger, M. & Langlois, M. A. Humoral Responses and Serological Assays in SARS-CoV-2 Infections. *Front Immunol* **11**, 610688 (2020).
94. Dogan, I. *et al.* Multiple layers of B cell memory with different effector functions. *Nat Immunol* **10**, (2009).
95. Pape, K. A., Taylor, J. J., Maul, R. W., Gearhart, P. J. & Jenkins, M. K. Different B cell populations mediate early and late memory during an endogenous immune response. *Science (1979)* **331**, (2011).
96. Woodruff, M. C. *et al.* Dysregulated naive B cells and de novo autoreactivity in severe COVID-19. *Nature* 2022 611:7934 **611**, 139–147 (2022).
97. Lee, W. S., Wheatley, A. K., Kent, S. J. & DeKosky, B. J. Antibody-dependent enhancement and SARS-CoV-2 vaccines and therapies. *Nat Microbiol* **5**, (2020).
98. Oliveira, R. A. S. *et al.* Previous dengue or zika virus exposure can drive to infection enhancement or neutralisation of other flaviviruses. *Mem Inst Oswaldo Cruz* **114**, (2019).
99. Martin, R. K. *et al.* B1 Cell IgE Impedes Mast Cell-Mediated Enhancement of Parasite Expulsion through B2 IgE Blockade. *Cell Rep* **22**, 1824–1834 (2018).
100. Nemazee, D. Mechanisms of central tolerance for B cells. *Nature Reviews Immunology* 2017 17:5 **17**, 281–294 (2017).

## References

101. Lee, S., Ko, Y. & Kim, T. J. Homeostasis and regulation of autoreactive B cells. *Cell Mol Immunol* **17**, 561 (2020).
102. Wardemann, H. *et al.* Predominant autoantibody production by early human B cell precursors. *Science (1979)* **301**, 1374–1377 (2003).
103. Cappione, A. *et al.* Germinal center exclusion of autoreactive B cells is defective in human systemic lupus erythematosus. *J Clin Invest* **115**, 3205–3216 (2005).
104. Zikherman, J., Parameswaran, R. & Weiss, A. Endogenous antigen tunes the responsiveness of naive B cells but not T cells. *Nature* *2012* *489:7414* **489**, 160–164 (2012).
105. Kara, E. E. & Nussenzweig, M. C. Redemption for self-reactive antibodies. *Science (1979)* **360**, 152–153 (2018).
106. Burnett, D. L. *et al.* Germinal center antibody mutation trajectories are determined by rapid self/foreign discrimination. *Science (1979)* **360**, 223–226 (2018).
107. Reed, J. H., Jackson, J., Christ, D. & Goodnow, C. C. Clonal redemption of autoantibodies by somatic hypermutation away from self-reactivity during human immunization. *Journal of Experimental Medicine* **213**, 1255–1265 (2016).
108. Wu, Y. C. B., Kipling, D. & Dunn-Walters, D. K. The relationship between CD27 negative and positive B cell populations in human peripheral blood. *Front Immunol* **2**, 17303 (2011).
109. Goodnow, C. C., Sprent, J., Barbara, B. F. & Vinuesa, C. G. Cellular and genetic mechanisms of self tolerance and autoimmunity. *Nature* vol. 435 Preprint at <https://doi.org/10.1038/nature03724> (2005).
110. Espéli, M. *et al.* FcγRIIb differentially regulates pre-immune and germinal center B cell tolerance in mouse and human. *Nat Commun* **10**, (2019).
111. Sakaguchi, S., Yamaguchi, T., Nomura, T. & Ono, M. Regulatory T Cells and Immune Tolerance. *Cell* vol. 133 Preprint at <https://doi.org/10.1016/j.cell.2008.05.009> (2008).
112. Christen, U., Hintermann, E., Holdener, M. & von Herrath, M. G. Viral triggers for autoimmunity: Is the ‘glass of molecular mimicry’ half full or half empty? *Journal of Autoimmunity* vol. 34 Preprint at <https://doi.org/10.1016/j.jaut.2009.08.001> (2010).
113. Cepok, S. *et al.* Short-lived plasma blasts are the main B cell effector subset during the course of multiple sclerosis. *Brain* **128**, (2005).
114. Roark, J. H., Bussel, J. B., Cines, D. B. & Siegel, D. L. Genetic analysis of autoantibodies in idiopathic thrombocytopenic purpura reveals evidence of clonal expansion and somatic mutation. *Blood* **100**, (2002).
115. Hirokawa, M. *et al.* High-throughput sequencing of IgG B-cell receptors reveals frequent usage of the rearranged IGHV4–28/IGHJ4 gene in primary immune thrombocytopenia. *Sci Rep* **9**, (2019).
116. Broketa, M. & Bruhns, P. Single-Cell Technologies for the Study of Antibody-Secreting Cells. *Front Immunol* **12**, (2022).
117. Morgan, D. & Tergaonkar, V. Unraveling B cell trajectories at single cell resolution. *Trends in Immunology* vol. 43 Preprint at <https://doi.org/10.1016/j.it.2022.01.003> (2022).

## References

118. Delaloy, C., Schuh, W., Jäck, H.-M., Bonaud, A. & Espéli, M. Single cell resolution of Plasma Cell fate programming in health and disease. *Eur J Immunol* (2021) doi:10.1002/EJI.202149216.
119. Greiff, V. *et al.* What are the current driving questions in immune repertoire research? *Cell Systems* vol. 13 Preprint at <https://doi.org/10.1016/j.cels.2022.08.006> (2022).
120. Kwak, K., Akkaya, M. & Pierce, S. K. B cell signaling in context. *Nature Immunology* 2019 20:8 **20**, 963–969 (2019).
121. Kräutler, N. J. *et al.* Differentiation of germinal center B cells into plasma cells is initiated by high-affinity antigen and completed by Tfh cells. *Journal of Experimental Medicine* **214**, 1259–1267 (2017).
122. Viant, C. *et al.* Antibody Affinity Shapes the Choice between Memory and Germinal Center B Cell Fates. *Cell* **183**, 1298-1311.e11 (2020).
123. Wong, R. *et al.* Affinity-restricted memory B cells dominate recall responses to heterologous flaviviruses. *Immunity* **53**, 1078 (2020).
124. Neumeier, D. *et al.* Phenotypic determinism and stochasticity in antibody repertoires of clonally expanded plasma cells. *Proc Natl Acad Sci U S A* **119**, (2022).
125. Kato, Y. *et al.* Multifaceted Effects of Antigen Valency on B Cell Response Composition and Differentiation In Vivo. *Immunity* **53**, (2020).
126. Ferapontov, A. *et al.* Antigen footprint governs activation of the B cell receptor. *Nature Communications* 2023 14:1 **14**, 1–20 (2023).
127. Muecksch, F. *et al.* Affinity maturation of SARS-CoV-2 neutralizing antibodies confers potency, breadth, and resilience to viral escape mutations. *Immunity* **54**, 1853 (2021).
128. Broketa, M. *et al.* Qualitative monitoring of SARS-CoV-2 mRNA vaccination in humans using droplet microfluidics. *JCI Insight* **8**, (2023).
129. Sokal, A. *et al.* mRNA vaccination of naive and COVID-19-recovered individuals elicits potent memory B cells that recognize SARS-CoV-2 variants. *Immunity* (2021) doi:10.1016/J.IMMUNI.2021.09.011.
130. Sokal, A. *et al.* Analysis of mRNA vaccination-elicited RBD-specific memory B cells reveals strong but incomplete immune escape of the SARS-CoV-2 Omicron variant. *Immunity* **55**, 1096-1104.e4 (2022).
131. Sokal, A. *et al.* SARS-CoV-2 Omicron BA.1 breakthrough infection drives late remodeling of the memory B cell repertoire in vaccinated individuals. *Immunity* **56**, 2137-2151.e7 (2023).
132. Eyer, K. *et al.* Single-cell deep phenotyping of IgG-secreting cells for high-resolution immune monitoring. *Nat Biotechnol* **35**, (2017).
133. Lu, N. *et al.* Label-free microfluidic cell sorting and detection for rapid blood analysis. *Lab Chip* **23**, 1226–1257 (2023).
134. Bucheli, O. T. M., Sigvaldadóttir, I. & Eyer, K. Measuring single-cell protein secretion in immunology: Technologies, advances, and applications. *European Journal of Immunology* vol. 51 1334–1347 Preprint at <https://doi.org/10.1002/eji.202048976> (2021).

## References

135. AO, O., CM, S., E, P., E, G. & JC, L. Screening individual hybridomas by microengraving to discover monoclonal antibodies. *Nat Protoc* **4**, 767–782 (2009).
136. Q, H., EM, B., B, N., DA, H. & JC, L. Multidimensional analysis of the frequencies and rates of cytokine secretion from single cells by quantitative microengraving. *Lab Chip* **10**, 1391–1400 (2010).
137. Gérard, A. *et al.* High-throughput single-cell activity-based screening and sequencing of antibodies using droplet microfluidics. *Nat Biotechnol* **38**, (2020).
138. Asrat, S. *et al.* TRAPnSeq allows high-throughput profiling of antigen-specific antibody-secreting cells. *Cell Reports Methods* **3**, 100522 (2023).
139. Pinder, C. L. *et al.* Isolation and Characterization of Antigen-Specific Plasmablasts Using a Novel Flow Cytometry–Based Ig Capture Assay. *The Journal of Immunology* **199**, (2017).
140. Minoshima, M. & Kikuchi, K. Photostable and photoswitching fluorescent dyes for super-resolution imaging. *Journal of Biological Inorganic Chemistry* vol. 22 Preprint at <https://doi.org/10.1007/s00775-016-1435-y> (2017).
141. Li, W. H. & Zheng, G. Photoactivatable fluorophores and techniques for biological imaging applications. *Photochemical and Photobiological Sciences* vol. 11 Preprint at <https://doi.org/10.1039/c2pp05342j> (2012).
142. Lincoln, R. *et al.* A general design of caging-group-free photoactivatable fluorophores for live-cell nanoscopy. *Nat Chem* **14**, (2022).
143. Butkevich, A. N. *et al.* Photoactivatable Fluorescent Dyes with Hydrophilic Caging Groups and Their Use in Multicolor Nanoscopy. *J Am Chem Soc* **143**, (2021).
144. Chan, C. L. *et al.* DROPLAY: laser writing of functional patterns within biological microdroplet displays. *Lab Chip* **16**, 4621–4627 (2016).
145. Quah, B. J. C. & Parish, C. R. The use of carboxyfluorescein diacetate succinimidyl ester (CFSE) to monitor lymphocyte proliferation. *Journal of Visualized Experiments* (2010) doi:10.3791/2259.
146. Lašt'ovička, J., Budinský, V., Špišek, R. & Bartůňková, J. Assessment of lymphocyte proliferation: CFSE kills dividing cells and modulates expression of activation markers. *Cell Immunol* **256**, 79–85 (2009).
147. Victora, G. D. *et al.* Germinal Center Dynamics Revealed by Multiphoton Microscopy Using a Photoactivatable Fluorescent Reporter. *Cell* **143**, 592 (2010).
148. Patterson, G. H. Photoactivation and Imaging of Optical Highlighter Fluorescent Proteins. *Curr Protoc Cytom* **CHAPTER**, Unit (2011).
149. Ugur, M., Kaminski, A. & Pabst, O. Lymph node  $\gamma\delta$  and  $\alpha\beta$  CD8<sup>+</sup> T cells share migratory properties. *Scientific Reports 2018 8:1* **8**, 1–10 (2018).
150. Zatulovskiy, E., Zhang, S., Berenson, D. F., Topacio, B. R. & Skotheim, J. M. Cell growth dilutes the cell cycle inhibitor Rb to trigger cell division. *Science (1979)* **369**, 466–471 (2020).
151. Carrell, J. & Groves, C. J. OMIP-043: Identification of human antibody secreting cell subsets. *Cytometry Part A* **93**, (2018).

## References

152. Canales-Herrerias, P. *et al.* High-affinity autoreactive plasma cells disseminate through multiple organs in patients with immune thrombocytopenic purpura. *Journal of Clinical Investigation* **132**, (2022).
153. Shlomchik, M. J. Sites and Stages of Autoreactive B Cell Activation and Regulation. *Immunity* vol. 28 Preprint at <https://doi.org/10.1016/j.immuni.2007.12.004> (2008).
154. Tzovara, I., Papadatou, I., Tzanoudaki, M. & Spoulou, V. Development of a novel flow cytometry method for detecting pneumococcal-specific B cells. *Cytometry Part A* **101**, (2022).
155. Mahendra, A. *et al.* Honing-in antigen-specific cells during antibody discovery: a user-friendly process to mine a deeper repertoire. *Commun Biol* **5**, (2022).
156. Adams, R. M., Mora, T., Walczak, A. M. & Kinney, J. B. Measuring the sequence-affinity landscape of antibodies with massively parallel titration curves. *Elife* **5**, (2016).
157. Hägglöf, T. *et al.* Continuous germinal center invasion contributes to the diversity of the immune response. *Cell* **186**, (2023).
158. Yang, D., Singh, A., Wu, H. & Kroe-Barrett, R. Determination of high-affinity antibody-antigen binding kinetics using four biosensor platforms. *Journal of Visualized Experiments* **2017**, (2017).
159. Sokal, A. *et al.* Maturation and persistence of the anti-SARS-CoV-2 memory B cell response. *Cell* **184**, (2021).
160. Jammes, F. C. & Maerkl, S. J. How single-cell immunology is benefiting from microfluidic technologies. *Microsystems & Nanoengineering* **2020 6:1** **6**, 1–14 (2020).
161. Giladi, A. & Amit, I. Single-Cell Genomics: A Stepping Stone for Future Immunology Discoveries. *Cell* vol. 172 Preprint at <https://doi.org/10.1016/j.cell.2017.11.011> (2018).
162. Ginhoux, F., Yalin, A., Dutertre, C. A. & Amit, I. Single-cell immunology: Past, present, and future. *Immunity* vol. 55 Preprint at <https://doi.org/10.1016/j.immuni.2022.02.006> (2022).
163. Kong, D. S. *et al.* Open-source, community-driven microfluidics with Metafluidics. *Nature Biotechnology* vol. 35 Preprint at <https://doi.org/10.1038/nbt.3873> (2017).